Technical Report No. IFAORS-143 1980

Anderson

INVESTIGATION OF MULTIPLE SCATTERING EFFECTS IN AEROSOLS

By

Adarsh Deepak
Principal Investigator

Final Report
For the period September 1978 - December 1979

Prepared for the

National Aeronautics and Space Administration
George C. Marshall Space Flight Center
Marshall Space Flight Center, Alabama 35812

Under

Contract NAS8-33135
B. J. Anderson, Technical Monitor
Space Sciences Laboratory

May 30, 1980

IFAORS
Institute for Atmospheric Optics and Remote Sensing
P.O. Box P, Hampton, Virginia 23666

Technical Report No. IFAORS-143 1980

INVESTIGATION OF MULTIPLE SCATTERING EFFECTS IN AEROSOLS

By

Adarsh Deepak
Principal Investigator

Final Report
For the period September 1978 - December 1979

Prepared for the

National Aeronautics and Space Administration
George C. Marshall Space Flight Center
Marshall Space Flight Center, Alabama 35812

Under

Contract NAS8-33135
B. J. Anderson, Technical Monitor
Space Sciences Laboratory

May 30, 1980

IFAORS
Institute for Atmospheric Optics and Remote Sensing
P.O. Box P, Hampton, Virginia 23666

TABLE OF CONTENTS

SUMMARY

This is the final report for NASA Contract NAS8-33135. This report presents the results of investigations on the various aspects of multiple scattering effects on visible and infrared laser beams transversing dense fog oil aerosols contained in a chamber (4' x 4' x 9'). In connection with these investigations the data for the time-history of aerosol optical depth, and the aerosol size distribution and mass concentration measurements were provided by Dr. Gerald C. Holst, Chemical Systems Laboratory. The report briefly describes: (i) the experimental details and measurements (Section 2); (ii) analytical representation of the aerosol size distribution data by two analytical models--the regularized power law distribution and the inverse modified gamma distribution (Section 3); (iii) retrieval of aerosol size distributions from multi-spectral optical depth measurements by two methods--the 2- and 3-parameter fast table search methods and the nonlinear least squares method (Section 4); (iv) modeling of the effects of aerosol microphysical (coagulation and evaporation) and dynamical processes (gravitational settling) on the temporal behavior of aerosol size distribution, and hence on the extinction of 4 laser beams with wavelengths - 0.44, 0.6328, 1.15 and 3.39 μm (Section 5); (v) and the exact and approximate formulations for four methods--Tam and Zardecki, Dolin-Fante, Arnush-Stotts, and our exact method--for computing the effects of multiple scattering on the transmittance of laser beams in dense aerosols, all of which are based on the solution of the radiative transfer equation under the small angle approximation (Section 6). In addition, the report identifies problem areas in which further research needs to be performed in the near future.

1. INTRODUCTION

Whenever a beam of radiation passes through an aerosol medium, its energy always decreases during transit. The loss of energy is due to either scattering or absorption or both in the medium. The term extinction is defined as the sum of absorption and scattering. The transmittance T for a parallel, monochromatic beam of radiation of wavelength λ after passage through an homogeneous aerosol layer of length L and extinction coefficient $\beta_{ext}(\lambda)$, in the single scattering (SS) approximation, is given by Bouguer's law, $T = e^{-\tau(\lambda)}$, where the optical depth $\tau(\lambda) = \beta_{ext}(\lambda)\, L$.

In SS, the scattered photon reaching the detector suffers only one scattering event; whereas, in multiple scattering (MS), it suffers more than one scattering event. Thus, the N^{th} order scattering refers to a case when a photon is scattered and rescattered N times before reaching the detector. The basis of the SS theory is that if one knows the scattering properties of an individual particle, then the scattering effect of N similar particles is simply N times that of a single particle (Ref. 1). Such a simple direct proportionality to N particles is what makes the SS theory so simple.

In the case of MS, this proportionality to N particles no longer holds, thereby making the theory very complicated. Therefore, except for a few researchers (Refs. 1-8), not much work has been done on experimental investigations on MS; even though relatively more work has been done on the theoretical aspects of MS (Refs. 9-19). Therefore, a coordinated research program was undertaken between the Institute for Atmospheric Optics and Remote Sensing (IFAORS), NASA-Marshall Space Flight Center (MSFC) and Army Aberdeen Chemical System Laboratory (CSL) to implement systematic research effort in the theoretical and experimental aspects of MS in aerosols in controlled laboratory environment. The theoretical research was performed at the Institute and the experimental work, at the NASA-MSFC and CSL. Important features of such a theoretical and experimental approach to MS investigations was that the numerical results based on theoretical MS models could be compared with experimental results and vice versa.

In this program, it was decided to start with the simple experiments on measurement of attenuation of visible and IR laser beams traversing through fog oil aerosols contained in a closed chamber. Simultaneous measurements of optical depth for three or four wavelengths were made as a function of time. In addition, measurements of the aerosol size distribution (SD) were made at two different times during such an experiment. The experimental details and the measurements are described in Section 2.

In order to get a better understanding of the experimental SD data, the first step was to represent the data with some commonly used analytic model(s) (Ref. 21). The results are described in Section 3.

The experimental results for $\tau(\lambda,t)$, provided us with data for three or four independent measurements of τ, corresponding to the three or four wavelengths, times t during the experiments, which were conducted for time periods of about 50 to 150 min. From these three independent measurements, it was possible to retrieve three unknown parameters characterizing the aerosol size distribution at time t. There are several methods for retrieving aerosol size distribution from τ versus λ data (Ref. 22). But, since the ultimate goal of our work was to develop a software that will provide on-line retrievals of the aerosol size distribution from laser beam extinction measurements, we worked on developing fast, approximate search methods, and compared the results with those obtained using a numerical inversion scheme, such as the Nonlinear Least Squares (NLLS) method. Validation of the results was conducted by checking them against the actual size distribution measurements. We developed the two-parameter and the three-parameter search methods, which will be discussed in Sections 4.1, 4.2, and 4.3 of this report. An error analysis of the retrieved size distribution results is given in Section 4.4.

The size distribution measurements and the retrievals show that as the time increases, the peak of the aerosol size distribution tends to shift toward larger radii and lower number densities. This means that processes other than simple sedimentation are also present. In order to explain the time behavior of the aerosol size distribution, we have to perform modeling and sensitivity studies, which involve developing models of aerosol microphysical and dynamical processes--considered separately or in combinations--to study how each process effects the time behavior of the size distribution and the optical depth

at the wavelengths involved. The results of a parametric modeling study to investigate the separate and combined effects of sedimentation, coagulation and evaporation/growth are discussed in Sections 5.1 and 5.2. The theoretical study of multiple scattering effects of laser beams in dense aerosols is discussed in Section 6.

2. EXPERIMENTAL DETAILS AND MEASUREMENTS

The experiments on laser beam propagation through dense aerosols were conducted at the Chemical Systems Laboratory (CSL) by Dr. Gerald Holst. Aerosols were placed inside a closed chamber, which is essentially a wooden box (approximately 9' x 5' x 4') blackened flat black on the inside and having entrance and exit apertures on opposite sides of the box for the passage of laser beams (Fig. 1). The experimental geometry is schematically illustrated in Fig. 2.

The laser beams used in the experiments were: λ = 441.6 nm (He-Cd); 632.8 nm (He-Ne); 1.15 μm (He-Ne); and 3.30 μm (He-Ne). The physical and optical properties of fog oil, used for aerosol generation, are given in Table 1.

Measurements of the time variation of optical depth for 3 or 4 wavelengths simultaneously, and of size distributions were made in a series of experiments. Data for three sets of these experiments performed on November 30, 1978, January 21, 1979 and February 22, 1979 were provided to us by Dr. G. Holst. Those are summarized in Table 2. Measurements of $\tau(\lambda,t)$ and $n(r)$ are described next.

Multiwavelength Optical Depth vs. Time Curves: Typically, with the box completely empty of fog oil aerosols, the laser beams were turned on, so that their beams after traversing through the empty box impinged on lens-pinhole-type detector systems (Fig. 2b), having very narrow fields of view, placed across the box opposite the lasers. The divergence angles of the laser beam was $\sim$ 2 millirad and the acceptance angle of the detector field of view was $\sim$ 13 millirad. Narrow angles were necessary to ensure that the errors due to forward scattering were negligibly small. The intensities were recorded on chart recorders which were adjusted to full scale, representing 100 percent transmission, when the box was empty. The chamber was then filled with fog oil aerosols by using the evaporation/condensation technique, which involves letting a certain amount of fog oil vapor inside the box through an inlet, and stirring the air in the box by turning on three or four upward-directed fans located at the bottom of the box. The chart recorders, one for each of the laser beams, continued to record the direct beam intensities, simultaneously. During the filling of the

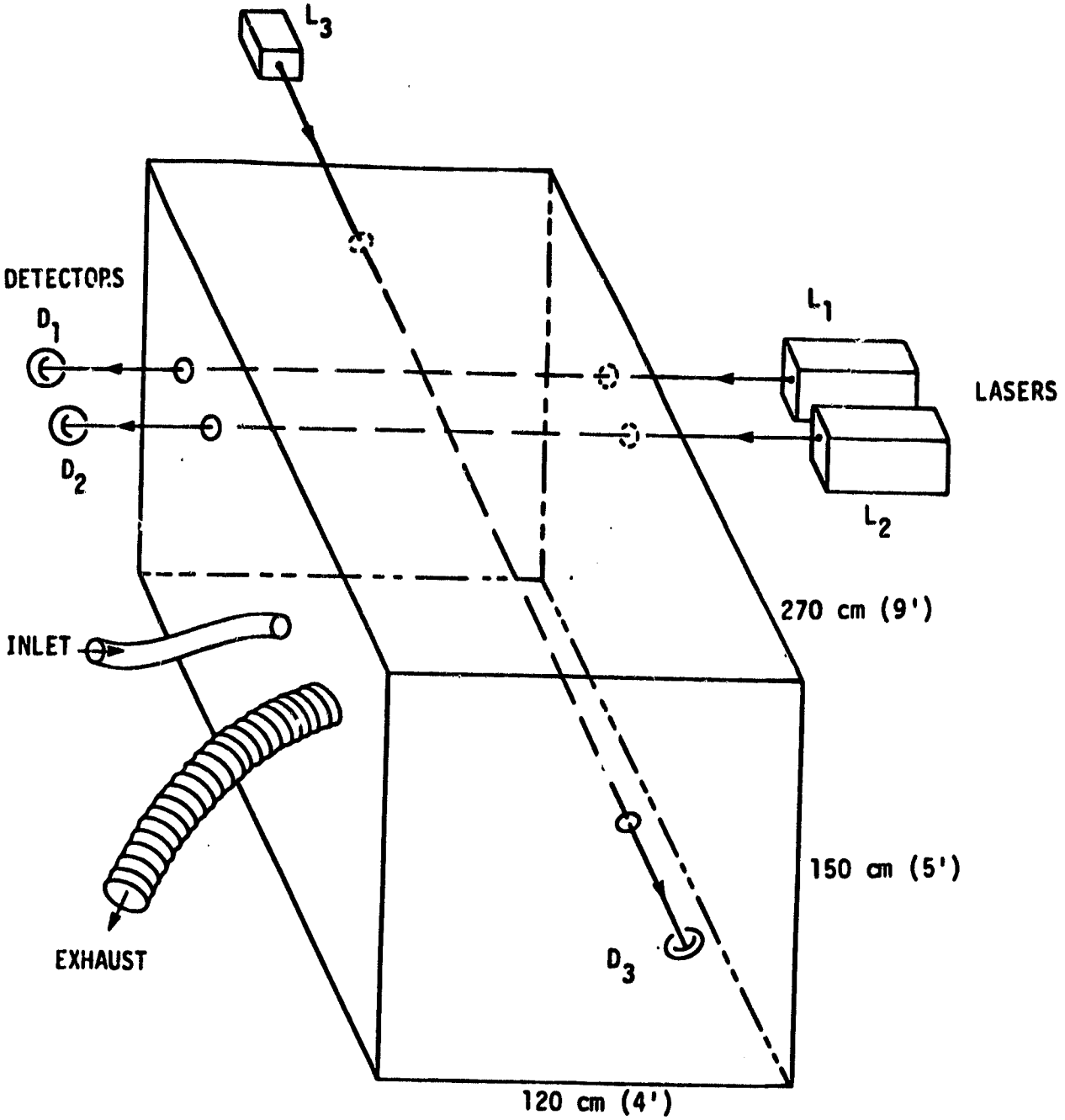

FIGURE 1. Schematic illustration of the experimental apparatus.

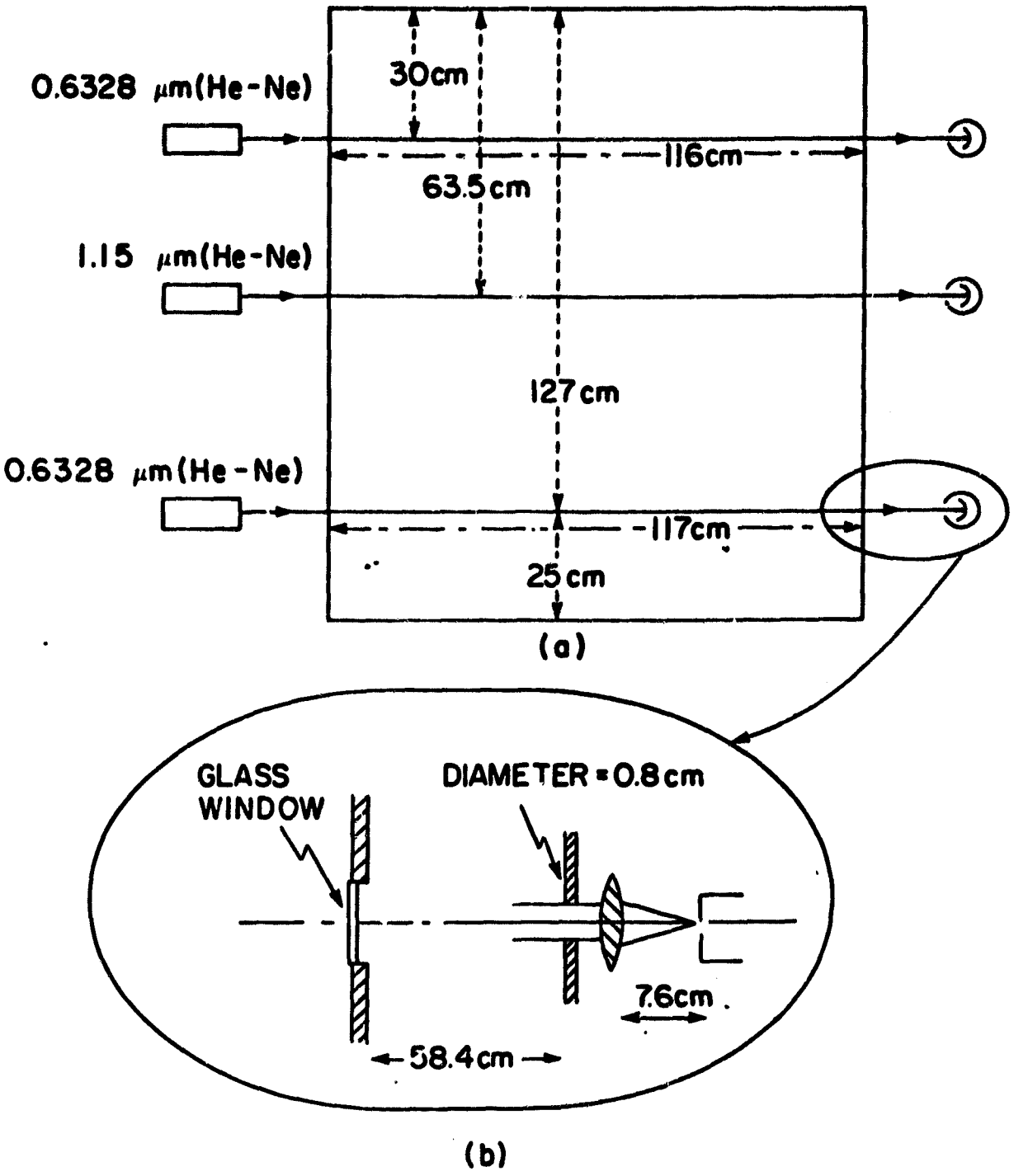

FIGURE 2. Schematic illustration of (a) the experimental geometry, and (b) the detector system.

TABLE 1. PROPERTIES OF FOG OIL (SGF #2)

Molal Average Boiling Point	= 354°C
Surface Tension (25°C)	= 34 dynes/cm
Specific Gravity (16°C)	= 0.9218 gm/cm^3
Molecular Weight	= 275
Vapor Pressure (99°C)	= 0.028 mm of Hg

λ (μm)	Refractive Index
0.4416	$1.5077-i\ (2.339 \times 10^{-5})$*
0.6328	$1.5077-i\ (9.527 \times 10^{-6})$*
1.15	$1.52 - i\ (1.378 \times 10^{-6})$*
3.39	1.44 - i (0.101)**
10.59	1.48 - i (0.163)**

*Obtained by Abbe Refractometer. Private communication by Dr. G. Holst

**Ref. 1: Dr. M. R. Querry's Values. Private communication.

TABLE 2. EXPERIMENTAL DATA SETS* FOR τ VS. t and n(r).

Measurement Set	Dates	Experimental Data Taken	Assumed Error
Set 1	11/30/78	(a) τ vs. t for λ = 0.6328, 1.15, and 3.39 μm	± 3%
		(b) n(r) at time t = 0.5 and 51.25 min	
		(c) mass concentration M_c at several times during the experiment	
Set 2	1/22/79	τ vs. t for λ = 0.6328, 1.15, and 3.39 μm	
Set 3	2/22/79	(a) τ vs. t for λ = 0.4416, .6328, 1.15, and 3.39 μm	± 3%
		(b) n(r) at time t = 2.5 and 62.00 min	
		(c) mass concentration M_c at several times during the experiment	

*Provided by Dr. G. Holst, CSL

chambers with fog oil aerosols, the intensities of the direct beams continued to decrease. When the aerosol appeared to be uniformly mixed, the fan was turned off, the time being referred to as t = 0 min. Thereafter, the intensity of 0.4416 and 0.6328 μm beams started to increase, while that of the other two laser beams (λ = 1.15 μm and 3.39 μm) first continued to decrease gradually and after a certain time started to increase. From the chart-recorder intensity measurements, it was easy to obtain temporal records of the optical depths, τ, for the laser beams by the use of Bouguer (Lambert-Beer) transmission law:

$$\frac{I(\lambda,t)}{I(\lambda,0)} = e^{-\tau(\lambda,t)}$$

where t is the time in minutes. The plots of $\tau(\lambda,t)$ vs. t curves for λ = 0.6328, 1.15 and 3.39 μm for Set 1 (November 30, 1978) are shown in Fig. 3. They show that for λ = 1.15 and 3.39 μm, τ first increased for about 20 and 30 min, respectively, and then started to decrease, indicating that the size distribution was changing with time. Similar plots of $\tau(\lambda,t)$ vs t for Sets 2 and 3 are shown in Figs. 4 and 5 respectively.

In addition, experiments were performed with two 0.6328 μm lasers placed at two different heights (see Fig. 2a) to make τ vs. t measurements, in order to investigate if there was any difference in the τ vs. t curves. Results for one such experiment are shown in Fig. 4 with curves marked upper and lower, which were close to within experimental error.

Aerosol Size Distribution Measurements: In addition, aerosol size distribution measurements were made with a ten-stage Andersen impactor twice during the transmission experiments for Sets 1 and 3. For Set 1, the measurements were made one at the beginning (t_1 = 0.5 min) and the second time near the end (t_2 = 51.25 min) and are shown in Fig. 6. From dN/d log d data, we derived the area and volume size distributions by calculating d^2(dN/d log d) and d^3(dN/d log d). The latter are useful representations as they give us some idea of the scattering effects and the mass distribution of aerosols. The three types of representations of aerosol size distribution are plotted for Set 1 and times t = 0.5 and 51.25 min in Figs. 7 and 8 on log-log graphs, which are identical in scale to the graphs in Ref. 21. For Set 3, the size distribution (dN/d log d) measurements were made at t = 2.5 min and 62.0 min, and the data is shown in Fig. 9. The data for mass concentration M_c measured at various times during the Set 1 and Set 3 experiments are shown in Fig. 10.

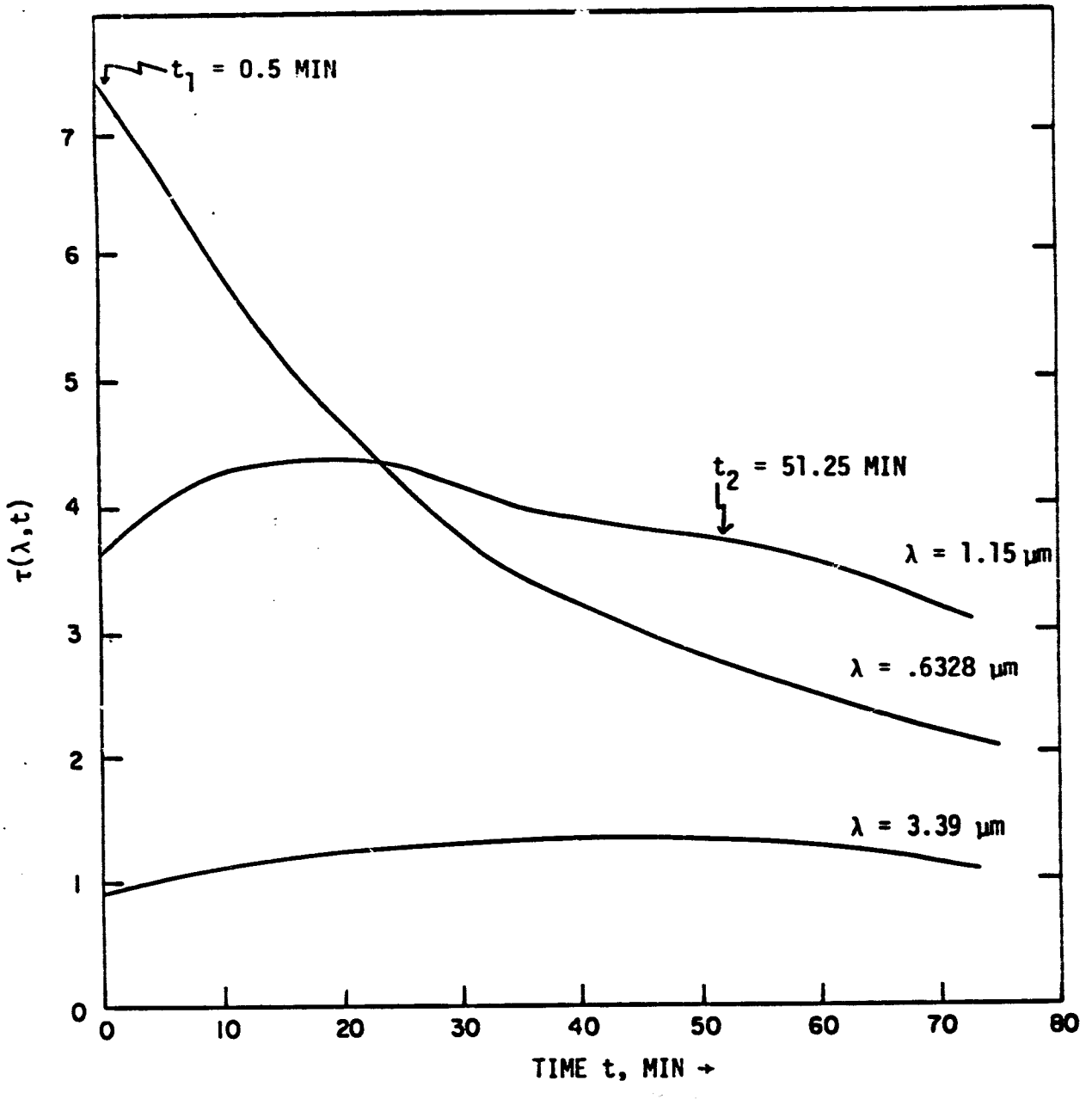

FIGURE 3. Set 1 data for τ vs. t for λ = 0.6328, 1.15 and 3.39 μm.

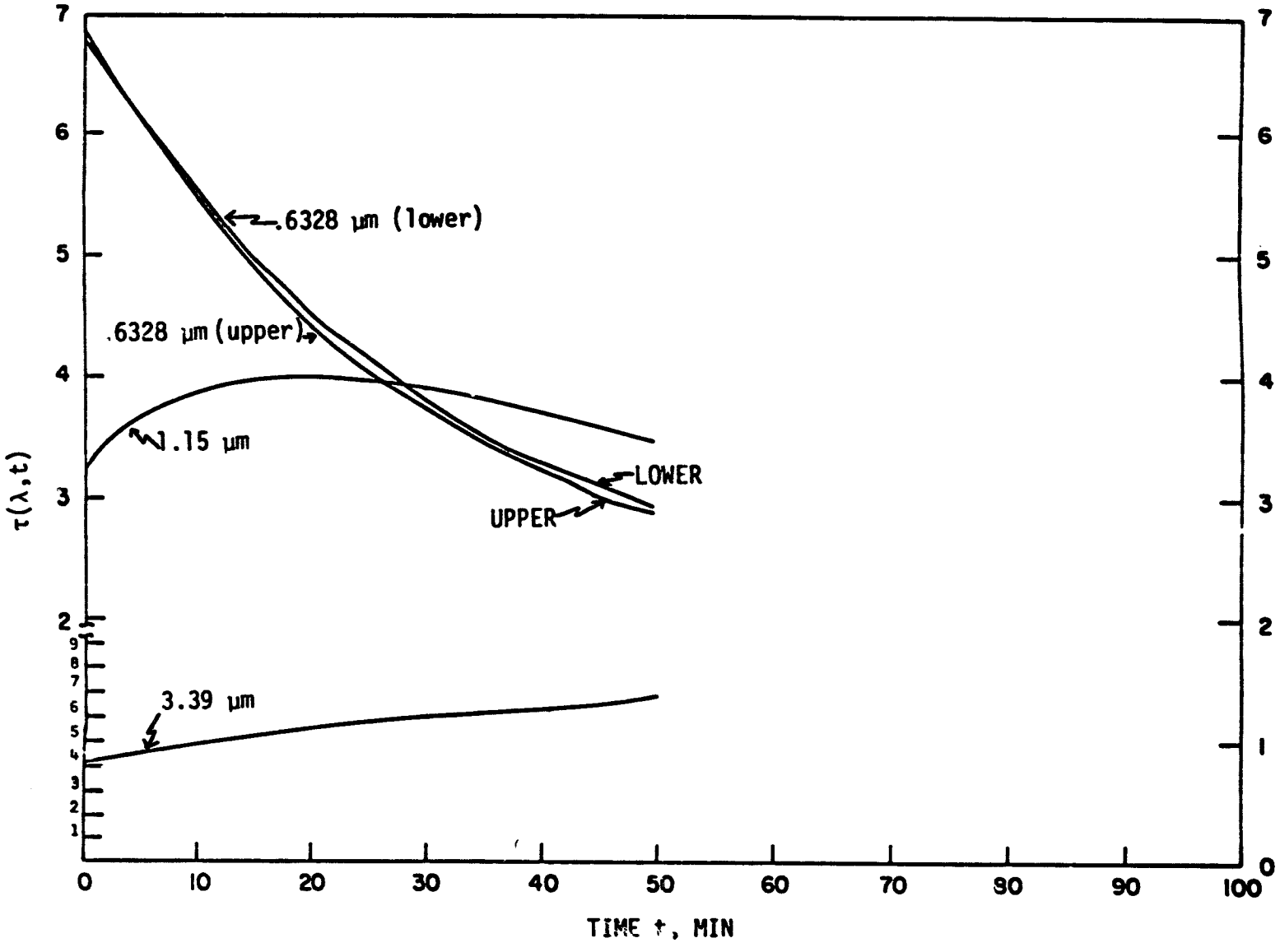

FIGURE 4. Set 2 data for τ vs. t for λ = 0.6328 μm laser beam located at 30 cm and 127 cm levels from the top of the box, and for λ = 1.15 and 3.39 μm laser beams at 63.5 cm level (see Fig. 2a).

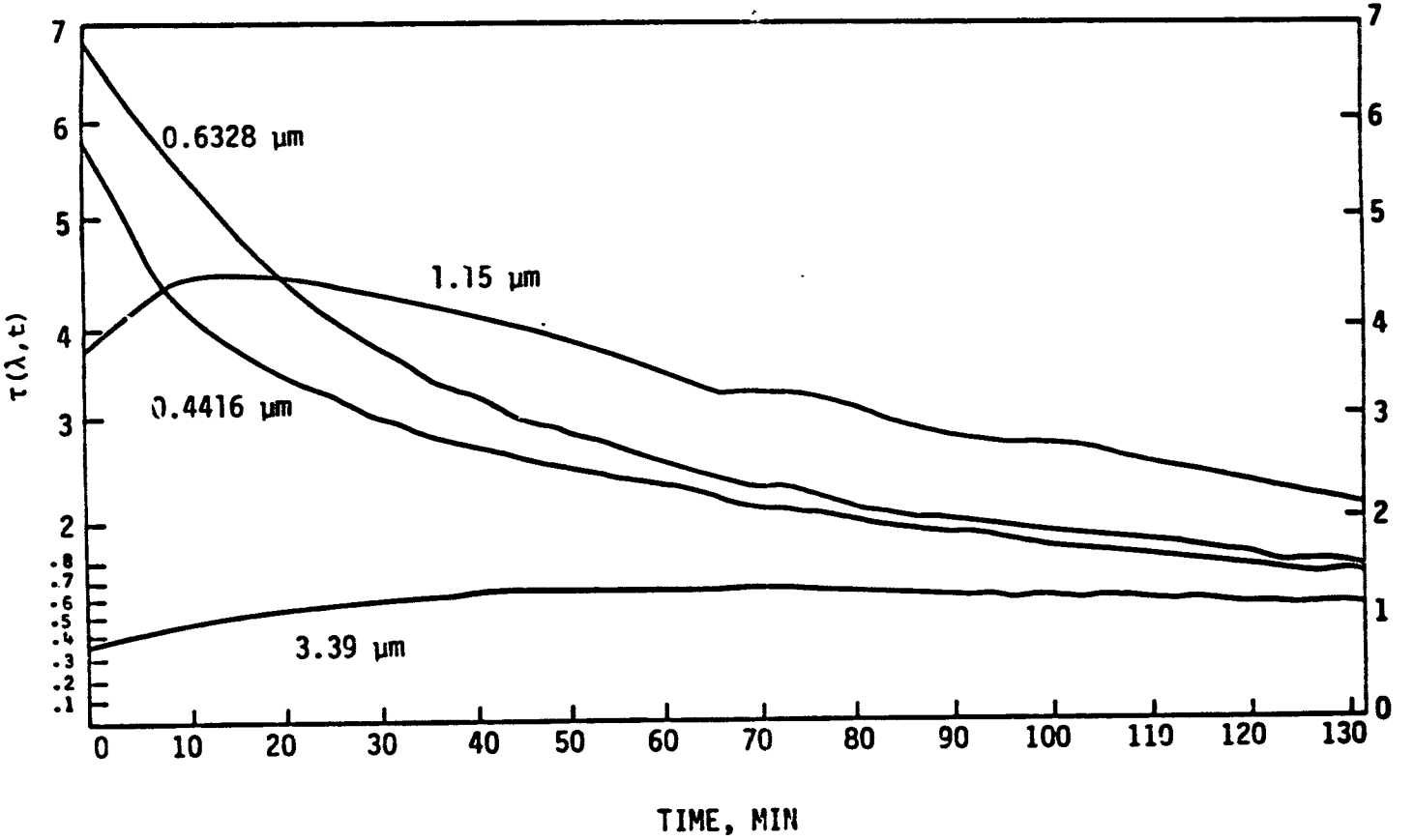

FIGURE 5. Set 3 data for optical depth versus time for λ = 0.4416, 0.6328, 1.15 and 3.39 μm.

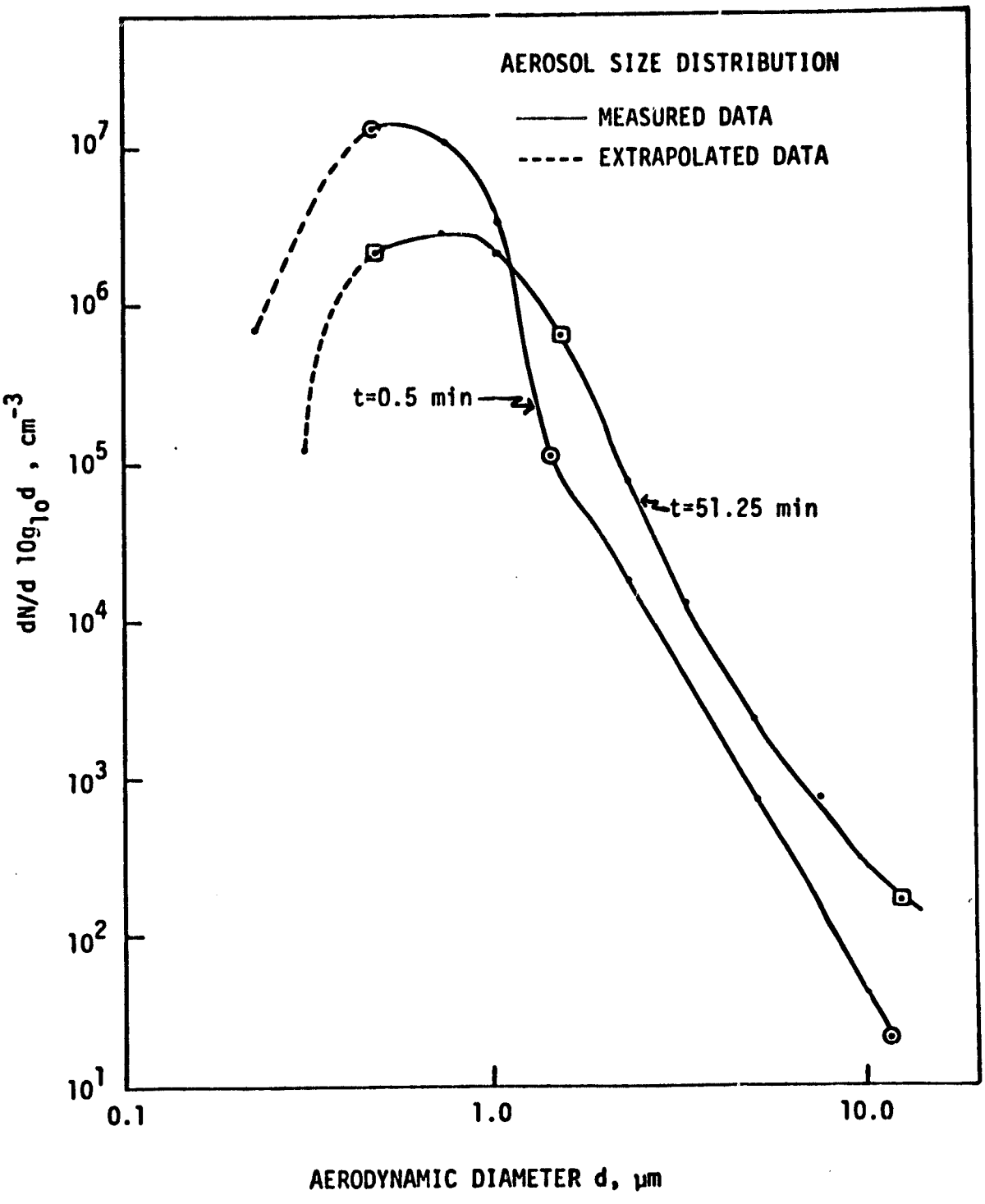

FIGURE 6. Set 1 data for the size distribution at times t = 0.5 and 51.25 min.

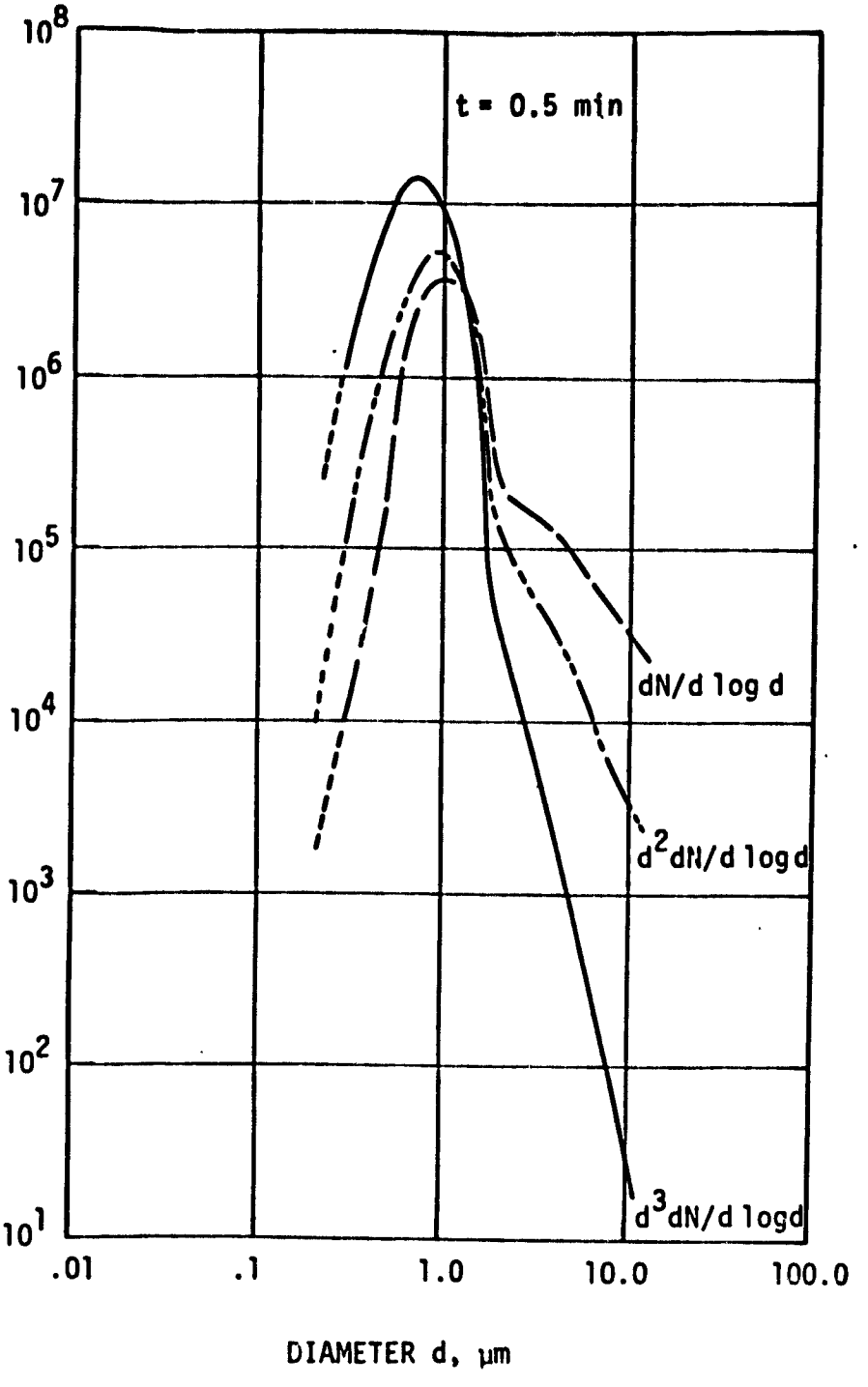

FIGURE 7. The number, area and volume size distribution curves for Set 1 at t = 0.5 min.

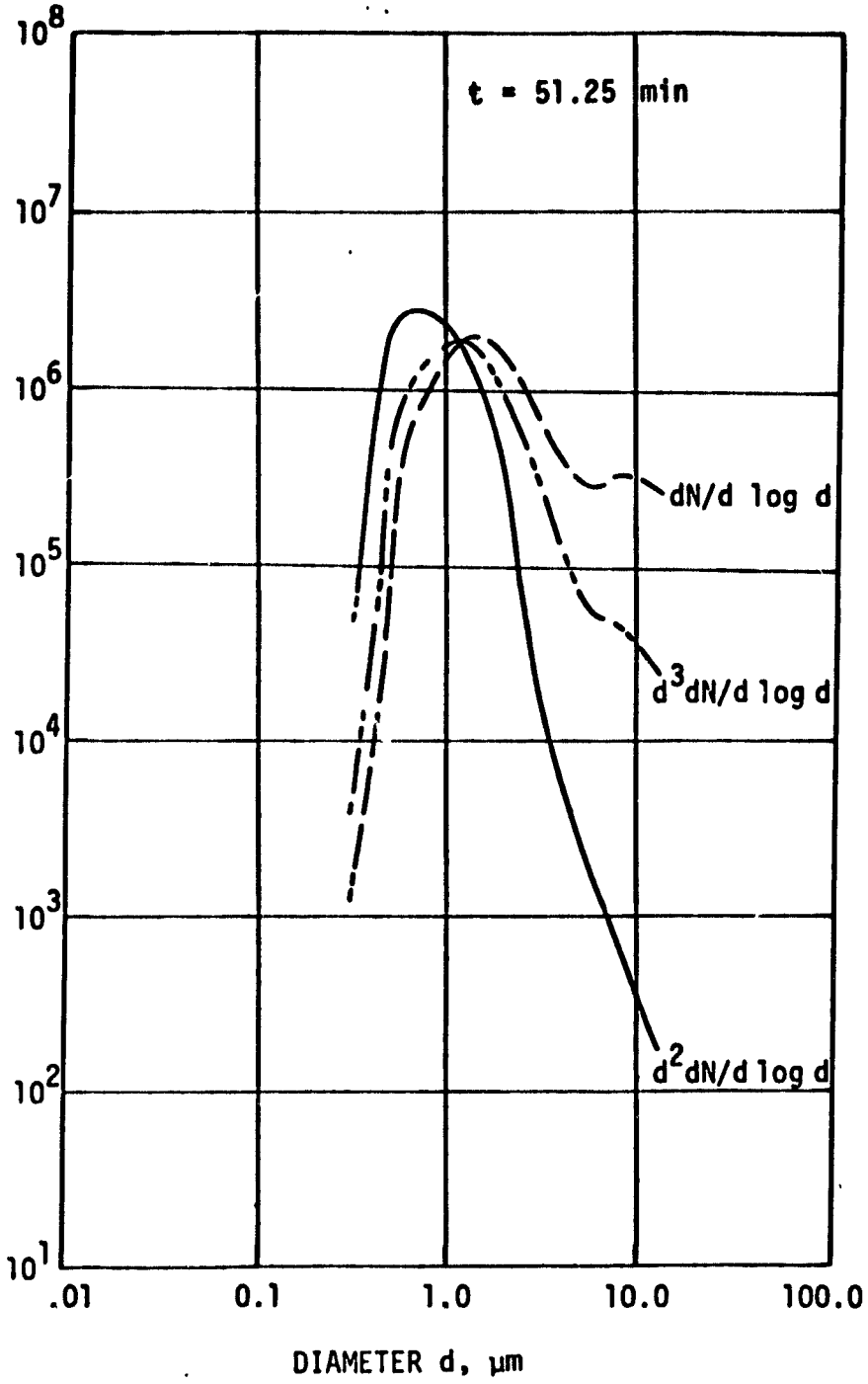

FIGURE 8. The number, area and volume size distribution curves for Set 1 at t = 51.25 min.

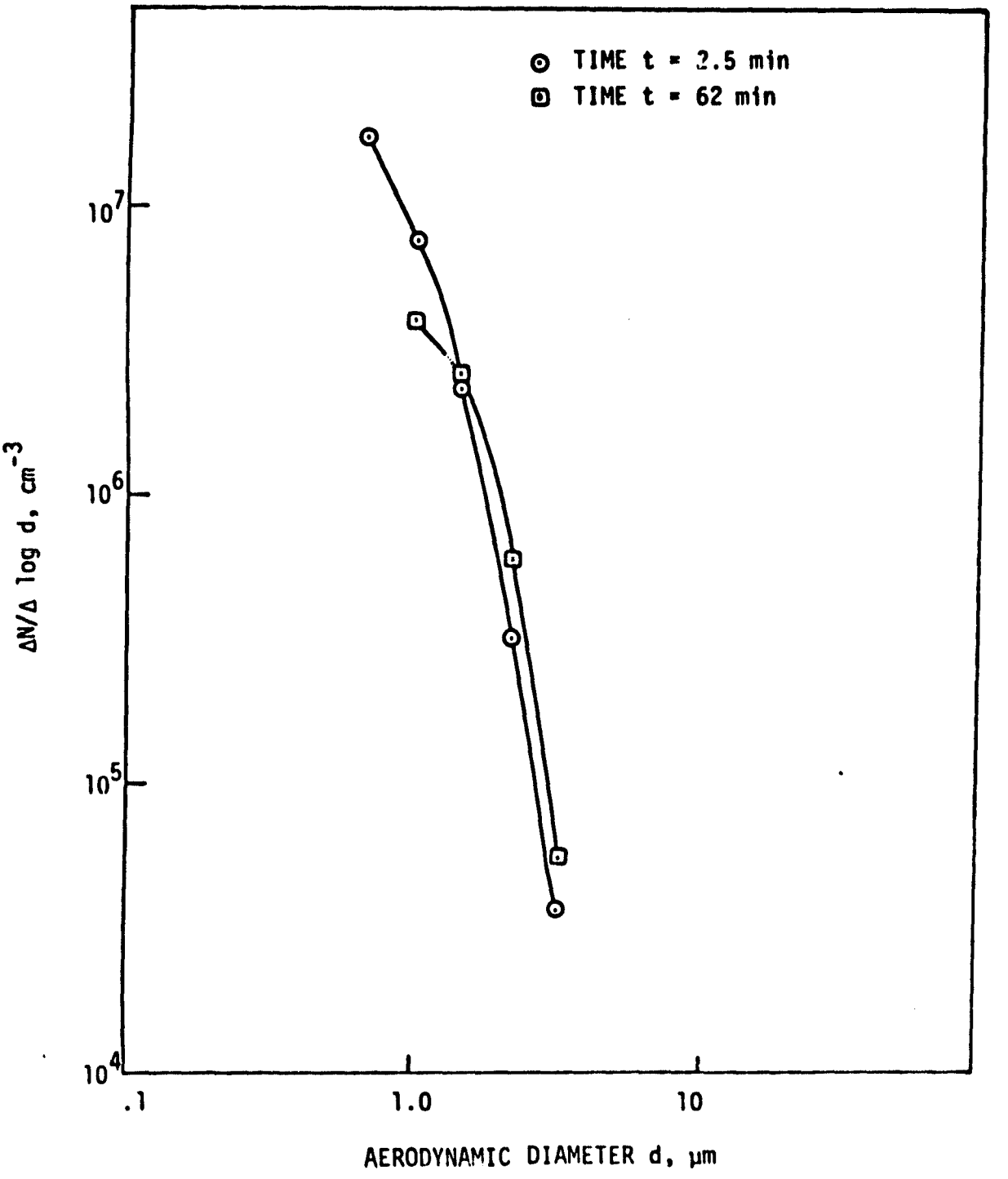

FIGURE 9. Set 3 data for size distributions at times t = 2.5 and 62 min.

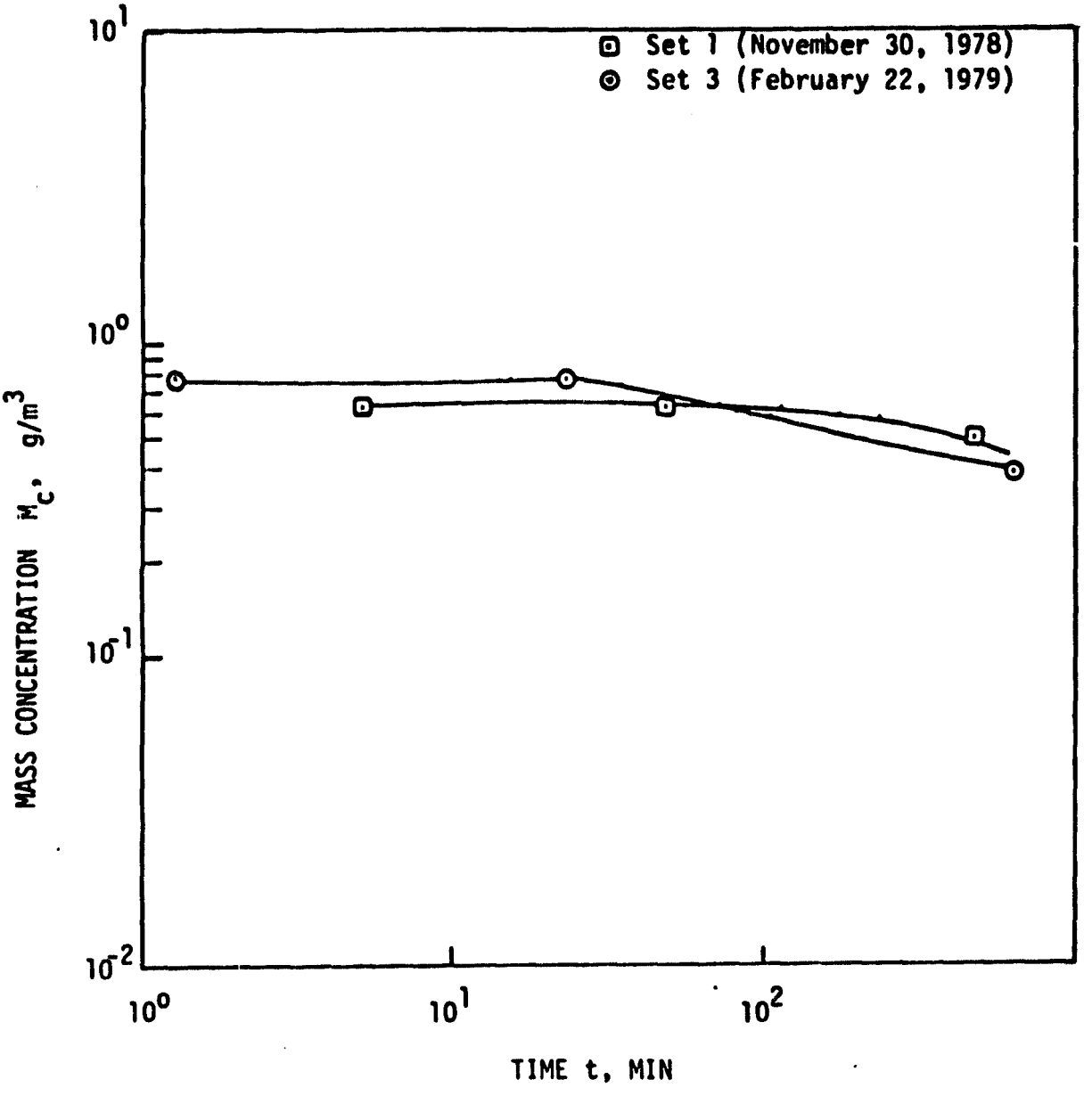

FIGURE 10. Set 1 and 3 data for mass concentration M_c as a function of time.

3. ANALYTIC REPRESENTATION OF AEROSOL SIZE DISTRIBUTION DATA

The Andersen Impactor data for the aerosol size distribution, $dN/d \log_{10} d$, measured at times t = 0.5 min and 51.25 min (Fig. 6) for Set 1 was converted to dN/dr, i.e. n(r), where r = d/2, and plotted on a log-log graph identical in size to the graphs in the parametrized graphical catalog for size distribution models (Ref. 21). By overlaying and matching the experimental data with the appropriate catalog graphs belonging to the selected analytic model, such as, Regularized Power Law Distribution (RPLD), Inverse Modified Gamma Distribution (IMGD), or Log Normal Distribution (LND), we obtained the first guess estimates for the model parameters p_i, i = 1, 2, ... Then by inputing these values as 1st guess estimates of the model parameters into a non-linear least squares (NLLS) program, we could quickly obtain the values of the p_i that provide the best fit to the experimental data. The n(r) data was thus fitted, in the least squares sense, with the following analytic models; RPLD, IMGD, LND, and two term models such as the IMGD plus power law and the LND plus power law distribution. From among these models, two gave the best fit to the experimental data. They are the Regularized Power Law Distribution (RPLD)

$$n(r) = \frac{p_1}{p_2} \frac{(r/p_2)^{p_3-1}}{(1 + (r/p_2)^{p_3})^{p_4}} \tag{1a}$$

and the Inverse Modified Gamma Distribution (IMGD)

$$n(r) = p_1 \frac{e^{-p_3/(r^{p_4})}}{r^{p_2}} \tag{1b}$$

The results of the fits to these two models are shown in Figs. 10-13 and discussed as follows:

(i) Figure 11 (Data at t = 0.5 min, RPLD model): The RPLD model gives good fits to the data for r < 0.1 μm or r > 2.0 μm; but in the 0.1 - 2.0 μm range the fit is not as good. (Circles denote the experimental data; squares,

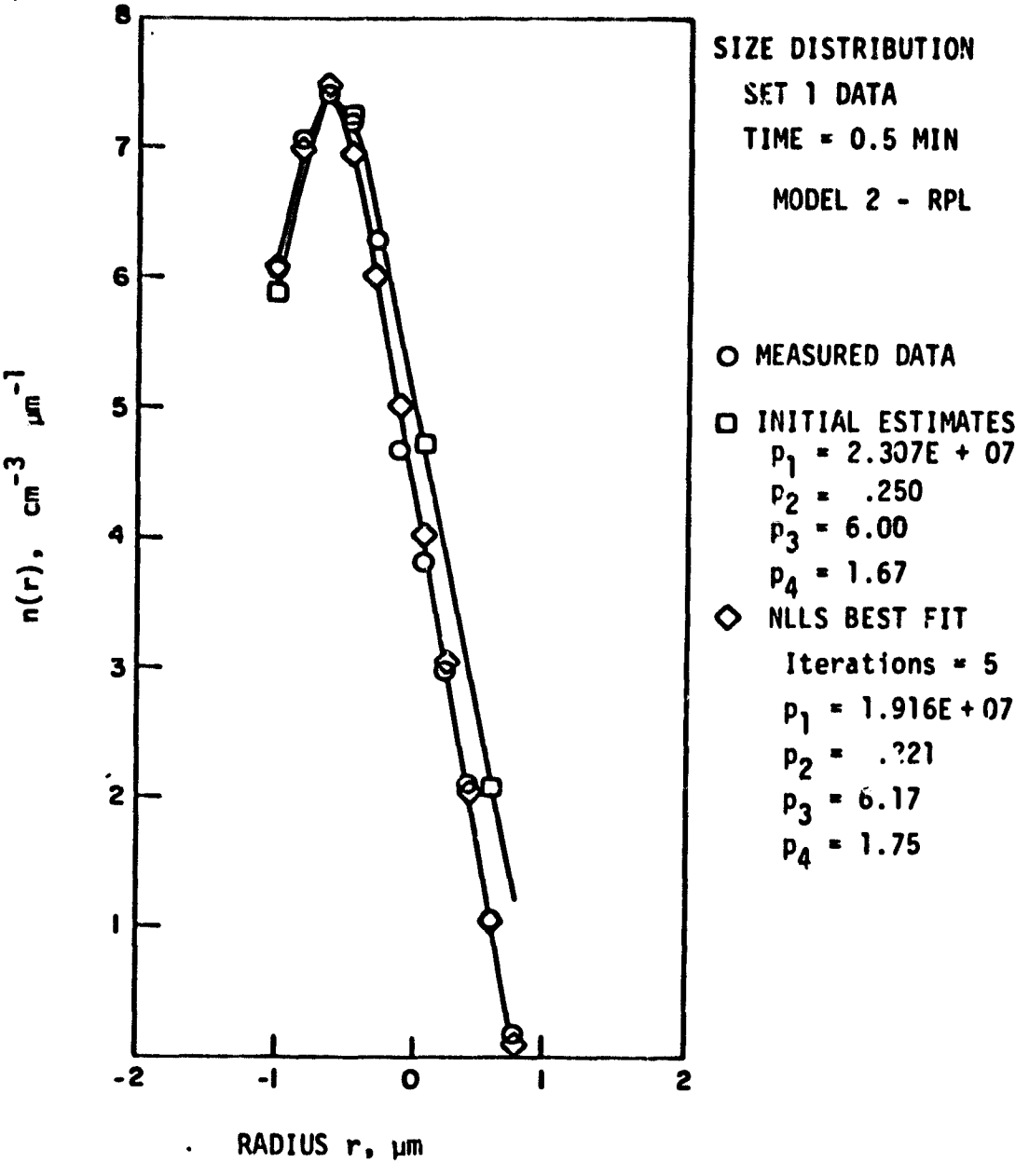

FIGURE 11. Analytic representation of Set 1, t = 0.5 min, size distribution data using a Regularized Power Law (RPL) Model.

the initial estimates of the model parameters p_i, i = 1, 2, 3, and 4; diamonds, the best fit values of p_i, obtained after convergence is reached in 7 iterations.)

(ii) Figure 12 (Data at t = 0.5 min, IMGD model): Good fits to data for r < 0.2 μm and r > 0.7 μm. The fit around the peak is somewhat poor.

(iii) Figure 13 (Data at t = 51.5 min, RPLD model): Final fits are quite good for most of the experimental data.

(iv) Figure 14 (Data at t = 51.5 min, IMGD model): Fits to the data are reasonably good.

It should be kept in mind that n(r) data in Set 1 shows a kink in the curve around 2.0 μm, thereby indicating that the size distribution is bimodal. But since the analytic models used to fit the data are unimodal, RPLD and IMGD models will not fit the data very well in the whole size range. Fitting with a two term bimodal analytic model was not attempted for Set 1 n(r) data, even though it has been used in the retrieval of size distributions from τ vs λ data as discussed in Section 4.3.

It should further be noted that in Figs. 6-8, the data for r < 0.3 μm are extrapolated data. No analytic fits were attempted for the Set 3 size distribution data for t = 2.5 and 62.0 min, shown in Fig. 9.

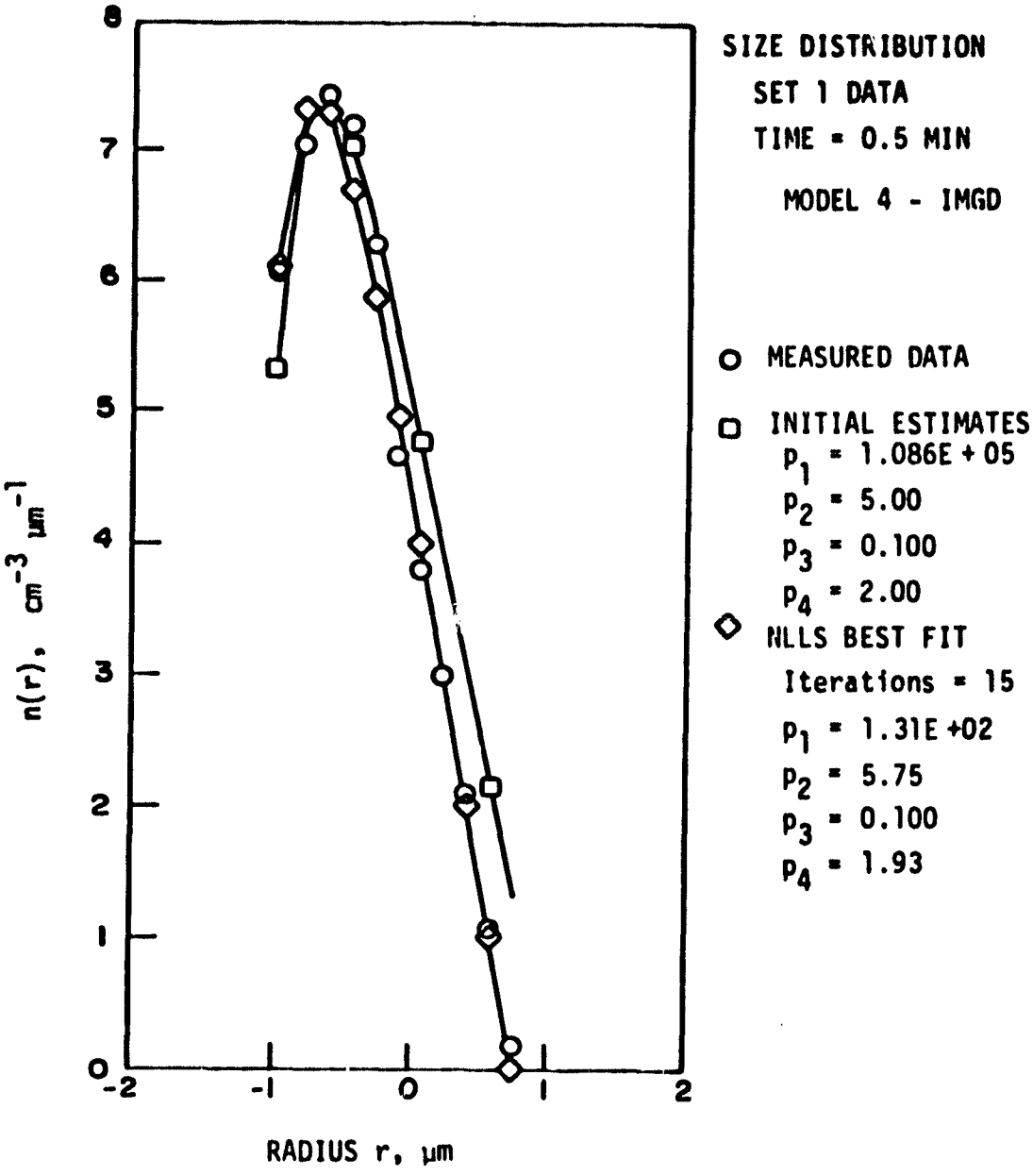

FIGURE 12. Analytic representation of Set 1, t = 0.5 min size distribution data using an Inverse Modified Gamma Distribution (IMGD) Model.

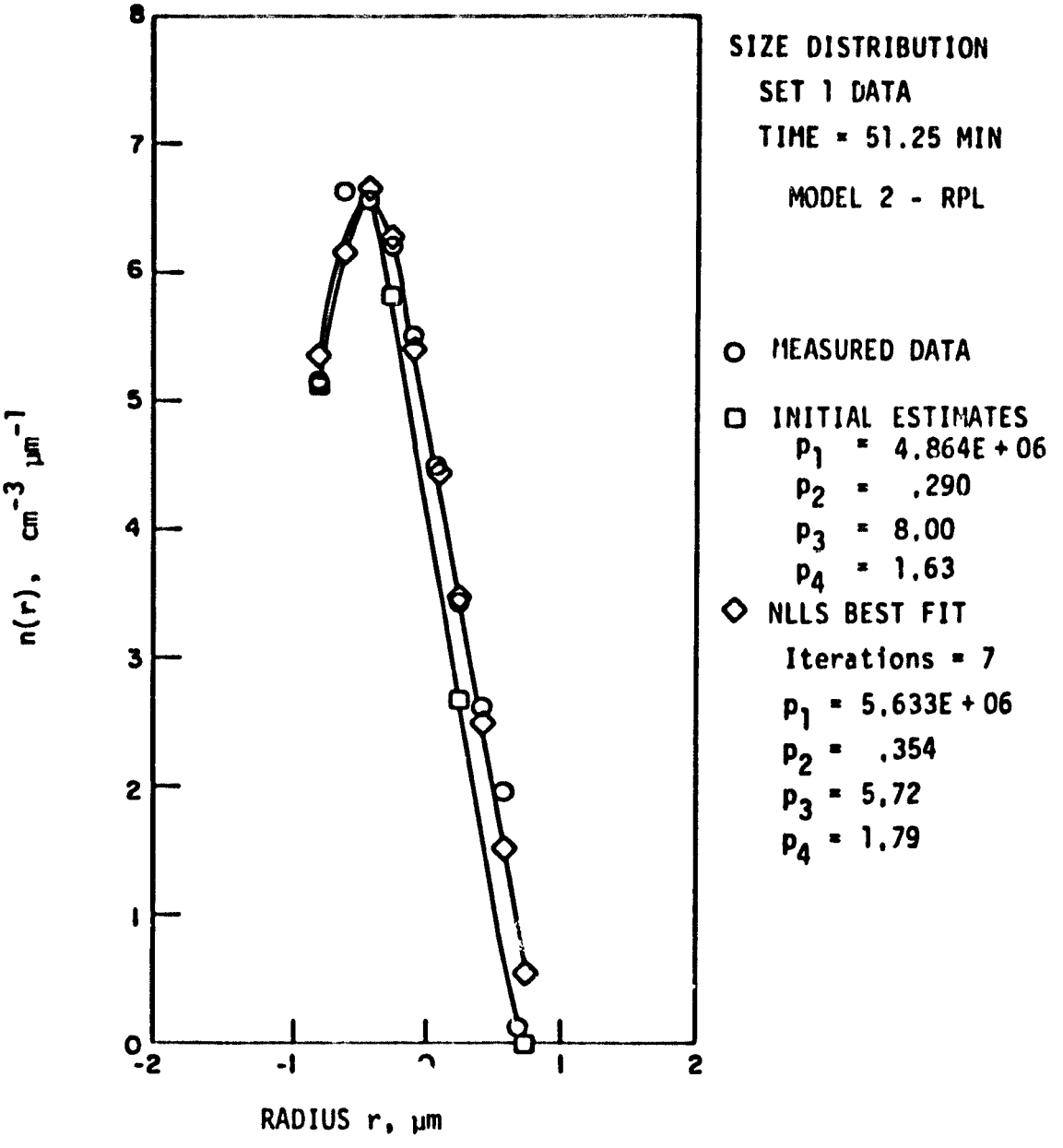

FIGURE 13. Analytic representation of Set 1, t = 51.25 min, size distribution data using an Regularized Power Law (RPL) Model.

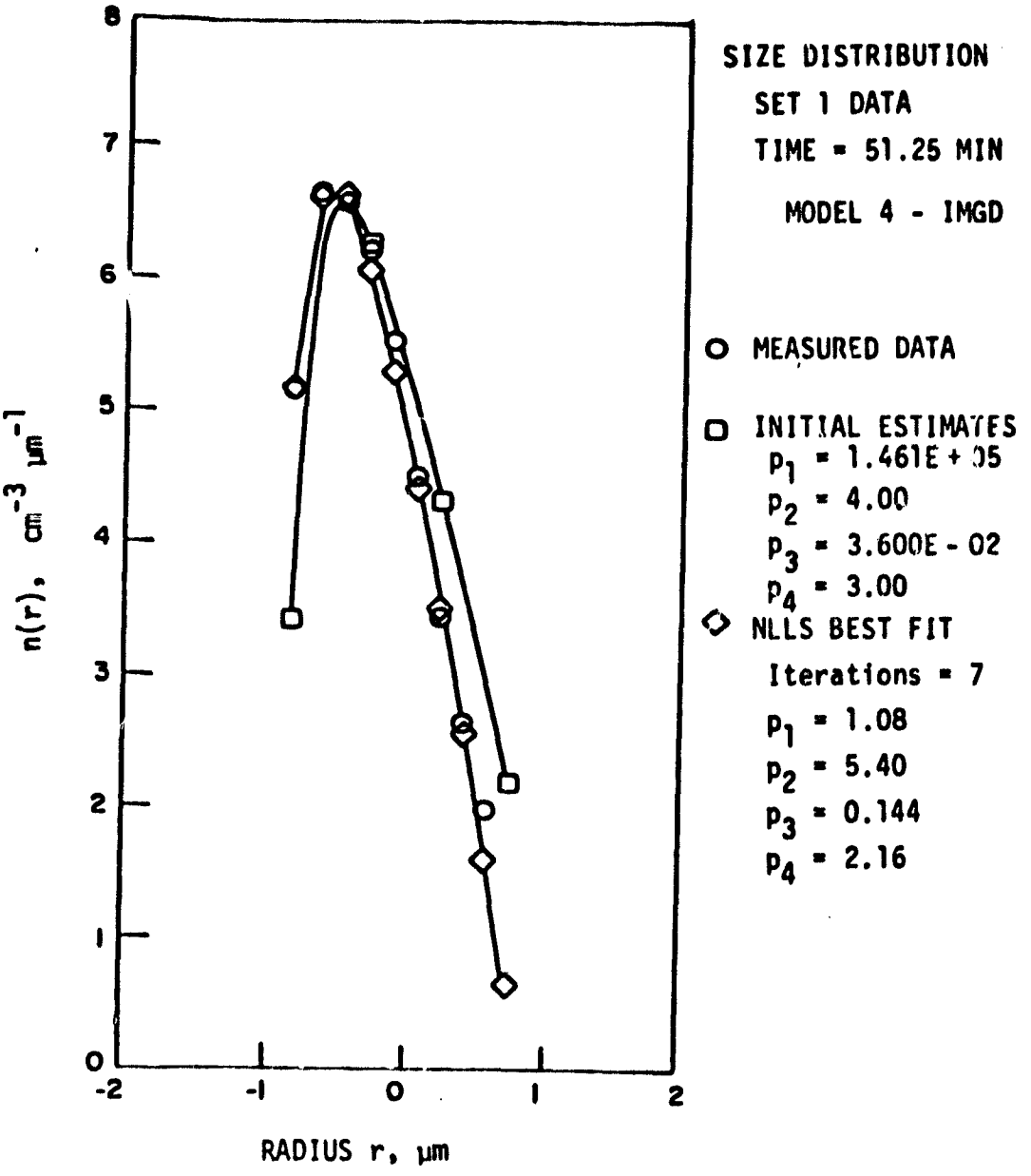

FIGURE 14. Analytic representation of Set 1, t = 51.25 min, size distribution data using an Inverse Modified Gamma Distribution (IMGD) Model.

4. RETRIEVAL OF AEROSOL SIZE DISTRIBUTION FROM MULTISPECTRAL OPTICAL DEPTH MEASUREMENTS

In Ref. 23 a method was described for retrieving size distributions of aerosols from single wavelength measurements of the decay of optical depth $\tau(t)$ with time t. This method is valid under three assumptions: (1) the particles are spherical and large (with radii $r \gtrsim 4/(\rho_p - \rho_m)^{\frac{1}{2}}$ μm, Ref. 24); (2) they se' .le in a quiet medium with a terminal velocity v_s given by Stokes' law (Ref. 25):

$$v_s = \frac{2}{9} (\rho_m - \rho_p)\, g\, r^2/\eta_m \qquad (1)$$

where ρ_m and ρ_p are the specific gravities of the medium and particles, respectively, g is the acceleration due to gravity, and η_m is the medium viscosity; and (3) scattering conditions are such that one can set $Q = 2.0$, which is a reasonable assumption for large particles for which $x > 8$, where $x = 2\pi r/\lambda$ and Q is the efficiency factor.

Any departures from the above conditions will yield errors in the results. For instance, if the particles are in stirred motion or undergoing microphysical changes (e.g., coagulation, evaporation, growth, etc.), the extinction-sedimentation inversion technique of Ref. 23 is not applicable. In that case one must make n independent measurements at any time t to retrieve n parameters needed to describe the size distribution. One simple way to achieve this is to make multispectral measurements of optical depth using n wavelengths.

There are a number of ways of retrieving the aerosol size distribution from multispectral extinction (or optical depth) measurements, such as numerical inversion techniques (e.g., Twomey-Chahine-type methods, Ref. 26), NLLS method of Box and Deepak (Ref. 27), and model dependent, table-search methods. The first two types of methods are iterative and can become quite time consuming; so, in the next three sections we shall describe fast approximate search methods. Comparisons of results will be made, wherever possible, with those obtained by the nonlinear least squares (NLLS) method.

Table Search Methods: The optical depth τ is defined by a Fredholm-type integral equation, namely,

$$\tau(\lambda,m) = \pi \int_0^\infty Q(x,m)\ r^2\ \eta(r)\ dr \qquad (2)$$

where $\eta(r)$ $[cm^{-2}\mu m^{-1}]$ is the path-integrated size distribution, Q is the Mie efficiency factor, r is radius (μm), and $m = m' - im''$ is the complex aerosol refractive index. The method described here is similar to, but more general than, that of the search method of Box and Lo (Ref. 28) in which they used a modified gamma distribution (MGD) model (Ref. 21), such as, Deirmendjian's Haze H model. In their method, they use a two-step approach--first step is to plot the τ vs. λ data on a semi-log or log-log graph paper and approximate it with a straight line, and then use a one-parameter, table-search method. But if the range of wavelengths is large, such a straight line approximation is not always possible. For such a case, we developed the two-parameter and three-parameter table-search methods (Refs. 29-30) which can deal with optical depth data for any range of wavelengths.

In these methods, sets of tables for the τ vs. λ values were generated for the two or three adjustable parameters of the size distribution model and the best fit parameters for a particular experimental data set were found by searching the tabulated data base to determine the combination of parameters that yield the best fit.

In addition, to the 2-parameter (Section 4.1) and 3-parameter (Section 4.2) methods, we extended the latter method to the case of two-term bimodal models, which is described in Section 4.3.

In Section 4.4, we discuss the effects of noise on percentage errors in the size distributions retrieved by the direct inversion (Ref. 23) of the single wavelength simulated data for τ versus t for the case of aerosols settling quietly under gravity.

4.1 FAST TABLE SEARCH (FTS) METHOD FOR RETRIEVAL OF AEROSOL SIZE DISTRIBUTION FROM MULTISPECTRAL EXTINCTION MEASUREMENTS: TWO-PARAMETER MODEL

In the 2-parameter method, we wish to obtain from the experimental τ vs. λ data, two parameters that characterize the size distribution, such as, the total number of particles in the column a and the mode radius parameter b. To determine a and b we assume an analytic model for the aerosol size distribution $\eta(r)$, with a and b as adjustable parameters, and then determine the combination of a and b by searching a precomputed tabulated data base of $\tau(\lambda)$--generated for a judicially selected mesh of a and b values--to obtain the best fit to the experimental $\tau(\lambda)$ data.

The tables should be generated for the same set of wavelengths with which the observations are made. Sensitivity of the search method retrievals to discrepancies in two sets of wavelengths--the one to generate the tables and the other for measurements --is discussed by Box, Box and Deepak (Ref. 30). In practice it was found easier to use the normalized path-integrated size distribution $\eta_o(r)$ to calculate the tables, where $\eta_o(r)$ is defined here as that size distribution for which $a = 1\ \mu m^{-2}$, so that

$$\int_0^\infty \eta_o(r)\ dr = 1 \tag{3}$$

The values of $\tau_o(\lambda)$, the normalized optical depth, are then calculated for a grid of values of b parameter of the selected $\eta(r)$ model, using values of $m = m' - im'$ corresponding to the wavelengths in the set. This procedure gives us a table of $\tau_o(\lambda)$ for preselected values of b.

The parameter a is defined by

$$\int_0^\infty \eta(r)\ dr = a,\ [\mu m^{-2}] \tag{4}$$

so that

$$\eta(r) = a\eta_o(r) \tag{5}$$

Note that $\eta(r)$ $[\mu m^{-3}]$ is related to the size distribution $n(r)$ $[cm^{-3}\mu m^{-1}]$ as

$$n(r) = \eta(r) \left[10^8/L(cm)\right] \tag{6}$$

where L(cm) is the length of the aerosol chamber traversed by laser beams.

For a given value of b, using the normalized optical depth tables one can calculate a from the relation

$$a = \frac{\sum_{i=1}^{N} \tau(\lambda_i)\, \tau_o(\lambda_i)}{\sum_{i=1}^{N} \tau_o^2(\lambda_i)} \qquad (7)$$

where $\tau(\lambda_i)$ are the measurements taken for wavelength set λ_i (i = 1, 2, ... N), and N is the number of wavelengths in the set.

The best value of a is calculated for each value of b using Eq. (7). To determine which pair of a and b values give the best fit to the $\tau(\lambda)$ data, we calculate χ_2, the sum of squares of the residuals, defined as

$$\chi^2 = \sum_{i=1}^{N} \left[\tau(\lambda_i) - a\tau_o(\lambda_i)\right]^2 \qquad (8)$$

for each pair of parameters, and determine which pair give the minimum χ^2 value. The usual pattern is such that as b increases, χ^2 will decrease to some value, and then begin to increase. The best-fit a,b pair corresponds to that point where χ^2 is a minimum.

Examples of the Search Method

The table-search method is illustrated by the use of two size distribution models, the Modified Gamma Distribution (MGD) and the Inverse Modified Gamma Distribution (IMGD) models (Ref. 21). The MGD has an exponential fall off for large particles with radii $r >> r_m$, the mode radius; whereas the IMGD has a power law fall off for $r >> r_m$. A brief description of the two models is given as follows.

Modified Gamma Distribution (MGD) Model:

In Ref. 21, the MGD model is defined as

$$n(r) = p_1 r^{p_2} \exp\left(-p_3 r^{p_4}\right) \qquad (9)$$

where the parameters p_2 and $p_4 = c$ are fixed; p_3 is the mode radius parameter b (units, μm^{-p_4}); and p_1, the scaling parameter, is chosen so that the total number of particles is a. For Eq. (9), the mode radius r_m is defined by

$$r_m = (p_2/p_3p_4)^{1/p_4} \tag{10}$$

and the kth moment, M_k, by

$$M_k = (p_1/p_2)p_3^{-(p_{24} + k/p_4)}\,\Gamma(p_{24} + k/p_4) \tag{11}$$

where

$$p_{24} = (p_2 + 1)/p_4 \tag{12}$$

From Eq.(10), one obtains

$$p_3 = \left(\frac{p_2}{p_4}\right) r_m^{-p_4} \tag{13}$$

and from Eq.(11), the total number of particles a or p as

$$a = M_o = \left(\frac{p_1}{p_4}\right) p_3^{-p_{24}}\,\Gamma(p_{24}) \tag{14}$$

Then substituting for p_1, p_3 and $p_4 = c$ into Eq. 9 one can rewrite n(r) in the form

$$n(r) = ac\left(\frac{p_2}{c}\right)^{p_4} r^{p_2} \exp\left[-\frac{p_2}{c}\,\frac{r}{b}^{c}\right]\left[b^{p_2 + 1}\Gamma p_{24}\right]^{-1} \tag{15}$$

where $p_{24} = (p_2 + 1)/c$.

Then the effective radius is given by

$$r_{eff} = b\left(\frac{c}{p_2}\right)^{1/c}\Gamma\left(\frac{p_2 + 4}{c}\right)\Big/\Gamma\left(\frac{p_2 + 3}{c}\right) \tag{16}$$

The special cases discussed here are obtained by giving different values to p_2 and p_4, shown here as follows.

a. Haze H: $p_2 = 2$, $p_4 = 1$

$$n(r) = \frac{1}{2}a\,b^3\,r^2\,e^{-br} \tag{17}$$

b. Haze L: $p_2 = 2$, $p_4 = 0.5$

$$n(r) = \frac{a}{240}\,b^6\,r^2\,e^{-b\sqrt{r}} \tag{18}$$

c. Haze CH: $p_2 = 2$, $p_4 = 3$

$$n(r) = 3\,a\,b\,r^2\,e^{-br^3} \tag{19}$$

Inverse Modified Gamma Distribution (IMGD) Model:

In Ref. 29, the IMGD model is defined as

$$n(r) = p_1 \exp\left[-p_3/r^{p_4}\right]/r^{p_2} \tag{20}$$

in which p_4 and $p_2 = c$ are fixed; p_3 is the mode radius parameter b (units, μm^{p_4}) and p_1 is chosen so that the total number of particles is a. The mode radius r_m is given by

$$r_m = (p_3 p_4/p_2)^{1/p_4} \tag{21}$$

and the kth moment M_k by

$$M_k = \left(\frac{p_1}{p_4}\right) p_4^{-(p_{42} - k/p_4)}\,\Gamma(p_{42} - k/p_4) \tag{22}$$

where

$$p_{42} = (p_2 - 1)/p_4 \tag{23}$$

and a, the total number of particles, is given by

$$a = M_o = \left(\frac{p_1}{p_4}\right) p_3^{-p_{42}}\,\Gamma(p_{42}) \tag{24}$$

Substituting for p_3 in Eq. (20), p_1 in Eq. (23), and $p_2 = c$ in Eq. (19), one can rewrite n(r) as

$$n(r) = \frac{a\,p_4\,b^{c-1}}{\Gamma p_{42}} \left(\frac{c}{p_4}\right)^{p_{42}} \exp\left[-\frac{c}{p_4}\left(\frac{b}{r}\right)^{p_4}\right] r^{-c} \tag{25}$$

The effective radius is then given by

$$r_{eff} = b\left(\frac{c}{p_4}\right)^{1/p_4} \Gamma\left(\frac{c-4}{p_4}\right) \Big/ \Gamma\left(\frac{c-3}{p_4}\right) \tag{26}$$

and the total mass concentration by

$$M_c = \frac{4\pi}{3L} \rho\, a\, b^3 \left(\frac{c}{p_4}\right)^{4/p_4} \Gamma\left(\frac{c-4}{p_4}\right) \Big/ \Gamma\left(\frac{c-1}{p_4}\right) \tag{27}$$

From Eqs. (25) and (26), one can easily see that if $c \leq 4$, then r_{eff} and M_c cannot be defined.

One special case used in the two-parameter method is for $p_2 = 4$ and $p_4 = 1$, which gives

$$n(r) = \frac{ab^3}{2}(e^{-b/r})/r^4 \tag{28}$$

with r^{-4} fall-off for $r >> r_m$. This will be referred to as HINV41 model.

Computation

In the formulation in Eqs. (7) and (8), it has been assumed that all measurements have been given equal weighting so far as the errors are concerned. (The case in which measurements are weighted according to the experimental error will be considered in Section 4.2.)

The tables of $\tau_o(\lambda_i)$ were computed for five wavelengths given in Table 1 in Sec. and for the parameter values for MGD and IMGD models given in Table 3.

The parameters a and b for each of four models (Haze H, Haze L, Haze CH and HINV41) were determined by the aforementioned method, and the results are given in Table 4. To determine how good these results are, numerical inversions of the data were also performed using a nonlinear least squares (NLLS) method and the results are also shown in Table 4. The approximate estimates for a and b were used as initial guesses for a and b in the NLLS program.

The mode radii and the modal values of the size distributions at the different times are given in Tables 5 and 6, respectively. The size distributions obtained by using the approximate estimates of the parameters for the different times during the experiment are plotted in Figs. 15 to 18, along with the experimental data for size distribution measurements taken at times t = 0.5 and 51.25 min by means of a ten-stage Andersen Cascade Impactor.

TABLE 3. VALUES OF THE PARAMETERS p_i FOR GENERATING THE TABLES FOR $\tau(\lambda)$

Parameters	MGD	IMGD
p_2	1.0, 2.0 and 3.0	
p_4		1.0, 2.0 and 3.0
c	0.3, 0.5, 1.0, 1.5 2.0 and 3.0	3.5, 4.0, 5.0, 6.0, 7.0 and 8.0
b	0.1 (0.1) 1.0 (0.5) 5.0	0.1 (0.1) 1.0 (0.5) 5.0

TABLE 4. THE RETRIEVED PARAMETERS a AND b BY SEARCH AND NLLS METHODS

Time (min)	Search Method			NLLS		
	a	b	χ^2	a	b	χ^2
Haze H						
0	14.100	15.00	0.0154	13.000	14.60	0.0017
20	3.130	9.00	0.0568	3.020	8.84	0.0182
40	1.510	7.00	0.1840	1.630	7.23	0.1102
52	1.400	7.00	0.1830	1.340	6.83	0.1391
80	1.190	7.00	0.2750	1.010	6.41	0.2256
Haze L						
0	40.100	19.00	0.0277	39.600	19.00	0.0017
20	6.530	14.00	0.2870	5.760	13.60	0.1927
40	3.820	13.00	0.5450	3.030	12.30	0.4356
52	2.500	12.00	0.5340	2.460	11.90	0.4624
80	2.120	12.00	0.5940	1.790	11.50	0.5314
Haze CH						
0	5.700	25.00	0.0092	5.760	25.30	0.8094
20	2.210	10.00	0.0086	2.120	9.40	0.0071
40	1.280	6.00	0.0021	1.280	6.02	0.0048
52	1.050	5.00	0.0015	1.040	4.92	0.0066
80	0.773	4.00	0.0085	0.704	3.44	0.0032
HINV41						
0	2110.000	0.05	1.5600	2894.000	0.0447	0.9520
20	21.400	0.25	1.5600	17.200	0.2760	1.2770
40	5.650	0.40	1.5700	4.690	0.4410	1.3690
52	3.990	0.45	1.4300	3.270	0.5010	1.2540
80	2.170	0.55	1.2600	1.950	0.5900	1.1240

TABLE 5. MODE RADII OF RETRIEVED SIZE DISTRIBUTIONS.

The Experimental Values of Mode Radius at t = 0.5 and 51.25 min are 0.22 and 0.3 μm, respectively

Model	Inversion method	Mode Radius (μm)				
		t = 0 min	20 min	40 min	52 min	80 min
Haze H						
	Search	0.1333	0.2222	0.2857	0.2857	0.2857
	NLLS	0.1370	0.2260	0.2770	0.2930	0.3120
Haze L						
	Search	0.0443	0.0816	0.0947	0.1111	0.1111
	NLLS	0.0445	0.0865	0.1060	0.1120	0.1210
Haze CH						
	Search	0.2991	0.4058	0.4811	0.5112	0.5506
	NLLS	0.3010	0.4180	0.4840	0.5170	0.5820
HINV41						
	Search	0.0125	0.0625	0.1000	0.1125	0.1375
	NLLS	0.0112	0.0691	0.1100	0.1250	0.1480

TABLE 6. MODAL VALUES OF SIZE DISTRIBUTIONS.

The Experimental Values of $n(r_m)$ at t = 0.5 and 51.25 min are 2.66(7)* and 5.0(6)* μm, respectively

Model	Inversion method	$n(r_m)$ t = 0 min	20 min	40 min	52 min	80 min
Haze H						
	Search	4.887(7)	6.516(6)	2.451(6)	2.269(6)	1.935(6)
	NLLS	4.380(7)	6.180(6)	2.720(6)	2.120(6)	1.500(6)
Haze L						
	Search	2.415(8)	2.138(7)	1.078(7)	6.004(6)	5.108(6)
	NLLS	2.371(8)	1.778(7)	7.680(6)	5.856(6)	3.936(6)
Haze CH						
	Search	1.650(7)	4.718(6)	2.305(6)	1.778(6)	1.221(6)
	NLLS	1.670(7)	4.430(6)	2.230(6)	1.760(6)	1.060(6)
HINV41						
	Search	8.431(10)	1.711(8)	2.826(7)	1.774(7)	7.889(6)
	NLLS	1.300(11)	1.250(8)	2.130(7)	1.310(7)	6.600(6)

*The number within the parentheses refers to the power of 10.

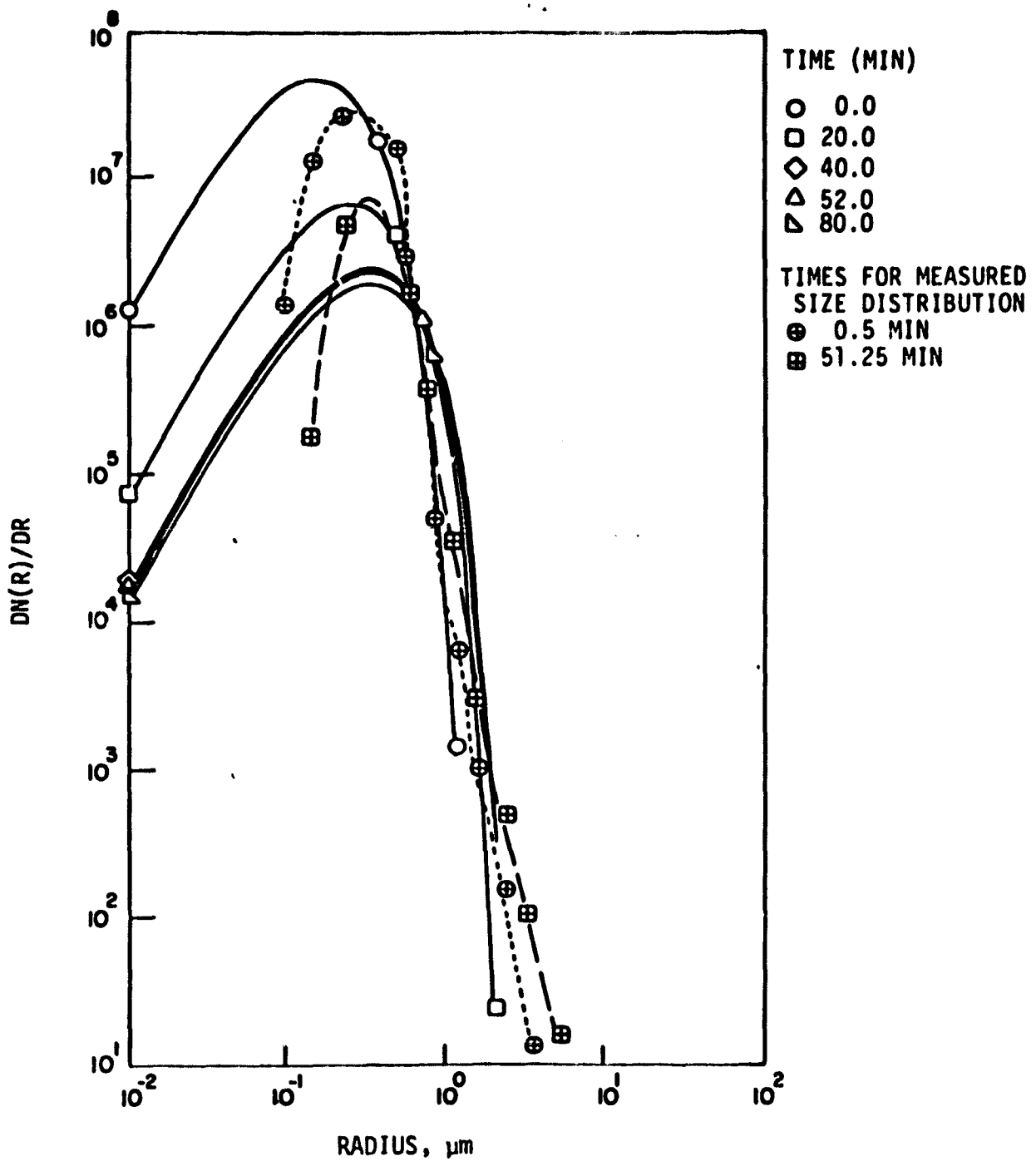

FIGURE 15. Retrieved size distributions for different times for Set 1 data using 2-parameter Haze H Model.

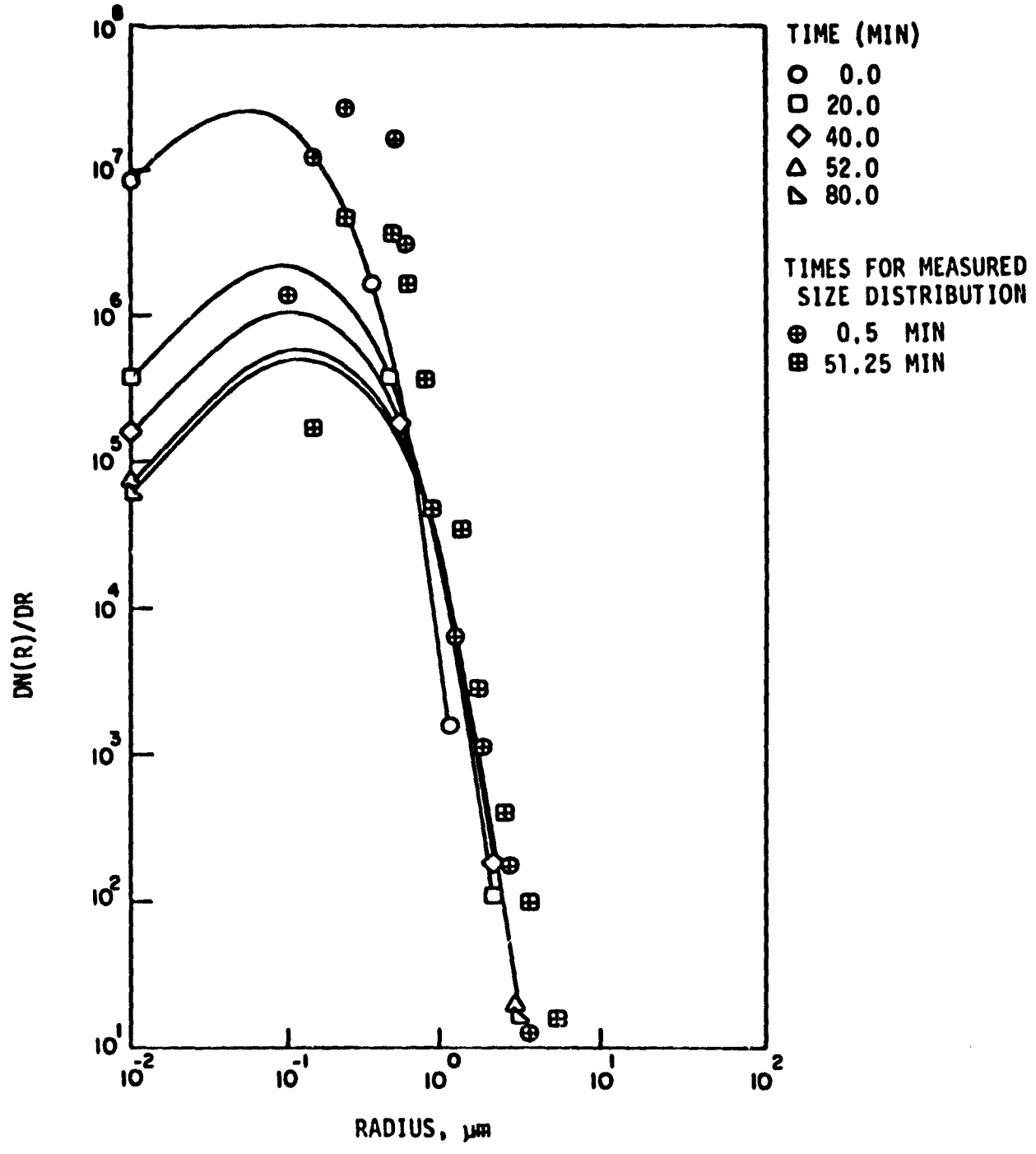

FIGURE 16. Retrieved size distributions for different times for Set 1 data using 2-parameter Haze L Model.

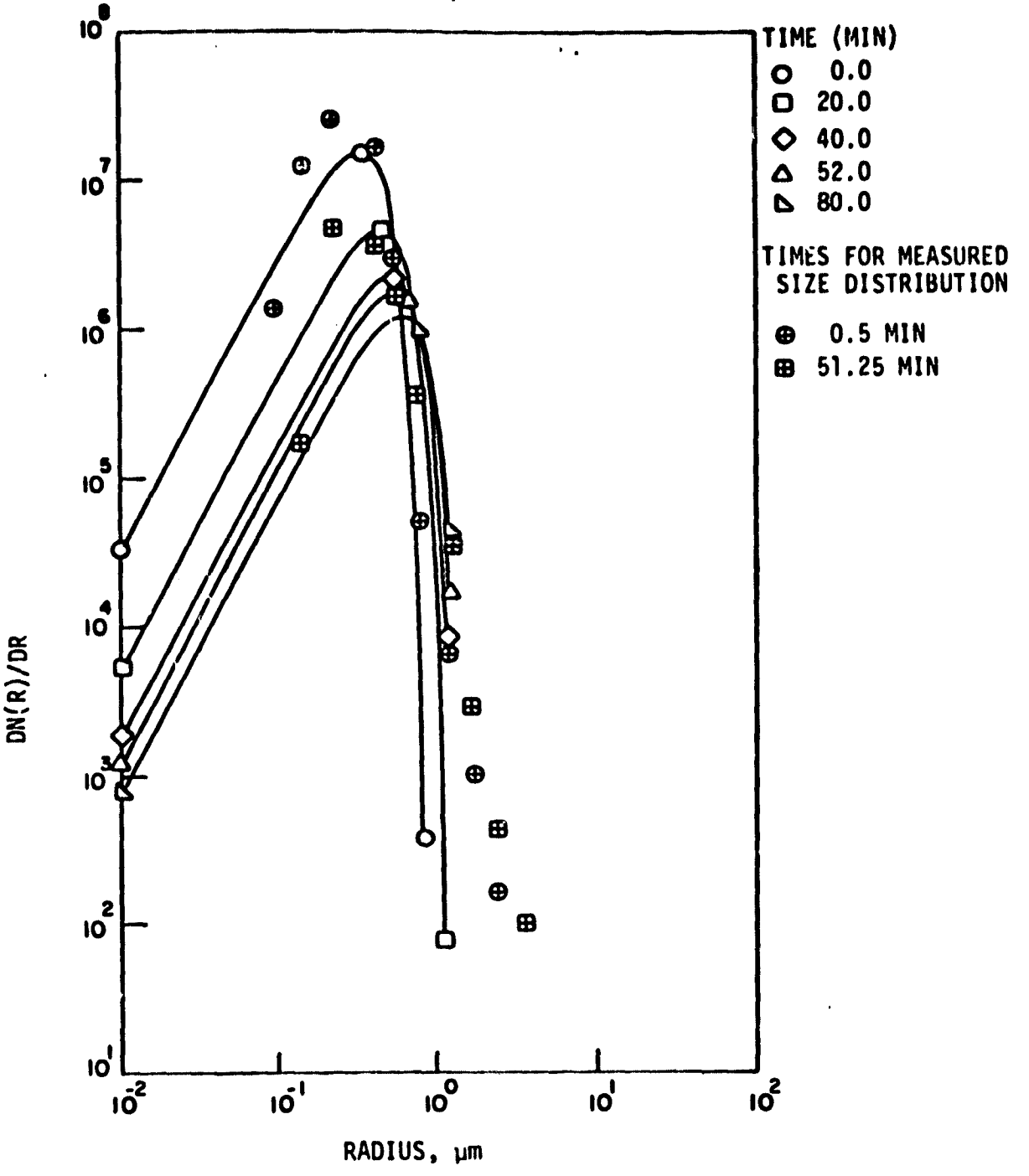

FIGURE 17. Retrieved size distributions for different times for Set 1 data using 2-parameter Haze CH Model.

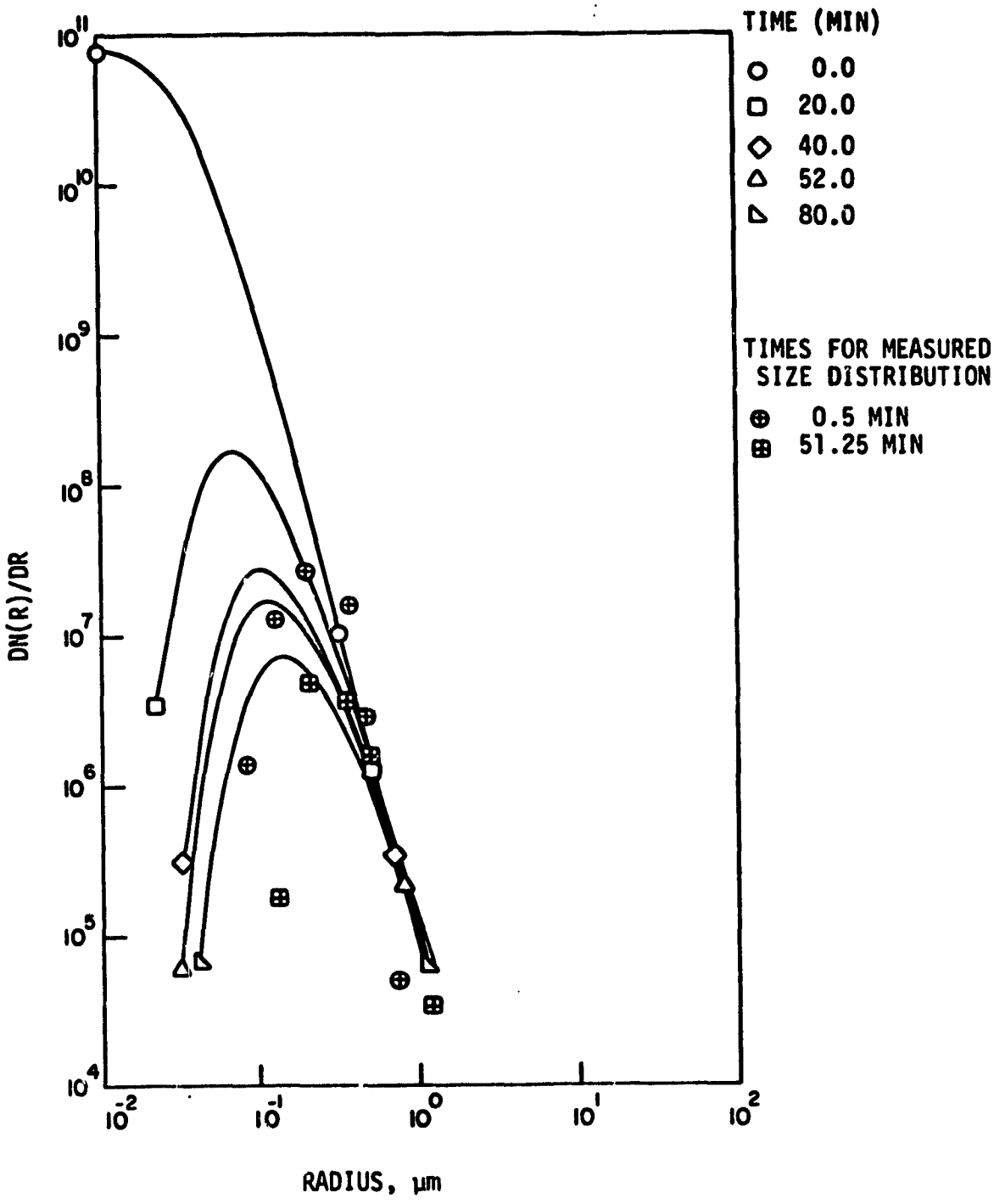

FIGURE 18. Retrieved size distributions using MODEL HINV 41 experimental data

Discussion of Results

1. Haze H Model

The retrieved size distribution results for the Haze H model are plotted in Fig. 15, for the different times at which the experimental $\tau(\lambda_i)$ data was available. This shows that as the time increases, r_m increases, whereas the total number of particles decreases. Comparisons of the retrieved n(r) curve for 0.0 min with experimental data taken at t = 0.5 min shows a fairly good agreement, the "true" mode radius is somewhat larger than retrieved value, but the modal values of n(r) are of the same magnitude. In the range $0.2 < r < 1.0$ μm there seems to be a good agreement between the retrieved and measured results.

Comparison of the retrieved curve at 52.0 min and the data taken at 51.25 min is not so good. Their mode radii compare rather well, but their modal values differ, the true value being somewhat higher than the measured value. The rate of fall-off agrees reasonably well in the range $0.7 < r < 2.0$ μm.

In Table 5, comparison of the search and NLLS results show quite a good agreement: b values differed by less than 5% in all cases, except for t = 80 min, for which they differed by less than 10%; 'a' values differed by less than 10%, except for t = 80 min for which the difference was less than 20%. The higher discrepancies in a values are due to the fact that in the search method the value of a depends on b, and hence errors in b will propagate and enhance the errors in a. Similarly, the mode radii differ by less than 5%, except for t = 80 min for which they differed by 10%; and the modal values by less than 15%, except for t = 80 min, for which the difference is 30%. Comparisons with the experimental results show that both search and NLLS methods underestimate the mode radii and overestimate the modal values at t = 0.0 and 52 min. At 52 min the mode radius estimates are good, but the maximum is underestimated by a factor of 2.

2. Haze L Model

The retrieved results for the Haze L model and experimental data points are plotted in Fig. 16. The shift in mode radius to larger values with increasing time and the corresponding drop in the total number of particles is evident, but neither the 0.0 min nor the 52.0 min curves agree very well with the measured values.

As was the case for Haze H, the agreement between the search and NLLS methods is quite good. The discrepancy between the b values was less than 6%

and the discrepancy between the a values was generally less than 20%. The discrepancies in the mode radii were less than 10%, but ranged up to 40% for the modal values. The calculated mode radii were much less than the "measured" mode radii for both methods for which data were available, but the modal values agreed quite well.

3. Haze CH

The results for this model are plotted in Fig.17. The increase in mode radius with increasing time and the decrease in the total number of particles is evident. The agreement between the 0.0 min curve and the measured size distribution at 0.5 min is quite good for $0.07 < r < 0.6$ μm, although the mode radius is about 35% higher than the"true"mode radius and the maximum is nearly 40% below the "true" maximum. The agreement between the 52 min and the measured values at 51.25 min is not quite as good. The mode radius is 70% higher than the true mode radius and the maximum is 20% higher than the true maximum.

Comparison of the parameters obtained by the search method and the NLLS inversion shows that agreement is quite good, within 5% in most cases. Agreement between mode radii and maxima for the two methods is also generally within about 5%.

4. HINV41

The results for this fit are plotted in Fig. 18. This model shows the shift to larger mode radii with increasing time and also the drop in the number of particles, but agreement between the measured and calculated size distributions is not good. The mode radii for the calculated distributions are higher than the true values and the maxima are much higher than the true maxima.

Comparison of the results obtained by the search method and the NLLS inversion show that the estimates for b differ by about 10% while the estimates for 'a' differ by up to 30%. The estimates of mode radii differ by about 10% while the differences in the maxima are of the order of 35%. These differences are much larger than were encountered with the Modified Gamma Distributions.

Conclusions

The results presented here indicate that the two-parameter search method is a practical method for obtaining estimates of the mode radius parameter b and number of particles a for the simple models considered so far. The agreement with the results for numerical NLLS inversion method was quite good and could easily be improved by using a smaller step-size for b in generating the tables.

Another distinct advantage of the search method is that it is much faster than the NLLS method. For example, using the search method, 98 sec of CP time was required to compute the tables and then determine the parameters for each of the five data sets used for four models. Using NLLS inversion, the times to determine the parameters for each of the five data sets for only one model ranged from 120 to 170 sec of CP time.

However, in order to improve the accuracy of the retrievals by the search method, we decided to extend this technique to determine three adjustable parameters, so that the method can be extended to determine the fall-off rate for $r >> r_m$. The three-parameter method is described in the next section.

4.2 FAST TABLE SEARCH (FTS) METHOD FOR RETRIEVAL OF AEROSOL SIZE DISTRIBUTION FROM MULTI-SPECTRAL EXTINCTION MEASUREMENTS: THREE-PARAMETER MODEL

In this section, we describe a three-parameter search method for determining aerosol size distributions from multispectral optical depth $\tau(\lambda)$ measurements, by retrieving three parameters characterizing the size distribution. It is an extension of the two-parameter method described in Section 4.1. Here, we attempt to obtain three parameters: the total number a of particles in the column, the mode radius parameter b, and the slope parameter c (corresponding to the rate of fall-off for large r). To determine a, b, and c, we assume an analytic model for the path-integrated size distribution $\eta(r)$ $[cm^{-2}\mu m^{-1}]$, with a, b, and c as adjustable parameters, and then determine the best combination of a, b, and c by searching precomputed sets of tables of $\tau(\lambda)$ for various combinations of mesh of values of the three parameters to obtain the best fit to the experimental $\tau(\lambda)$ data.

To calculate the tables of $\tau(\lambda)$, we again work with the normalized size distribution $\eta_o(r)$, defined by Eq. (3). Similarly, the path-integrated size distribution $\eta(r)$ is defined by Eq. (5). Thus, using $\eta_o(r)$, tables for the normalized optical depth $\tau_o(\lambda)$ can be calculated for different values of b and c as given in Table 3. Each table is for one value of c and consists of $\tau_o(\lambda)$ values for different b values.

It will be assumed here that the measured optical thickness $\tau(\lambda_i)$ is given by

$$\tau(\lambda_i) = a\,\tau_o(\lambda_i) + \varepsilon_i \tag{29}$$

where ε_i is the error.

For a given value of b, the parameter a can be found from the relation

$$a = \frac{\sum_{i=1}^{N} \tau(\lambda_i)\,\tau_o(\lambda_i)/\sigma_i^2}{\sum_{i=1}^{N} \tau_o^2(\lambda_i)/\sigma_i^2} \tag{30}$$

where N is the total number of independent measurements and σ_i are the experimental errors in the measured values of $\tau(\lambda_i)$.

The best-fit parameter set of a, b, and c for a given set of $\tau(\lambda)$ measurements is the combination which minimizes the weighted mean sum of squares of the residuals χ^2 defined as

$$\chi^2 = \sum_{i=1}^{N} (\varepsilon_i/\sigma_i)^2$$

$$= \sum_{i=1}^{N} \left[\frac{\tau(\lambda_i) - a\tau_o(\lambda_i)}{\sigma_i}\right]^2 \qquad (31)$$

If $\chi^2 \leq N$, the calculated values are consistent with measured values of the optical thickness, within the experimental error.

After the best fit parameters have been obtained, one can easily calculate the effective radius r_{eff} (μm) and total mass concentration M_c ($g/\mu m^3$) from

$$r_{eff} = M_3/M_2 = \frac{\int_0^\infty r^3 \eta(r)\,dr}{\int_0^\infty r^2 \eta(r)\,dr} \qquad (32)$$

$$M_c = \frac{4\pi\rho}{3}\frac{M_3}{L} \qquad (33)$$

where M_2 and M_3 are the second and third moments of the size distribution, ρ is the particle density, and L is the beam path length within the aerosol media.

Computations

It was assumed that the error in the optical thickness measurements was ± 3%. In calculating a and χ^2, the measurements were weighted according to the assumed experimental error. In Section 4.2 for the two-parameter, all measurements were given equal weighting resulting in a bias toward the small wavelengths, i.e., good estimates at $\lambda = 3.39$ μm, for which the τ is much smaller.

In generating the tables of τ values, we assume analytic models for $\eta(r)$, such as, Modified Gamma Distribution (MGD) and Inverse Modified Gamma Distribution (IMGD), and use pre-selected values for the parameters p_1, b and c given in Table 3. The aerosol refractive values for four wavelengths (0.4416, 0.6328, 1.15, and 3.39 μm) are given in Table 2.

Measurements

The measurements of $\tau(\lambda, t)$ for Set 1, Set 2, and Set 3 data (Table 2) are shown in Figs. 3-5, and the measurements of size distribution for Set 1 and Set 3 are shown in Figs. 6 and 9.

Discussion of Results

The three-parameter search method was used to invert the $\tau(\lambda, t)$ data for Set 1, Set 2 and Set 3 in order to retrieve aerosol size distributions represented by two analytic models--the MGD and the IMGD. The results for the three sets are discussed as follows.

Set 1 Data - MGD Model: The results for the observed and calculated τ, show that they are in reasonably good agreement. The results for the goodness of fit for the MGD model are shown in Table 7, which gives χ^2 values for the three different values of the MGD parameter p_2 at different times t = 0, 20, 40, 52, and 80 min during the experiment. Remembering that $\chi^2 \leq N$ indicates an acceptable fit and that N = 3 for the particular set of data, we see that, in general, all the three values of p_2, with $p_2 = 2.0$ being slightly better than the other two.

The measured and the calculated values of the mass concentrations, as functions of time are shown in Table 8. The calculated values are 15% to 40% higher than measured values, with their difference increasing as time increases. Measurements seem to indicate that the aerosol size distribution is bimodal and this may contribute to over-estimation of the total mass concentration. The calculated values of M_c for the three values of p_2 differ by less than 2%.

The effective radii of the time varying size distribution are shown in Table 9. The r_{eff} values at any time for different p_2 values differed by less than 10%; but r_{eff} increases as time increases. The r_{eff} values for the measured size distributions at t = 0.5 and 51.25 min differed by less than 5% from values calculated from retrieved results.

The measured and retrieved size distributions are plotted in Figs. 19 to 21 for three values of p_2. All the three figures show that as time increases, the size distribution shifts toward larger particles and number density decreases. The exponential fall-off of MGD for larger r is too

TABLE 7. GOODNESS OF FIT FOR THREE VALUES OF MGD PARAMETER p_2 AND FOR SET 1 DATA

Time (min)	χ^2		
	$p_2 = 1.0$	$p_2 = 2.0$	$p_2 = 3.0$
0	0.36	0.27	9.41
20	1.45	2.11	2.64
40	2.73	5.85	0.13
52	6.10	0.10	3.27
80	13.00	2.56	5.06

TABLE 8. COMPARISON OF MEASURED AND CALCULATED MASS CONCENTRATIONS M_c FOR SET 1

Measured		Calculated			
Time (min)	g/m^3	Time (min)	g/m^3		
			$p_2 = 1.0$	$p_2 = 2.0$	$p_2 = 3.0$
0.50	0.653	0	0.761	0.748	0.758
20.50	0.606	20	0.734	0.726	0.732
40.50	0.541	40	0.681	0.686	0.681
51.25	0.492	52	0.688	0.677	0.687

TABLE 9. EFFECTIVE RADIUS AS A FUNCTION OF TIME FOR MGD AND SET 1

Time (min)	Effective Radius r_{eff} (μm)			
	From measured size distribution	Search Method		
		$p_2 = 1.0$	$p_2 = 2.0$	$p_2 = 3.0$
0	0.366	0.365	0.380	0.357
20		0.510	0.507	0.536
40		0.583	0.602	0.536
52	0.624	0.656	0.634	0.655
80		0.656	0.697	0.714

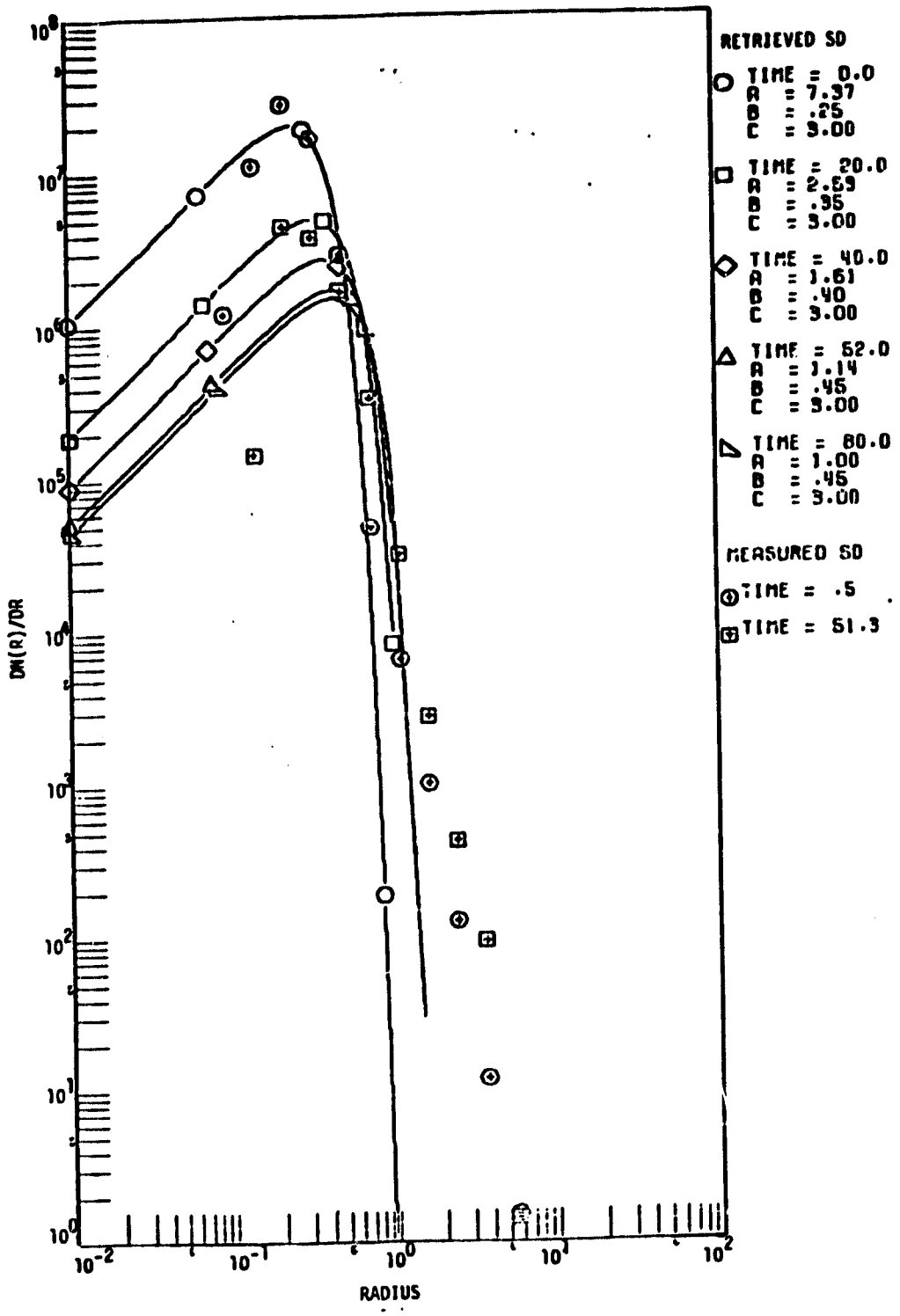

FIGURE 19. Retrieved size distribution for different times for Set 1 data using 3-parameter MGD Model with $p_2 = 1.0$; and measured size distribution.

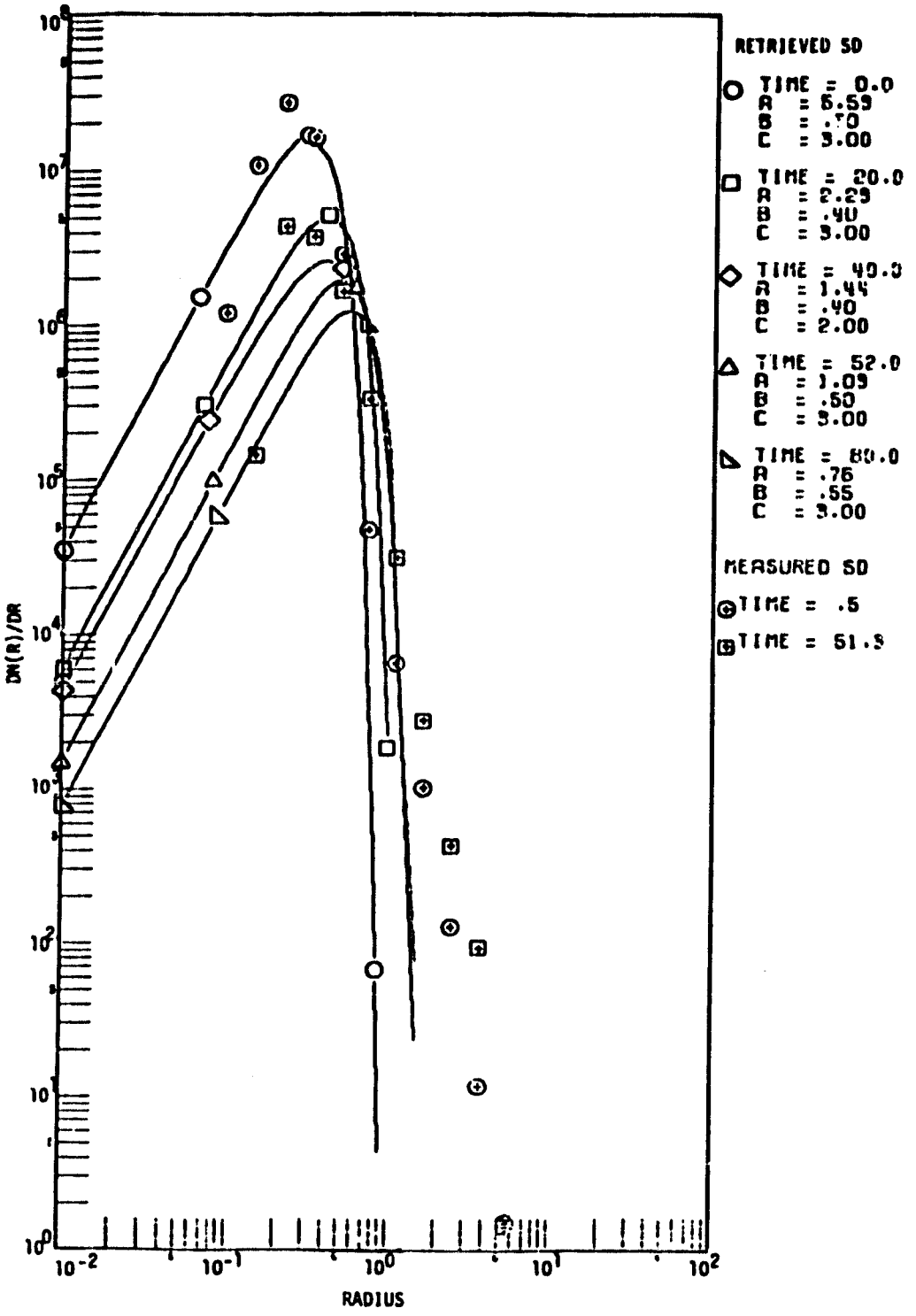

FIGURE 20. Retrieved size distributions for different times for Set 1 data using 3-parameter MGD Model with p_2 = 2.0; and measured size distribution.

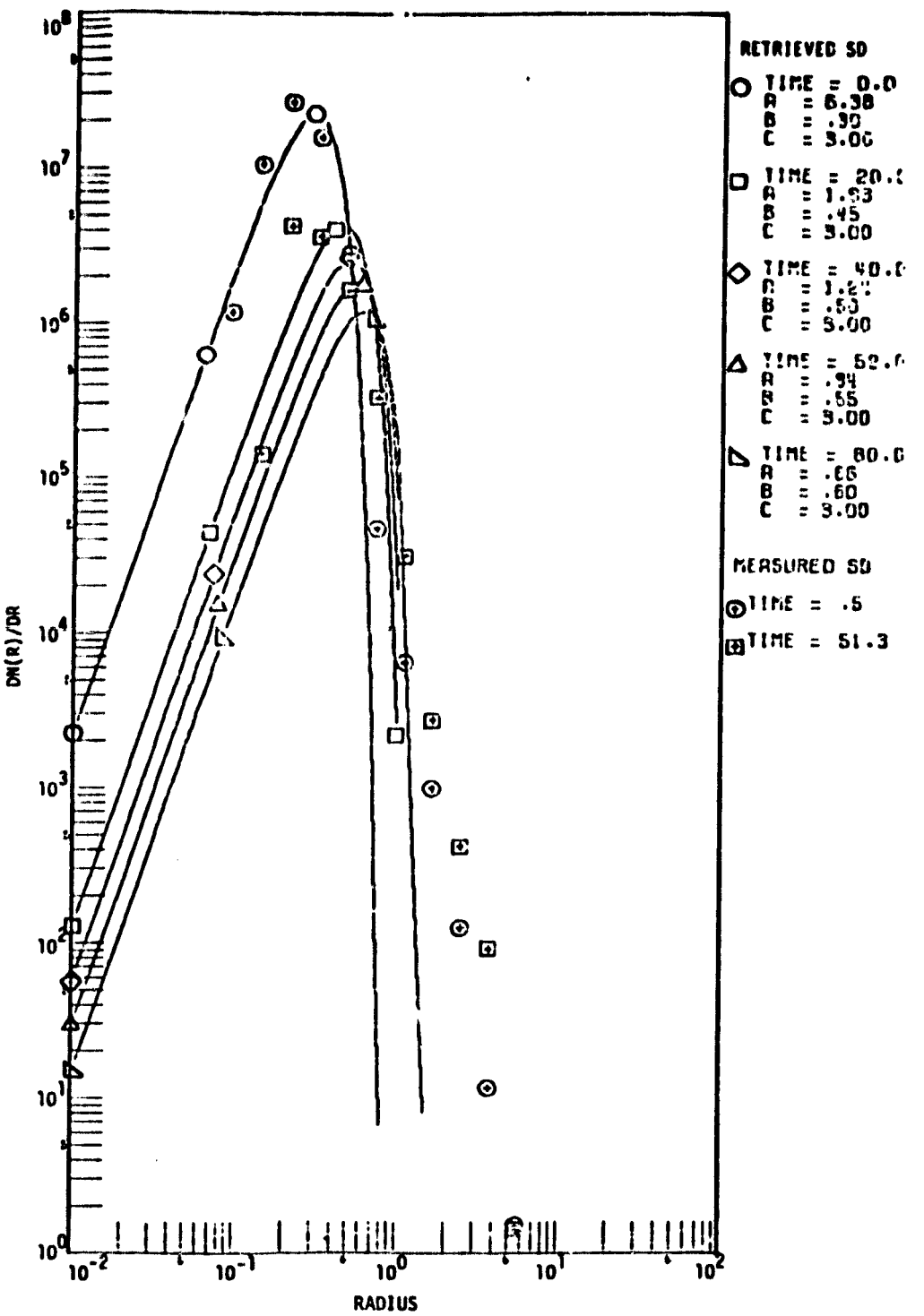

FIGURE 21. Retrieved size distributions for different times for Set 1 data using 3-parameter MGD Model with p_2 = 3.0; and measured size distribution.

steep to match with the measured distribution, but the MGD for the two cases of p_2 = 2.0 and 3.0, does model the small radius ($r \to 0$) region well, especially for t = 0.0 min case.

Comparison of Results Obtained with the Two- and Three-Parameter Search Methods: In the three-parameter method, the best value for c was 3.0. In the two-parameter method (Sec. 4.1), three models were considered, one of which, namely Haze CH, had parameters p_2 = 2.0 and p_3 (or c) = 3.0 and is, therefore, similar to the three-parameter case with p_2 = 2.0, as shown in Table 10. One can easily see in Table 10 that even though the two-parameter fit used equal weighting for all data points, yet the retrieved results are consistent with those retrieved using the three-parameter method, in which measurements were weighted according to the assumed experimental error of $\pm$ 3%.

Set 1 Data - IMGD Model: The results for the observed and calculated optical thickness show that they are in poor agreement. Table 11 gives χ^2 for the different values of p_4 at the different times. In all cases, $\chi^2 > N$ indicating a poor fit, although there is some improvement as p_4 increases and the fall-off of size distribution as $r \to 0$ becomes sharper.

Table 12 gives the measured and calculated mass concentrations as a function of time. The calculated mass concentrations are consistently 25% to 40% higher than the measured values. The value of p_4 appears to have little effect on the calculated concentrations since the values are in agreement to within 2% except at 0.0 min where they differ by up to 10%.

Table 13 lists effective radius as a function of time for the different values of p_4. The value of p_4 has little effect on the effective radius; the difference between the calculated radii is less than 10% except at 0.0 min where it is 25%. The radii for p_4 = 2.0 and p_4 = 3.0 differ from the values for the measured size distribution by less than 10%.

Figures 22 to 24 are plots of the measured and calculated size distributions for the different values of p_4. In each case, the best fit for the calculated distributions was with c = 8.0. For p_2 = 1.0 and p_2 = 2.0, this was in good agreement with the measured distribution in the region $r \to \infty$. For p_4 = 3.0, it was a little steep.

TABLE 10. COMPARISON OF TWO-PARAMETER MODEL WITH THREE-PARAMETER MODEL FOR SET 1

Time (min)	Two-parameter model			Three-parameter model		
	a	r_m*	χ^2	a	b	χ^2
0	5.700	0.299	0.009	5.590	0.30	0.272
20	2.210	0.406	0.009	2.290	0.40	0.110
52	1.050	0.511	0.002	1.090	0.50	0.099
82	0.773	0.551	0.009	0.757	0.55	0.560

* r_m = mode radius. For the two-parameter model, this is given by $(2/3b)^{1/3}$ where b is the mode radius parameter.

TABLE 11. GOODNESS OF FIT FOR IMGD AND SET 1

Time (min)	χ^2		
	$p_4 = 1.0$	$p_4 = 2.0$	$p_4 = 3.0$
0	53.1	19.8	16.80
20	57.0	20.5	13.00
40	60.3	22.8	8.89
52	63.1	16.5	10.90
80	65.6	29.0	11.90

TABLE 12. COMPARISON OF MEASURED AND CALCULATED MASS CONCENTRATIONS FOR SET 1

Measured		Calculated			
Time (min)	Mass conc. (g/m^3)	Time (min)	Mass Concentration		
			$p_4 = 1.0$	$p_4 = 2.0$	$p_4 = 3.0$
0.50	0.653	0	0.839	0.763	0.785
20.50	0.606	20	0.741	0.728	0.728
40.50	0.541	40	0.683	0.672	0.678
51.25	0.492	52	0.697	0.685	0.690

TABLE 13. EFFECTIVE RADIUS AS A FUNCTION OF TIME FOR IMGD AND SET 1

Time (min)	Effective radius r_{eff} (μm)			
	From measured size distribution	Search method		
		$p_4 = 1.0$	$p_4 = 2.0$	$p_4 = 3.0$
0	0.366	0.30	0.376	0.343
20		0.50	0.527	0.549
40		0.60	0.602	0.617
52	0.624	0.70	0.677	0.686
80		0.70	0.752	0.686

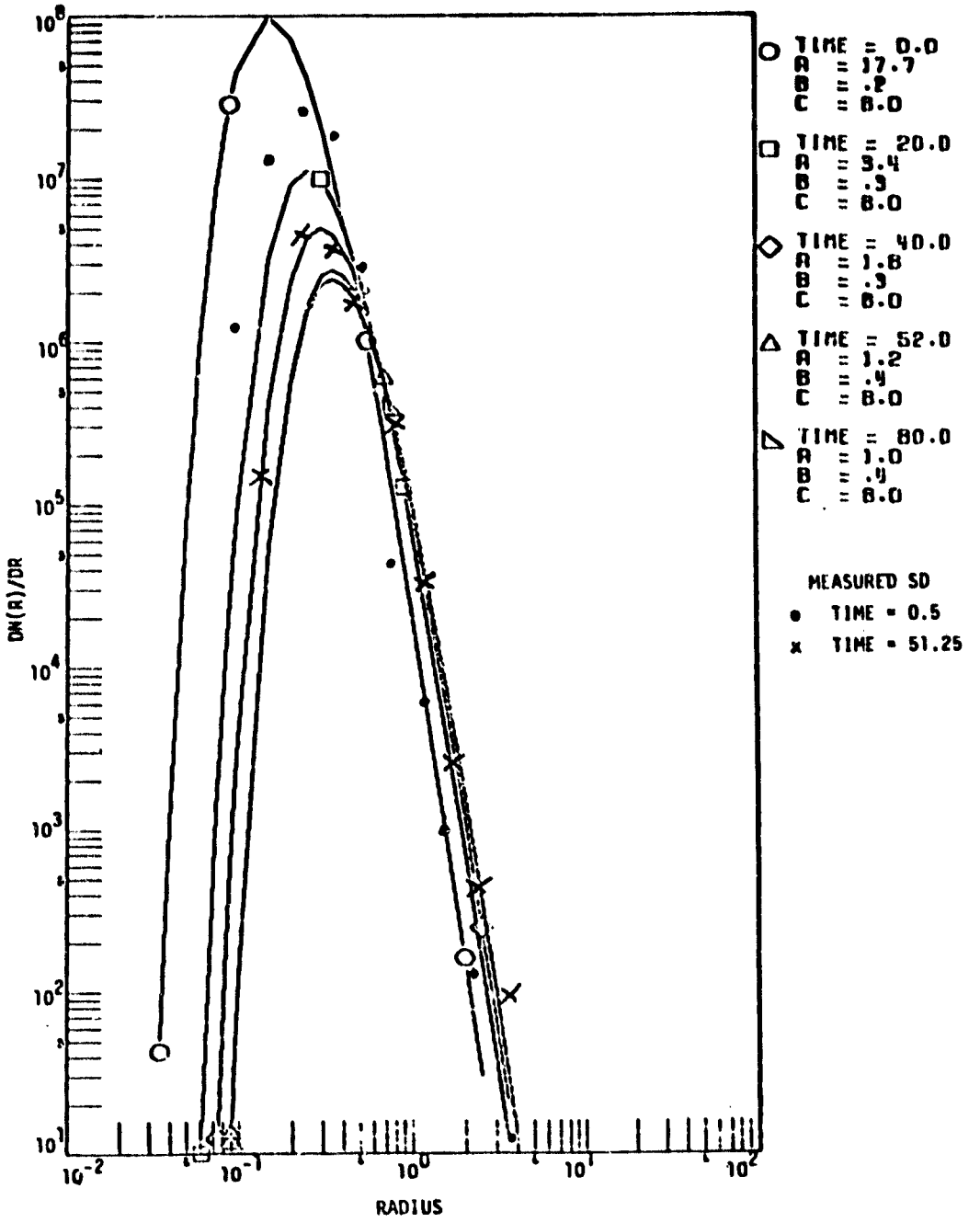

FIGURE 22. Retrieved distributions for different times for Set 1 data using 3-parameter IMGD Model with p_4 = 1.0; and measured size distribution.

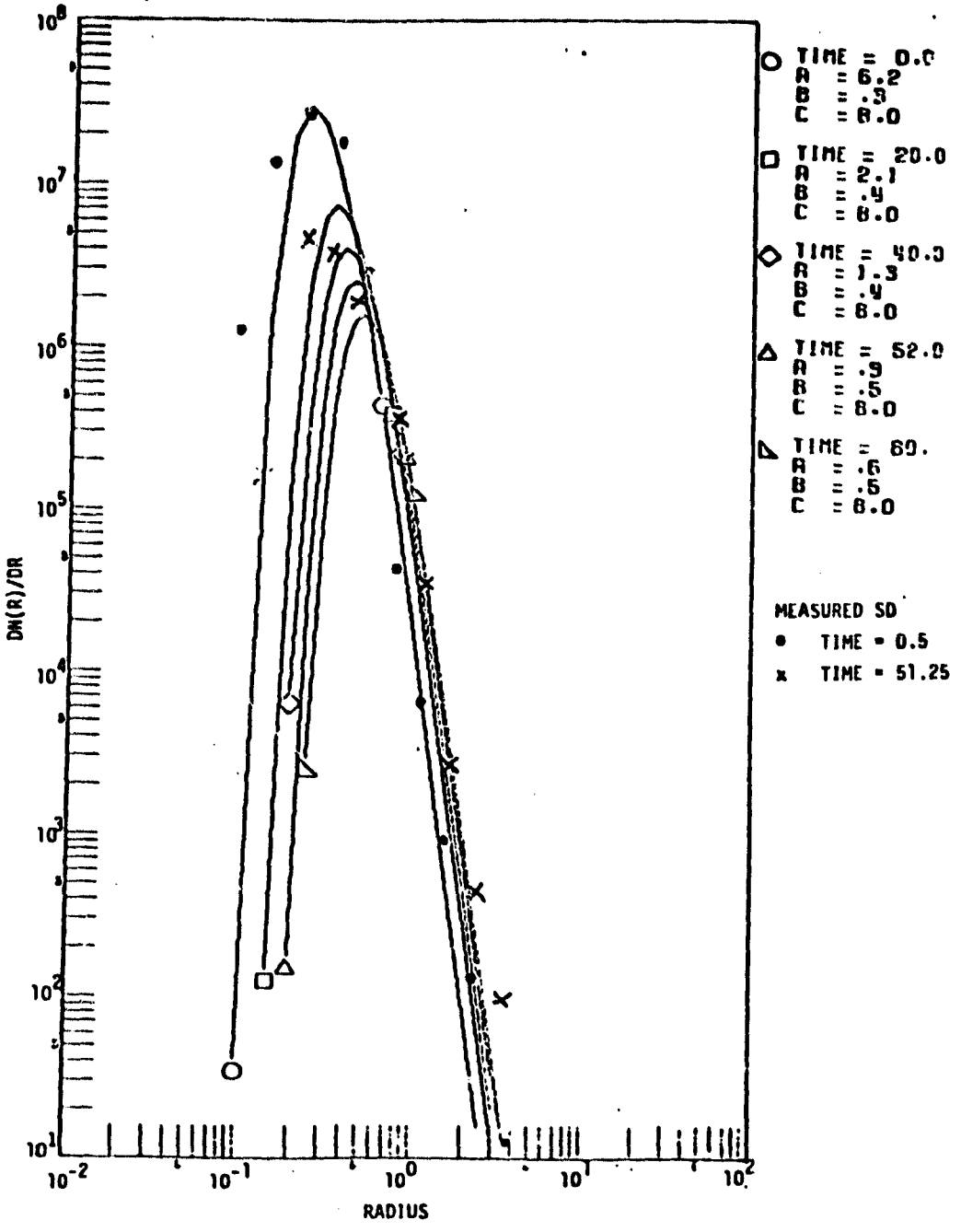

FIGURE 23. Retrieved distributions for different times for Set 1 data using 3-parameter IMGD Model with $p_4 = 2.0$; and measured size distribution.

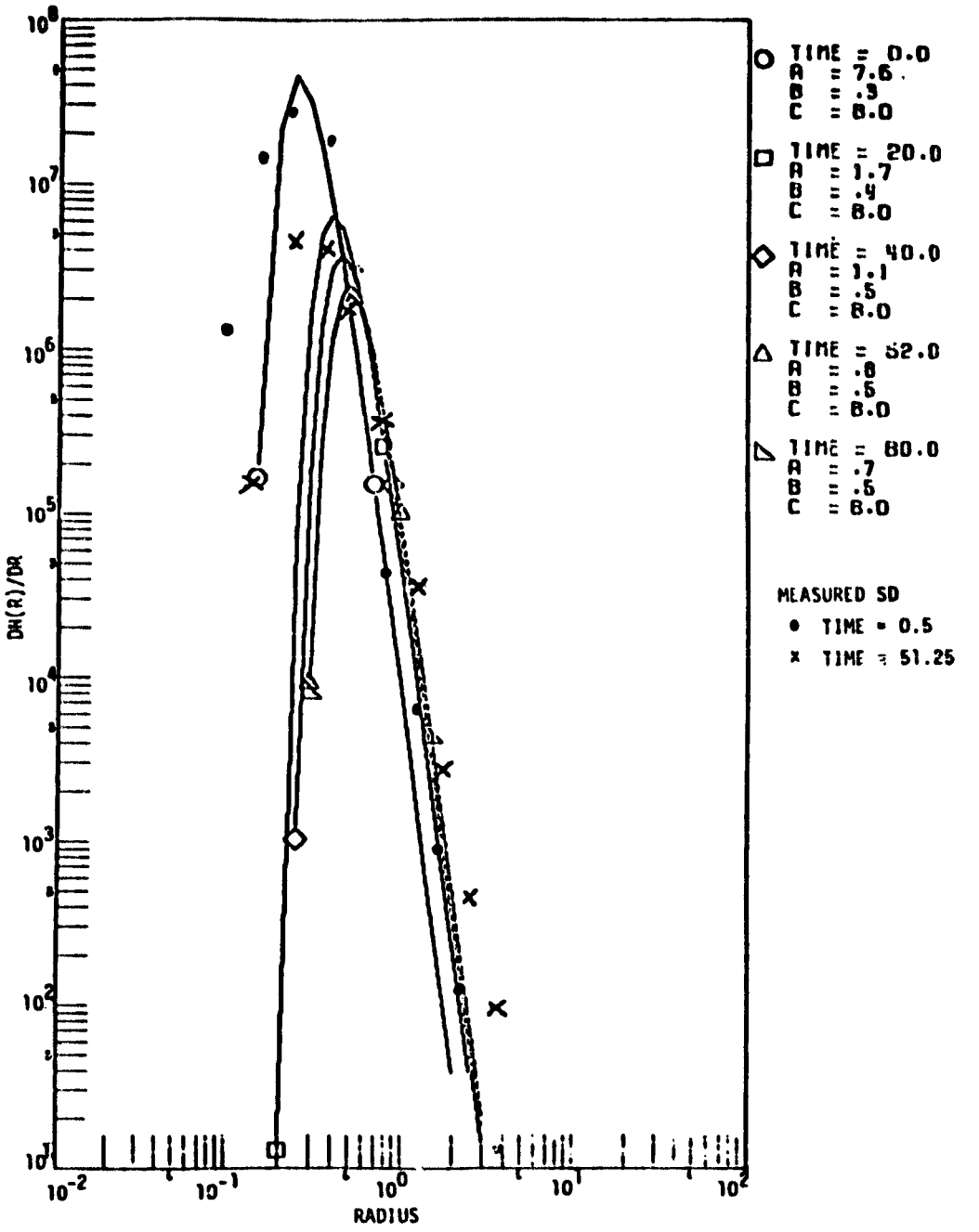

FIGURE 24. Retrieved distributions for different times for Set 1 data using 3-parameter IMGD Model using p_4 = 3.0; and measured size distribution.

The best agreement between the measured and calculated distribuitons at 0.5 min was obtained with $p_4 = 2.0$ and at 51.25 min with $p_4 = 1.0$. The calculated distributions for $p_4 = 3.0$ were much narrower than the measured distributions.

Set 2 Data - MGD Model: The results of applying the search method to this data are not so good. Table 14 gives the χ^2 values for the different values of p_2 at different times. We see from this table that no value of p_2 can be considered to be any better than any other, although at each time at least one distribution satisfies the criteria for an acceptable fit, $\chi^2 \leq 3$.

Figures 25 to 27 are plots of the calculated size distribution for the different values of p_2. There is a shift to larger particles and a decrease in the total number of particles as the time increases.

Set 2 Data - IMGD Model: The results of applying the search method to this data are generally poor as is evident from Table 15 which gives χ^2 as a function of p_4 and time. There is some improvement as p_4 increases and the distribution becomes narrower but even $p_4 = 3.0$ is a very poor fit.

Figures 28-30 are plots of the calculated size distribution. All of the plots show a shift toward larger particles and a decrease in the total number of particles as the experiment progresses.

Set 3 Data - MGD Model: The results of applying the search method to these data are in reasonably good agreement. In many cases, the observed and calculated optical thicknessès are in agreement to within the experimental error. There were four measurements in this data set and we see from Table 16 that on a number of occasions $\chi^2 > 4$ indicating a poor fit.

Comparison of the measured and calculated mass concentrations shows that, in most cases, they are in agreement to within 5% and the maximum difference is 12% (Table 17). The value of the fixed parameter p_2 has little effect on the calculated concentrations since they are in agreement to within 5%. This indicates that the Modified Gamma Distribution is a suitable model for obtaining the mass concentration for this particular data set.

TABLE 14. GOODNESS OF FIT FOR MGD FOR SET 2

Time (min)	χ^2		
	$p_2 = 1.0$	$p_2 = 2.0$	$p_2 = 3.0$
0	15.40	6.360	0.393
20	4.26	0.258	11.300
30	13.00	3.580	2.690
40	1.58	4.560	0.334
50	4.58	0.365	4.030

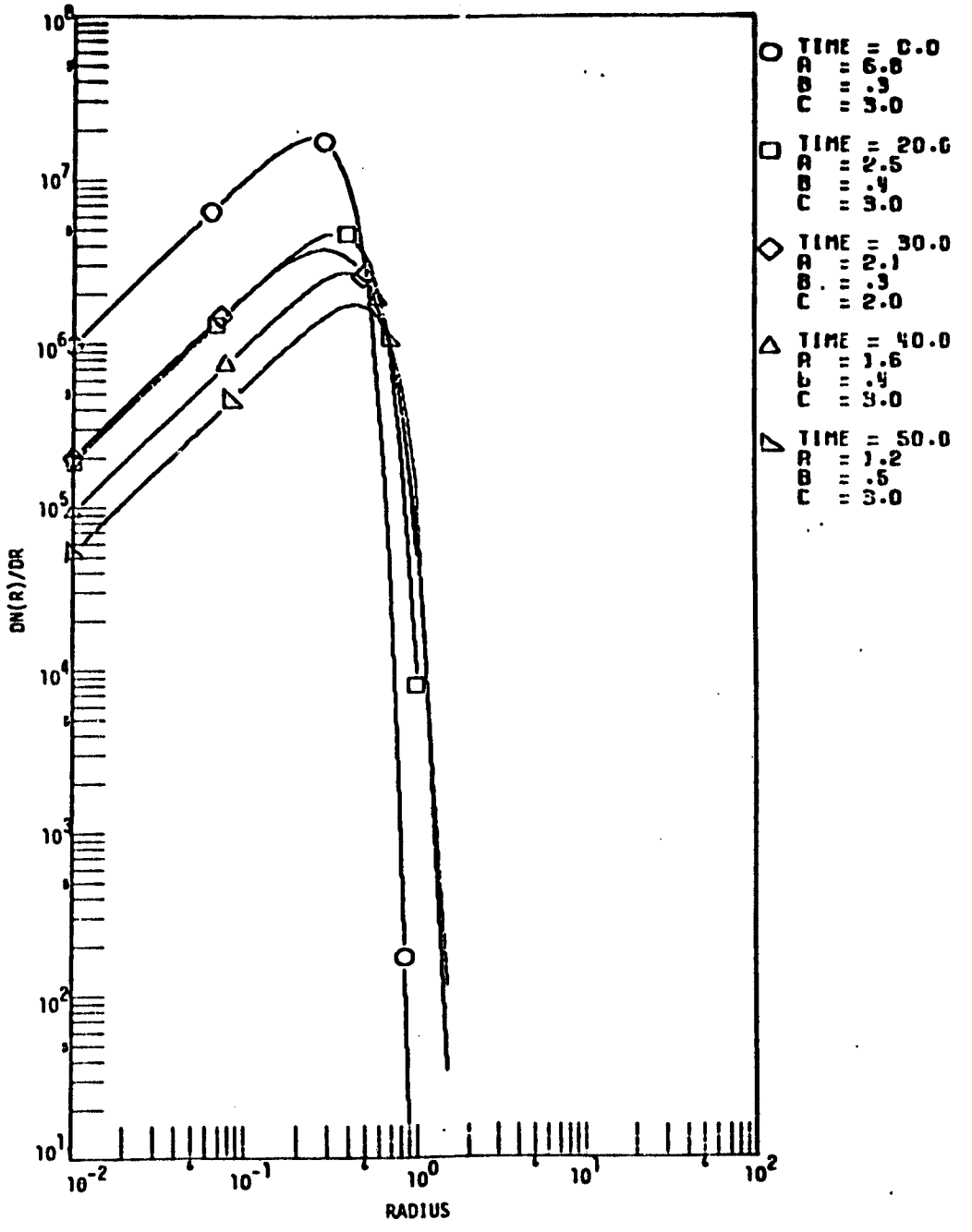

FIGURE 25. Retrieved distributions for different times for Set 2 data using 3-parameter MGD Model with $p_2 = 1.0$

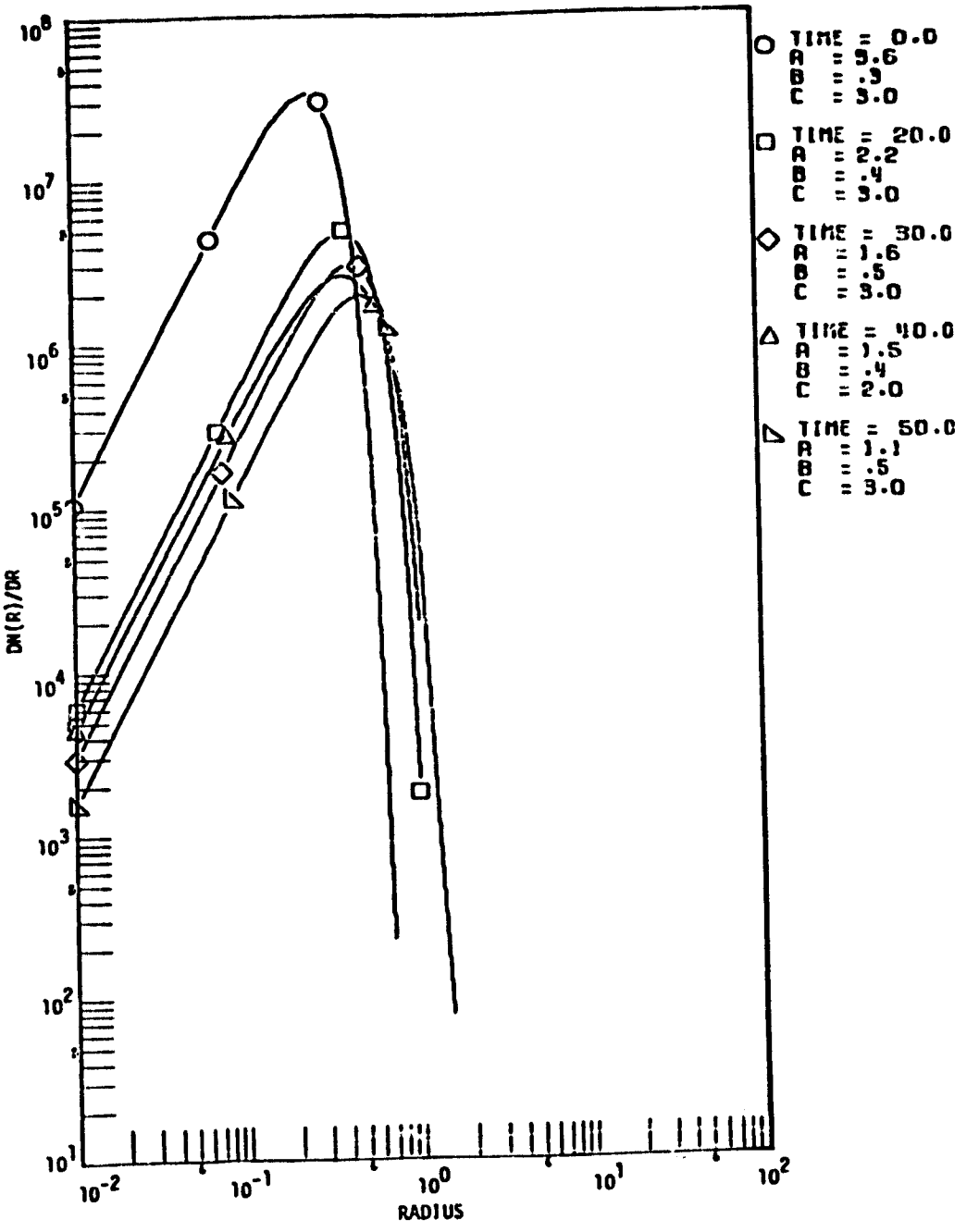

FIGURE 26. Retrieved distributions for different times for Set 2 data using 3-parameter MGD Model with $p_2 = 2.0$

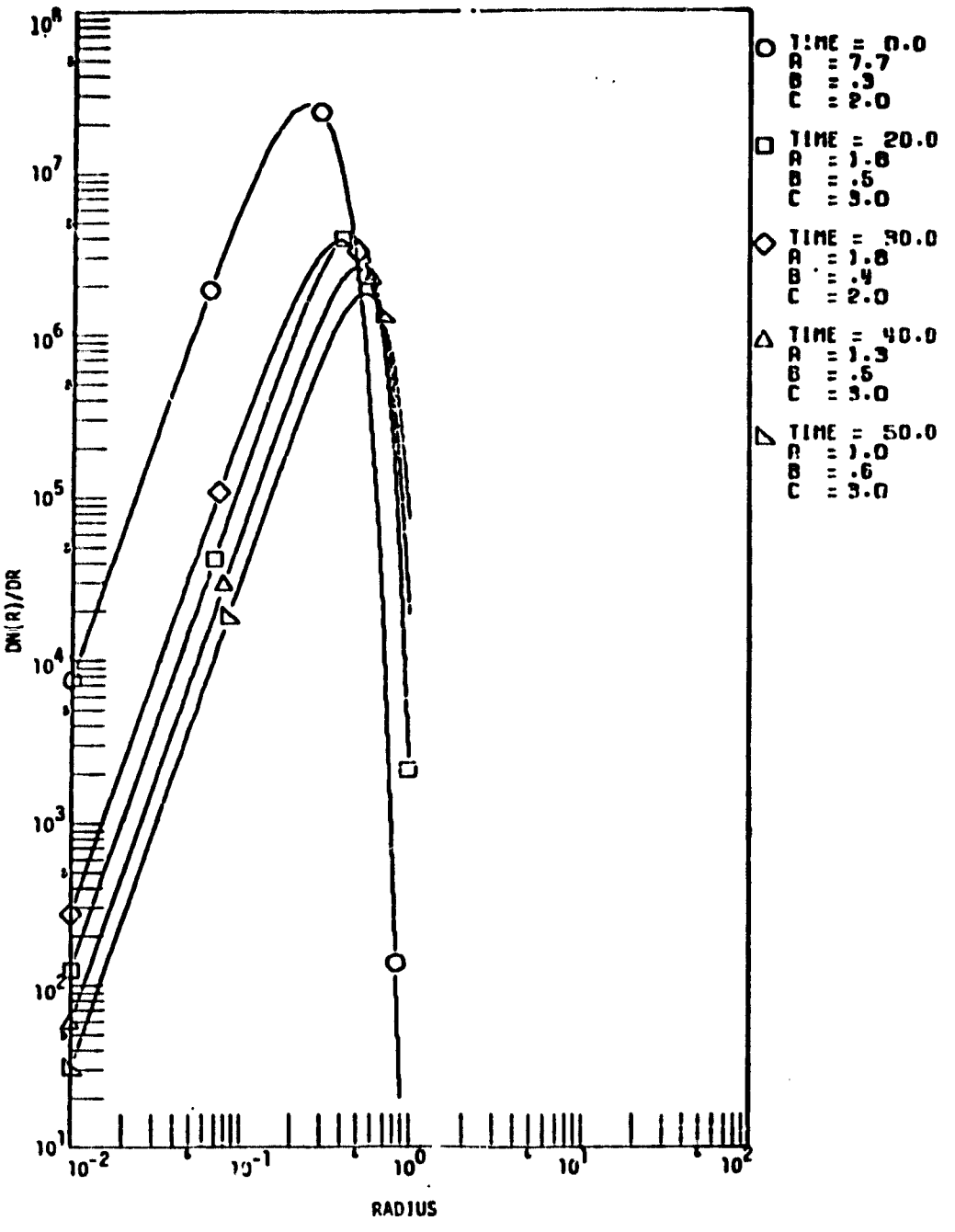

FIGURE 27. Retrieved distributions for different times for Set 2 data using 3-parameter MGD Model with $p_2 = 3.0$

TABLE 15. GOODNESS OF FIT FOR IMGD AND SET 2

Time (min)	χ^2		
	$p_4 = 1.0$	$p_4 = 2.0$	$p_4 = 3.0$
0	62.4	18.6	8.16
20	57.7	21.2	19.80
30	68.3	28.6	16.30
40	55.0	19.3	6.87
50	56.7	13.0	8.78

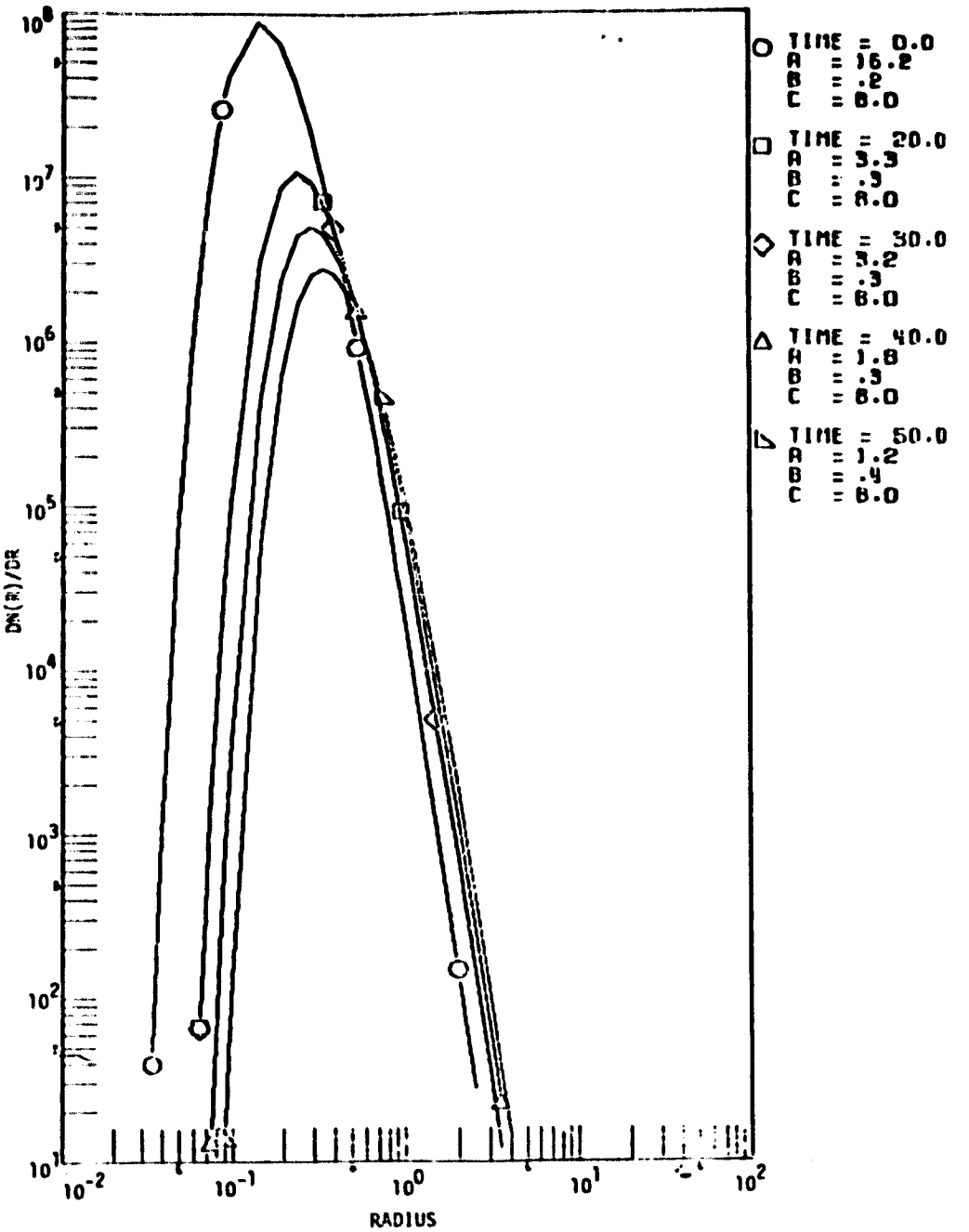

FIGURE 28. Retrieved distributions for different times for Set 2 data using 3-parameter IMGD Model with $p_4 = 1.0$

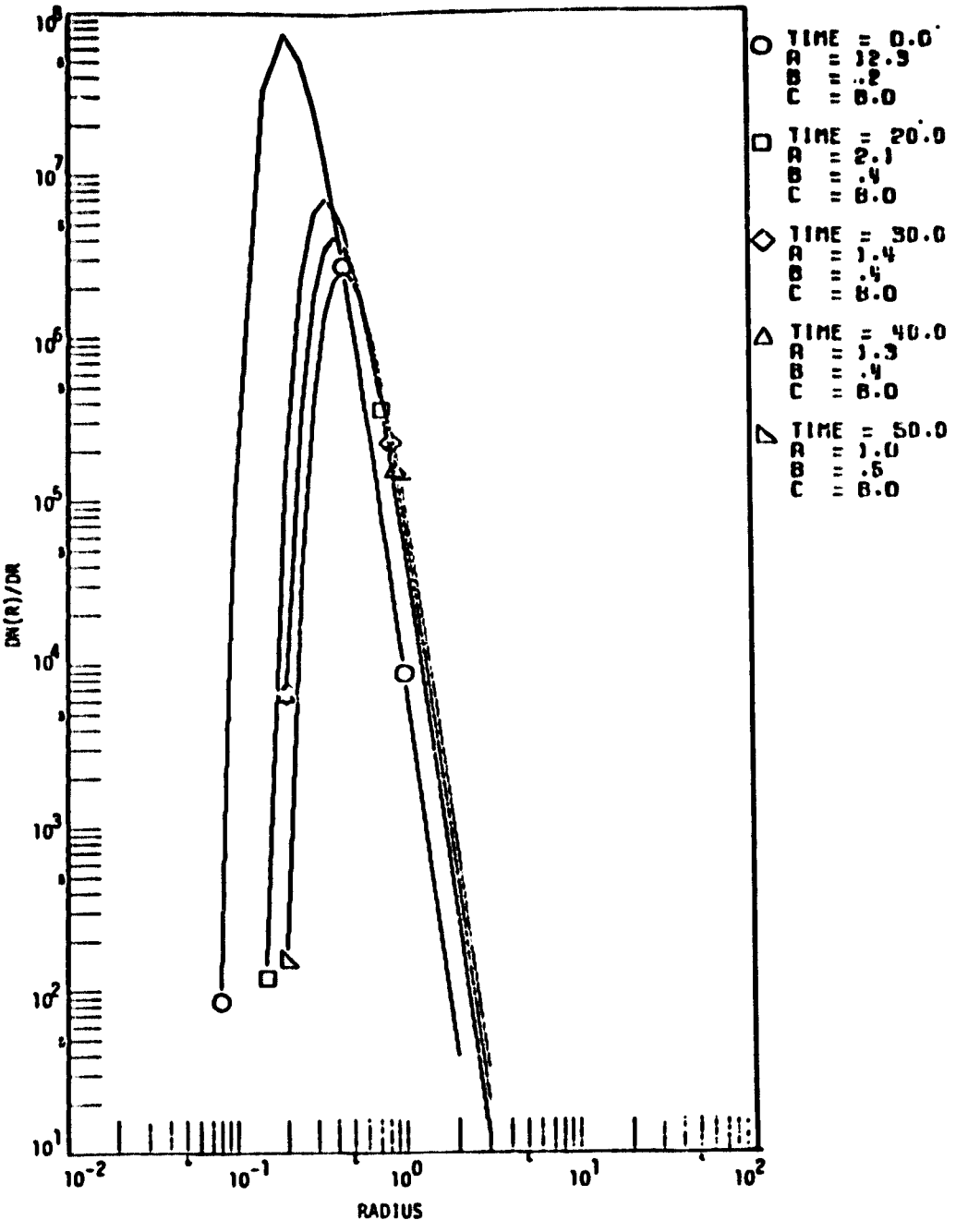

FIGURE 29. Retrieved distributions for different times for Set 2 data using 3-parameter IMGD Model with p_4 = 2.0

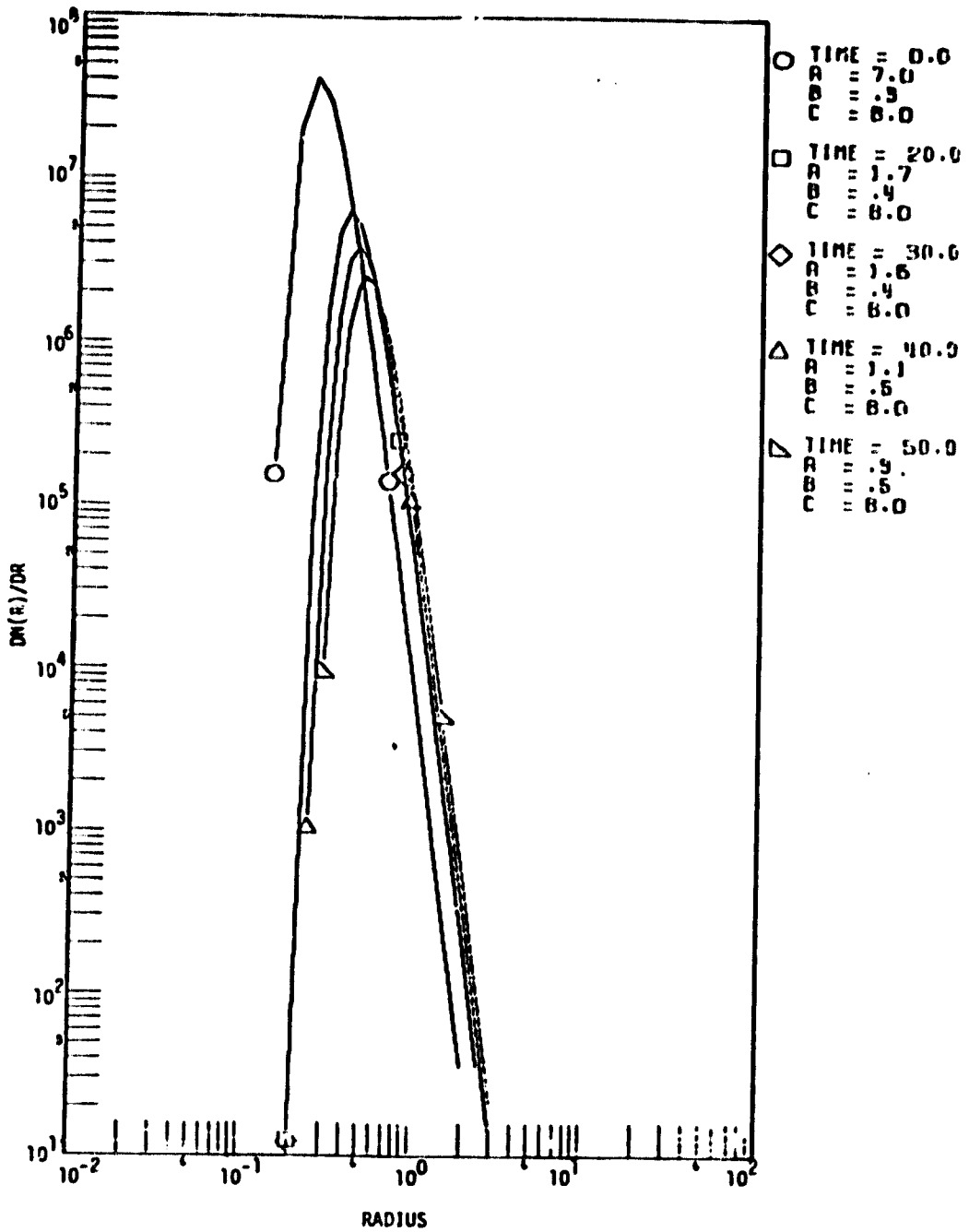

FIGURE 30. Retrieved distributions for different times for Set 2 data using 3-parameter IMGD Model with $p_4 = 3.0$

TABLE 16. GOODNESS OF FIT FOR MGD AND SET 3

Time (min)	χ^2		
	$p_2 = 1.0$	$p_2 = 2.0$	$p_2 = 3.0$
2	25.80	16.50	14.300
30	15.30	3.17	14.000
62	3.75	7.29	0.697
100	9.23	4.77	4.600
150	6.54	3.68	3.330

TABLE 17. COMPARISON OF MEASURED AND CALCULATED MASS CONCENTRATIONS FOR SET 3

Measured		Calculated			
Time (min)	Mass conc. (g/m^3)	Time (min)	Mass concentration (g/m^3)		
			$p_2 = 1.0$	$p_2 = 2.0$	$p_2 = 3.0$
0.5	0.76	2	0.733	0.723	0.738
30.5	0.72	30	0.736	0.730	0.747
58.5	0.65				
		62	0.636	0.622	0.638
67.5	0.62				
87.5	0.59				
		100	0.548	0.566	0.558
122.5	0.46				
152.5	0.40	150	0.436	0.445	0.442

The effective radii as a function of time for the different values of the fixed parameter p_2 are given in Table 18. The radii increase steadily with time and the values differ by less than 10% for the different values of p_2. The effective radii at 2.5 min and 62.0 min could not be determined from the small number of size distribution measurements to compare with the search method results.

The measured and calculated size distributions are plotted in Figs. 31 to 33. As time passes, there is a shift toward larger particles and the total number of particles decreases. For all values of p_2, the calculated distributions drop off faster than the measured size distributions as $r \to \infty$. Lack of measurements for $r < 3$ μm means that no conclusions can be drawn about how well the calculated distributions model the overall features of the aerosol size distribution.

Set 3 Data - IMGD Model: The results of using the search method to fit these data are very poor. Remembering that for this data set $\chi^2 \leq 4$ indicates a good fit, we see From Table 19 that the fits are generally very poor. The measured and calculated mass concentrations are in agreement to within 10%, except at 150 min where the difference is 18.5% (Table 20). Table 21 shows the calculated and measured results of r_{eff}.

The observed and calculated size distributions are plotted in Figs. 34 to 36. The calculated distributions show a steady shift toward larger particles and a decrease in the total number of particles with time. This is consistent with the behavior of the measured distributions but the calculated distributions fall off more rapidly as $r \to \infty$.

Comparison of the Search Method and Nonlinear Least Squares

The Modified Gamma Distribution was fitted to the τ versus λ data using a Nonlinear Least Squares (NLLS) code. The initial estimates for the parameters in the NLLS program were the best fit estimates obtained by the search method. The purpose was to see how close the NLLS final estimates were to the search method estimates.

The formula used in the NLLS code was that given in Eq. 9 of Section 4.1 since this is the simplest expression for the Modified Gamma Distribution. The parameters a and b can be calculated from p_1, p_2, p_3, and p_4 using Eqs. 14 and 10 of Section 4.1.

TABLE 18. EFFECTIVE RADIUS AS A FUNCTION OF TIME FOR MGD AND SET 3

Time (min)	Effective radius (μm)		
	p_2 = 1.0	p_2 = 2.0	p_2 = 3.0
2	0.376	0.380	0.407
30	0.583	0.571	0.595
62	0.656	0.634	0.655
100	0.729	0.761	0.746
150	0.802	0.824	0.814

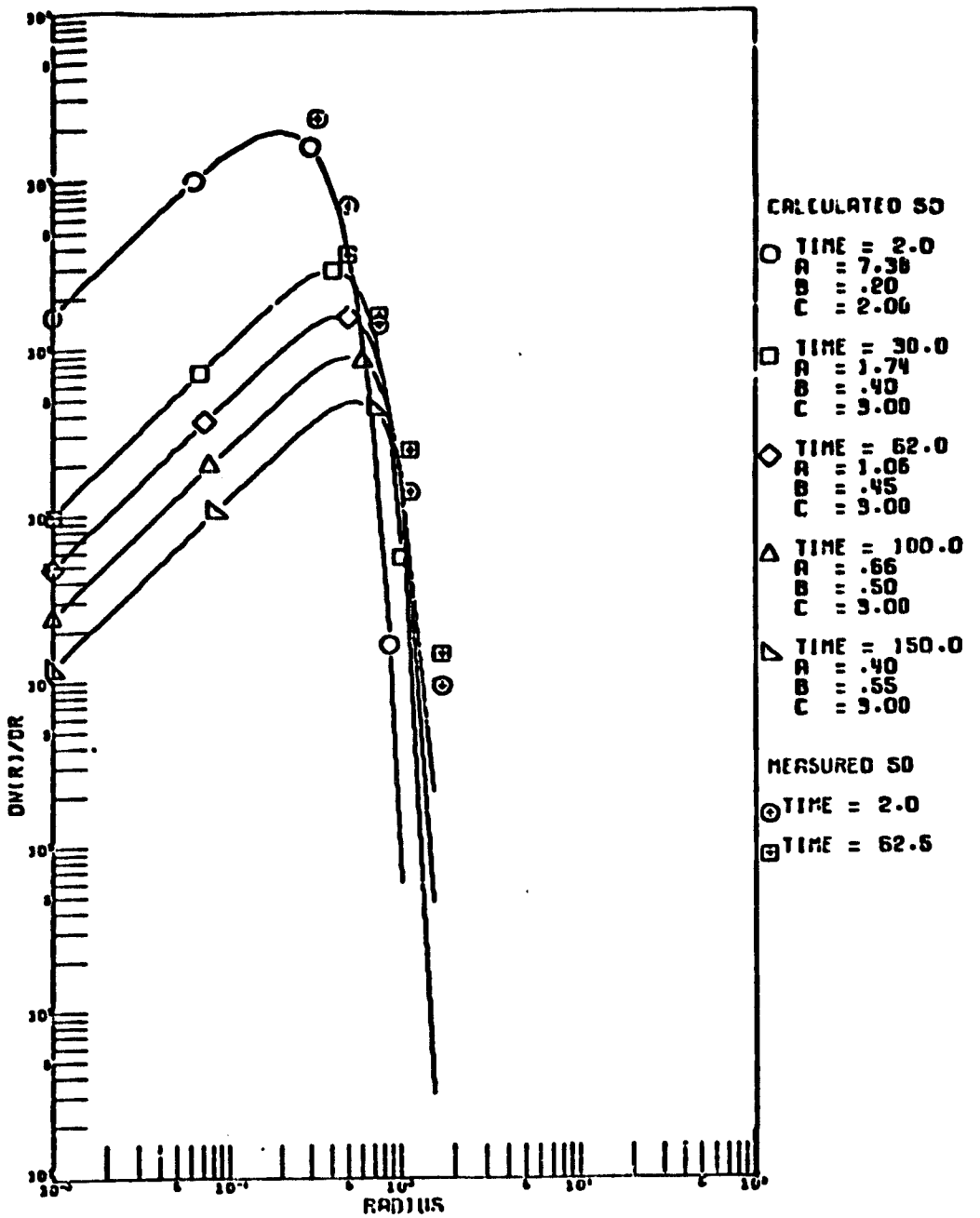

FIGURE 31. Retrieved distributions for different times for Set 3 data using 3-parameter MGD Model with $p_2 = 1.0$; and measured size distribution.

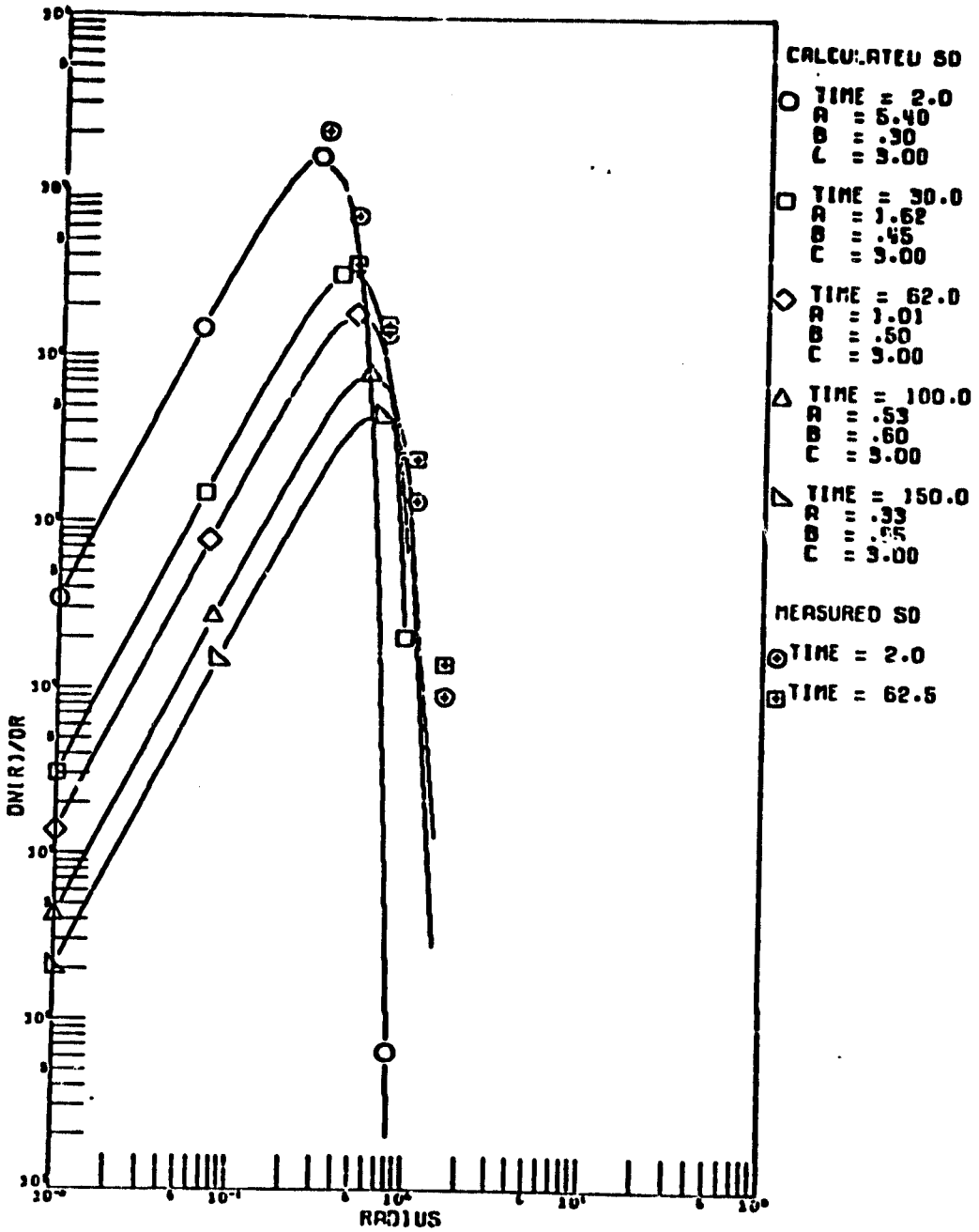

FIGURE 32. Retrieved distributions for different times for Set 3 data using 3-parameter MGD Model with $p_2 = 2.0$; and measured size distribution.

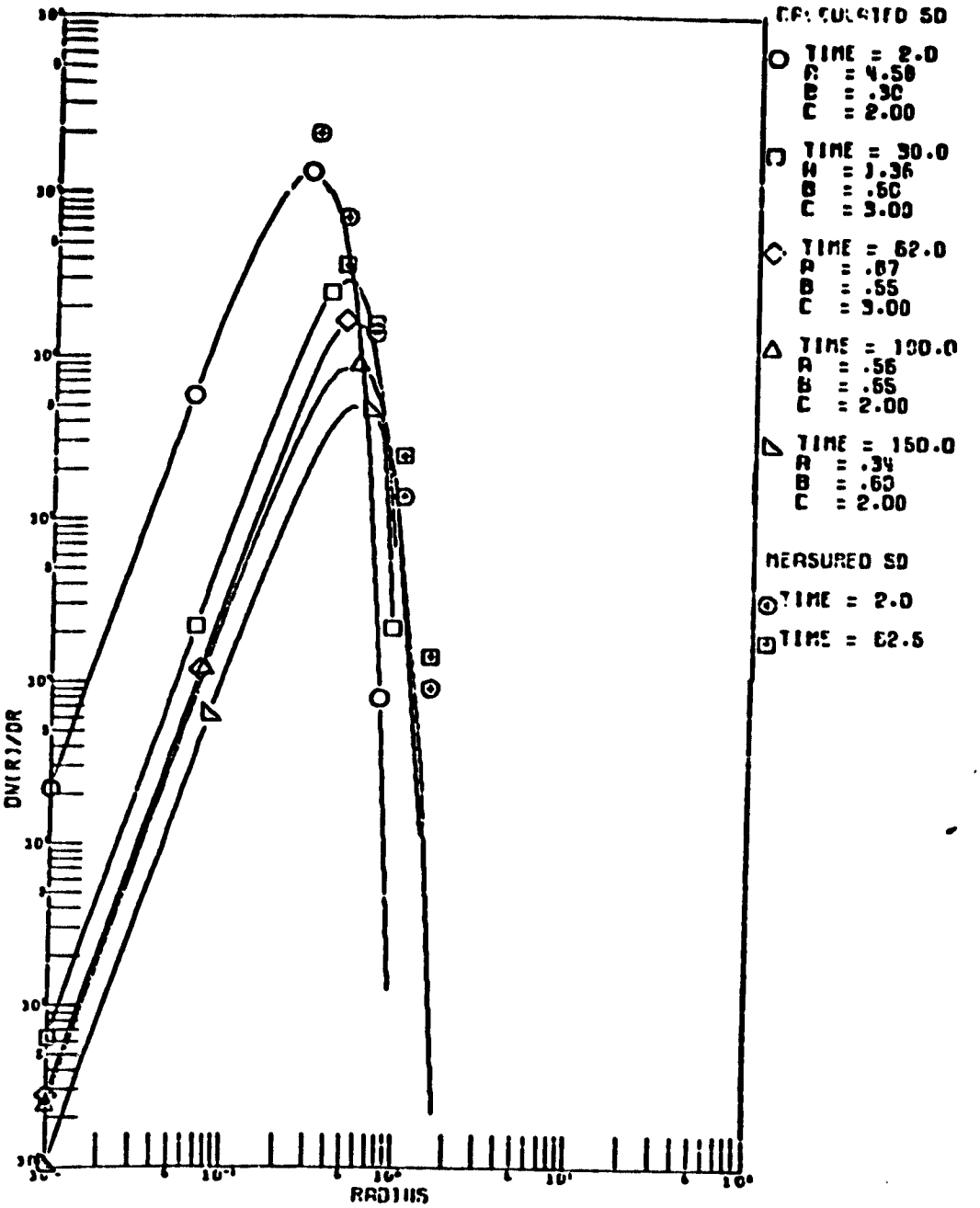

FIGURE 33. Retrieved distributions for different times for Set 3 data using 3-parameter MGD Model with $p_3 = 3.0$; and measured size distribution.

TABLE 19. GOODNESS OF FIT FOR IMGD AND SET 3

Time (min)	χ^2		
	$p_4 = 1.0$	$p_4 = 2.0$	$p_4 = 3.0$
2	139.0	74.6	31.100
30	89.2	38.4	31.000
62	58.2	22.2	15.000
100	47.0	10.9	1.550
150	37.1	4.37	0.613

TABLE 20. COMPARISON OF MEASURED AND CALCULATED MASS CONCENTRATIONS FOR SET 3

Measured		Calculated			
Time (min)	Mass conc. (g/m^3)	Time (min)	Mass concentration (g/m^3)		
			$p_4 = 1.0$	$p_4 = 2.0$	$p_4 = 3.0$
0.5	0.76	2	0.728	0.710	0.724
30.5	0.72	30	0.725	0.737	0.699
58.5	0.65				
		62	0.649	0.644	0.656
67.5	0.62				
87.5	0.59				
		100	0.579	0.562	0.568
122.5	0.46				
152.5	0.40	150	0.473	0.450	0.449

TABLE 21. EFFECTIVE RADIUS AS A FUNCTION OF TIME FOR IMGD AND SET 3

Time (min)	Effective radius (μm)		
	$p_4 = 1.0$	$p_4 = 2.0$	$p_4 = 3.0$
2	0.40	0.376	0.412
30	0.60	0.602	0.549
62	0.70	0.677	0.686
100	0.80	0.752	0.754
150	0.90	0.827	0.823

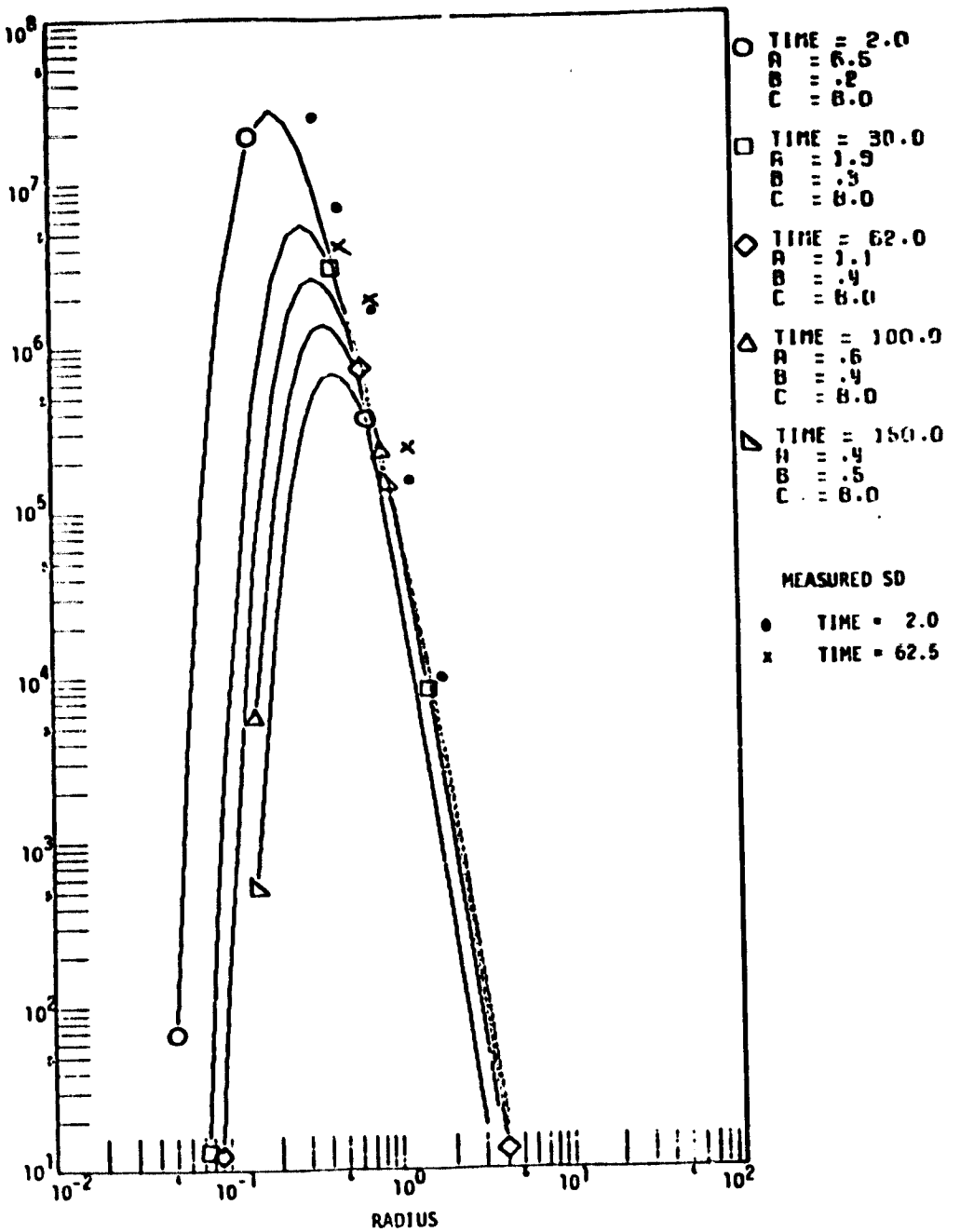

FIGURE 34. Retrieved distributions for different times for Set 3 data using 3-parameter IMGD Model with $p_4 = 1.0$; and measured size distribution.

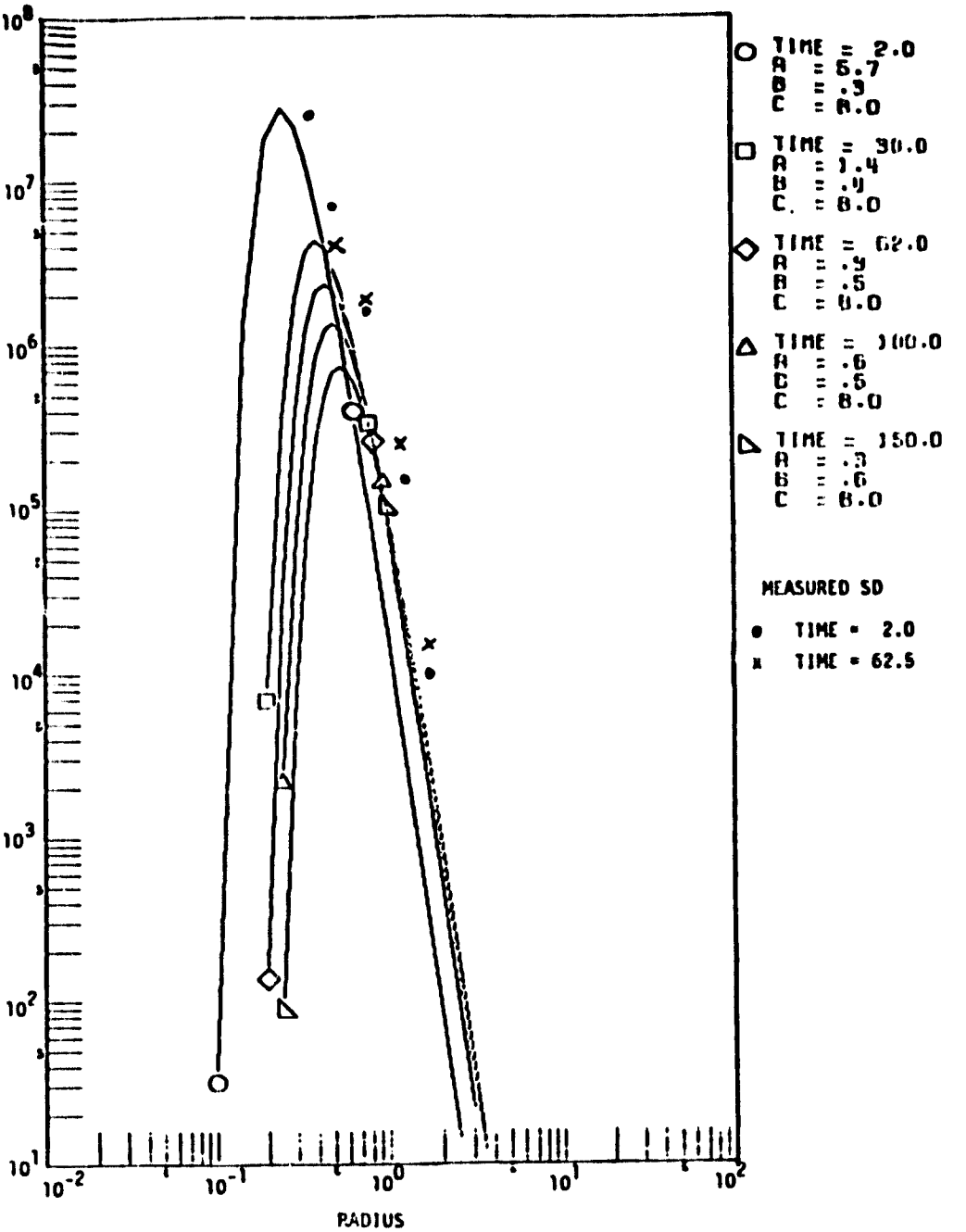

FIGURE 35. Retrieved distributions for different times for Set 3 data using 3-parameter IMGD Model with $p_4 = 2.0$; and measured size distribution.

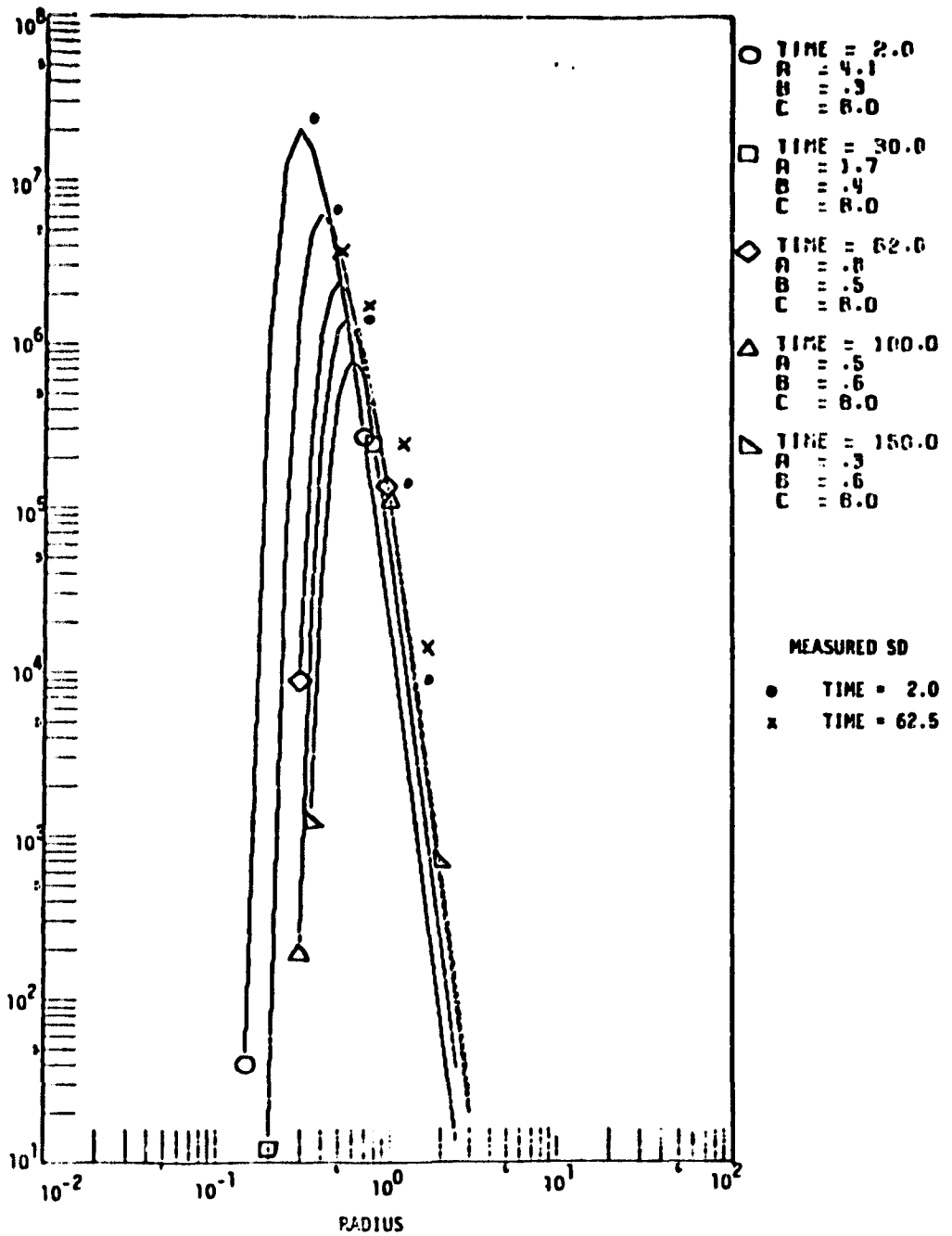

FIGURE 36. Retrieved distributions for different times for Set 3 data using 3-parameter IMGD Model with $p_4 = 3.0$; and measured size distribution.

The results for Set 1 are given in Tables 22 and 23, for Set 2 in Tables 24 and 25, and for Set 3 in Tables 26 and 27. For all three sets, the NLLS results for $p_2 = 3.0$ with $\chi^2 >> 3$ and improbable values for $c(\sim 20)$ so these results will not be considered in the following discussion. The poor results for $p_2 = 3.0$ may have been because the NLLS code was not suitable for fitting such a narrow size distribution.

The NLLS estimates of "a" for the three days were generally within 10% of the search method estimates and the largest difference was 15%. For "b" the NLLS estimates were generally within 5% of the search method estimates although differences up to 15% were noted. The differences between the NLLS estimates of "b" and the search method estimates were less than the step size used in the search method except at 2 min on Set 3 where the NLLS estimate for "b" with $p_2 = 1.0$ is much higher.

The biggest differences between the NLLS estimates and the search method are for c, where the NLLS estimates are consistently 20% to 30% lower than the search method estimates. The exception to this is in the case of t = 2 min on Set 3 for $p_2 = 1.0$ where the NLLS estimate is double the search method estimate. The differences between the NLLS estimates and the search method estimates were generally less than the step size in c.

The effective radii calculated using the NLLS estimates were generally within 10% of the values calculated using the search method estimates. For Set 1 the NLLS estimates of effective radius were up to 10% higher than the values calculated from the measured size distribution, compared to 5% for the search method.

The mass concentrations calculated from the NLLS estimates differed by less than 10% from those calculated using the search method except for Set 1 where it rose to 35% for $p_2 = 2.0$. The NLLS estimates of mass concentration were up to 50% higher than the measured mass concentrations for $p_2 = 1.0$. This dropped to 30% for $p_2 = 2.0$.

The NLLS estimates of mass concentration for Set 3 differed from the measured values by less than 10% compared with 12% for the search method.

The search method is much faster and thus cheaper to use than the NLLS. For both MGD and IMGD, the search method took 16 seconds to do 45 complete table searches and generate the required reports. The

TABLE 22. COMPARISON OF SEARCH METHOD AND NONLINEAR LEAST SQUARES FOR SET 1

Time (min)	Search method				NLLS			
	a	b	c	χ^2	a	b	c	χ^2
p_2 = 1.0								
0	7.370	0.24	3.0	0.356	6.740	0.233	2.32	18.370
20	2.590	0.35	3.0	1.450	2.464	0.331	2.44	0.916
40	1.610	0.40	3.0	2.730	1.516	0.380	2.43	0.723
52	1.140	0.45	3.0	6.100	1.159	0.441	2.76	0.301
80	1.000	0.45	3.0	13.000	0.904	0.443	2.53	0.657
p_2 = 2.0								
0	5.590	0.30	3.0	0.272	5.144	0.297	2.45	24.220
20	2.290	0.40	3.0	2.110	2.035	0.401	2.41	3.338
40	1.440	0.40	2.0	5.850	1.407	0.398	1.83	1.098
52	1.090	0.50	3.0	0.099	1.013	0.494	2.42	0.050
80	0.757	0.55	3.0	2.560	0.740	0.546	2.64	1.928
p_2 = 3.0								
0	6.380	0.30	3.0	9.410	0.157	1.069	26.30	1084.000
20	1.830	0.45	3.0	2.640	0.199	1.074	18.90	803.000
40	1.240	0.50	3.0	0.126	0.233	1.050	27.90	299.000
52	0.938	0.55	3.0	3.270	0.209	1.090	18.30	405.000
80	0.664	0.60	3.0	5.060	0.193	1.096	18.00	298.000

TABLE 23. COMPARISON OF SEARCH METHOD AND NONLINEAR LEAST SQUARES FOR SET 1

Time (min)	Search method		NLLS	
	r_{eff}	M_c	r_{eff}	M_c
p_2 = 1.0				
0	0.365	0.761	0.394	0.813
20	0.510	0.734	0.543	0.791
40	0.583	0.681	0.624	0.738
52	0.656	0.688	0.672	0.733
80	0.656	0.605	0.710	0.657
p_2 = 2,0				
0	0.380	0.748	0.407	0.797
20	0.507	0.726	0.553	0.785
40	0.602	0.686	0.628	0.683
52	0.634	0.677	0.680	0.589
80	0.697	0.624	0.725	0.463
p_2 = 3.0				
0	0.357	0.758	0.987	0.450
20	0.536	0.732	1.008	0.606
40	0.595	0.681	0.966	0.628
52	0.655	0.687	1.025	0.668
80	0.714	0.632	1.032	0.628

TABLE 24. COMPARISON OF SEARCH METHOD AND NONLINEAR LEAST SQUARES FOR SET 2

Time (min)	Search Method				NLLS			
	a	b	c	χ^2	a	b	c	χ^2
p_2 = 1.0								
0	6.750	0.25	3.0	15.40	7.458	0.241	2.79	3.508
20	2.530	0.35	3.0	4.26	2.532	0.334	2.58	3.358
30	2.130	0.30	2.0	13.00	2.187	0.295	1.91	0.496
40	1.640	0.40	3.0	1.58	1.541	0.379	2.42	0.196
50	1.170	0.45	3.0	4.58	1.178	0.438	2.70	0.032
p_2 = 2.0								
0	9.590	0.25	3.0	6.36	7.034	0.250	2.14	33.376
20	2.230	0.40	3.0	0.258	2.111	0.395	2.48	6.269
30	1.570	0.45	3.0	3.58	1.558	0.445	2.63	3.929
40	1.460	0.40	2.0	4.56	1.430	0.398	1.83	0.427
50	1.120	0.50	3.0	0.365	1.068	0.499	2.39	0.396
p_2 = 3.0								
0	7.730	0.25	2.0	0.393	0.178	0.994	21.50	986.000
20	1.770	0.45	3.0	11.300	0.179	1.088	21.40	853.000
30	1.830	0.40	2.0	2.690	0.197	1.084	17.70	699.000
40	1.260	0.50	3.0	0.334	0.206	1.087	18.50	543.000
50	0.959	0.55	3.0	4.030	0.216	1.090	18.30	394.000

TABLE 25. COMPARISON OF SEARCH METHOD AND NONLINEAR LEAST SQUARES FOR SET 2

Time (min)	Search method		NLLS	
	r_{eff}	M_c	r_{eff}	M_c
p_2 = 1.0				
0	0.365	0.697	0.365	0.758
20	0.510	0.715	0.530	0.768
30	0.564	0.714	0.575	0.761
40	0.583	0.691	0.625	0.752
50	0.656	0.705	0.675	0.751
p_2 = 2.0				
0	0.317	0.742	0.363	0.754
20	0.507	0.708	0.538	0.765
30	0.571	0.710	0.592	0.764
40	0.602	0.696	0.627	0.749
50	0.634	0.693	0.691	0.812
p_2 = 3.0				
0	0.339	0.721	0.926	0.420
20	0.536	0.711	1.014	0.556
30	0.543	0.698	1.022	0.624
40	0.595	0.691	1.022	0.651
50	0.655	0.702	1.025	0.689

TABLE 26. COMPARISON OF SEARCH METHOD AND NONLINEAR LEAST SQUARES FOR SET 3

Time (min)	Search method				NLLS			
	a	b	c	χ^2	a	b	c	χ^2
p_2 = 1.0								
2	7.380	0.20	2.0	25.800	4.820	0.325	3.98	7.853
30	1.740	0.40	3.0	15.300	1.769	0.394	2.79	4.927
62	1.060	0.45	3.0	3.750	1.007	0.431	2.51	4.213
100	0.664	0.50	3.0	9.230	0.625	0.477	2.47	13.454
150	0.397	0.55	3.0	6.540	0.404	0.484	2.25	13.473
p_2 = 2.0								
2	5.400	0.30	3.0	16.500	4.037	0.300	2.35	5.017
62	1.010	0.50	3.0	7.290	0.884	0.494	2.27	1.160
100	0.529	0.60	3.0	4.770	0.520	0.597	2.73	4.293
150	0.327	0.65	3.0	3.680	0.326	0.648	2.80	3.575
p_2 = 3.0								
2	4.580	0.30	2.0	14.300	0.181	1.060	26.30	1661.000
30	1.360	0.50	3.0	14.000	0.221	1.088	18.30	904.000
62	0.871	0.55	3.0	0.697	0.208	1.095	19.10	431.000
100	0.562	0.55	2.0	4.600	0.173	1.112	11.70	383.000
150	0.342	0.60	2.0	3.330	0.133	1.119	10.40	269.000

TABLE 27. COMPARISON OF SEARCH METHOD AND NONLINEAR LEAST SQUARES FOR SET 3

Time (min)	Search method		NLLS	
	r_{eff}	M_c	r_{eff}	M_c
p_2 = 1.0				
2	0.400	0.728	0.418	0.727
30	0.600	0.725	0.597	0.785
62	0.700	0.649	0.695	0.683
100	0.800	0.579	0.776	0.589
150	0.900	0.473	0.837	0.463
p_2 = 2.0				
2	0.376	0.710	0.418	0.678
30	0.602	0.737	0.601	0.782
62	0.677	0.644	0.700	0.688
100	0.752	0.562	0.783	0.594
150	0.827	0.450	0.842	0.465
p_2 = 3.0				
2	0.412	0.724	0.978	0.505
30	0.549	0.699	1.023	0.702
62	0.686	0.656	1.028	0.670
100	0.754	0.568	1.079	0.639
150	0.823	0.449	1.096	0.513

45 searches were for five sets of data for each of the three sets for each of the three values of the fixed parameters.

The NLLS code is an iterative one and thus the amount of time taken to determine the best fit parameters depends on how quickly it converges. A total of 48 fits were done. These correspond to the 45 searches done by the NLLS, with three being repeated. The total time required for these fits was 1705 seconds which averages to about 36 seconds per fit. As has been pointed out above the length of time taken for one NLLS fit depends on the number of iterations. The total number of iterations in the above 48 fits was 387 which is approximately 4.4 seconds per iteration. Since none of the NLLS fits converged in less than three iterations, even with good initial estimates, the NLLS is much slower than the search method.

Discussion and Conclusions

The results presented in this report indicate that useful information about aerosol size distributions can be obtained from multispectral measurements of optical thickness using the three parameter search method. It was found that the Modified Gamma Distribution generally gave a better fit to the τ vs λ curve and better estimates of the effective radius and mass concentration than the Inverse Modified Gamma Distribution. On the other hand, the Inverse Modified Gamma Distribution gave better agreement with the measured and calculated size distributions in the region $r \to \infty$.

It is not clear from the results presented here whether the Inverse Modified Gamma Distribution is an unsuitable model or whether the problem lies mainly in the values selected for the parameters, particularly the fixed parameter p_4. More work will be necessary in order to answer this question.

The similarity between the NLLS estimates and the search method estimates indicates that the search method is capable of giving good estimates of the parameters if the grids are well chosen. The fact that the NLLS estimates for c were consistently lower than the search method estimates indicates that an extra value of c is needed, around 2.5, in the search method grid.

The search method has a definite cost advantage over NLLS and the fact that it is much faster, and is not an iterative process, would be important if information about the size distribution were to be obtained from the τ versus λ measurements on an on-line basis during the course of an experiment. The search method estimates also provide good initial estimates for the NLLS. This is important for rapid convergence.

The Modified Gamma Distribution generally falls off faster than the measured distributions as $r \to \infty$ but it seems likely that this will not be of great importance if the distribution gives good estimates of the effective radius and total mass concentration. This applies particularly when only a few measurements are available, as was the case here, since good estimates of these features indicate that the essential nature of the distribution has been captured and the retrieved distribution can be considered an equivalent distribution.

At present, in determining the best fit parameters for the 3-parameter search method, the complete table for each value of c is searched, which is probably not the most efficient way. Further work needs to be done on this aspect in order to make the three parameter method more efficient.

4.3 FAST TABLE SEARCH (FTS) METHOD FOR RETRIEVAL OF AEROSOL SIZE DISTRIBUTION FROM MULTI-SPECTRAL EXTINCTION MEASUREMENTS: TWO-TERM BIMODAL MODEL

Since the measured size distribution in Fig. 6 for Set 1 shows a kink around r = 1 μm, thereby suggesting a bimodal distribution, it was decided to see whether any improvement in fits to the $\tau(\lambda,t)$ data could be obtained by using a two-term analytic model representing a bimodal size distribution. The model chosen was the sum of two Haze H distributions, i.e.,

$$n(r) = \frac{a_1 b_1^3}{2} r^2 e^{-b_1 r} + \frac{a_2 b_2^3}{2} r^2 e^{-b_2 r} \qquad (34)$$

where each term represents a mode of a bimodal size distribution, and adjustable parameters are as follows:

a_1 = total number of particles in the first mode
b_1 = mode radius for the first mode
a_2 = total number of particles in the second mode
b_2 = mode radius for the second mode.

Since data for only three wavelengths were available for Set 1 and there are four parameters to be determined, it was decided to fix b_1 and b_2 and then determine a_1 and a_2 from the data. If the distribution changes with time, this would presumably be reflected in changes in the relative proportions of the two modes.

The values chosen for the b's were 15.0 for b_1 and 7.0 for b_2, which corresponded to the best fit values for Haze H fitted to extinction data taken at times 0 and 52 min. The values of a_1 and a_2 were found by solving the three simultaneous equations

$$\tau(\lambda_i) = a_1 \tau_1(\lambda_i) + a_2 \tau_2(\lambda_i), \qquad i = 1, 2, 3 \qquad (35)$$

in the least squares sense; where $\tau(\lambda_i)$ are measured data, $\tau_1(\lambda_i)$ and $\tau_2(\lambda_i)$ are the extinction values for the first and second modes, calculated by using the normalized size distribution $\eta_o(r)$, defined as in Eq. 3 in Section 4.1.

Tables of the $\tau_o(\lambda_i)$ were calculated as described in Sections 4.1 and 4.2.

The expressions for a_1 and a_2 are then given by

$$a_1 = \frac{\sum_{i=1} \tau(\lambda_i)\,\tau_1(\lambda_i) \cdot \Sigma\,\tau_1(\lambda_i)\,\tau_2(\lambda_i) - a_2(\Sigma\,\tau_1(\lambda_i)\tau_2(\lambda_i)^2}{\sum_i \tau_1^2(\lambda_i) - \sum_i \tau_1(\lambda_i)\tau_2(\lambda_i)}$$

$$a_2 = \frac{\sum_i \tau(\lambda_i)\,\tau_1(\lambda_i) \sum \tau_1(\lambda_i)\,\tau_2(\lambda_i) - \sum_i \tau(\lambda_i)\,\tau_2(\lambda_i) \sum_i \tau_1^2(\lambda_i)}{[\sum_i \tau_1(\lambda_i)\,\tau_2(\lambda_i)]^2 - \sum_i \tau_1^2(\lambda_i) \sum_i \tau_2^2(\lambda_i)} \quad (36)$$

Equation (34) was also solved for a_1 and a_2 using a nonlinear least squares code. Since the system is in fact linear if neither b_1 nor b_2 are to be determined, this is not the most efficient method of solving the equation.

Results

The distributions obtained for 0.0 and 52.0 for both methods are given in Figs. 37 and 38 and the parameter estimates are given in Table 27. Figure 37 shows that both methods give distributions which agree quite well with the measured distribution, especially for $r > 0.5$ μm. The mode radii of the calculated distributions tend to be lower than the mode radius for the data while the maxima are higher.

Table 28 gives a comparison of the calculated and true extinction values for the different wavelengths. It can be seen that both methods give good estimates for the extinction at 0.6328 μm and 1.15 μm but the nonlinear least squares estimate is better for the 3.39 μm data. It is interesting to note the differences in the values of a_1 and a_2 obtained by the two methods.

Figure 38 shows that the linear method gives a reasonably good fit to the measured size distribution while the nonlinear least squares (NLLS) fit is very poor. One problem with the NLLS fit is that all the values are a factor of 10 to 15 too low and also the run had not reached convergence in 10 iterations.

A problem to be noted in the case of both these methods is that for the 52 min data, a_1 is negative and this gives rise to nonphysical negative size distributions for $r < 0.2$ μm. The problem of getting negative parameters is always a possibility wherever two analytic terms are added as was done here.

TABLE 27: PARAMETERS FOR SET 1 DATA AND TWO TERM HAZE H + HAZE H MODEL

Time (min)		Search Method	NLLS
0.0	a_1	13.72	2.281×10^4
	a_2	0.066	18.0
52.0	a_1	-1.199	-121.0
	a_2	1.[illegible]	15.9

TABLE 28: COMPARISON OF $\tau(\lambda)$ VALUES FOR SET 1 DATA

		$\tau(\lambda)$		
Time (min)	λ (μm)	Measured *	Search Method	NLLS
0.0	0.6328	6.8	6.81	6.80
	1.15	3.7	3.67	3.70
	3.39	0.45	0.53	0.44
52.0	0.6328	6.8	2.85	0.17
	1.15	3.7	3.47	0.20
	3.39	0.45	0.99	0.05

*at times t = 0.0 and 51.25 min

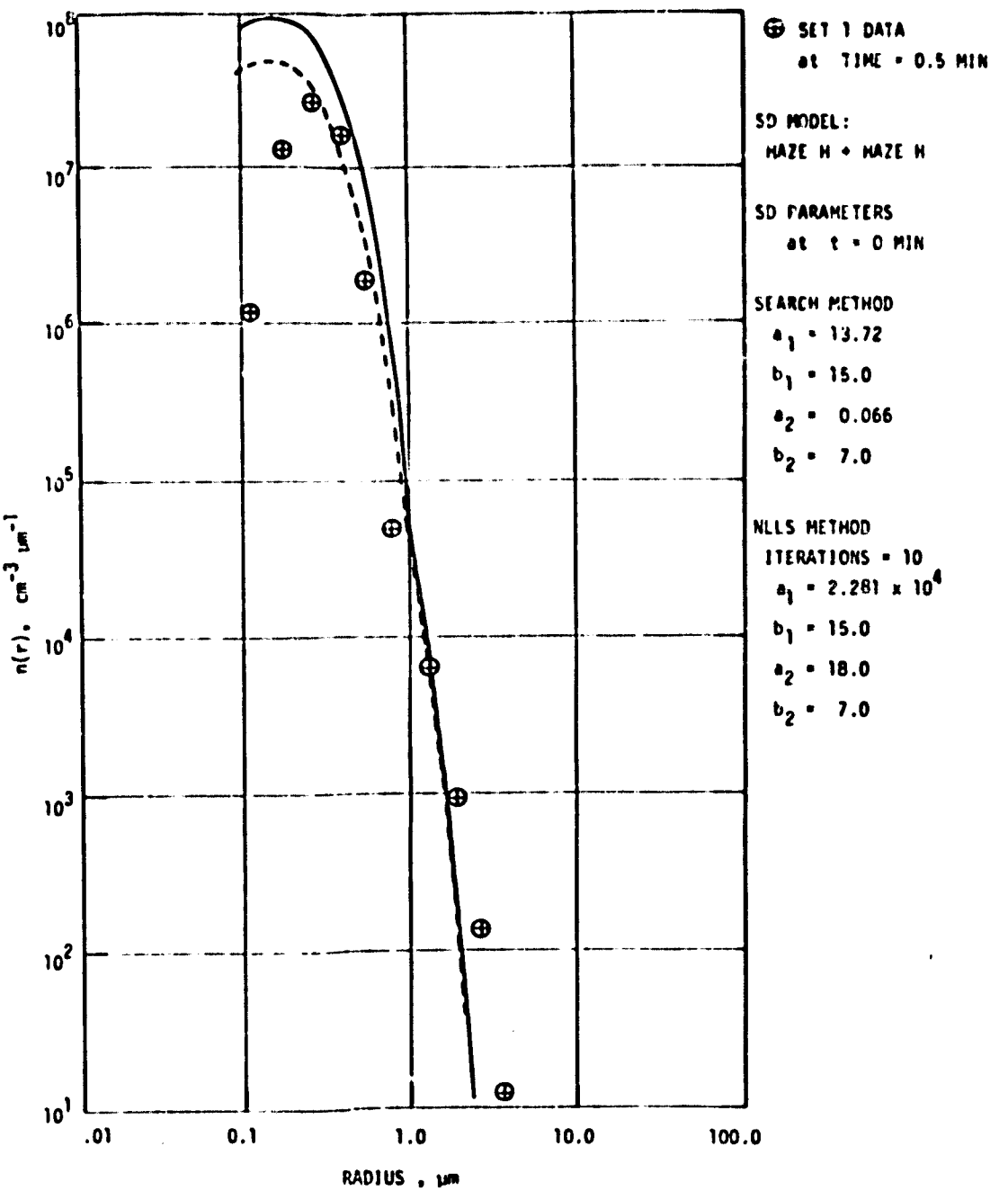

FIGURE 37. Size distributions for Set 1 data: ⊕ denotes measurements at t = 0.5 min; dashed line, retrievals by NLLS code at t = 0; and solid line, retrievals by search method at t = 0.

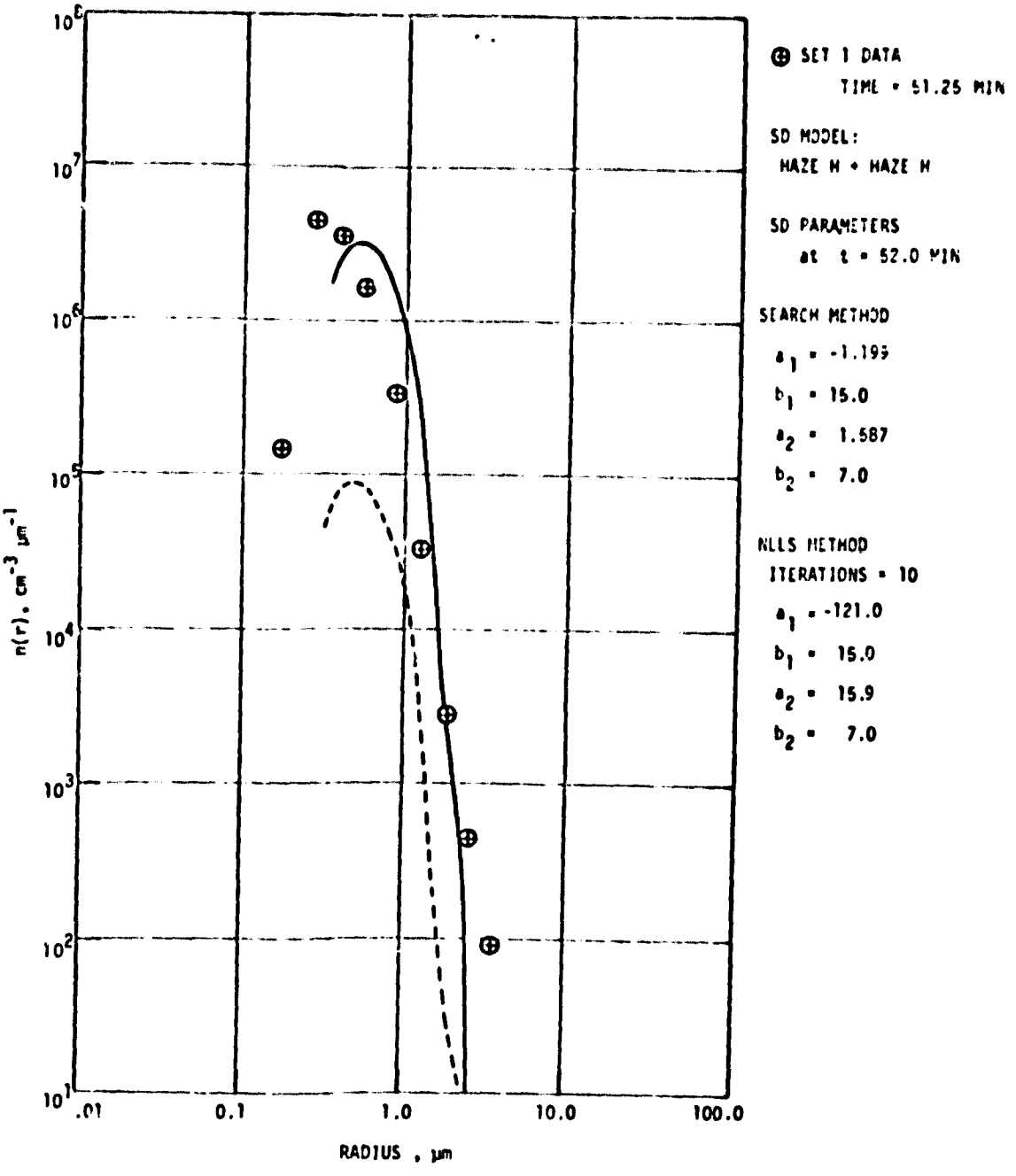

FIGURE 38. Size distributions for Set 1 data: ⊕ denotes measurements at t = 51.25 min; dashed line, retrievals by NLLS code at t = 52 min; and solid line, retrievals by search meth[illegible] at t = 52 min.

Figures 39 and 40 give the plots of dN/d log d, d^2dN/d log d and d^3dN/d log d for 0.0 and 52.0 min, respectively. When these plots are compared with the corresponding plots for the measured n(r) data given in Figs. 7 and 8 it is seen that even with the sum of two Haze H terms, the bimodality in retrieved results is not too clear.

The calculated curves for the 0.0 min data are a little broader than the measured curves but do peak at about the same diameters and have very similar maxima. The calculated curves are very similar to the measured curves in the region $0.5 < d < 2$ μm, but the calculated curves drop off too steeply beyond this point.

The calculated curves for the 52.0 min data peak a higher diameter than the measured curves and although the maximum for the dN/d log d curve is lower than the measured value, the maxima for the other two curves are higher than the calculated values.

Conclusions

The use of a two-term model does appear to have some merit in determining aerosol size distribution from $\tau(\lambda)$ data, but it should be clearly stated that three independent measurements are really not enough to obtain accurate results. Certainly if details such as the bimodal peaks and valleys in the curves are to be determined, more wavelengths are necessary. However, for the sake of completeness we decided to include this case in the final report.

There are a number of problems inherent in the method used here. Since only three wavelengths were available, it was necessary to fix the mode radius parameters for the two terms. To be done most efectively, this requires some *a priori* knowledge of the aerosol size distribution.

Another problem is the possibility that terms will be subtracted, rather than added, as happened with the data for 52 min. This opens up the possibility of negative size distributions which is clearly a physical impossibility. Further work using greater number of independent measurements taken for different wavelengths, needs to be done to draw firm conclusions about the accuracy of the results.

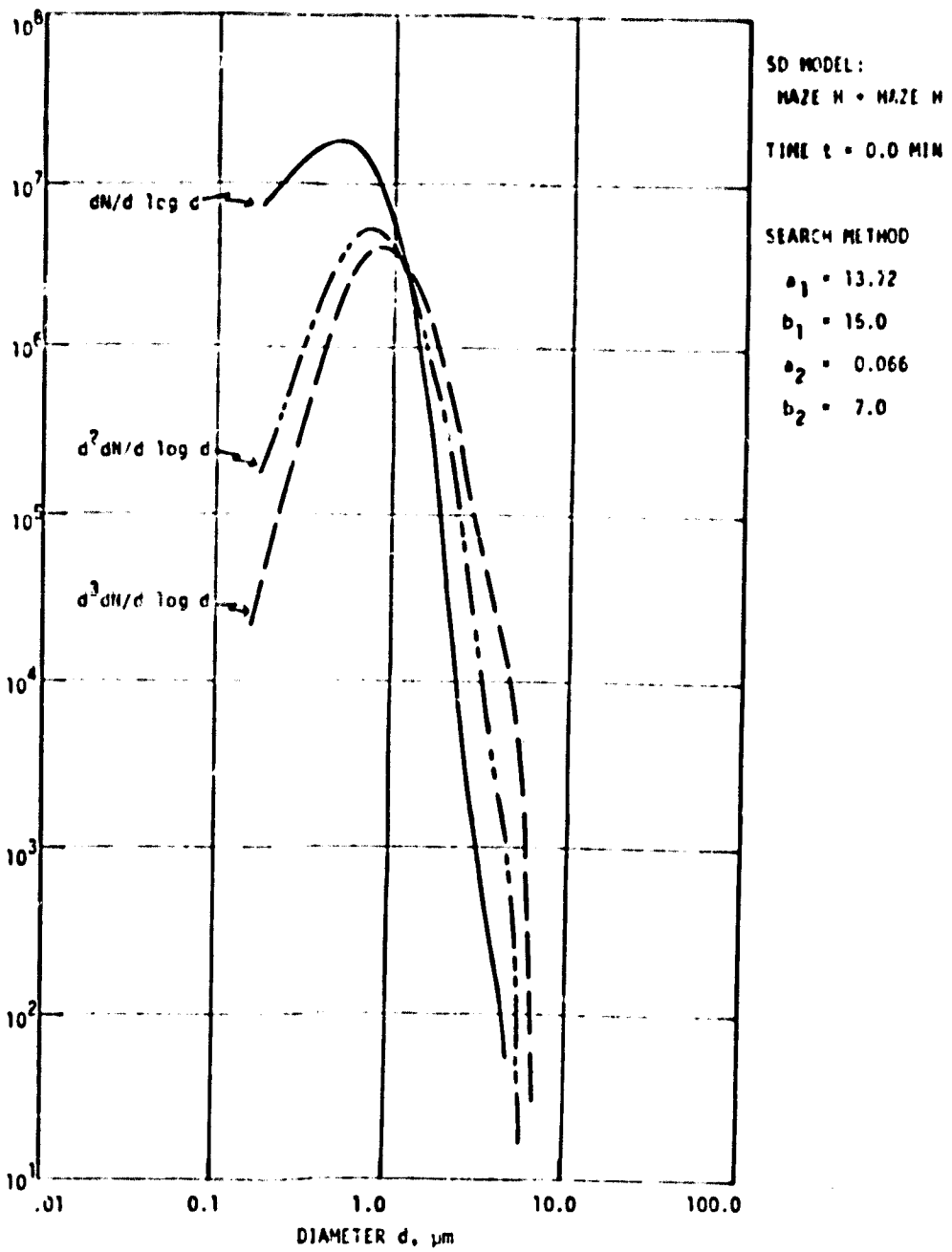

FIGURE 39. Three representations (or moments) for Fig. 37 retrieved size distribution: number-, area-, and volume-, log size distributions.

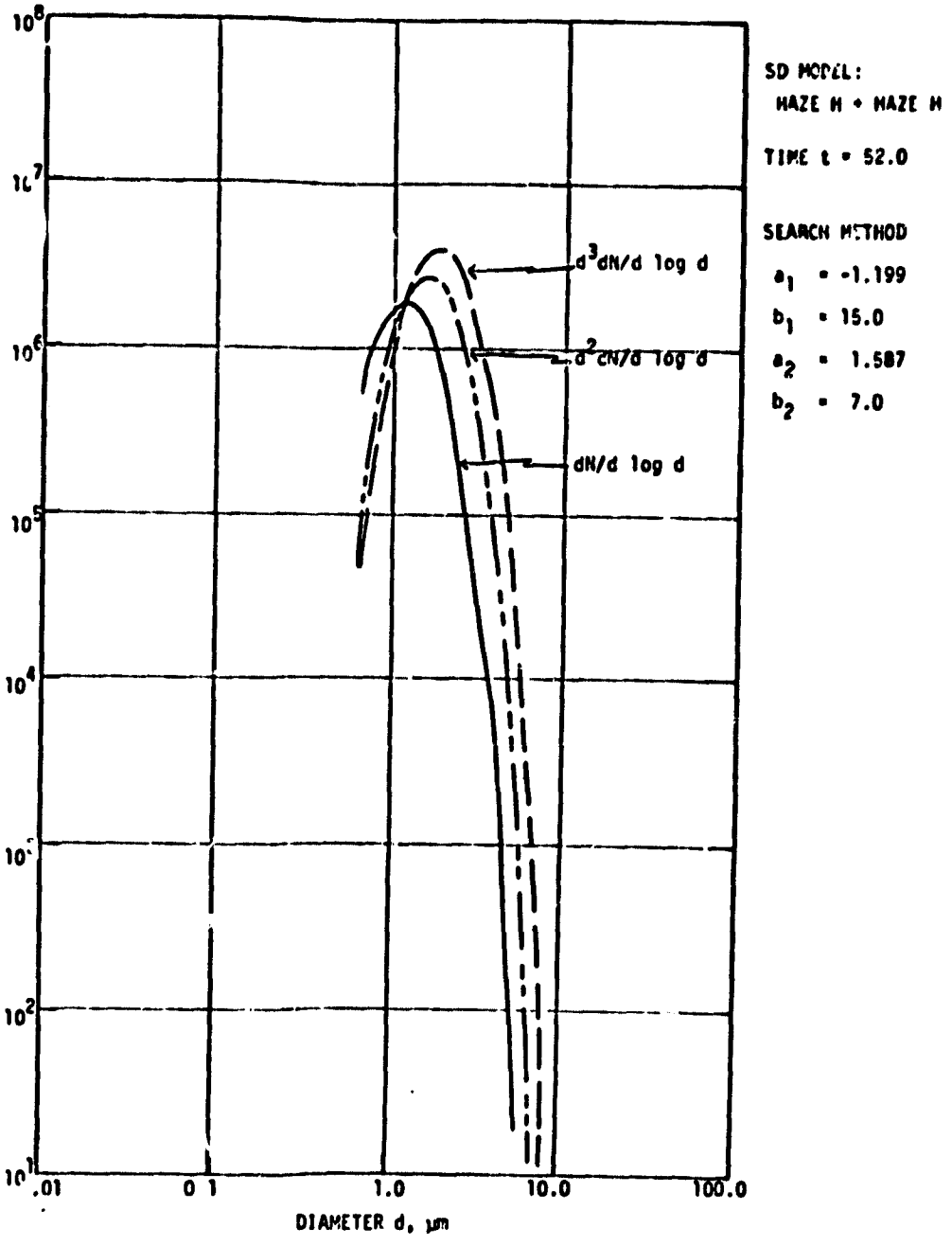

FIGURE 40. Three representations (or moments) for Fig. 38 retrieved size distribution: number-, area-, and volume-, log size distributions.

C-2

4.4 ERROR ANALYSIS OF RETRIEVED AEROSOL SIZE DISTRIBUTION

In order to understand how the (random) errors in optical depth measurements effect the accuracy of retrieved size distribution results, the following numerical experiment was performed. Inversions of the simulated $\tau(\lambda)$ data were performed by a nonlinear least squares (NLLS) program.

In the numerical experiment, the aerosol size distribution n(r) ($cm^{-3}\ \mu m^{-1}$) was represented by an analytic model, such as, log-normal distribution (LND) with three adjustable parameters p_i (i = 1, 2, and 3), defined as (in Ref. 21):

$$n(r) = \frac{p_1}{\sqrt{2\pi}\ p_3\ r}\ \exp\left[-\frac{1}{2}\left(\frac{\ln r - \ln p_2}{p_3}\right)^2\right] \tag{37}$$

where p_1 is the scaling parameter associated with the total number of particles, p_2 is the mode radius parameter, and p_3 the polydispersity parameter. Then, if Stokes' settling is assumed (Ref. 23), the optical depth τ at any time t is defined by

$$\tau(t) = \pi L \int_{r_1}^{r_2(t)} r^2\ Q(x,m)\ n(r)\ dr \tag{38}$$

where

$$r_2(t) = (\alpha/t)^{1/2} \tag{39}$$

Q(x,m) is the Mie efficiency factor, m = m' - im" is the complex aerosol refractive index, and α is defined in Eq. (51) Section 5.1.

Values of τ were calculated for various times t in the time period 10 to 3000 secs, for three wavelengths λ = 0.4416, 0.6328 and 1.15 μm, using the following input data: $p_1 = 8 \times 10^4$, $p_2 = 2.0$ and $p_3 = 0.5$; m = 1.47 - i(0); path length L = 120 cm; distance from top to laser beam height, h = 100 cm; and particle specific gravity $\rho_p = 2.0$. The calculated values of $\tau(\lambda,t)$ vs t then provide the simulated (measurement) data. Adding no random noise to these simulated data, and using as inputs in the NLLS code first estimates for the three parameters p_i of n(r) different from the values

of p_i used to produce the simulated data, we obtain in a few iterations the best fit values p_1', p_2' and p_3' for the parameters. The program also yields the errors p_1', p_2' and p_3' in the retrieved parameters p_i'. Then the error in the retrieved size distribution n'(r), obtained by using p_i' in Eq. (1), is given by

$$\frac{\Delta n'(r)}{n'(r)} = \frac{\partial n'}{\partial p_1'} \Delta p_1' + \frac{\partial n'}{\partial p_2'} \Delta p_2' + \frac{\partial n'}{\partial p_3'} \Delta p_3' \tag{40}$$

The errors in the τ' due to errors in p_i' are given by the relation

$$\frac{\Delta \tau'}{\tau'} = \frac{\partial \tau}{\partial p_1'} \Delta p_i' + \frac{\partial \tau}{\partial p_2'} \Delta p_2' + \frac{\partial \tau}{\partial p_3'} \Delta p_3' \tag{41}$$

Next, add random noise to the simulated values of $\tau(t)$ (obtained by using $p_1 = 8 \times 10^4$, $p_1 = 2.0$, $p_3 = 0.5$). The random number generator is used to obtain numbers randomly distributed with a mean value equal to zero, and variance equal to unity, i.e., N(0,1). These numbers were then converted to a distribution which has a mean μ and variance σ^2, by using the following relation:

$$X = RN * \sigma + \mu \tag{42}$$

where X is the random number which is $N(\mu, \sigma^2)$, and RN is the random number which is N(0,1), the number generated by the program.

It was assumed that the mean of the errors was zero and the standard deviation, σ, could be expressed as a percentage of the measurement. Thus,

$$\tau_N = \tau(1 + X) \tag{43}$$

where τ_N is the new measurement with the noise added.

The values of σ used were 0.01, 0.02, 0.05 corresponding to 1%, 2%, and 5% noise level.

Discussion of Results

The simulated (measurement) data for $\tau(\lambda)$ were inverted using a non-linear least squares (NLLS) program. With no noise added to the simulated data, the retrieved size distribution parameters agreed almost perfectly with the true values, any discrepancy being negligibly small.

When noise was added to the simulated data, five sets of noisy data were generated for each of the three noise levels (1%, 2%, and 5%), by

generating the random numbers five times separately, to allow a better examination of the accuracy of the inversions of noisy data. Each set was then inverted separately. The results are summarized in Table 29.

For 1% Noise

For λ = 0.4416 μm, the ranges of errors in the retrieved values of p_1 was 0.66% to 0.84%; in p_2, 0.61% to 0.78%; and in p_3, 0.74% to 0.95%.

For λ = 0.6328 μm, the ranges of errors in p_1 was 0.64T to 0.84%; in p_2, 0.55% to 0.78%; and in p_3, 0.65% to 0.96%. The range of errors seems to widen slightly for the larger wavelengths.

For 2% Noise

When the noise in the data increases, Table 29 shows that ranges of errors in p_1, p_2, and p_3 for λ = 0.4416 μm are 1.30T to 1.66%, 1.21% to 2.11%, and 1.46% to 1.92%, respectively; for λ = 0.6328 μm, 1.19% to 1.67%, 1.12% to 1.55%, and 1.29% to 1.87%, respectively. Again, we notice that for the larger wavelengths, the range of errors increases somewhat.

Errors in Calculated τ' vs t

The retrieved parameters p_i' were used to plot the retrieved size distributions $n'(r)$, which in turn were used to obtain the calculated (retrieved) τ' vs t data. Table 30 shows the results of expected percentage errors in the calculated values and the ratio of the calculated to the true τ values (at selected timen in the period 10-3000 sec) for each of the three noise levels. These results are for only one wavelength; viz., λ = 0.4416 μm, and for inversion on only one set of data. The trends obtained from these results will be typical for other cases as well.

Examination of Table 30 shows that for the three noise levels, the percentage errors in the calculated values are generally greater than the percentage difference between calculated and true values, indicating that the inversion is quite good, even with 5% noise added. One notices that as the noise level increases, then both the percentage error in the calculated value and the percentage difference between calculated and true values tend to increase.

The percentage errors in calculated values are least in the time period 200-1200 sec (i.e., the r_2 region 1.87-4.57 μm). This corresponds to the region where percentage errors in retrieved size distributions are also minimum and to the region near the peak where the size distribution is changing less rapidly than for very small size ($r \to 0$) or very large size ($r \to \infty$) particles.

Errors in Retrieved Size Distribution

From the errors in the retrieved parameters, the errors in the retrieved size distribution can easily be calculated by using the Eq. (40). For data with no noise, the errors were negligibly small, as would be expected; but they become significant when noise is added to the data. Discussions will be restricted to the particle size range $0.1 < r < 20$ μm. The results are plotted in Fig. 41.

For 1% noise, the error decreases from about 11% at radius 0.1 μm to 1.5% at 2.0 μm, then increases to 7.5% at 20 μm. For 2% noise, the error decreases from 22% at radius 0.1 μm to 3% at 2 μm, and then increases again to 15% at 20 μm. The rate of change of percent error is greater for 2% noise data than for the 1% noise data. Thus, as the level of noise in the data increases, the uncertainty in the retrieved parameter P increases and this in turn leads to an increase in the uncertainty in the size distributions.

TABLE 29. RETRIEVED VALUES FOR THE SIZE DISTRIBUTION PARAMETERS AND THE PERCENTAGE ERRORS FOR THE NO-NOISE AND NOISY DATA

True Values: $P_1 = 8 \times 10^4$; $p_2 = 2.0$; $p_3 = 0.5$

		Retrieved parameters and percentage errors										
λ (μm)	Noise Level (%)	P_1	Error ΔP_1	σ_1 (%)	p_2	Error Δp_2	σ_2 (%)	p_3	Error Δp_3	σ_3 (%)	Fit	Std. dev. σ
0.4416	0	7.98(4)	8.513(-1)	1.06(-5)	2.0	1.98(-7)	9.9(-6)	0.5	5.97(-8)	1.19(-5)	100.0	5.62(-3)
	1.0	8.001(4)	586	0.73	2.00	1.36(-2)	0.68	0.502	4.1(-3)	0.82	99.98	2.355(-2)
		8.038(4)	535	0.67	1.99	1.237(-2)	0.62	0.505	3.721(-3)	0.74	99.983	2.129(-2)
		7.982(4)	669	0.84	2.00	1.555(-2)	0.78	0.496	4.717(-3)	0.95	99.97	2.723(-2)
		7.976(4)	524	0.66	2.01	1.229(-2)	0.61	0.50	3.685(-3)	0.74	99.98	2.137(-2)
		7.984(4)	601	0.75	2.00	1.395(-2)	0.70	0.495	4.241(-3)	0.86	99.978	2.446(-2)
	2.0	8.002(4)	1.175(3)	1.47	2.00	2.73(-2)	2.11	0.503	8.217(-3)	1.63	99.918	4.710(-2)
		7.964(4)	1.326(3)	1.66	2.01	3.083(-2)	1.53	0.491	9.404(-3)	1.92	99.889	5.444(-2)
		7.953(4)	1.037(3)	1.30	2.02	2.451(-2)	1.21	0.501	7.316(-2)	1.46	99.935	4.274(-2)
		8.076(4)	1.087(3)	1.35	1.98	2.396(-2)	1.26	0.510	7.483(-3)	1.47	99.934	4.258(-2)
		7.967(4)	1.194(3)	1.50	2.01	2.767(-2)	1.38	0.490	8.472(-3)	1.73	99.9094	4.894(-2)
	5.0	8.003(4)	2.967(3)	3.69	1.99	6.9(-2)	3.47	0.508	2.067(-2)	4.07	99.49	0.118
		8.193(4)	2.839(3)	3.47	1.95	6.411(-2)	3.29	0.526	1.903(-2)	3.62	99.59	0.106
		7.90(4)	3.212(3)	4.07	2.02	7.495(-2)	3.71	0.477	2.324(-2)	4.87	99.298	0.136
		7.879(4)	2.507(3)	3.18	2.06	6.089(-2)	2.96	0.501	1.788(-2)	3.57	99.615	0.017
		7.916(4)	2.918(3)	3.69	2.01	6.749(-2)	3.36	0.475	2.111(-2)	4.44	99.411	0.123

TABLE 29 (CONTINUED)

λ (μm)	Noise Level (%)	Retrieved parameters and percentage errors										
		p_1	Errors	σ_1 (%)	p_2	Error	σ_2 (%)	p_3	Error	σ_3 (%)	Fit	Std. dev. σ
0.6328	0	8.0(4)	8.513(-3)	1.06(-5)	2.0	1.977(-7)	9.89(-6)	0.5	5.969(-8)	1.19(-5)	100.0	5.616(-13)
	1.0	8.021(4)	589	0.73	1.99	1.366(-2)	0.69	0.504	4.156(-3)	0.82	99.979	2.417(-2)
		7.953(4)	665	0.84	2.01	1.562(-2)	0.78	0.497	4.763(-3)	0.96	99.97	2.806(-2)
		8.037(4)	553	0.66	1.99	1.239(-2)	0.63	0.508	3.744(-3)	0.74	99.983	2.189(-2)
		8.038(4)	469	0.58	1.98	1.09(-2)	0.55	0.508	3.296(-3)	0.65	99.987	1.919(-2)
		8.065(4)	518	0.64	1.98	1.194(-2)	0.60	0.506	3.628(-3)	0.72	99.984	2.114(-2)
	2.0	8.043(4)	1.201(3)	1.49	1.97	2.767(-2)	1.40	0.509	8.418(-3)	1.65	99.915	4.832(-2)
		7.906(4)	1.318(3)	1.67	2.01	3.115(-2)	1.55	0.494	9.257(-3)	1.87	99.886	5.614(-2)
		8.071(4)	1.085(3)	1.34	1.98	2.517(-2)	1.27	0.515	7.554(-3)	1.47	99.933	4.386(-2)
		8.076(4)	959	1.19	1.97	2.215(-2)	1.12	0.516	6.664(-3)	1.29	99.948	3.837(-2)
		8.137(4)	1.062(3)	1.31	1.96	2.417(-2)	1.31	0.512	7.334(-3)	1.43	99.936	4.4228(-2)
	5.0	8.128(4)	3.204(3)	3.94	1.92	7.20(-2)	3.75	0.524	2.191(-2)	4.18	99.451	0.121
		7.770(4)	3.214(3)	4.14	2.03	7.729(-2)	3.81	0.484	2.383(-2)	4.92	99.269	0.140
		8.156(4)	2.849(3)	3.49	1.95	6.558(-2)	3.36	0.535	1.933(-2)	3.61	99.588	0.110
		8.192(4)	2.562(3)	3.13	1.92	5.803(-2)	3.02	0.540	1.722(-2)	3.19	99.676	9.585(-2)
		8.355(4)	2.864(3)	3.43	1.91	6.258(-2)	3.28	0.532	1.894(-2)	3.56	99.598	0.106

TABLE 29 (CONTINUED)

λ (μm)	Noise Level (%)	Retrieved parameters and percentage errors										
		p_1	Errors	σ_1 (%)	p_2	Error	σ_2 (%)	p_3	Error	σ_3 (%)	Fit	Std. dev. σ
1.15	0	8.0(4)	0.191		2.0	4.564(-6)		0.5	1.423(-6)		100.0	5.859(-11)
	2.0	7.949(4)	1.146(3)	1.44	2.02	2.765(-2)	1.37	0.493	8.631(-3)	1.75	99.90	5.574(-2)
		7.955(4)	886	1.11	2.02	2.148(-2)	1.06	0.499	6.652(-3)	1.33	99.941	4.284(-2)
		8.04(4)	1.693(3)	2.11	1.97	4.042(-2)	2.05	0.518	1.248(-2)	2.41	99.803	7.773(-2)
		7.894(4)	1.327(3)	1.68	2.04	3.207(-2)	1.57	0.477	1.013(-2)	2.12	99.857	6.639(-2)
		8.108(4)	928	1.14	1.97	2.18(-2)	1.11	0.508	6.82(-3)	1.34	99.939	4.305(-2)
	5.0	7.872(4)	2.777(3)	3.53	2.05	6.784(-2)	3.31	0.482	2.121(-2)	4.40	99.387	0.139
		7.883(4)	2.166(3)	2.75	2.04	5.351(-2)	2.62	0.497	1.64(-2)	3.30	99.695	0.107
		8.10(4)	4.486(3)	5.54	1.92	0.106	5.52	0.545	3.243(-2)	5.95	98.778	0.194
		7.75(4)	3.14(3)	4.05	2.10	7.66(-2)	3.65	0.446	2.47(-2)	5.54	99.093	0.167
		8.277(4)	2.423(3)	2.93	1.93	5.528(-2)	2.86	0.519	1.737(-2)	3.35	99.619	0.108

TABLE 30: FIRST SET OF SIMULATED DATA

λ = 0.4416 μm

Time	1% Noise		2% Noise		5% Noise	
sec	% error	Calc/True	% error	Calc/True	% error	Calc/True
10	1.71	1.0012	3.43	1.0023	8.22	1.0258
20	1.69	1.0011	3.40	1.0022	8.12	1.0246
50	1.58	1.0007	3.18	1.001	7.49	1.017
100	1.35	0.9997	2.71	0.9994	7.15	1.0034
150	1.17	0.9952	2.35	0.998	5.51	0.9941
200	1.05	0.9985	2.11	0.997	4.96	0.9884
250	0.98	0.9982	1.97	0.9964	4.63	0.9809
300	0.94	0.9980	1.89	0.996	4.43	0.984
400	0.91	0.9978	1.83	0.9957	4.27	0.9846
500	0.92	0.9979	1.84	0.9959	4.27	0.9879
600	0.94	0.9981	1.89	0.9963	4.35	0.9930
700	0.97	0.9984	1.95	0.9968	4.47	0.9988
800	1.005	0.9974	2.01	0.9974	4.61	1.0048
900	1.05	0.9991	2.10	0.9982	4.78	1.0124
1000	1.089	0.9995	2.18	0.9965	4.95	1.0188
1200	1.18	1.0002	2.36	1.0004	5.31	1.0323
1500	1.35	1.0133	2.70	1.0028	6.00	1.0552
1700	1.46	1.0023	2.93	1.0044	6.46	1.0691
2000	1.63	1.0033	3.25	1.0064	7.09	1.0875
3000	2.29	0.9954	4.57	1.0138	9.71	1.1568
SD	2.35×10^{-2}		4.71×10^{-2}		0.106	

Note that in almost all cases scale value agrees with true values to well within the error.

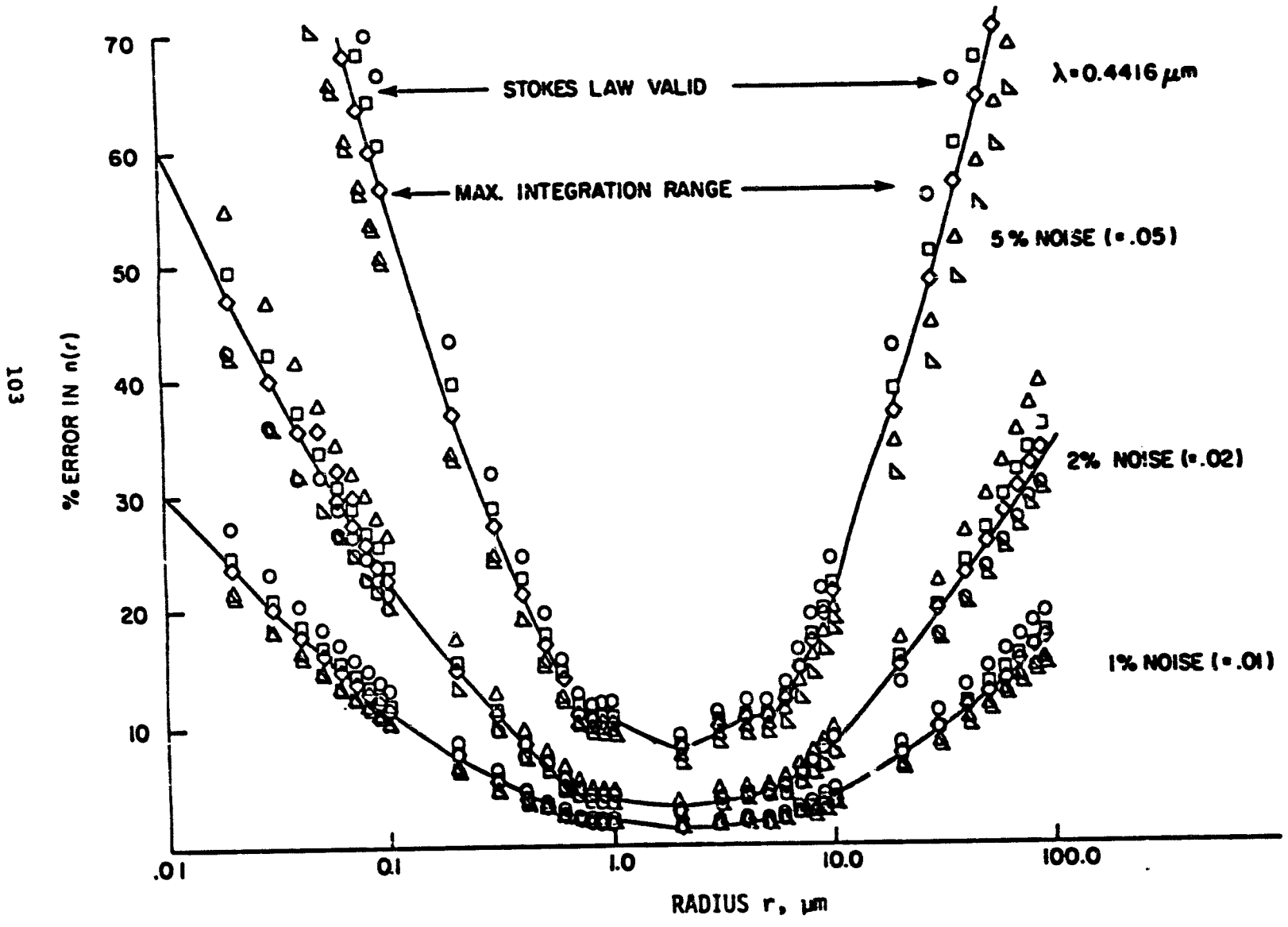

FIGURE 41. Effects of noise on percentage errors in the retrieved size distributions (for the case of sedimentation under gravity) obtained from the single wavelength simulated (measurements) data for τ vs t by using the direct inversion approach of Ref. 23.

5. MODELING OF EFFECTS OF AEROSOL MICROPHYSICAL AND DYNAMICAL PROCESSES ON LASER BEAM PROPAGATION

The measurements of $\tau(\lambda,t)$ vs t, shown in Figs. 3-5 (Section 2) show that the optical depth of aerosols varies with time. The reason for this time behavior of τ is that the size distribution n(r) could be varying in time. Here we assume that during the course of the experiment, no chemical reaction takes place and the change of the chemical composition of the aerosol particles due to microphysical processes is very small, so that the refractive index of the particle remains constant. Results obtained from $\tau(\lambda,t)$ data for different times as described in Section 4.0 show that the size distribution varies with time in such a way that the size distribution peak value decreases with time whereas the mode radius shifts toward larger radii. These results are also confirmed by the size distribution measurements (Section 2). The question that arises then is how to explain the time variation of n(r) and $\tau(\lambda)$. The processes which affect the time behavior of aerosol particles can be one or more of the following dynamical and microphysical processes:

Dynamical processes:

a. Gravitational settling
b. Stirred settling
c. Convective Flow due to thermal gradients
d. Molecular Diffusion

Microphysical processes:

e. Thermal Coagulation
f. Forced Coagulation
g. Growth/Evaporation
h. Nucleation

In order to understand how each, or a combination, of these processes affect the attenuation of visible and IR laser beams with time, we need to perform modeling and sensitivity studies, first for the simple processes, and later on, for processes of greater complexity. We decided to model first the idealized situations of gravitational settling, thermal coagulation and evaporation or growth, for various initial aerosol size distributions. The theories, computations and results of these studies are discussed in Sections 5.1 and 5.2.

5.1 EFFECTS OF AEROSOL COAGULATION AND SEDIMENTATION ON VISIBLE/INFRARED LASER BEAMS

Introduction

In order to understand the separate and combined effects of coagulation and sedimentation on the transmittance of laser beams through artificial aerosol medium, a joint extinction-coagulation-sedimentation (ECS) model has been set up. This report describes the results of a parametric study performed to show the effects of the two processes on the time variation of transmittance of visible/IR laser beams through fog oil aerosols settling under gravity in a quiet chamber. In this study, the initial size distributions at zero time were varied systematically in such a way that their mode diameters lay in the range 0.4 μm to 2.2 μm. Then using the Mie theory results in the ECS model, the corresponding time variation of the optical depth during a typical simulated (experiment) run of 0 to 100 min is studied for each of the initial size distributions. Preliminary results indicate that for the conditions under investigation, coagulation in predominant for small particles (diameters < 1.4 μm), whereas sedimentation is predominant for large particles (diameters > 2.0 μm).

The attempt was to develop a model that could explain the time behavior of extinction measurements given in Section 2. The theories of differential settling and thermal coagulation, described in the aforementioned references, Fuch's book (Ref. 31) and Yue and Deepak (Ref. 32) and Deepak and Yue (Ref. 33), are briefly discussed in later sections.

Theoretical Considerations

For the optical geometry of the experiment being simulated in this numerical study, consider a box containing a polydisperse aerosol settling quietly under gravity, through which traverse four visible and infrared laser beams, all of them being at the same depth from the box top (Fig. 1 in Section 2).

A plane electromagnetic wave of wavelength λ and intensity I_o after traversing a distance L through a polydisperse aerosol is attenuated to an intensity I, which is given by Bouguer's (Lambert-Beer's) Law, namely

$$I(\lambda,t) = I_o(\lambda) \exp[-\tau(\lambda,t)] \tag{44}$$

where the time dependent optical depth $\tau(\lambda,t)$ is defined by

$$\tau(\lambda,t) = \int_0^L \beta_{ext}(\lambda,t)\,d\ell$$

$$= \int_{r_1(t)}^{r_2(t)} \int_0^L Q_{ext}(x,m)\pi r^2 n(r,t)\,dr\,d\ell \tag{45}$$

where t is the time, β_{ext} (cm^{-1}) is the volume extinction coefficient, $Q_{ext}(x,m)$ is the efficiency factor, $x = 2\pi r/\lambda$ is the size parameter, $m = m' - m''$ is the particle complex refractive index, $n(r)$ is the size distribution ($cm^{-3}\,\mu m^{-1}$), and r_1 and r_2 are the upper and lower limits of the aerosol radii.

If we assume that the size distribution remains uniform along the paths of the laser beams in the aerosol medium, then

$$\tau(\lambda,t) = \pi L \int_{r_1(t)}^{r_2(t)} Q_{ext}(x,m) r^2 n(r,t)\,dr \tag{46}$$

We consider here that changes in the aerosol size distribution and hence the optical depths, with time t occur due to only two microphysical processes, namely, coagulation and sedimentation. Thus the results of a joint extinction-coagulation-sedimentation (ECS) model will be described here.

One aim of this study was to determine the conditions under which each of two processes dominates; the other was to develop a multispectral extinction measurement technique to study the microphysical processes in general. For this purpose a numerical parametric study was undertaken which involved inputting different starting size distributions $n(r,0)$ at $t = 0$ into Eq. (46) and computing the $\tau(\lambda,t)$ as f function t for different λ. Use of analytic model(s) (Ref. 21) for size distribution is best suited for such a study. Thus results were obtained with the regularized power law (RPL) model which is defined as

$$n(r,0) = \frac{p_1}{p_2} \frac{\left[r/p_2\right]^{p_3-1}}{\left[1 + (r/p_2)^{p_3}\right]^{p_4}} \qquad (47)$$

For which the mode radius r_m is given by

$$r_m = p_2 \left(\frac{p_3-1}{1 + p_3(p_4-1)}\right)^{1/p_3} \qquad (48)$$

where the parameters p_1, p_2, p_3, and p_4 are adjustable constants which can be judiciously selected to yield the initial size distributions of interest. The RPL model is discussed in detail by Deepak and Box (Ref. 21). For $r >> r_m$, Eq. (47) reduces to a power law, namely, $n(r) \rightarrow r^{(-p_4+1)}$.

Theory of Differential Settling: Stokes' law states that the terminal velocity v_s of a spherical particle settling under gravity in a quiet medium is given by

$$v_s = \frac{2}{9} \frac{(\rho_p-\rho_m)\, g r^2}{\eta_m} \qquad (49)$$

where ρ_m and ρ_p are densities of the particle and medium, respectively, r is the particle radius and η_m is the medium viscosity.

Hence, if a column of uniformly distributed aerosols has a height h at t = 0, no particles of radii greater than r(t) will be present at that level anywhere in the column at time t, where

$$r(t) = \left(\frac{\alpha}{t}\right)^{\frac{1}{2}} \qquad (50)$$

and

$$\alpha = \frac{9}{2} \frac{\eta_m h}{(\rho_p-\rho_m)g} \qquad (51)$$

The upper limit r_2 in Eq. (46) is then given by r(t).

For air, the specific gravity, $\rho_{air} = 1.22 \times 10^{-3}$ and viscosity, $\eta_{air} = 1.818 \times 10^{-4}$ poise (dynes -sec/cm^2); and g 981 cm/sec^2. Thus, for oil droplets, specific gravity $\rho = 0.85$, so that $v_g = 1.01925 \times 10^{-1} r^2$ (mm/sec) and for water droplets settling in quiet air, $\rho = 1.0$, so that $v = 1.1991 \times 10^{-1} r^2$ (mm/sec). Some values of r and v_s for oil and water droplets settling in quiet air are given in Table 31.

Theory of Thermal Coagulation: When aerosol particles come into contact and coalesce or adhere to one another, the process is called coagulation. If this occurs due to their Brownian motion, then it is referred to as thermal coagulation (Ref. 31). A brief theory of Brownian coagulation, based on Fuchs' treatment, is given as follows:

The time evolution of the number concentration N(r,t) having radius r in the range r to r + dr at time t, can be expressed as

TABLE 31. STOKES' VELOCITY FOR SPHERES VARIOUS RADII SETTLING IN QUIET AIR IN A CHAMBER.

Specific gravity of: air, $\rho_{air} = 1.22 \times 10^{-3}$

fog oil, $\rho_{oil} = 0.9218$

Viscosity of air, $\eta_{air} = 1.818 \times 10^{-4}$ poise (dynes -sec/cm^2)

Droplet Radius r(μm)	Stokes' Velocity, v_s	
	Fog Oil Droplets (mm/sec)	Water Droplets (mm/sec)
0.1 μm	1.019×10^{-3}	1.199×10^{-3}
0.5 μm	2.547×10^{-2}	3.00×10^{-2}
1.0 μm	1.019×10^{-1}	1.199×10^{-1}
2.0 μm	2.038×10^{-1}	2.398×10^{-1}
5.0 μm	2.547	3.00
10.0 μm	10.19	11.99

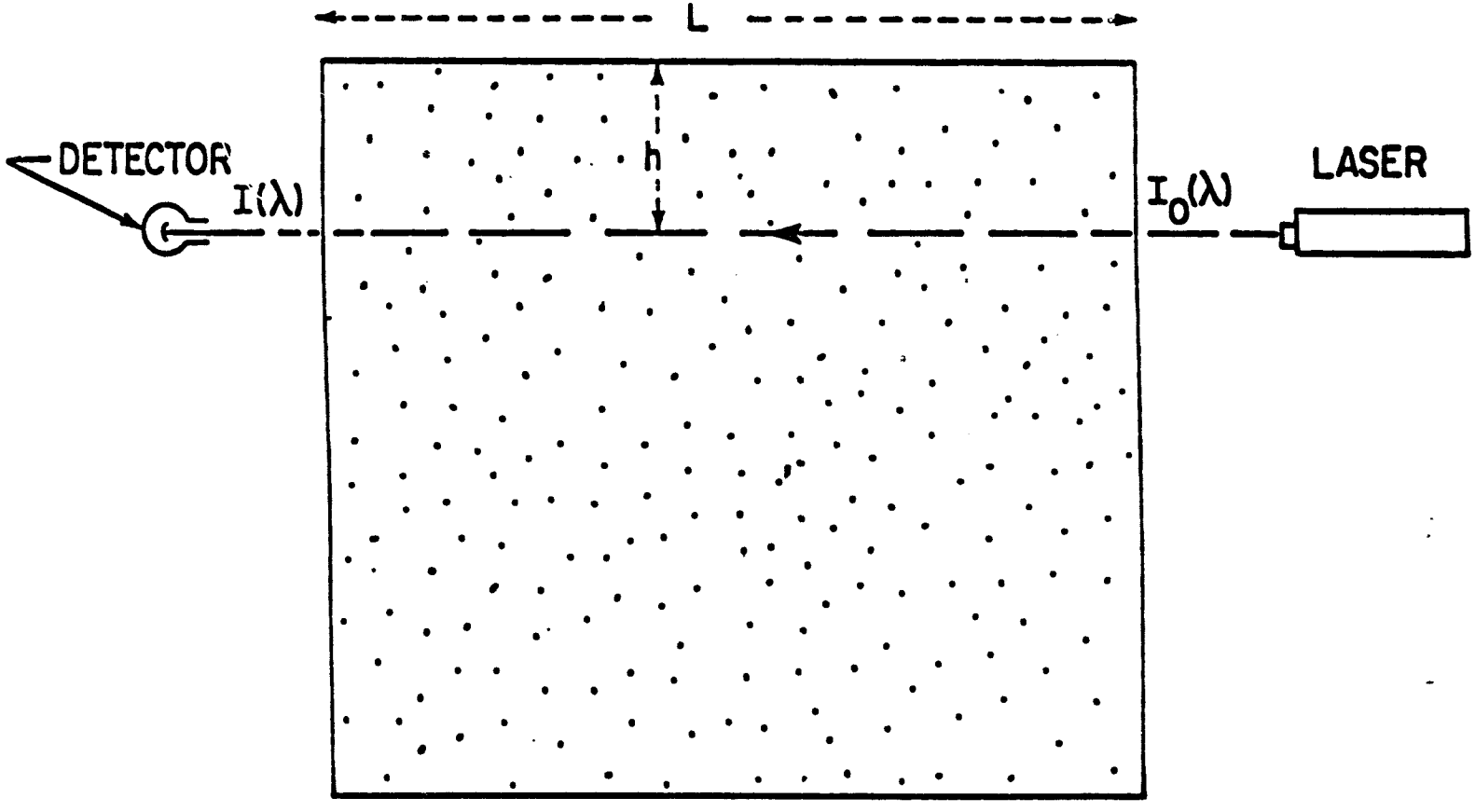

FIGURE 42. Schematics of the Optics of a Laser Beam Transmission Experiment.

$$\frac{\partial N(r,t)}{\partial t} = -N(r,t) \int_0^\infty K(r,r')\ N(r',t)\ dr'$$

$$+ \frac{1}{2} \int_0^\infty \int_0^\infty K(r_i,r_j)\ N(r_i,t)\ N(r_j,t)\ dr_i\ dr_j \qquad (52)$$

where $K(r_i, r_j)$ is the coagulation kernel or frequency of collisions (per unit volume) between particles of radius r_i and particles of radius r_j.

The first term on the right hand side of Eq. (52) describes the reduction of number of particles with radius r by the coagulation between particles with radius r and other particles. The second term on the right hand side of Eq. (52) describes the production of new particles with radius r by the coagulation between particles with radius r_i and particles with radius r_j, so that r_i and r_j are related by the equation

$$r_i^3 + r_j^3 = r_{ij}^3 \qquad (53)$$

The coagulation kernel as derived by Fuchs (Ref. 31) is given by

$$K(r_i,r_j) = K_{ij} = 4\pi r_{ij} D_{ij} \left[\frac{r_{ij}}{r_{ij}+\delta_{ij}} + \frac{4D_{ij}}{G_{ij} r_{ij}} \right]^{-1} \qquad (54)$$

where

$$\left.\begin{aligned} r_{ij} &= r_i + r_j \\ D_{ij} &= D_i + D_j \\ G_{ij} &= (G_i^2 + G_j^2)^{1/2} \\ \delta_{ij} &= (\delta_i^2 + \delta_j^2)^{1/2} \end{aligned}\right\} \qquad (55)$$

and r_i and r_j are the radii of particles in the i^{th} and j^{th} "bins"; the quantities D_i, D_j are diffusion coefficients which can be calculated from the Einstein relation, $D = kTB$, where k is the Boltzmann constant, T, the absolute temperature, and B, the mobility given by

$$B = \frac{1}{6\pi\eta_m r}\left(1 + 1.246\,K_n + 0.42\,K_n\, e^{-\frac{0.87}{K_n}}\right) \tag{56}$$

where η_m is the viscosity of air, and K_n is the Knudsen number, defined by the relation

$$K_n = \frac{\ell\ eff}{r} \tag{57}$$

where

$$\ell\ eff = (\pi n d^2 \mu^{1/2})^{-1} \tag{58}$$

is the effective mean free path of air molecules, n is the number density of air molecules; $d = 1/2\,(d_{air} + d_{aerosol})$, the d's being diameters of an air molecule and a molecule of the particle under consideration; and,

$\mu = \frac{M_{air}}{M_{air} + M_{aerosol}}$, the M's being the molecular weight for air and for the particle. G_i is the kinetic velocity of a particle

$$G_i = \sqrt{\frac{8KT}{\pi m_i}}, \tag{59}$$

where m_i is the mass of the particle, and δ_i is a correction factor given by

$$\delta_i = \frac{1}{6r\ell_b}\left\{(2r_i + \ell_b)^3 - (4r_i^2 + \ell_b^2)^{3/2}\right\} - 2r_i \tag{60}$$

where

$$\ell_b = \frac{8D_i}{\pi G_i} \tag{61}$$

In order to calculate the change of aerosol size distribution with time by computer programming, we have converted the continuous evolution equation into an approximate discrete equation by the following formula:

$$r_i = r_1\, 2^{\frac{1}{3}(i-1)} \tag{62}$$

where r_1 is the radius of the smallest aerosol. Numerical values 2 and $\frac{1}{3}$ in Eq. (62) are chosen so that the volume of one aerosol in bin i is twice

the volume of one aerosol in the preceding bin. In our model, we have used 35 bins to cover the aerosol size spectrum from 0.01 μm to about 25 μm.

Computations and Results

A parametric study of the separate and combined effects of sedimentation and coagulation on the optical depths for four wavelengths (λ = 0.4416, 0.6328, 1.15, and 3.39 μm) has been carried out for fog oil aerosols, using the RPL size distribution model in Eq. (47). The input data for the physical properties of fog oil, including the real and imaginary parts of complex refractive index for fog oil at the four wavelengths, are given in Table 1, Section 2; h = 62.5 cm and L = 117 cm. Optical extinction values were computed with the use of Mie theory computer codes. The geometry of the simulated optical system is shown by the schematic illustration in Fig. 42.

In the RPL model, we assume different initial mode diameters d_m at t = 0 by choosing parameters $p_3 = p_4 = 4.0$ and different values of the parameters p_2. Parameter p_1 is the scaling parameter which is obtained by normalizing $\tau = 7.0$ for $\lambda = 0.6328$ μm at t = 0. The choice of the value 7.0 for normalization purposes has no special meaning other than the fact that it is representative of the experimental conditions under investigation. Computations were carried out for different initial size distributions with a different mode radii obtained by choosing different sets of p_i. For clarity, the results of only three sets of p_i values (Table 32) are discussed here. The size distributions obtained at times t = 0, 1.5, 25, 50, 75 and 100 min during a simulated (experiment) run are graphically illustrated in Figs. 42 to 48. Figures 43, 45, and 47 are for coagulation and sedimentation combined and Figs. 44, 46 and 48 are for coagulation alone. For sedimentation alone, the shape of the size distribution should remain the same as the initial one at t = 0 min, except that the upper diameter "cut off" (d_{max}) continues to decrease as time increases. For example, at the times given, the d_{max} = 20.48, 15.96, 3.91, 2.76, 2.26, and 1.95 μm, respectively. These values correspond to a beam (Fig. 42) at h = 63.5 cm and fog oil droplets with $\rho_p = 0.9214$ settling under gravity in air with viscosity $\eta_m = 1.813 \times 10^{-4}$

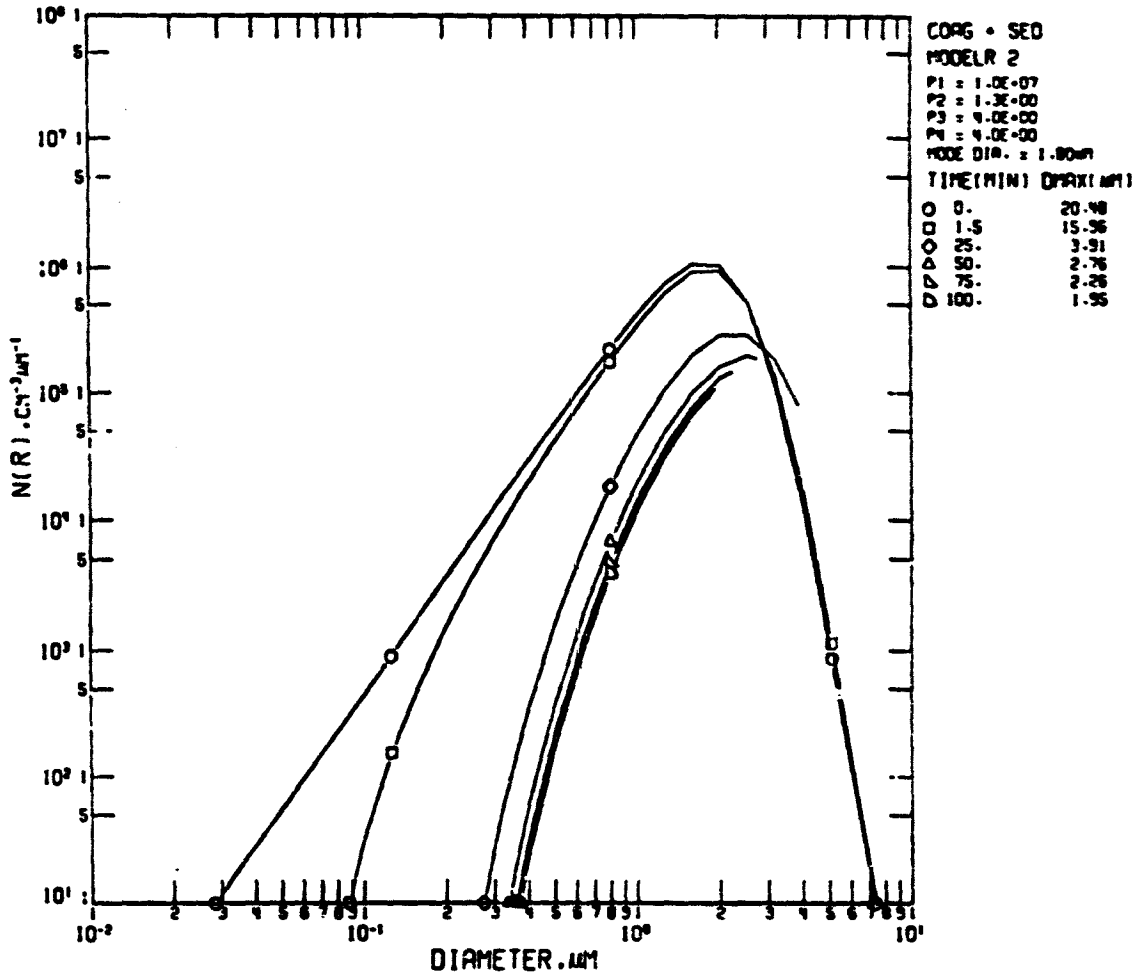

FIGURE 43. Aerosol size distributions at times t = 0, 1.5, 25, 50, 75, 100 min due to coagulation + sedimentation. Initial mode diamter d_m = 1.8 μm.

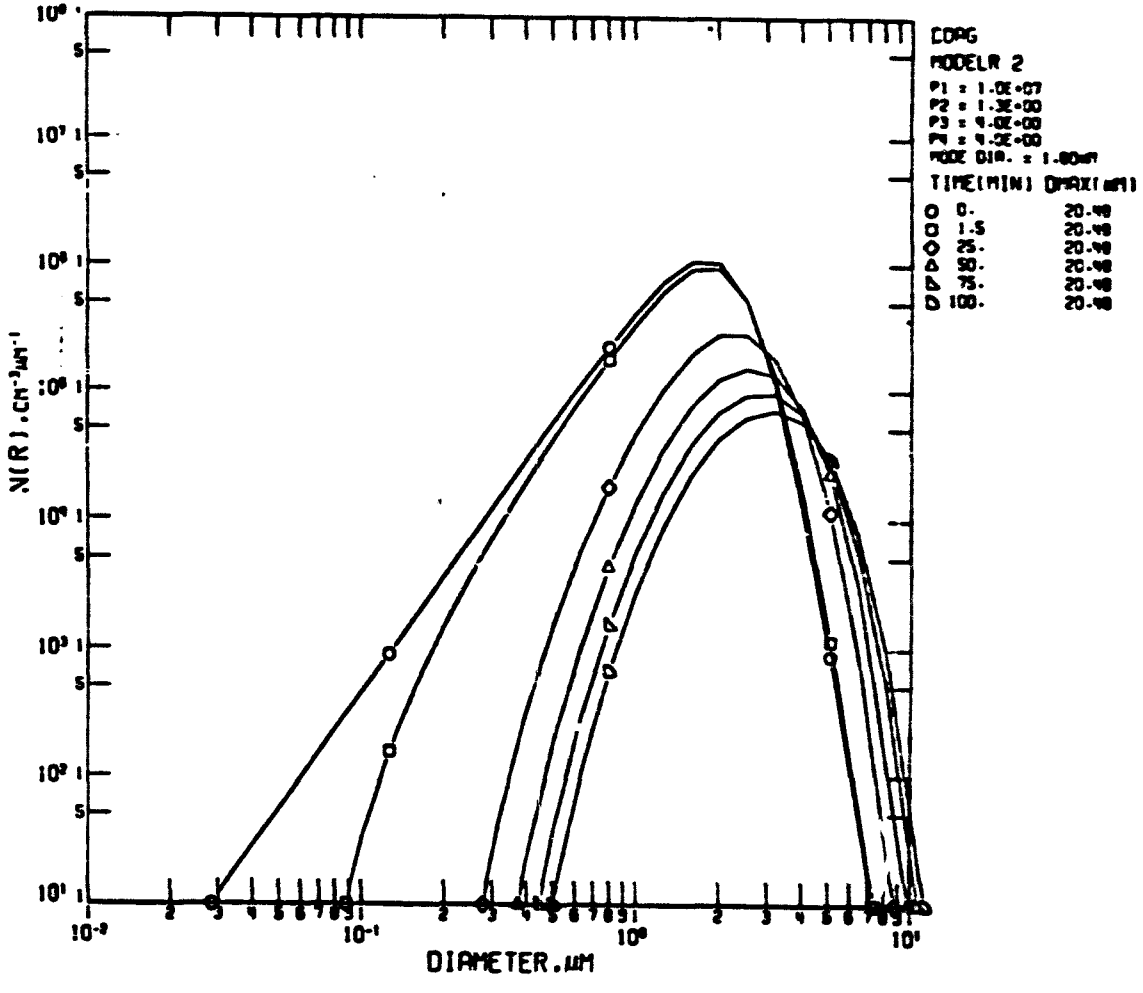

FIGURE 44. Aerosol size distributions at times t = 0, 1.5, 25, 50, 75, 100 min due to coagulation alone. Initial mode diameter d_m = 1.8 μm.

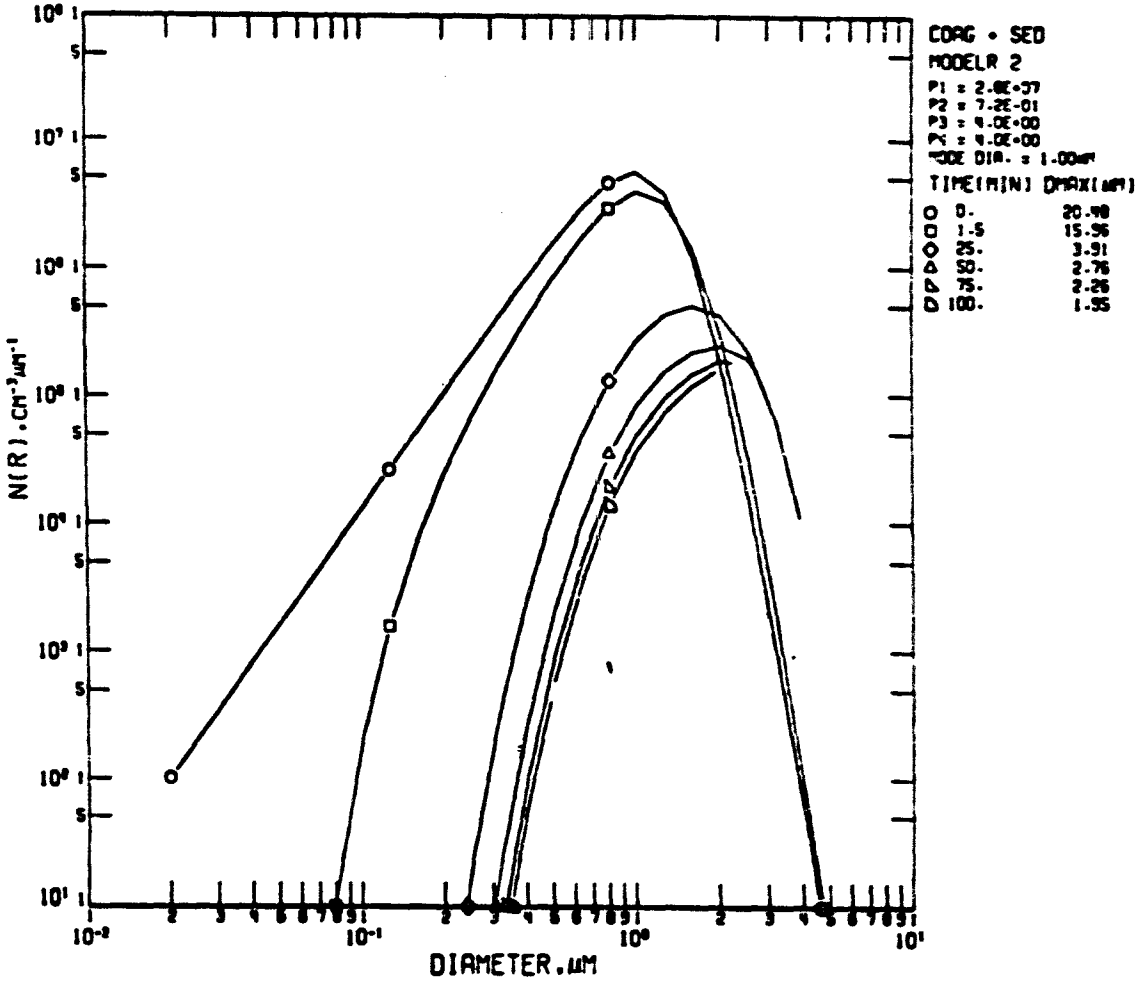

FIGURE 45. Aerosol size distributions at times t = 0, 1.5, 25, 50, 75, 100 min due to coagulation + sedimentation. Initial mode diameter d_m = 1.0 μm.

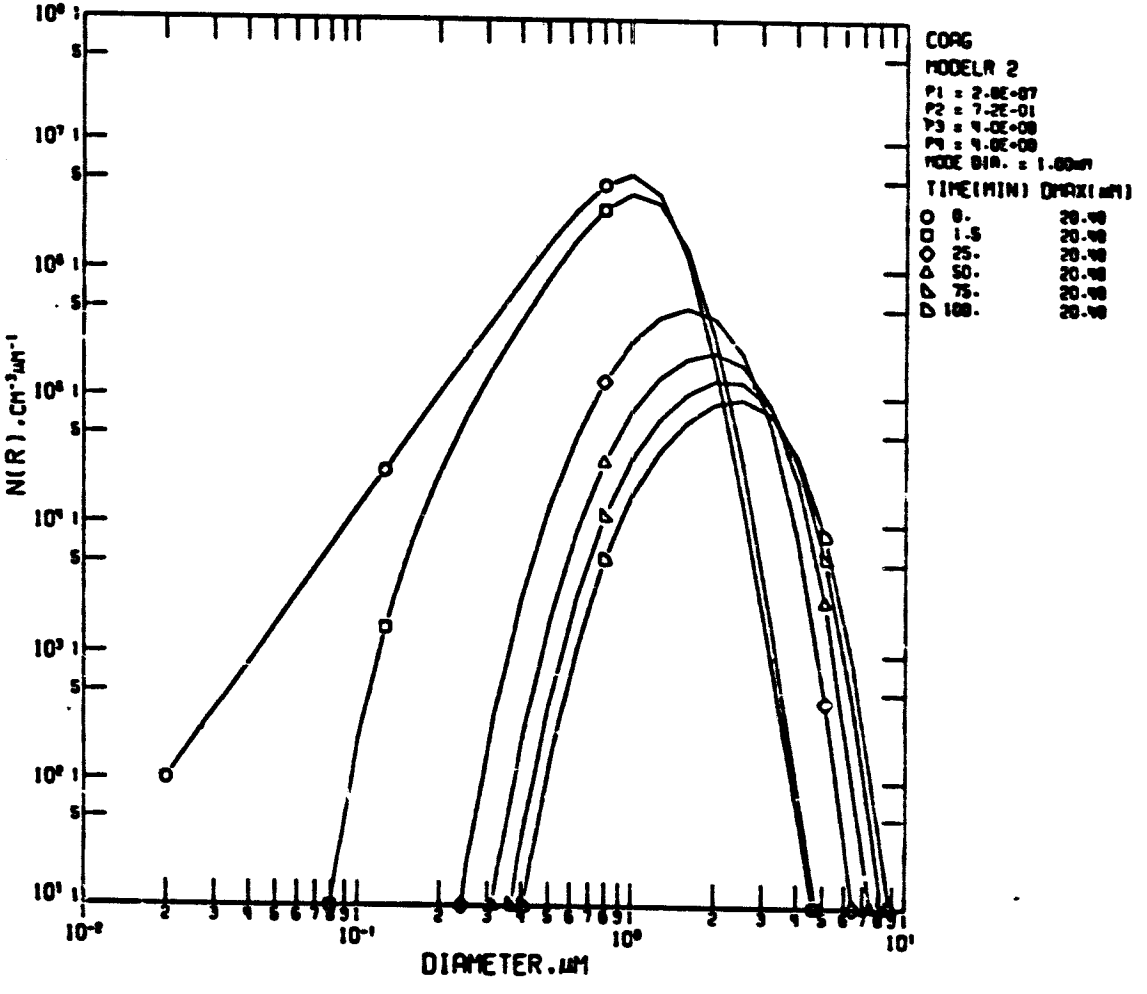

FIGURE 46. Aerosol size distributions at times t = 0, 1.5, 25, 50, 75, 100 min due to coagulation alone. Initial mode diameter d_m = 1.0 μm.

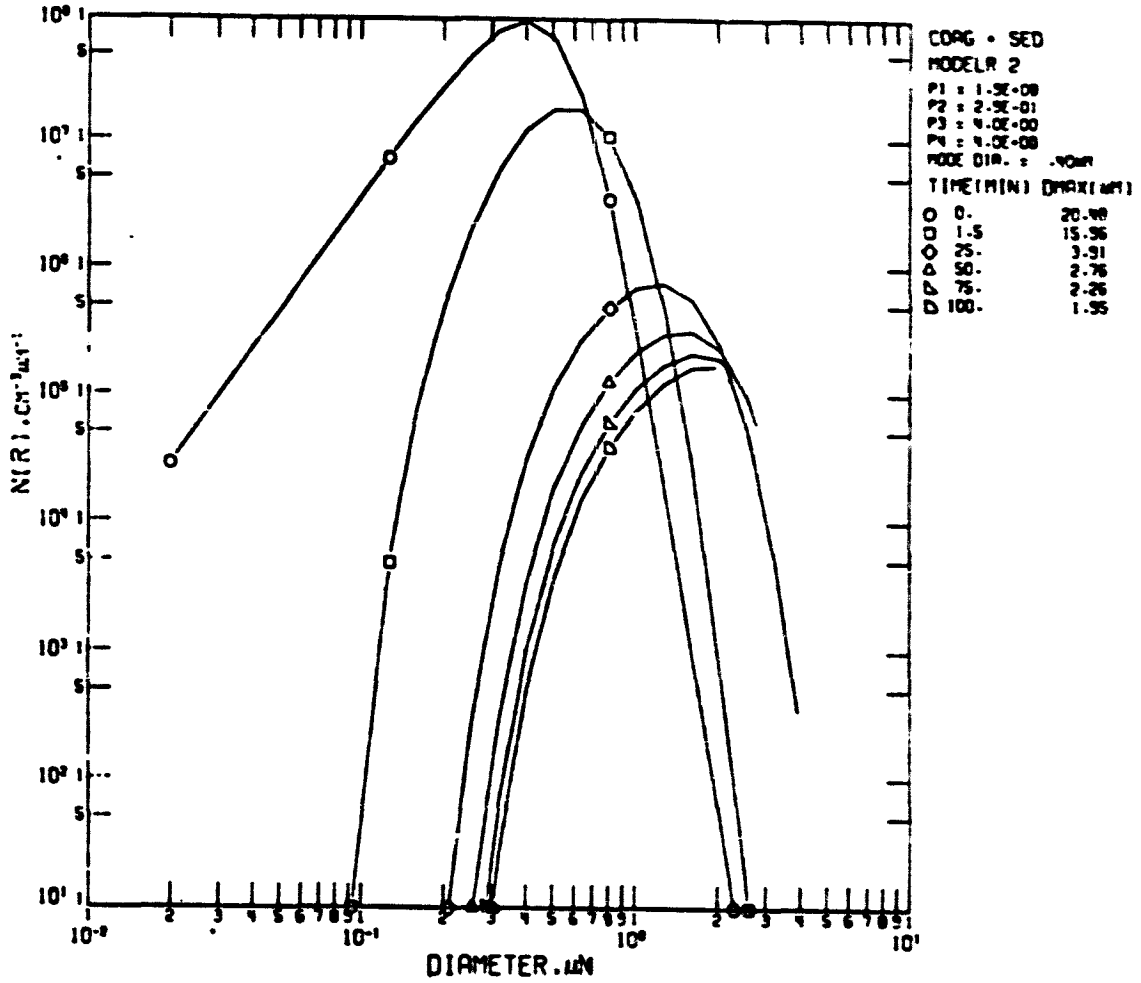

FIGURE 47. Aerosol size distributions at times t = 0, 1.5, 25, 50, 75, 100 min due to coagulation + sedimentation. Initial mode diameter d_m = 0.4 μm.

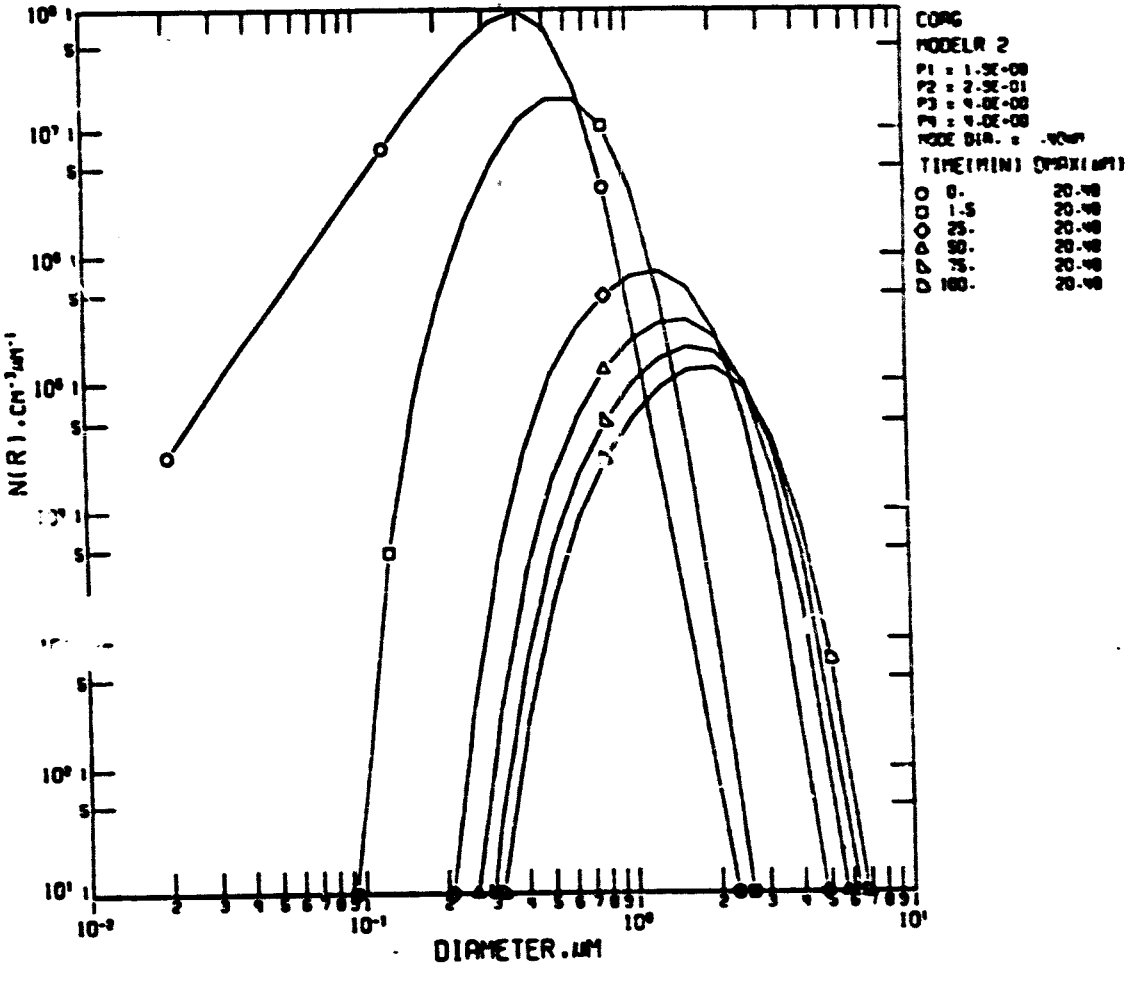

FIGURE 48. Aerosol size distributions at times t = 0, 1.5, 25, 50, 75, 100 min due to coagulation alone. Initial mode diameter d_m = 0.4 μm.

TABLE 32. SUMMARY OF THE PERTINENT VARIABLES INVOLVED IN THE PARAMETRIC MODELING STUDY.

Analytic model	Initial parameters at t = 0				Initial mode diameter[a]	Figure
	p_1	p_2	p_3	p_4	d_m (μm)	
Regularized power law size distribtuion, $n(r) = \frac{p_1}{p_2} \frac{\left[r/p_2\right]^{p_3 - 1}}{\left[1 + \left(\frac{r}{p_2}\right)^{p_3}\right]^{p_4}}$	6.8×10^6	1.60	4.0	4.0	1.80	Fig. 43,44
	1.6×10^7	1.00	4.0	4.0	1.00	Fig. 45,46
	6.1×10^7	0.43	4.0	4.0	0.40	Fig. 47,48

[a] Mode diameter, $d_m = 2p_2 \left[\frac{p_3 - 1}{1 + p_3 (p_4 - 1)}\right]^{1/p_3}$

and $\rho_m = 1.225 \times 10^{-3}$ (Eq. 49). The results for the time dependence of $\tau(\lambda)$, obtained for the different initial size distributions by the use of the ECS model are shown in Figs 49 to 57. The results for the combined coagulation + sedimentation effects are illustrated in Figs. 49, 52, and 55; while those due to coagulation and sedimentation separately are shown in Figs. 50, 53 and 56, and 51, 54, and 57, respectively.

Discussion of Results and Conclusions

From this study it becomes evident that using the RPL size distribution model, the relative strengths of the coagulation and sedimentation effects on τ vs t behavior depend on the initial mode diameter d_m such that coagulation effects dominate for d_m less than about 1.0 to 1.4 μm; while sedimentation effects dominate for d_m greater than about 1.8 μm.

The initial aerosol size distribution with the largest mode diameter (viz., $d_m = 1.8$ μm) is shown in Fig. 2. A comparison between Figs. 50 and 51 shows that the sedimentation effect is dominant, since the coagulation effect causes a slow time variation of τ for all four laser beams (Fig. 50). But, when the initial $d_m = 1.0$ μm coagulation effects on $\tau(\lambda,t)$ seem to become comparable to sedimentation effects, as shown in Figs. 52, 53, and 54. Figure 52 for the combined effects shows that for $\lambda = 3.39$ μm, τ initially increases for the first 20.5 min, and decreases thereafter; for other wavelengths, it simply decreases with time. For coagulation alone τ peaks at 49.5 min for $\lambda = 3.39$ μm (Fig. 53).

When $d_m = 0.4$ μm, the sedimentation effects on τ vs. t are insignificant (Figs. 55, 56, and 57); but due to the increase in small particles, coagulation becomes increasingly dominant, thereby causing the time rate of change of d_m to increase. This in turn causes the time variation of τ to differ for the differing wavelengths; e.g., for initial $d_m = 1.8$ μm, the τ vs. t curves depict a modal behavior for $\lambda = 3.39$ μm, but not for the other three wavelengths. But as the initial d_m is reduced, the modal behavior of τ vs. t curve becomes extended to smaller and smaller wavelengths. Thus, when initial $d_m = 0.4$ μm, τ vs. t curve for $\lambda = 1.15$ μm depicts a model behavior as well.

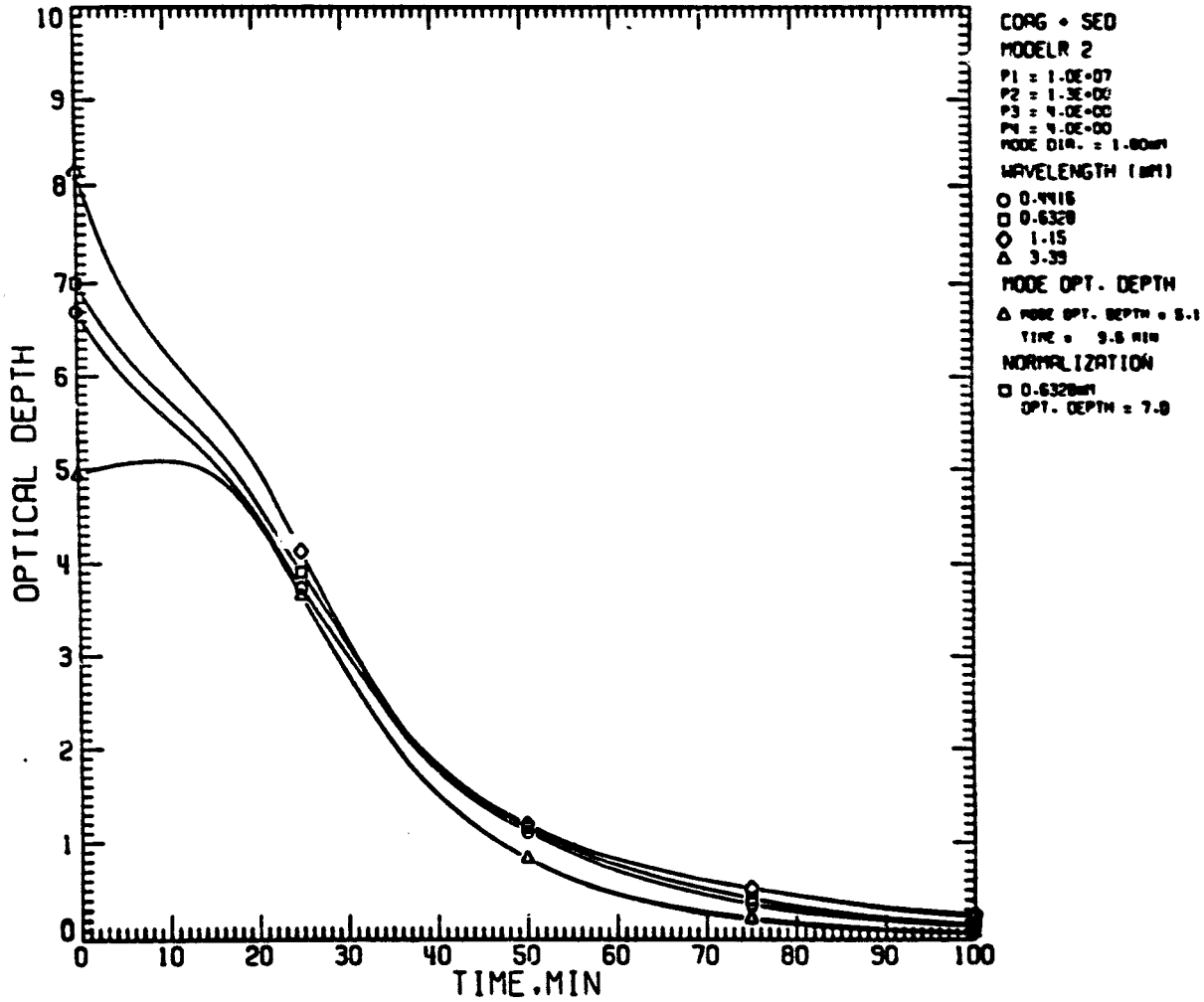

FIGURE 49. Optical depth τ vs. time t data for wavelengths 0.4416, 0.6328, 1.15, 3.39 μm for coagulation + sedimentation. Initial mode diameter d_m = 1.8 μm.

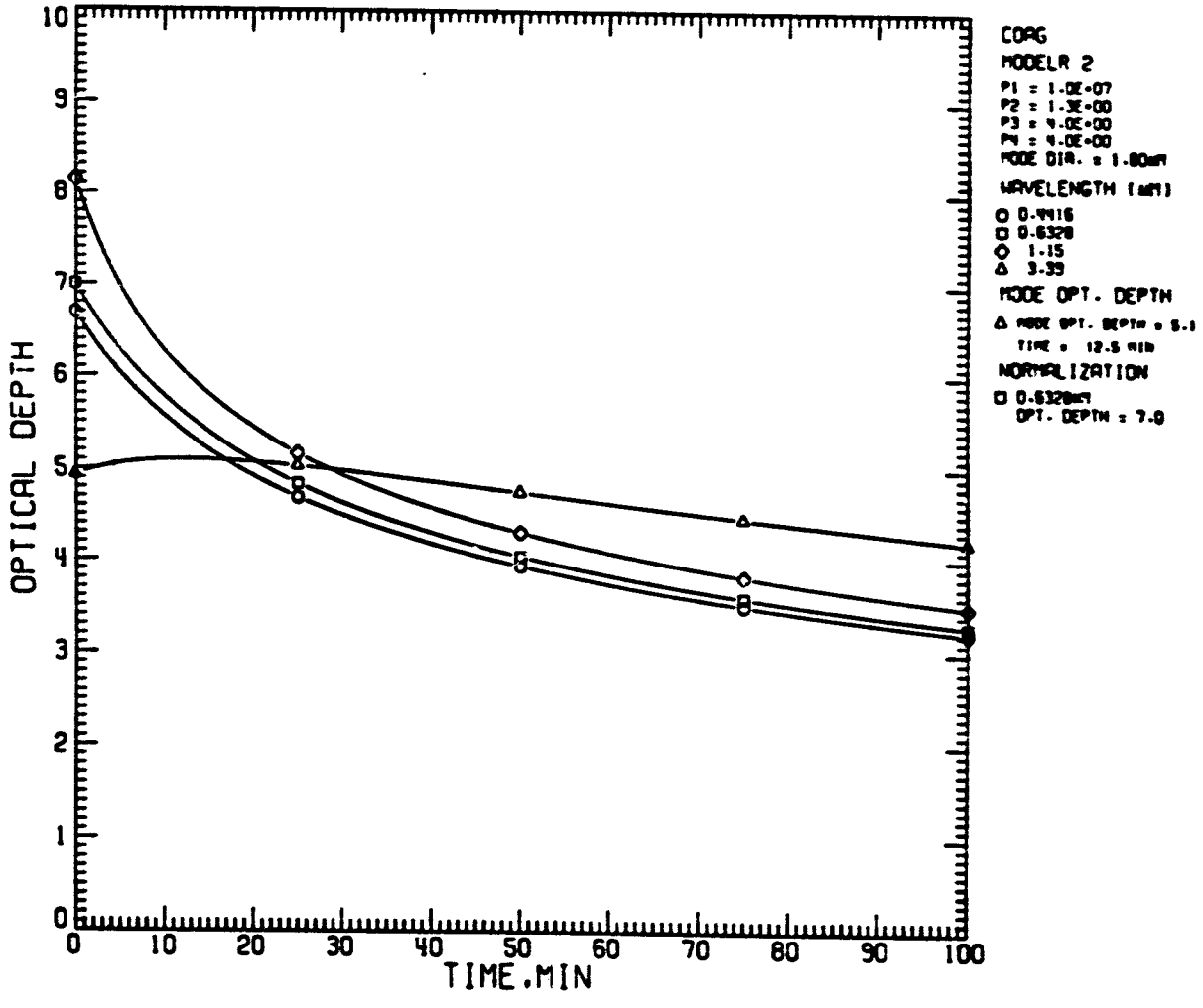

FIGURE 50. Optical depth τ vs. time t data for wavelengths 0.4416, 0.6328, 1.15, 3.39 μm for coagulation alone. Initial mode diameter d_m = 1.8 μm.

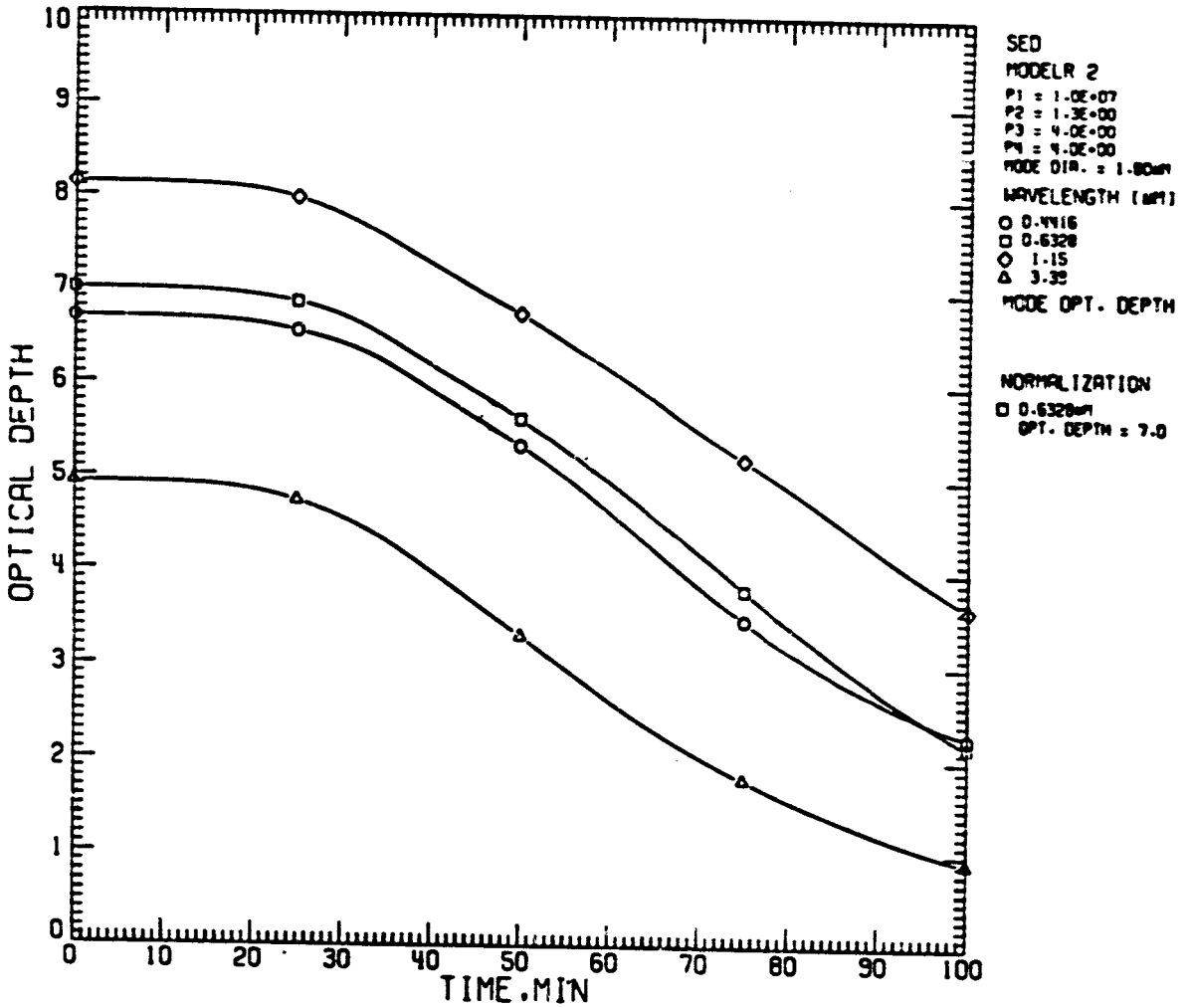

FIGURE 51. Optical depth τ vs. time t data for wavelengths 0.4416, 0.6328, 1.15, 3.39 μm for sedimentation alone. Initial mode diameter d_m = 1.8 μm.

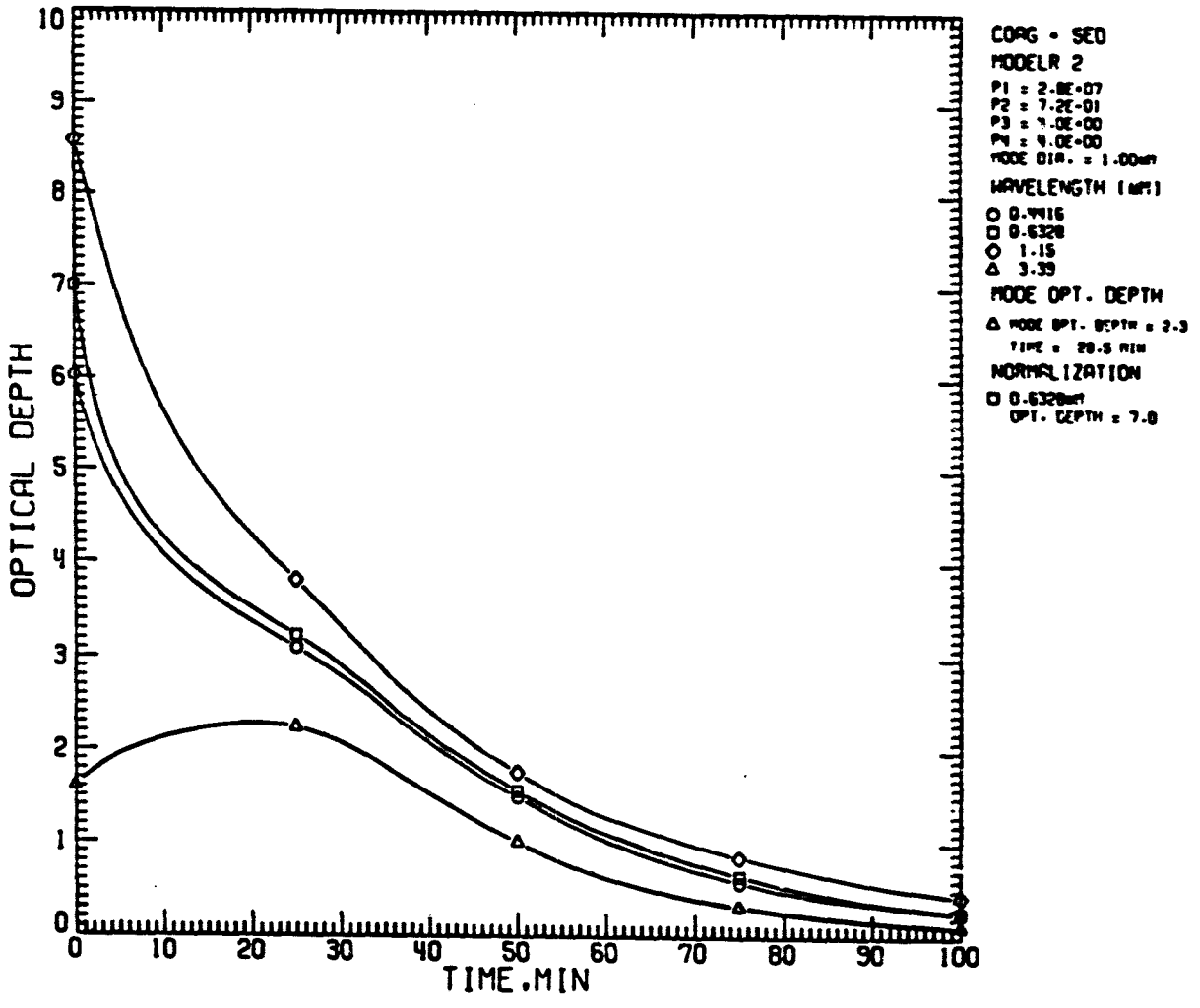

FIGURE 52. Optical depth τ vs. time t data for wavelengths 0.4416, 0.6328, 1.15, 3.39 μm for coagulation + sedimentation. Initial mode diameter d_m = 1.0 μm.

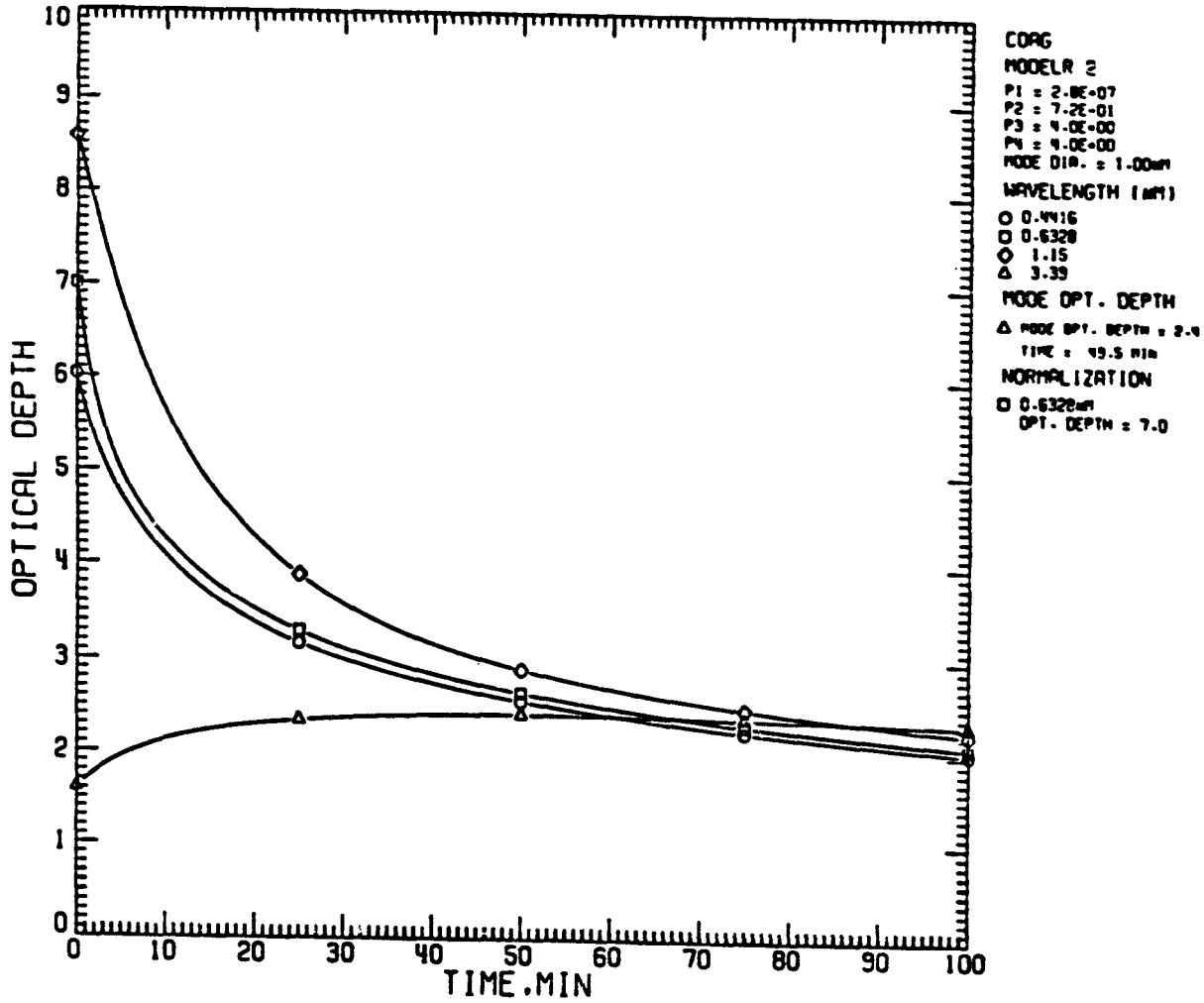

FIGURE 53. Optical depth τ vs. time t data for wavelengths 0.4416, 0.6328, 1.15, 3.39 μm for coagulation alone. Initial mode diameter d_m = 1.0 μm.

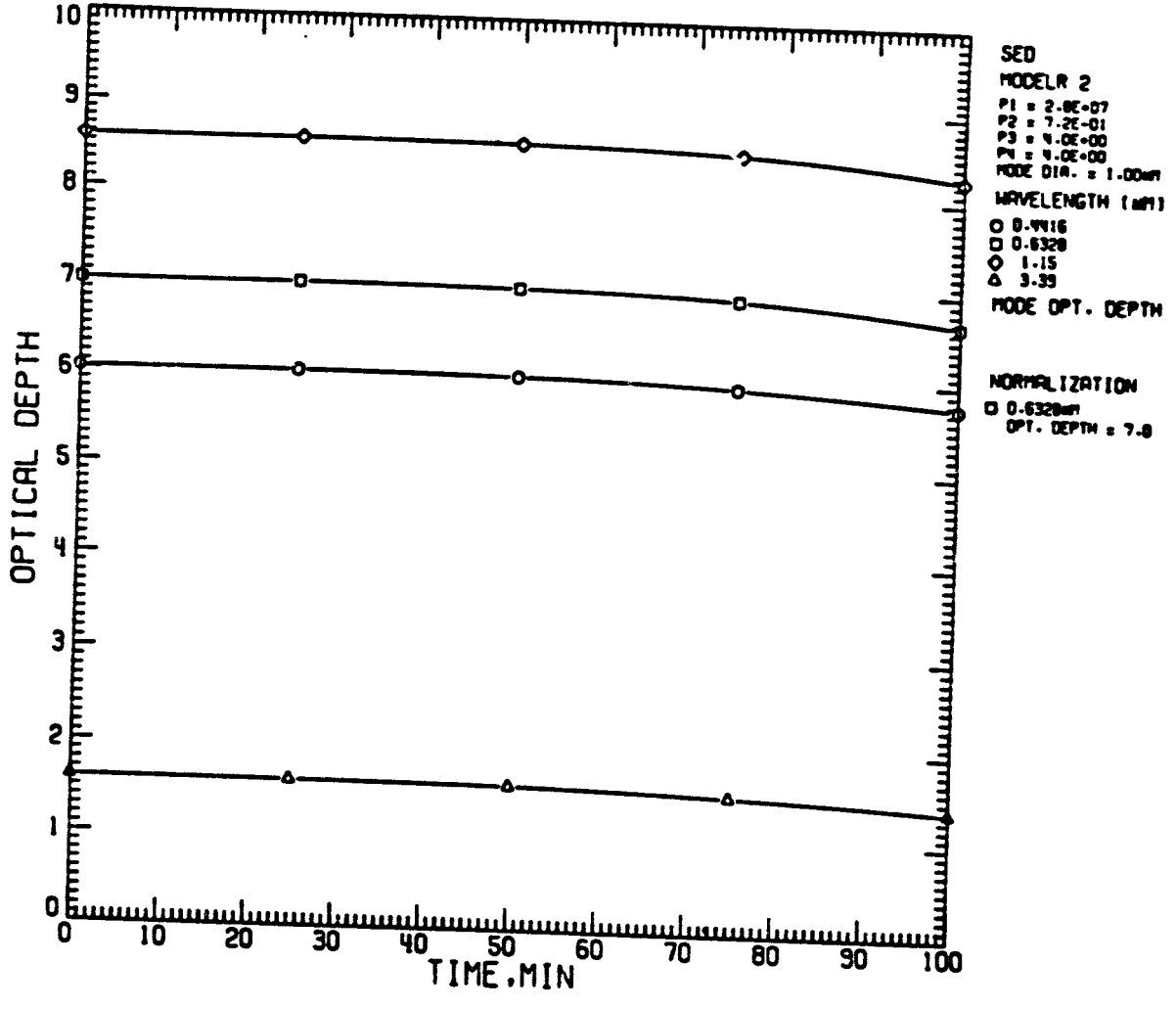

FIGURE 54. Optical depth τ vs. time t data for wavelengtns 0.4416, 0.6328, 1.15, 3.39 µm for sedimentation alone. Initial mode diameter d_m = 1.0 µm.

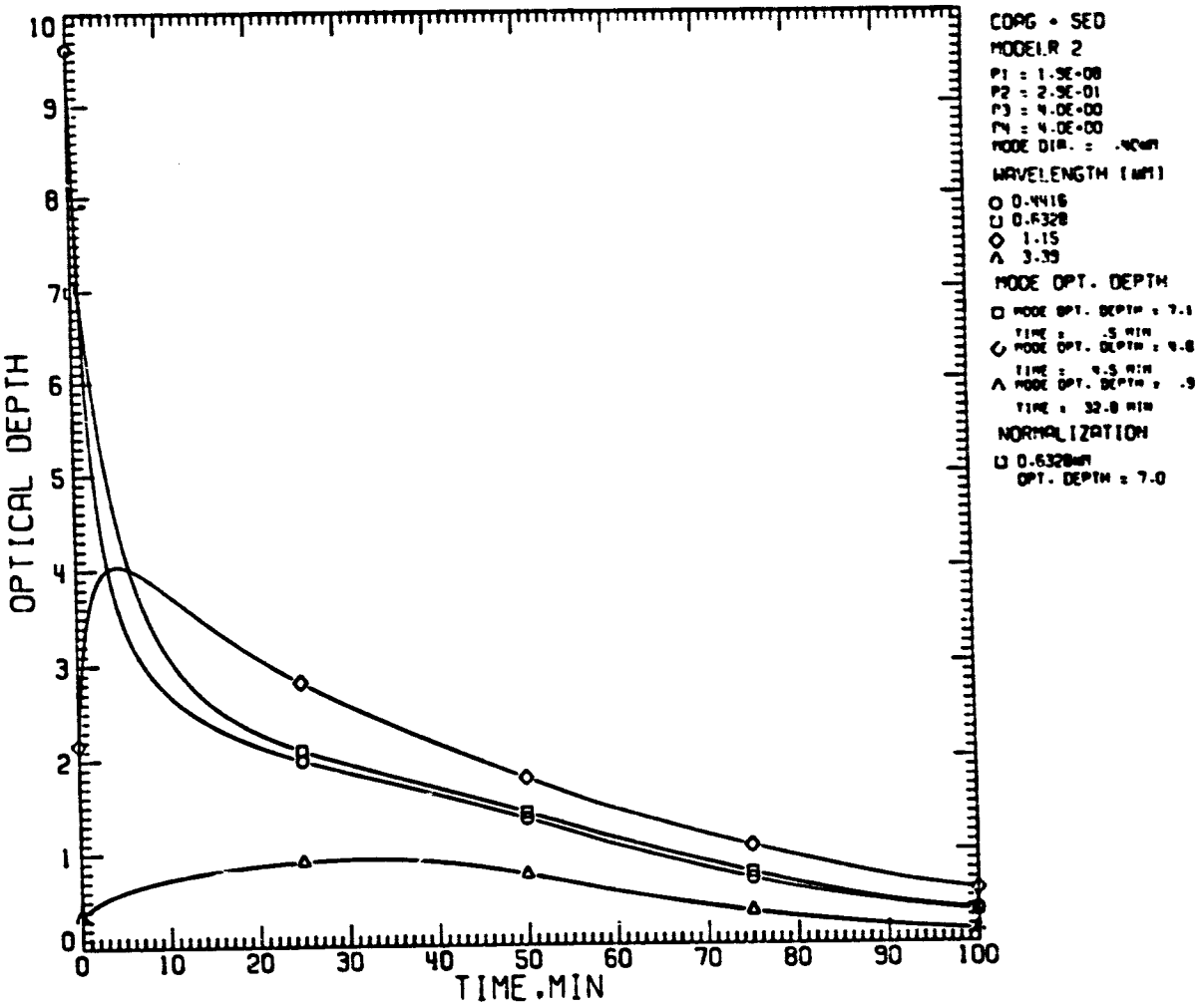

FIGURE 55. Optical depth τ vs. time t data for wavelengths 0.4416, 0.6328, 1.15, 3.39 μm for coagulation + sedimentation. Initial mode diameter d_m = 0.4 μm.

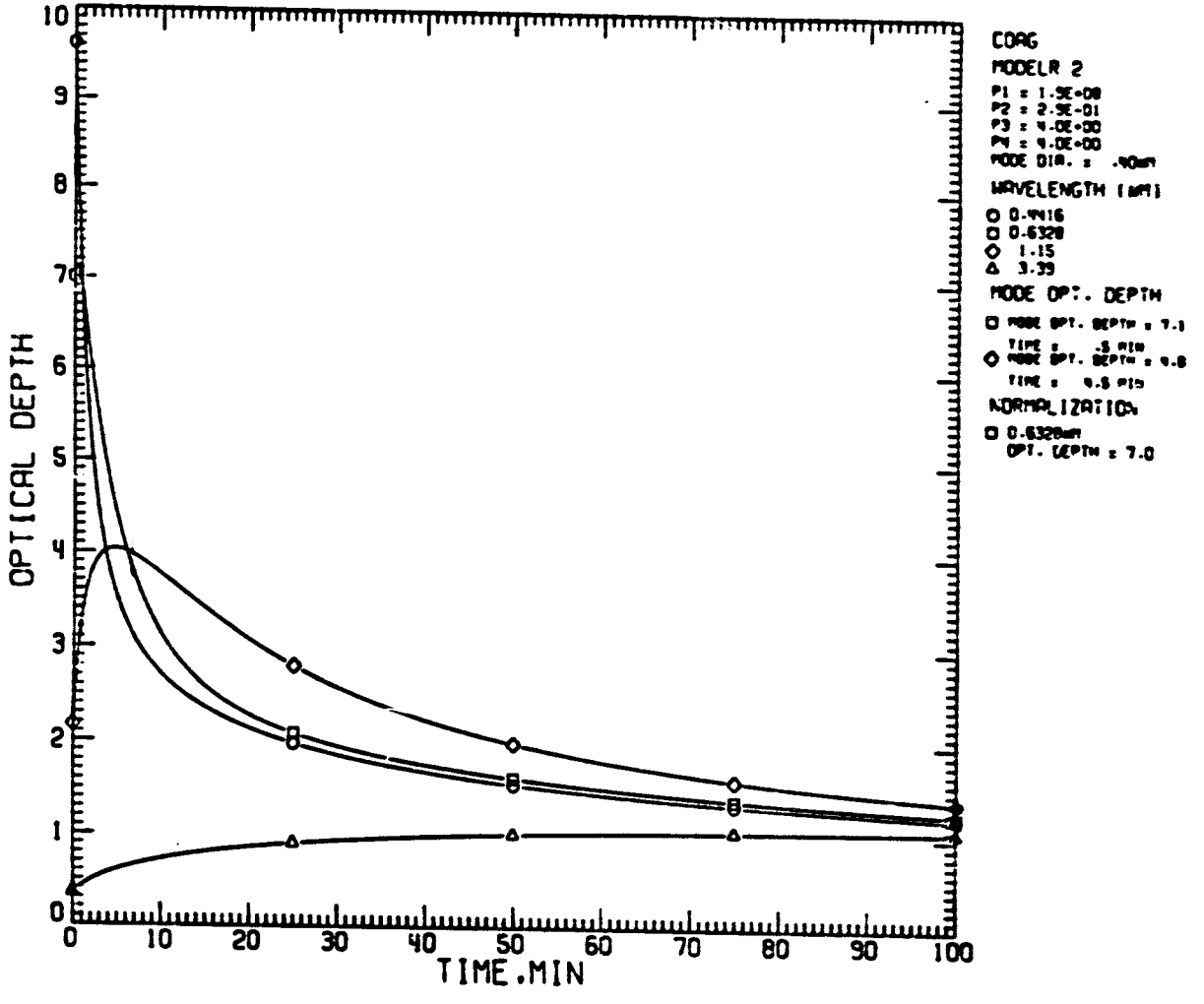

FIGURE 56. Optical depth τ vs. time t data for wavelengths 0.4416, 0.6328, 1.15, 3.39 μm for coagulation alone. Initial mode diameter d_m = 0.4 μm.

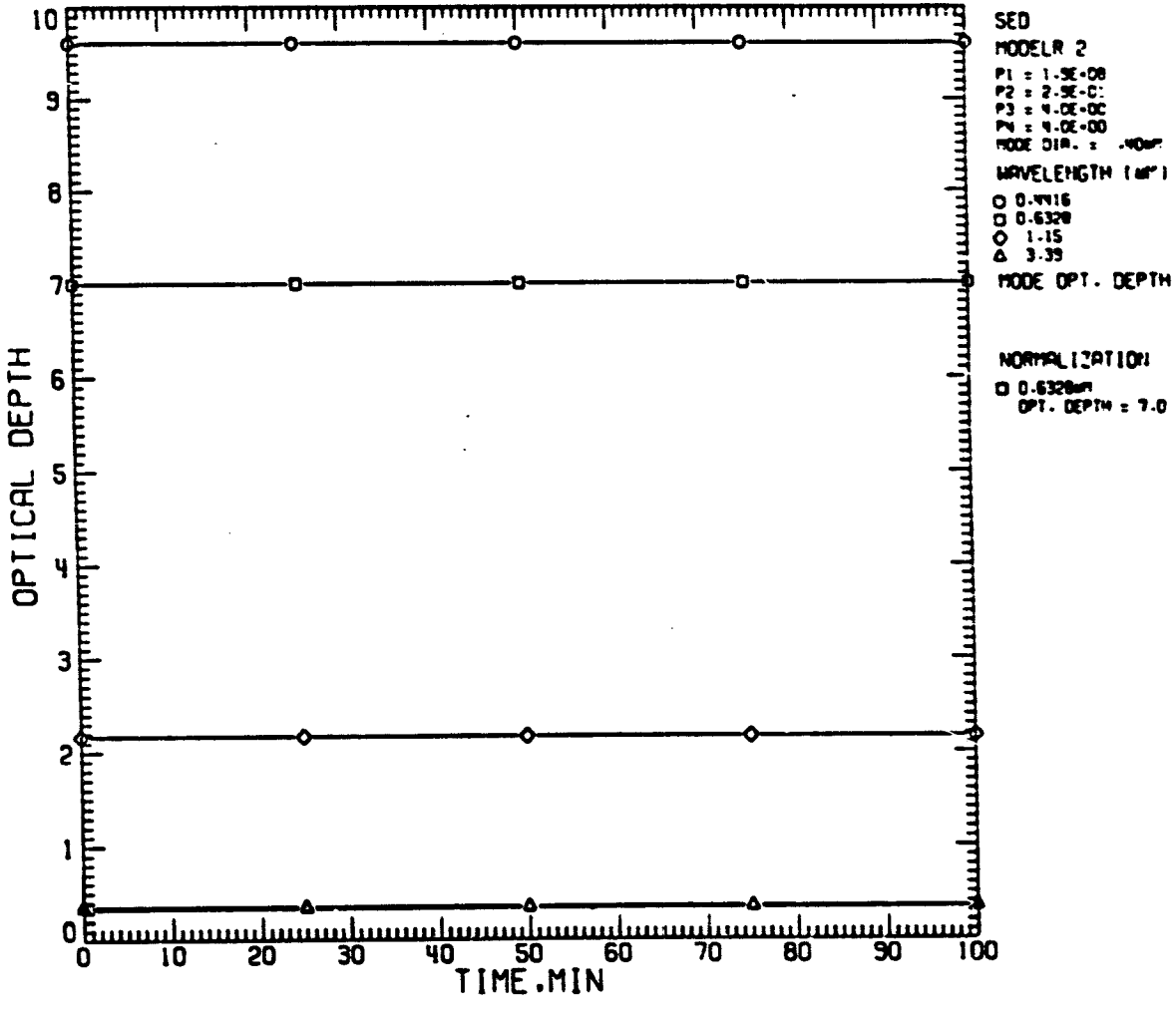

FIGURE 57. Optical depth τ vs. time t data for wavelengths 0.4416, 0.6328, 1.15, 3.39 μm for sedimentation alone. Initial mode diameter d_m = 0.4 μm.

The results described here are only preliminary and are based on only one size distribution model and in which only the mode diameter was varied. Even on the basis of these somewhat scant results, one can easily conclude the relative importance of coagulation and sedimentation mechanisms depends on several parameters, such as, wavelength, L and h (Fig. 42), and relative concentration of smaller size particles given by the mode diameter d_m.

Such a parametric study, in addition to providing an understanding of the effect of coagulation on laser beam propagation in aerosols, can lead to the development of simple and accurate experimental techniques for investigating the average microphysical processes. An important conclusion that can be drawn from such a study is that by performing the extinction experiment for a single wavelength in the visible region, one can easily miss noticing the effects of processes like coagulation. Therefore, it is recommended, as was proposed in Ref.32, that in order to get a more realistic picture, one must perform these measurements at multiwavelengths, preferably spanning a wide spectral range, from the visible to the IR. Work is under way to extend this parametric study to include stirred settling effects of polydispersity and number concentration, particles of different chemical composition (refractive index) and shapes.

5.2 MODELING THE TRANSMISSION OF VISIBLE/IR LASER BEAMS IN POLYDISPERSE AEROSOL PARTICLES UNDERGOING COAGULATION AND EVAPORATION OR GROWTH PROCESSES

According to the well-known Bouguer's (Lambert-Beer's) law, the ratio of the intensities of a plane electromagnetic wave after and before traversing a distance through a polydisperse aerosol is a function of the optical depth of the medium. The value of this optical depth depends on the size distribution and optical properties of the aerosol particles under consideration. If we assume that during the course of the experiment, no chemical reaction takes place and the change of the chemical composition of the aerosol particles due to microphysical processes is very small, we can assume that the refractive index of the particle remains constant. However, the aerosol size distribution will be inadvertantly changed and consequently the transmission of visible/IR laser beams in polydisperse aerosol particles will show a time-dependent behavior. The processes which will affect the size distribution of aerosol particles can be divided into two categories: dynamical processes and microphysical processes. The name of each process and condition under which size distribution will be significantly affected are outlined as follows:

Dynamical Processes

a. gravitational settling--will affect the larger particles
b. stirred settling--particles of all sizes will be affected depending on the time duration and strength of stirring
c. free convection due to thermal gradient--particles of all sizes will be affected depending on the magnitude of the thermal gradient
d. molecular diffusion--depends on the total area of the enclosure exposed to the aerosol particle.

Microphysical Processes

a. thermal coagulation--depends on three factors: time, concentration of particle and spread of the particle size distribution
The longer the experimental time, the higher the concentration of particles and the more spread of particle size spectrum will make the coagulation process more dominant in changing the aerosol size distribution.

b. forced coagulation--depends on whether external force other than gravitation is present

c. growth or evaporation--depends on the physical properties (temperature, vapor pressure) of the particle and air parcels surrounding the particle.

d. nucleation--depends on the concentration of gaseous species in the ambient (under ordinary conditions, this process can be ignored.)

Since more than one process will be taking place at the same time and different processes will be coupling with each other, numerical simulation of the change of optical depth for aerosols undergoing different dynamical and microphysical processes at the same time will be very complicated and the effect of each process to the transmission of laser beams can hardly be interpreted. The effect of each process will be studied separately and in this section, we concentrate on the study of the effect of evaporation/growth on the temporal change of optical depth. Since the data for vapor pressures of fog oil were not available, we proceeded to obtain numerical results for water fog aerosols, which contain solution of sea salt.

We assume that the amount of sea salt particles in each particle is such that the water vapor pressure above the surface of the particle is in equilibrium with that in the ambient. We have the familiar expression

$$S = 1 + \frac{A}{r} - \frac{B\, r_d^3}{r^3} \tag{63}$$

where

$$A = \frac{2\sigma'}{\rho' RT} \tag{64}$$

$$B = \frac{i\, \rho_d\, M_w}{M_s \rho_w} \tag{65}$$

where S = relative humidity, r = radius of droplet, r_d = radius of dry salt

σ' = surface tension of the aqueous solution

ρ' = density of the aqueous solution

R = universal gas constant

T = absolute temperature

i = Van Hoff factor

ρ_d = density of the dry particles

ρ_w = density of water

M_w = molecular weight of water

M_s = molecular weight of the soluble salt

The amount of sea-salt in each droplet can easily be calculated by applying Eq. (63). As soon as the relative humidity of the ambient air is changed, the equilibrium radius will be changed accordingly. In order to estimate the effect of relative humidity on the size distribution of fog, we have used the measured size distribution of fog at R.H. = 99.5% to calculate the value of r_d for each value of r at that relative humidity. We assume that the dry salts are sodium chloride particles. Then we calculate the size distribution at an environment of R.H. = 98.5% and 97.5%. The measured size distribution at 99.5% and the calculated size distributions at R.H. = 98.5% and 97.5% are shown in Fig. 58. It can be seen that a small change of relative humidity will cause a significant change in the aerosol size distribution, especially for those aerosols with larger radii.

In our model studies, we assume that the aerosol particles in the enclosure are sea-salt containing particles whose initial size distribution can be described by the regularized power law (RPL) model, defined by Eqs. (47 and 48) in Section 5.1.

We assume $p_3 = 4.0$, $p_4 = 4.0$ and the mode radius $r_m = 1.4$ μm. From Eq. (48), the value of p_2 can be calculated. The value of p_1 is adjusted so that the optical depth at $\lambda = 0.6328$ μm is 7.0. We arbitrarily let the relative humidity of the ambient air change at a rate of 1% per hour. The change of the optical depth with time for different wavelengths is shown in Figs. 59(a) and (b). From our preliminary results, it can be seen that even a very slow change of temperature will cause a great change of optical depth. This is primarily due to the fact that equilibrium sizes of solution droplets are very sensitive to the relative humidity of the ambient air. It is expected that if the aerosol particles under consideration are oil fogs, the effect of condensation/ evaporation on the optical depth will not be so significant.

The computer programs to study the combined effects of coagulation and evaporation on laser beam propagation have been developed, but have not been optimized as yet. Work is still in progress. Therefore, the results for the combined effects of coagulation and evaporation are not shown here.

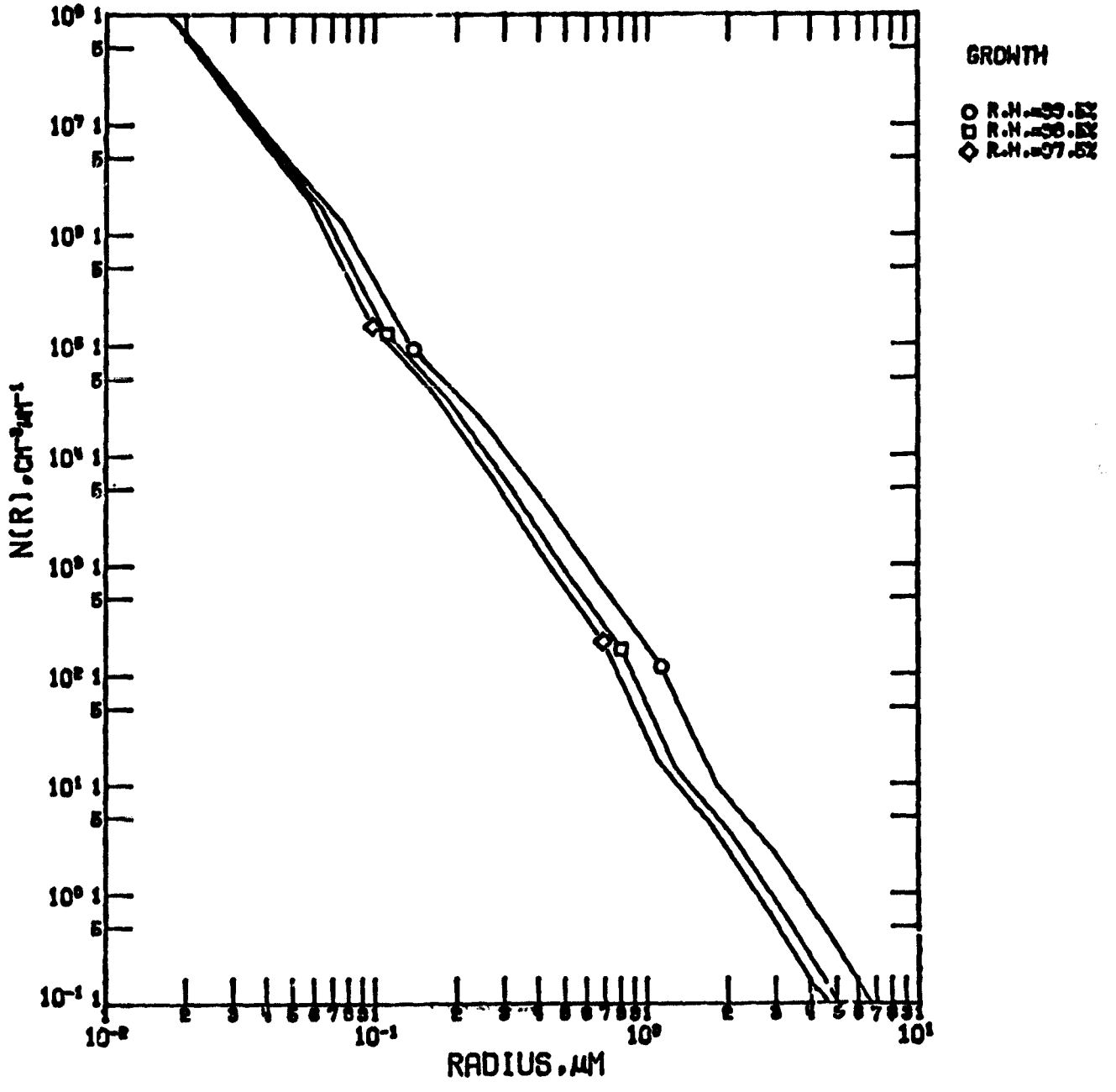

FIGURE 58. Measured (at R.H. = 99.5%) and calculated (at R.H. = 98.5 and 97.5%) size distributions.

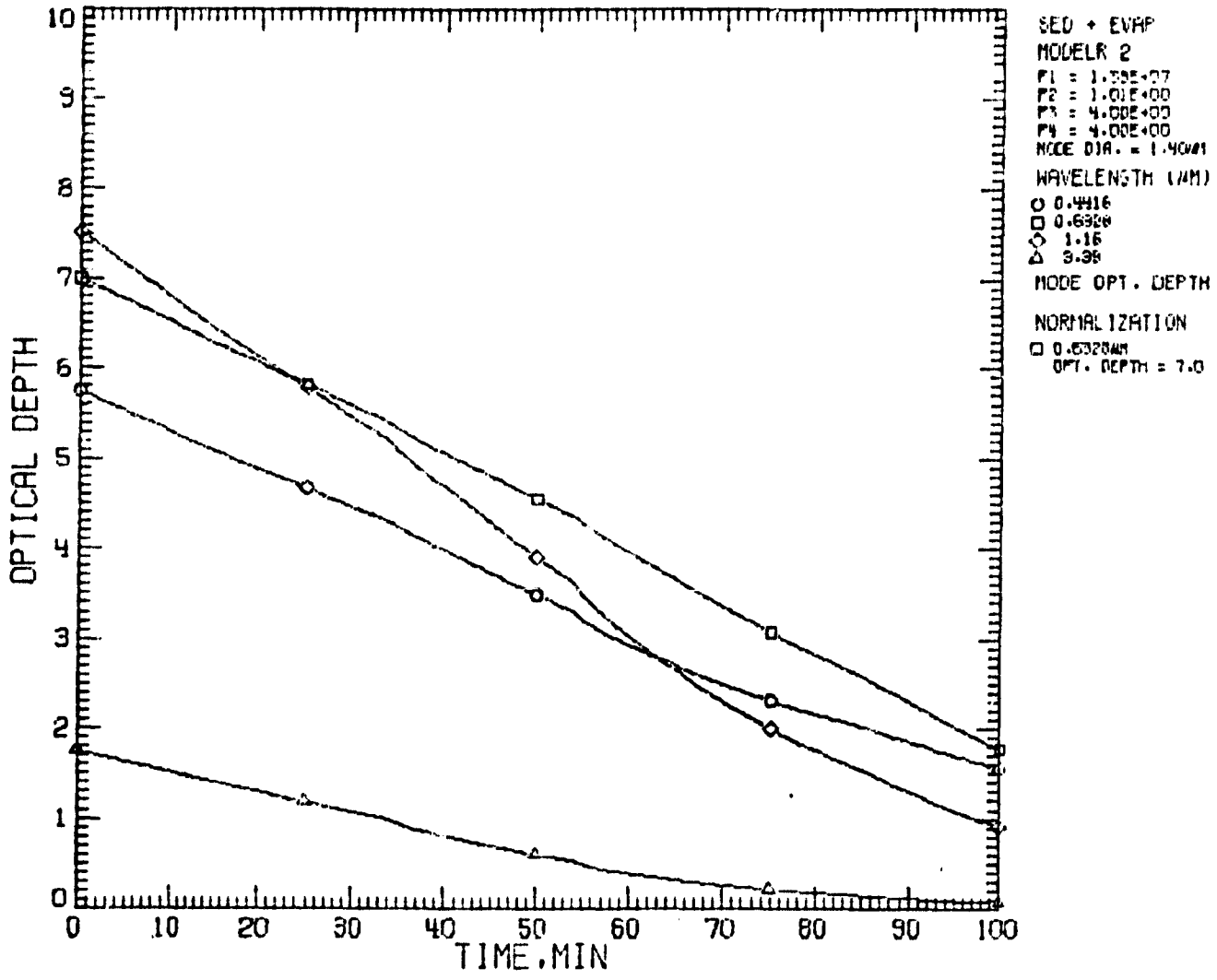

Figure 59(a). Optical depth versus time for particles undergoing sedimentation + evaporation when the relative humidity changes by one percent per hour.

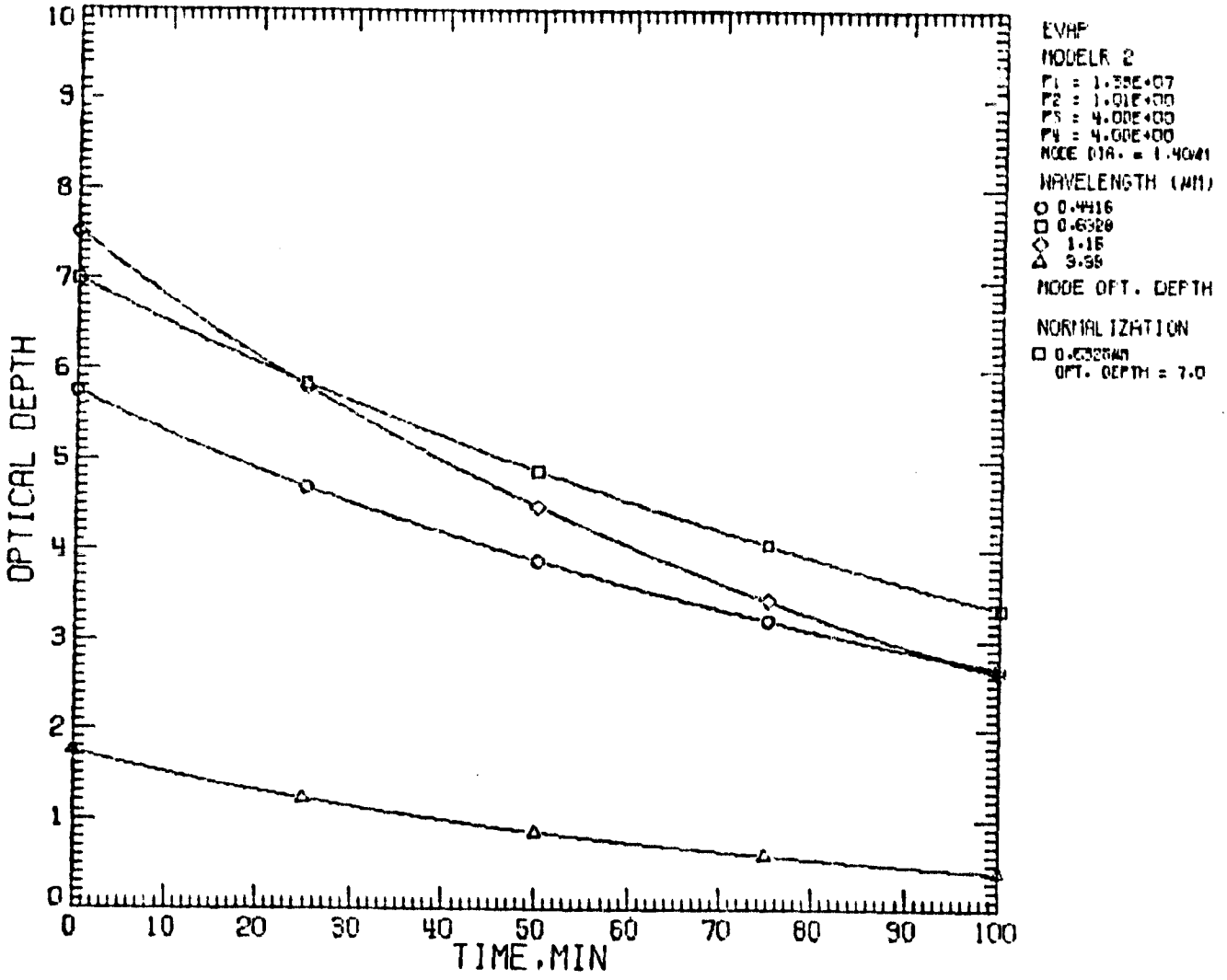

Figure 59(b). Optical depth versus time for particles undergoing evaporation when the relative humidity changes by one percent per hour.

6. MULTIPLE SCATTERING EFFECTS OF LASER BEAMS TRAVERSING DENSE AEROSOLS

In recent years there has been a considerable increase in interest in the problem of multiple scattering effects on laser beam propagation in an aerosol media. In two recent papers (Ref. 34, 35), we have investigated the case of forward (single) scattering as it effects the transmittance or extinction coefficient measurements for plane parallel (collimated) beam of radiation traversing aerosol media. In an earlier work (Refs. 5 , 6), we used the successive scattering approach to determine the beam broadening effects of second and third order scattering on a collimated pencil of radiation (white light). Since then several papers have appeared in open literature on the subject of aerosol effects on laser beams.

Most of the approaches adopted in MS studies of beams of radiation are based on the assumption of small-angle approximation. They can be categorized as either analytic approaches (Refs. 36-46) or successive scattering computer simulation approaches (Refs. 47-51). Some of these studies deal with incomplete MS problems, namely, with two or three orders of scattering (Refs. 6, 52-55.

Among the analytic methods, most of the approaches are based on the solution of the radiative transfer equation (RTE) for narrow collimated beams traversing dense particulate (aerosols or colloid) media (Refs. 38, 41, 56-61). An exact solution of the RTE for beams traversing media with highly anisotropic phase functions, is possible only by making the small angle approximation. However, to obtain quantitative results, one needs to make further approximations, each leading to markedly different results. A brief review of three approximations will be discussed in the next section.

If a relatively narrow beam propagates in a scattering medium, photons are constantly removed from the beam. However, if the scatterers are of a size equal to or greater than the radiation wavelength, such as in the case of smoke, dust, or fog particles compared to visible wavelengths, then

most scattering events will result in a comparatively small deflection of the photon. This may lead to a gradual spreading of the original beam, both in thickness and angle.

In this report, we examine the signal that may be detected, as functions of both experimental geometry and the properties of the scattering medium. We shall employ the small-angle approximation to the equation of radiative transfer, which ignores photons which have suffered large deflections as they will be assumed lost. In order to obtain tractable answers, it will prove necessary to assume simple analytic forms for the scattering phase function and the initial beam profile. Nevertheless, the analysis presented in this report will be as free as possible of unnecessary approximations. The work discussed in Section 6.1 has been reported in Ref. 45.

6.1 GENERAL SOLUTION OF RTE IN THE SMALL ANGLE APPROXIMATION

Let $I(z, \underset{\sim}{r}, \hat{\underset{\sim}{\Omega}})\, d\underset{\sim}{V}\, d\hat{\underset{\sim}{\Omega}}$ be the intensity of radiation (or the number of photons) in a volume element $d\underset{\sim}{V}$ centered at the point z, $\underset{\sim}{r} = (x, y)$, and travelling within a cone of solid angle $d\hat{\underset{\sim}{\Omega}}$ centered about the direction $\hat{\underset{\sim}{\Omega}}$. Then I satisfies the radiative transfer equation, which we may write (Refs. 43 and 44).

$$\left[\hat{\underset{\sim}{\Omega}} \cdot \nabla + \sigma\right] I(z, \underset{\sim}{r}, \hat{\underset{\sim}{\Omega}}) = \omega_o \sigma \int P(\hat{\underset{\sim}{n}} \cdot \hat{\underset{\sim}{n}}')\, I(z, \underset{\sim}{r}, \hat{\underset{\sim}{n}}')\, d\hat{\underset{\sim}{n}}' \qquad (66)$$

where σ is the extinction coefficient (km^{-1})

ω_o is the albedo of single scattering

$\psi = \cos^{-1}(\hat{\underset{\sim}{n}} \cdot \hat{\underset{\sim}{n}}')$ is the scattering angle

and $P(\psi)$ is the scattering phase function (sr^{-1})

Even allowing for cylindrical symmetry about the axis of propagation (the z axis), Eq. (66) is exceedingly hard to solve numerically. However since the diameter of our detector will always be small compared to the total propagation distance, we may safely assume that all photons which are eventually detected will have spent their flight time travelling essentially parallel to the z-axis. We may thus set $\cos\theta = 1$, where θ is the angle the photon makes with the z axis.

Note that this approximation ignores the contribution from all photons which undergo at least one large-angle scattering event. All such photons will clearly need to undergo at least a second large-angle scattering event, and maybe even a third, in order for them to reach the detector. As we are assuming that the phase function, P, is strongly forward-peaked, the probability of two or more large-angle scatterings is clearly very small, and thus the neglected contribution will be small.

The main effect of this assumption is to replace the unit propagation vector by

$$\hat{\underset{\sim}{n}} \equiv (n_z, \underset{\sim}{n}_\perp) \to (1, \underset{\sim}{n}_\perp) \tag{67}$$

Although this new propagation vector is no longer correctly normalized, this should not cause any problems, as the number of photons for which $|\underset{\sim}{n}_\perp| \ll 1$ does not hold, will clearly be small.

The second effect is that we may use $\underset{\sim}{n}_\perp - \underset{\sim}{n}'_\perp$ as the argument of P in Eq. 1, i.e.,

$$P(\hat{n} \cdot \hat{n}') \to P(\underset{\sim}{n}_\perp - \underset{\sim}{n}'_\perp) \tag{68}$$

and third effect is to replace the limits of this (two dimensional) integral by $\pm \infty$. With these points in mind, we may now rewrite Eq.(66) as

$$\left(\frac{\partial}{\partial z} + \underset{\sim}{n}_\perp \cdot \frac{\partial}{\partial \underset{\sim}{r}} + \sigma\right) I(z, \underset{\sim}{r}, \underset{\sim}{n}_\perp) = \omega_o \sigma \int_{-\infty}^{\infty} \int P(\underset{\sim}{n}_\perp - \underset{\sim}{n}'_\perp)\, I(z, \underset{\sim}{r}, \underset{\sim}{n}'_\perp)\, d\underset{\sim}{n}'_\perp \tag{69}$$

Equation (69) is referred to as the radiative transfer equation (RTE) in the small-angle approximation. Its main advantage over Eq. (66) is in the simplification of the directional derivative. This equation has been used extensively in the theory of foil penetration by fast charged particles (Refs. 62-64). Though Wentzel (Ref. 3) was the first to use the small-angle approximation for charged particle transfer, the first person to employ this equation in the field of radiative transfer appears to be Dolin (Ref. 59).

One further result of the small-angle approximation is that all detected photons are assumed to have travelled the same distance. Thus their time of travel is constant, and a pulse will undergo no time-dispersion.

Formal Solution

Equation (69) may be solved, at least formally, by the use of Fourier transform techniques. Introducing the definitions

$$\hat{I}(z, \underset{\sim}{\eta}, \underset{\sim}{\xi}) = (2\pi)^{-2} \int_{-\infty}^{\infty}\iint I(z, \underset{\sim}{r}, \underset{\sim}{n}) \, e^{i(\underset{\sim}{\eta}\cdot\underset{\sim}{r} + \underset{\sim}{\xi}\cdot\underset{\sim}{n}_\perp)} \, d\underset{\sim}{r} \, d\underset{\sim}{n}_\perp \tag{70}$$

and $$\hat{P}(\underset{\sim}{\xi}) = (2\pi)^{-1} \int_{-\infty}^{\infty}\int P(\underset{\sim}{n}_\perp) \, e^{i \, \underset{\sim}{\xi}\cdot\underset{\sim}{n}_\perp} \, d\underset{\sim}{n}_\perp \tag{71}$$

we take the double Fourier transform of Eq. (69) to obtain (Ref. 59).

$$\left[\frac{\partial}{\partial z} - \underset{\sim}{\eta} \cdot \frac{\partial}{\partial \underset{\sim}{\xi}} + \sigma\right] \hat{I}(z, \underset{\sim}{\eta}, \underset{\sim}{\xi}) = 2\pi \, \omega_o \sigma \, \hat{P}(\underset{\sim}{\xi}) \, \hat{I}(z, \underset{\sim}{\eta}, \underset{\sim}{\xi}) \tag{72}$$

Equation (72) is easily solved, to yield (Refs. 59, 64).

$$\hat{I}(z, \underset{\sim}{\eta}, \underset{\sim}{\xi}) = \hat{I}_o(\underset{\sim}{\eta}, \underset{\sim}{\xi} + z \, \underset{\sim}{\eta}) \, e^{-\sigma z + \Omega} \tag{73}$$

where

$$\Omega \equiv \Omega(z, \underset{\sim}{\eta}, \underset{\sim}{\xi}) = 2\pi \, \omega_o \sigma \int_0^z \hat{P}(|\underset{\sim}{\xi} + z' \, \underset{\sim}{\eta}|) \, dz' \tag{74}$$

and $\hat{I}_o(\underset{\sim}{\eta}, \underset{\sim}{\xi})$ is the Fourier transform of the initial intensity distribution (incident beam profile) at $z = 0$.

To obtain the intensity distribution at any point in the medium, it is merely necessary to re-transform Eq. (73) (Refs. 64 and 65).

$$I(z, \underset{\sim}{r}, \underset{\sim}{n}_\perp) = (2\pi)^{-2} \int\int\int\int_{-\infty}^{\infty} \hat{I}(z, \underset{\sim}{\eta}, \underset{\sim}{\xi}) \, e^{-i(\underset{\sim}{\eta} \cdot \underset{\sim}{r} + \underset{\sim}{\xi} \cdot \underset{\sim}{n}_\perp)} \, d\underset{\sim}{\eta} \, d\underset{\sim}{\xi} \qquad (75)$$

where $\hat{I}$ is given by Eq. (73).

In Eqs. (74) and (75), there are five integrations to be performed in order to obtain numerical values of the specific intensity $I(z, \underset{\sim}{r}, \underset{\sim}{n}_\perp)$. In principle, it should be possible to perform these integrations numerically; but in practice it is prohibitively expensive to do this using computers such as CDC 6600 and 7600, due to the necessity of evaluating the 4-dimensional Fourier transform in Eq. (75).

One way to make the problem tractable is to convert the integration over the rapidly oscillating function $\exp[-i(\underset{\sim}{\eta} \cdot \underset{\sim}{r} + \underset{\sim}{\xi} \cdot \underset{\sim}{n}_\perp)]$ in the Fourier transform into integration over a distance z of a slowly varying function, even though multi-dimensional. Such an approach was adopted by Tam and Zardecki (Ref. 43) for the case of a Gaussian phase function. They expanded the exponential factor containing Ω into a power series, in which each term could be analytically integrated over the four variables $(\underset{\sim}{\eta}, \underset{\sim}{\xi})$. The multi-dimensional integration over z then has to be done numerically by employing any of of the standard procedures, such as, method of Lyness (Ref. 66), Conroy (Ref. 67, 68), Monte Carlo (Ref. 69), etc. The details of the method are described in a later section. It should be noted that the approach of Tam and Zardecki has not yet been tried for non-Gaussian phase functions.

Another approach, which is approximate but considerably simpler since it avoids multi-dimensional integration, was used by Arnush (Ref. 38) and Stotts (Ref. 61) in solving the problem of a radiative transfer of a collimated beam. Arnush (Ref. 38) treated the case of a narrow collimated beam in ocean, and Stotts (Ref. 61), that of a laser beam traversing particulate medium. In both cases, they solved a non-homogeneous RTE (containing a source term) under homogeneous boundary conditions. In this report, we consider a homogeneous RTE (in which source term is absent) and solve it under non-homogeneous boundary conditions. As is well known (Ref. 70), the two formulations are essentially equivalent. Therefore, their method, which will be referred to hereafter as the Arnush-Stotts type (AST)

approximation, could be adapted to our case.

The AST approximation basically involves a series expansion of the integrand, in Ω (Eq. 74), and retaining the first two terms, which subsequently enables one to perform analytically the 4-dimensional integration in Eq. (75). The details will be discussed in a later section.

There is yet another approximate method, which avoids the difficulties of carrying out multi-dimensional integration numerically. This method, hereafter referred to as the Dolin-Fante method, essentially involves the expansion of $I(z, \underset{\sim}{r}, \underset{\sim}{n}'_\perp)$ in the integrand of Eq. (69) in a Taylor series about $\underset{\sim}{n}'_\perp = \underset{\sim}{n}_\perp$. Subsequently, the RTE in the small-angle approximation (Eq. 75) is replaced by a system of two equations--one for the unscattered radiance $I^{(o)}$, and the other for $I^{(o)}$ and the scattered radiance $I^{(s)}$. Once the equation for $I^{(o)}$ is solved, $I^{(s)}$ can be found by solving a non-homogeneous RTE, with the source term being determined in terms of $I^{(o)}$. The details of the method are explained in a later section.

In the work reported here, we evaluated the detected power *P* for a δ-function laser beam propagating through dense aerosols for different phase function models. The other quantities of interest are irradiance and the beam spread. For which the formulations are given below but no computations have been performed as yet.

Quantities of Interest: Irradiance, Power Detected and Beam Spread

Irradiance: In this study, it is the irradiance (flux density) and received power, rather than radiance, which is of interest to us. Using the relation between irradiance, N, and radiance, I, we may simplify Eq. (75) (Refs. 59 and 65).

$$N(z, \underset{\sim}{r}) \equiv \int_{2\pi} I(z, \underset{\sim}{r}, \underset{\sim}{n}_\perp)[\hat{\underset{\sim}{n}} \cdot \hat{\underset{\sim}{z}}] \, d\hat{\underset{\sim}{n}}$$

$$\simeq \int_{-\infty}^{\infty}\int I(z, \underset{\sim}{r}, \underset{\sim}{n}_\perp) \, d\underset{\sim}{n}_\perp \tag{76}$$

$$= \int_{-\infty}^{\infty}\int \hat{I}(z, \underset{\sim}{\eta}, \underset{\sim}{0}) \, e^{-i \, \underset{\sim}{\eta}\cdot\underset{\sim}{r}} \, d\underset{\sim}{\eta} \tag{77}$$

With the elimination of $\underset{\sim}{\xi}$ in Eq. (77), we may simplify Eqs. (73) and (74)

$$\hat{I}(z, \underset{\sim}{\eta}, \underset{\sim}{0}) = \hat{I}_o(\underset{\sim}{\eta}, z\,\underset{\sim}{\eta})\, e^{-\sigma z + \Omega_o} \tag{73'}$$

where $$\Omega_o = 2\pi\, \omega_o \sigma \int_0^z \hat{P}(|z'\,\eta|)\, dz' \tag{74'}$$

Equation (77) can now be further simplified by an appeal to symmetry. Since $P(\psi)$ clearly depends only on the scalar $|\underset{\sim}{n}_\perp|$, and not on the vector $\underset{\sim}{n}_\perp$, $\hat{P}$ $\hat{P}$ will similarly be a scalar function, as will Ω_o. Similarly, if we assume that the incident beam profile is circularly symmetric, then $\hat{I}_o(\underset{\sim}{\eta}, z, \underset{\sim}{\eta})$ will also be a scalar function of η. Thus $\hat{I}(z, \eta, 0)$ will be a scalar function, and Eq. (77) becomes

$$N(z, \underset{\sim}{r}) = 2\pi \int_0^\infty J_o(\eta\, r)\, \hat{I}(z, \eta, 0)\, \eta\, d\eta \tag{77'}$$

From Eq. (77') we see immediately that N is a scalar function of r, as we would expect from the above symmetry arguments. A more tractable expression for the case of δ-function will be given later in Eq. (96).

Detected Power: In most instances, of course, what we are most interested in (and what we physically measure) is the power received by some detector. This will involve the integration of Eq. (77') over the area of the detector, perhaps modulated by a response function. If we assume a coaxial, circular detector of radius R, with a flat response, then we have

$$P(z, R) = 2\pi \int_0^R N(z, r)\, r\, dr$$

$$= 4\pi^2\, e^{-\sigma z} \int_0^\infty J_1(\eta\, R)\, \hat{I}_o(\eta, z\,\eta)\, e^{\Omega_o}\, R\, d\eta \tag{78}$$

This result should prove amenable to numerical integration, especially if a relatively simple expression for Ω_o can be obtained. Sample results will be presented.

One useful result which can be obtained analytically, is the total power crossing a surface z = constant:

$$P(z, \infty) = \int_{-\infty}^{\infty}\int N(z, \underset{\sim}{r})\, d\underset{\sim}{r}$$

$$= \int \int_{-\infty}^{\infty}\int \int \hat{I}(z, \underset{\sim}{\eta}, \underset{\sim}{0})\, e^{-i \underset{\sim}{\eta} \cdot \underset{\sim}{r}}\, d\underset{\sim}{\eta}\, d\underset{\sim}{r}$$

$$= 4\pi^2\, \hat{I}(z, 0, 0)$$

$$= 4\pi^2\, \hat{I}_o(0, 0)\, e^{-\sigma z + 2\pi \omega_o \sigma z \hat{P}(0)}$$

$$= F_o\, e^{-(1 - \omega_o)\sigma z} \qquad (79)$$

where F_o is the incident total power, and we have used the fact that $\hat{P}(0) = (2\pi)^{-1}$. From Eq. (79) we see that the only energy removed from the beam is that lost by absorption, i.e., there is no backscatter.

Beam Spread: One further parameter which will often prove useful is the beam spread, which we may define as

$$\langle r^2 \rangle = \int_0^{\infty} N(z, r)\, r^3\, dr \,/\, \int_0^{\infty} N(z, r)\, r\, dr$$

$$= 2\pi\, F_o^{-1}\, e^{(1 - \omega_o)\sigma z} \int_0^{\infty} N(z, r)\, r^3\, dr \qquad (80)$$

EXACT SOLUTIONS OF RTE IN SMALL ANGLE APPROXIMATION FOR GAUSSIAN BEAM AND VARIOUS PHSE FUNCTIONS

In this section, we shall devise expressions for the two quantities--namely, P and $\langle r^2 \rangle$ --from the solution of the RTE in the small angle approximation, for the case of a laser beam, with a Gaussian intensity profile, traversing a scattering medium, represented by four simple phase function models--one Gaussian and three non-Gaussian (viz., two exponential and binomial) functions. An alternative expression for the beam profile N will also be given.

The power detected will be obtained for a collimated beam with zero width in space, and the expressions for beam spread, for any realistic beam. At the entrance ($z = 0$) to the scattering medium, a laser beam profile is represented by a Gaussian functional form, both for the radial intensity distribution, and the angular divergence, given by

$$I_o(\underset{\sim}{r}, \underset{\sim}{n}_\perp) = F_o \beta^2 \gamma^2 \pi^{-2} \exp(-\beta^2 \underset{\sim}{n}_\perp^2 - \gamma^2 \underset{\sim}{r}^2) \tag{81}$$

This may be easily transformed, and, in particular, we have

$$\hat{I}_o(\eta, z\eta) = F_o (2\pi)^{-2} \exp(-\eta^2 / 4\gamma^2 - z^2 \eta^2 / 4\beta^2) \tag{82}$$

In general, the laser beam profile will be well-collimated, so that β and γ will be large. The inclusion of Eq. (82) in Eq. (78) will in no way complicate the numerical integration, though in our examples later we will allow both to go to infinity, so as to reduce the number of parameters whose influence should be examined. In all practical calculations, however, realistic values of both parameters should be included. Next, we obtain the three quantities for the four phase function models.

Gaussian Phase Function

A Gaussian functional form is also often employed to describe $P(\psi)$, since it can approximate the forward peak of the scattering pattern for a spherical particle on which a plane wave is incident. Thus,

$$P(\psi) = 2\alpha^2 e^{-\alpha^2 \psi^2} / 2\pi \tag{83}$$

where α is an adjustable parameter, which controls the shape of the forward peak and is related to the rms scattering angle $\overline{\psi}$ defined as

$$\overline{\psi^2} = 2\pi \int_0^\infty P(\psi)\ \psi^3\ d\psi \tag{83a}$$

It is easily shown that for the Gaussian case $\overline{\psi^2} = \alpha^{-2}$. (Though α will usually be large, it will rarely, if ever, be as large as β or γ.)

Taking the Fourier transform of Eq. (83), we find

$$\hat{P}(\xi) = \int_0^\infty J_o(\xi\ \psi)\ P(\psi)\ \psi\ d\psi \tag{71'}$$

$$= e^{-\xi^2/4\ \alpha^2}\ /\ 2\pi \tag{84}$$

and hence $\Omega_o = \omega_o \sigma\ \eta^{-1}\ \alpha \sqrt{\pi}\ \mathrm{erf}\ (z\eta/2\alpha)$ (85)

Substituting Eqs. (16) and (19) into (12) we find

$$P(z, R) = F_o\ R \int_0^\infty J_1(\eta\ R)\ \exp\ [\omega_o \sigma\ \eta^{-1}\ \alpha\ \sqrt{\pi}\ \mathrm{erf}\ (z\eta/2\alpha)$$

$$- \sigma z - \eta^2/4\ \gamma^2 - z^2\ \eta^2/4\ \beta^2]\ d\eta \tag{86}$$

Equation (86) is an exact equation, which can be solved numerically for various values of β and γ. In order to reduce the number of parameters, we make a simplification in Eq. (86) and consider the limiting case of $\beta, \gamma \to \infty$. This physically implies that the beam is collimated and has zero width in space. Then, by making the variable changes

$$\tau = \sigma z$$

$$\tau_s = \omega_o \tau$$

$$G = R/z\ (\overline{\psi^2})^{1/2}$$

$$\chi = \eta R$$

Equation (86) can be reduced to

$$P(z, R) = F_o e^{-\tau} \int_0^\infty J_1(\chi) \exp \left[\tau_s \sqrt{\pi}\, G\chi^{-1} \operatorname{erf} (\chi/2G)\right] d\chi \tag{87}$$

The power of the unscattered beam at an optical depth of τ is, of course, $F_o e^{-\tau}$. Thus, the presence of forward scattering has increased the detected power by the amplification factor A, given by

$$A(\tau_s, G) = \int_0^\infty J_1(\chi) \exp \left[\tau_s \sqrt{\pi}\, G\, \chi^{-1} \operatorname{erf}(\chi/2G)\right] d\chi \tag{88}$$

where A is a function of two parameters; τ_s, the scattering optical thickness, and G, the geometry factor.

Finally, we may obtain the beam spread for the general case of a beam given by Eq. (81) by substituting from Eqs. (77) and (82) into Eq. (80):

$$\langle r^2 \rangle = \tau_s\, z^2/3\alpha^2 + z^2/\beta^2 + \gamma^{-2} \tag{89}$$

In general, the first term should dominate, except perhaps, close to the point of entry into the medium.

Non-Gaussian Phase Functions

Although the Gaussian form in Eq. (83) is a popular model for the forward peak of the phase function, it is often a good idea to examine other models, to make sure that none of the results are simply an artifact of the Gaussian model. In this section, therefore, we shall examine a number of other functional forms which may be (and have also been) used to model anisotropic phase functions. We shall follow essentially the same steps as in the previous section, and present only the results, unless further explanation is necessary.

Exponential Phase Functions:

For a infinitely narrow beam

$$P(\psi) = \alpha^2\, e^{-\alpha \psi}/2\pi \tag{90a}$$

$$\hat{P}(\xi) = \alpha^3(\alpha^2 + \xi^2)^{-3/2} / 2\pi \tag{90b}$$

$$\Omega_o = \tau_s (1 + y^2/6)^{-1/2} \tag{90c}$$

where $$y = z\,\eta/\alpha = \chi/G \tag{91}$$

Thus $$A(\tau_s, G) = \int_0^\infty J_1(\chi) \exp\left[\tau_s(1 + \chi^2/6\,G^2)^{-1/2}\right] d\chi \tag{90d}$$

and for a general beam

$$\langle r^2 \rangle = 2\,\tau_s\, z^2/\alpha^2 + z^2/\beta^2 + \gamma^{-2} \tag{90e}$$

Phase Function for Sea Water: Similarly, for the infinitely narrow beam

$$P(\psi) = \alpha\,\psi^{-1}\, e^{-\alpha\,\psi}/2\pi \tag{92a}$$

$$\hat{P}(\xi) = \alpha(\alpha^2 + \xi^2)^{-1/2}/\,2\pi \tag{92b}$$

$$\Omega_o = \sqrt{2}\,\tau_s\, y^{-1} \ln\left[y/\sqrt{2} + (1 + \tfrac{1}{2}\,y^2)^{1/2}\right] \tag{92c}$$

$$A(\tau_s, G) = \int_0^\infty J_1(\chi) \exp\left\{\tau_s \sqrt{2}\, G\chi^{-1} \ln\left[\chi/G\,\sqrt{2} + (1 + \tfrac{1}{2}\,\chi^2 G^{-2})^{1/2}\right]\right\} d\chi \tag{92d}$$

and, for a general beam

$$\langle r^2 \rangle = 2\,\tau_s\, z^2 / 3\,\alpha^2 + z^2 / \beta^2 + \gamma^{-2} \tag{92e}$$

Note that, although Eq. (92a) implies $P(0) = \infty$, the inclusion of the correct solid angle factor leads to a finite result for the amount of light scattered through any angle. In fact, Eq. (92a) has been employed by Bravo-Zhivotovskiy *et al.* *et al.* (Ref. 65) to model the phase function of sea water.

Binomial Phase Functions:

This time, we consider phase functions based on the functional form $(1 + \alpha^2\psi^2)^{-\mu-1}$. We will need the result that

$$\int_0^\infty J_o(\eta\psi)\ (1 + \alpha^2\psi^2)^{-\mu-1}\ \psi\ d\psi = (\eta/2\alpha)^\mu\ K_\mu\ (\eta/\alpha)\ /\ \alpha^2\Gamma(\mu + 1) \qquad (93)$$

where K_μ is the modified Bessel function of the second kind. Thus if

$$P_\mu(\psi) = 2\ \mu\ \alpha^2\ (1 + \alpha^2\psi^2)^{-\mu-1}\ /\ 2\pi \qquad (94a)$$

$$\hat{P}_\mu(\xi) = (\xi/2\alpha)^\mu\ K_\mu\ (\xi/\alpha)\ /\pi\ \Gamma\ (\mu) \qquad (94b)$$

$$\Omega_o = \tau_s\ \sqrt{\pi}\ \Gamma(\mu + \tfrac{1}{2})\ \left[K_\mu\ (y')\ L_{\mu-1}(y') + K_{\mu-1}(y')\ L_\mu(y')\right]\ /\ \Gamma(\mu) \qquad (94c)$$

where $y' = y\sqrt{\mu-1}$

and L_μ is the modified Struve function of order μ.

The expression for A may be easily written down. For $\mu > 1$, we may obtain the beam spread for a general beam (β, γ finite)

$$\langle r^2\rangle = \tau_s\ z^2/3\ \alpha^2(\mu - 1) + z^2/\beta^2 + \gamma^{-2} \qquad (94d$$

Note that if μ is an odd half-integer, Eq. (94c) may be expressed in terms of exponential functions. For example, for $\mu = 3/2$ we find that for infinitely narrow beam ($\beta,\ r \to \infty$)

$$\Omega_o(3/2) = \tau_s\ \left[2\ \sqrt{2}\ y^{-1} - e^{-y/\sqrt{2}}\ (1 + 2\ \sqrt{2}\ y^{-1})\right] \qquad (95)$$

$$A(\tau_s,\ G) = \int_0^\infty J_1(\chi)\ \exp\left\{\tau_s\ \left[2\ \sqrt{2}\ G\chi^{-1} - e^{-\chi/G\sqrt{2}}\ (1 + 2\ \sqrt{2}\ G\chi^{-1})\right]\right\}\ d\chi \qquad (95'$$

Beam Profile N(r)

The irradiance profile of the expanding beam is also a quantity of interest, even though no numerical results are presented here. The formal expression for the transverse irradiance profile is given by Eq. (77'). In most cases, this expression is well behaved. However, for the special case of $\beta, \gamma \to \infty$, Eq. (77') will diverge. Therefore, an alternative expression for N(r) may be obtained either by integration by parts of Eq. (77') or by differentiating Eq. (78). Adopting the second approach and setting $I_o = F_o(2\pi)^{-2}$, we obtain

$$N(r) = \frac{1}{2\pi R} \frac{dP}{dR}$$

$$= - F_o(2\pi)^{-1} r^{-2} e^{-\tau} \int_0^\infty J_1(\chi)\, e^{\Omega_o}\, \Omega_o'\, y\, d\chi \qquad (96)$$

where the prime denotes differentiation of Ω_o with respect to y (Eq. 91). With the exception of the sea-water phase function, Ω_o goes as y^{-1} for large y, and so Ω_o' goes as y^{-2}, and convergence is assured.

THREE ALTERNATIVE APPROACHES FOR SOLVING THE RTE

For the sake of completeness, we shall give the mathematical formulations for three methods--one exact (Tam and Zardecki method) and two approximate (Arnush-Stotts type and Dolin-Fante) methods. However, computations will be performed for only the Arnush-Stotts.

Tam and Zardecki's Exact Method

The method of Tam and Zardecki is exact, at least in principle, but requires the evaluation of multidimensional integration, the order of which is equal to the order of multiple scattering required. We will restrict this discussion to the case of the Gaussian phase function only.

The Tam and Zardecki method consists in expanding exp (Ω_o) in a Taylor series, before performing the integration over z' (Eq. 74'). Thus inserting Eq. (84) in Eq. (74'), and performing the Taylor expansion, yields

$$\exp(\Omega_o) = 1 + \sum_{m=1}^{\infty} \frac{\tau_s^m}{z^m\, m!} \int_0^z \cdots \int_0^z dz_1 \cdots dz_m \exp\{-\eta^2 \sum_{i=1}^{m} z_i^2 / 4\alpha^2\} \qquad (97)$$

We may now perform the inverse Fourier transform (Eq. 77') to yield

$$N(z, r) = F_o\, e^{-\tau} (\pi z^2)^{-1} \sum_{m=0}^{\infty} \frac{\tau_s^m}{m!} N_m(z, r) \qquad (98)$$

where $$N_o = \frac{z^2 \beta^2 \gamma^2}{z^2 \gamma^2 + \beta^2} \exp\{-\frac{r^2 \beta^2 \gamma^2}{z^2 \gamma^2 + \beta^2}\} \qquad (99a)$$

and $$N_m = \int_0^1 \cdots \int_0^1 dz_1 \cdots dz_m\, \Lambda_m^{-1} \exp\left[-r^2/z^2\, \Lambda_m\right] \qquad (99b)$$

where $$\Lambda_m = \alpha^{-2} \sum_{i=1}^{m} z_i^2 + \beta^{-2} + z^{-2} \gamma^{-2} \qquad (99c)$$

We may note in particular that N_1 may be evaluated analytically in terms of the error function. The resulting expression is quite complicated, except in the case where β and γ go to infinity, in which case we get

$$N_1(z, r) = \alpha^2 \sqrt{\pi}\, [1 - \mathrm{erf}(g)] / 2g \qquad (100a)$$

where $$g = r\, \alpha / z \qquad (100b)$$

Turning our attention to the power received, we obtain an expression similar to Eqs. (98) and (99), viz.

$$P(z, R) = F_o e^{-\tau} \sum_{m=1}^{\infty} \frac{\tau_s^m}{m!} P_m(z, R) \tag{101}$$

where $P_o = 1 - \exp\left\{-\frac{R^2 \beta^2 \gamma^2}{z^2 \gamma^2 + \beta^2}\right\}$ (102a)

and $P_m = \int_0^1 \cdots \int_0^1 dz_1 \cdots dz_m \left\{1 - \exp\left[-R^2/z^2 \Lambda_m\right]\right\}$ (102b)

Note that, from Eqs. (101) and (102), Eq. (79) may be obtained trivially. As with N_1, P_1 is also analytic, and in the simple case of $\beta, \gamma \to \infty$, we obtain

$$P_1(z, R) = 1 - e^{-G^2} + G\sqrt{\pi}\left[1 - \text{erf}(G)\right] \tag{103}$$

The number of terms required for the convergence of the series in Eqs. (98) and (101) grows steadily with τ_s, and so in some case for large optical thicknesses it may become prohibitively expensive to use it. Nevertheless, these results have one use in that Tam and Zardecki (Ref. 43) have shown that the mth order terms in Eqs. (98) and (101) correspond to the contribution from mth order scattering. This in itself is a useful result.

Another use suggests itself, however. The Gaussian phase function is simply a model, with the parameters α and ω_o available for adjustment to match "real" scattering patterns. Since we now have a simple expression for the singly-scattered contribution, we may compare it with that produced by a real phase function, and adjust α and ω_o accordingly. Then we may use the results outlined

above to estimate the multiply - scattered contribution from such a phase function. Comparisons with second and higher order contributions are also possible. This should increase our confidence in the worth of results obtained from a model phase function.

Arnush - Stotts (A-S) Type Approximate Method

In order to extract analytic answers, Arnush (Ref. 38) and Stotts (Ref. 61) have expanded $\hat{P}$ to second order before performing the integration to obtain Ω. (Series expansion of Ω would yield the same result.) Arnush has used Bravo-Zhivotovskiy's (Ref. 65) sea water phase function, Eq. (92a), while Stotts orininall used a Gaussian phase function, Eq. (83) and more recently the sea water phase function. This approximation is sufficient to provide the correct values for both $P(z,\infty)$, and $\langle r^2 \rangle$.

We start by re-writing the definition of Ω_o, as follows:

$$\Omega_o = 2\pi\, \omega_o\, \sigma z\, (\eta z)^{-1} \int_0^{\eta z} \hat{P}(t)\, dt$$

$$= 2\pi\, \omega_o\, \sigma z\, (\eta z)^{-1} \int_0^{\eta z} \int_0^{\infty} J_o(t\psi)\, P(\psi)\, \psi\, d\psi\, dt \qquad (104)$$

Expanding J_o as a power series leads to

$$\Omega_o = \omega_o\, \sigma z\, (1 - \eta^2 z^2\, \overline{\psi^2}/12 \ldots) \qquad (105)$$

where $\overline{\psi^2}$ is defined by Eq. (83a).

It is complicated, but reasonably straightforward to obtain the following expression for the beam spread parameter:

$$\langle r^2 \rangle = \frac{1}{3}\, \omega_o\, \sigma z^3\, \overline{\psi^2} + z^2/\beta^2 + \gamma^{-2} \qquad (106)$$

Ignoring the higher order terms in Eq. (105), we may insert this expression into Eq. (77') to obtain

$$N(z, r) = F_o \exp\left[-(1 - \omega_o)\tau - r^2/\langle r^2\rangle\right] / \pi \langle r^2\rangle \qquad (107)$$

Similarly, integration of Eq. (78) leads to

$$P(z, R) = F_o\, e^{-(1 - \omega_o)\tau}\left[1 - e^{-R^2/\langle r^2\rangle}\right] \qquad (108)$$

Taking the limits $\beta, \gamma \to \infty$, we may re-express Eq. (108) in more familiar terms

$$P(z, R) = F_o\, e^{-(1 - \omega_o)\tau}\left[1 - \exp\left(-3G^2/\tau_s\right)\right] \qquad (108')$$

$$\text{i.e.} \quad A(\tau_s, G) = e^{\tau_s}\left[1 - \exp\left(-3G^2/\tau_s\right)\right] \qquad (109)$$

Expansion of Ω_o to second order in y is equivalent to an asymptotic expansion to second order in G^{-1}, or R^{-1}. Thus we may expect this approximation to be accurate for large values of G or R. However, its behaviour for small values of these parameters is quite different from that of the exact results quoted in previous sections. Thus we cannot expect this approximation to prove particularly useful for our problem, as shown later by numerical comparisons. In fact, one finds values of A which are less than unity!

For our problem, of course, we are concerned with small values of R and G, and hence we are interested in the behavior of Ω_o for large values of y, i.e., its asymptotic expansion. The phase function model of Eq. (92a) does not have an asymptotic expansion, due to the fact that $P(0) = \infty$. For the other cases we may easily show that

$$\Omega_o \sim \tau_s \tilde{q}/y \tag{110}$$

where $$\tilde{q} = 2\pi \int_0^\infty P(\psi)\, d\psi / \alpha \tag{111}$$

Thus for a Gaussian (Eq. (83)), $\tilde{q} = \sqrt{\pi}$; Eq. (90a) gives $\tilde{q} = 1$; and Eq. (94a) gives $\tilde{q} = \mu\, B(\frac{1}{2}, \mu + \frac{1}{2})$, where B is the beta function. (For $\mu = \frac{3}{2}$, for example, $\tilde{q} = 2$.)

For large values of y, the Arnush-Stotts approximation to Ω_o goes to (minus) infinity, and so we cannot expect this approximation to accurately predict the power received by a small detector.

Dolin - Fante (D-F) Approximate method

Dolin (Ref.60) and Fante (Ref. 57) have argued that the angular shape of the scattered intensity should be a much more slowly varying function than $P(\psi)$, and have thus extracted it from the integral on the right side of Eq.(69) After separating the scattered intensity from the unscattered, and Fourier transforming, they arrive at the following expressions

$$\hat{I}^u(z, \underset{\sim}{\eta}, \underset{\sim}{0}) = e^{-\sigma z}\, \hat{I}_o(\underset{\sim}{\eta}, z\, \underset{\sim}{\eta}) \tag{112a}$$

and $$\hat{I}^s(z, \underset{\sim}{\eta}, \underset{\sim}{0}) = \hat{I}_o(\underset{\sim}{\eta}, z\, \underset{\sim}{\eta}) \int_0^z dz' \exp\left[-\sigma z' - \int_{z'}^z \lambda(t, \underset{\sim}{\eta}, z\, \underset{\sim}{\eta})\, dt\right] \cdot \omega_o \sigma\, \hat{P}\left[\underset{\sim}{\eta}\,(z - z')\right] \tag{112b}$$

where $$\lambda(t, \underset{\sim}{\eta}, z\,\underset{\sim}{\eta}) = \frac{1}{4}\omega_o\sigma\,\overline{\psi^2}\;|z\,\underset{\sim}{\eta} - t\underset{\sim}{\eta}|^2 + (1-\omega_o)\sigma \tag{113a}$$

$$\int_{z'}^{z}\lambda(t,\eta,z)\,dt = \frac{1}{12}\omega_o\sigma\,\overline{\psi^2}\,\eta^2(z^3 - z'^3) + (1-\omega_o)\,\sigma\,(z-z') \tag{113b}$$

where $\overline{\psi^2}$ is defined in Eq. (83a).

Equations (112) and (113) may now be inserted in Eqs. (77') or (78) as required. Although $\hat{P}$ is no longer exponentiated, this result is complicated by the additional (finite) integration over z'. In the case of a Gaussian phase function, it is possible to reverse the orders of these two integrals, and perform that over η, to give

$$A = e^{\omega_o\tau} - \omega_o\tau\int_0^1 dt\,\exp\left[\omega_o\tau\,t - G^2/(\tfrac{1}{3}\omega_o\tau\;t^3 + t^2)\right] \tag{114}$$

Our calculations show that this approximation is reasonably accurate, except in those situations where τ is large and G is small. In the Numerical Results section, we will compare the predictions of Eq. (114) with those of Eq. (88). As it is not possible to perform any of the integrals for any of the other phase function models, we have limited our examination of this approximation to the case of the Gaussian phase function.

NUMERICAL RESULTS

In this section, we shall present some typical results based on our exact formulation and the Arnush-Stotts type approximate method. We shall examine 4 phase function models: Gaussian (Eq. 83), both exponential models (Eqs. 90a and 92a), and the binomial model with $\mu = 3/2$ (Eq. 94a). To simplify discussion we shall refer to the phase function model of Eq. (90) as the exponential model and that of Eq. (92) as the sea-water model.

We start by examining the phase functions themselves. It is, of course, much simpler to plot the normalized phase functions, $\bar{P}$, rather than P, where $\bar{P}$ is defined by

$$\bar{P} = 2\pi P / \alpha^2 \qquad (115)$$

Unlike P, $\bar{P}$ is now a function of only one variable, $\alpha\psi$. In Figure 60, we plot $\bar{P}$ against $\alpha\psi$, for $0 \leq \alpha\psi \leq 3.5$. We noted earlier that the sea water and binomial models have identical values of the parameter q (Eqs. 105). From Fig. 60 we see that these two models are quite close over a wide range of values of $\alpha\psi$.

The next function we examine graphically in Ω_o. In Figure 61 we plot Ω_o/τ_s against y for all 4 phase functions, as well as the Arnush-Stotts approximation. From this log-log plot, the asymptotic behaviour of the 4 phase functions is apparent, particularly that of the sea-water phase function, which has no asymptotic expansion. Although it is not obvious from this figure, the curve for the binomial phase function actually lies slightly above the sea-water curve for y values less than about 3. Finally we note that for y values greater than 2, the results obtained by the Arnush-Stotts approximation differ markedly from those by our exact formulation, rapidly approaching large negative values for y greater than 4.

We turn now to a discussion of the amplification factor, A, and the power received, *P*, as predicted by these 4 models, and also the Arnush-Stotts type approximation. We have evaluated both A and *P* for G between 0.01 and 1.0, and τ_s between 0.5 and 15.0. (Throughout, we have assumed $\beta, \gamma \to \infty$.)

In the Appendix to this report, we have included a listing of the FORTRAN program used to generate this data, along with a brief explanation and sample output.

In Figure 62 we plot A against G for a series of τ_s values, for the Gaussian model. In Figure 63 we plot *P* against τ_s (assuming unit incident power) for a series of values G; again for the Gaussian model. Also shown on this plot is the transmission, T, which represents the power that would be received if all scattered light was lost. These two graphs clearly indicate the important role that forward scattering can play in the detection of transmitted beams, especially for optical thicknesses of the order of 10 or higher.

In Figure 64 we plot A as a function of G for τ_s = 4.0 and 10.0, for all four model phase functions, for our formulation as well as the Arnush Stotts approximation. In the latter case, one finds values of A which are less than unity. Note that the binomial and sea water curves cross for both τ_s values (see Fig. 61). For large values of G, we see that there is little to choose between the four phase function models.

In Figure 65, we plot (A - 1.0) against G in log-log form for τ = 1.0, in order to emphasize the linear relationship implied by Eq. (A3) in the Appendix. We see that for G less than 0.3, the integral term in Eq. (A3) makes a negligible contribution. In Figure 66, we plot (A - 1.0) against G for τ = 5.0. Here we see that the integral term in Eq. (A3) is starting to make a contribution. Also in this graph we have included the Arnush-Stotts and Dolin-Fante approximation results. The Dolin-Fante result was not included in Figure 65 as it could not be distinguished from the exact result for the Gaussian phase function.

CONCLUDING REMARKS

The propagation of a laser beam in an optically dense medium such as a fog, dust storm, or smoke is a problem of growing importance, both for communication and detection purposes. Although such dense media lead to a significant attenuation of the primary beam, much of the scattered radiation may still be found close to the beam axis, and will thus be available for detection by a suitable detector.

In this report, we have examined the spreading of a laser beam using the small-angle-scattering approximation to the equation of transfer. This approximation appears eminently suited for the study of beam propagation in fog, dust, or smoke media, where the scattering phase function is highly anisotropic. As well as the standard Gaussian model phase function, three other model phase functions have also been examined. The Gaussian functional form was used to describe the initial beam spread and profile, although the analysis is somewhat simpler (and the resulting expressions tidier) if the limiting case is taken.

All the numerical results presented in this paper have been based on the assumption of a narrow, collimated beam. We may remark, however, that the results and expressions presented in this report (e.g., Eq. 86) for the finite beam may be applied with full generality.

We have also examined a number of approximations which have been used to further simplify the expressions we have derived. The Arnush-Stotts approximation is quite suitable for use in the asymptotic regions, at large distances from the beam axis. However, the behavior of the solutions close to the beam axis is governed by the parameter $\tilde{g}$, the zeroth moment of the phase function. This moment weights the contribution from scattering through very small angles far more highly than does the parameter χ^{-2}, the rms scattering angle, or third moment. In fact, for small R (i.e., small G), one may expand Eq. (88) to first order (c.f., Eq.103)

$$A(\tau_s, G) \simeq 1 + \tau_s \tilde{g} G + \ldots \qquad (116)$$

Finally, we may remark that the method proposed by Tam and Zardecki makes a useful contribution by providing a connection between realistic (Mie) phase functions, and the parameters which must be used in the model phase functions used in this report. Further work on the applications of this method is recommended.

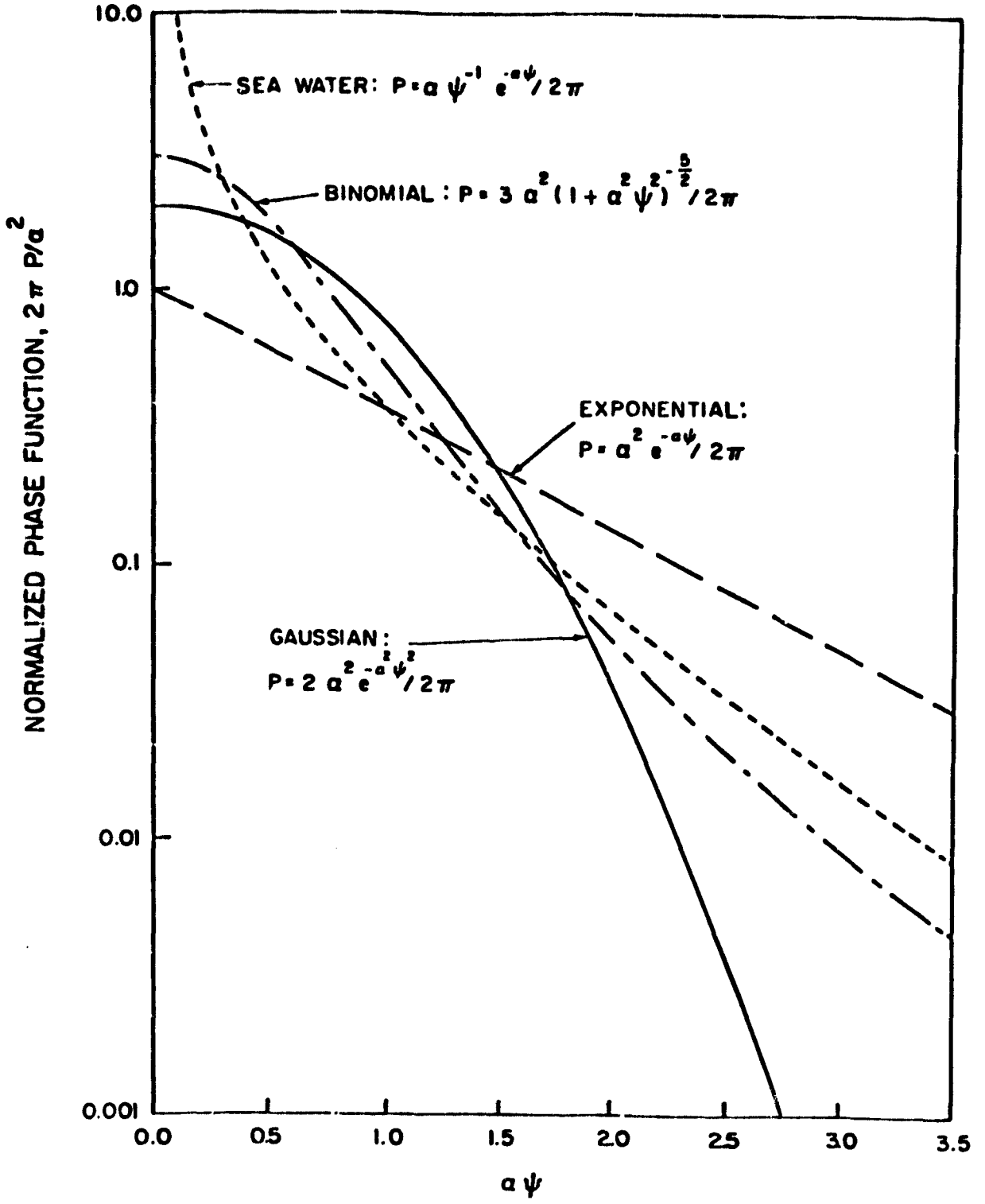

FIGURE 60. Normalized phase function $\overline{P}$ vs. $\chi\psi$ for four model phase functions.

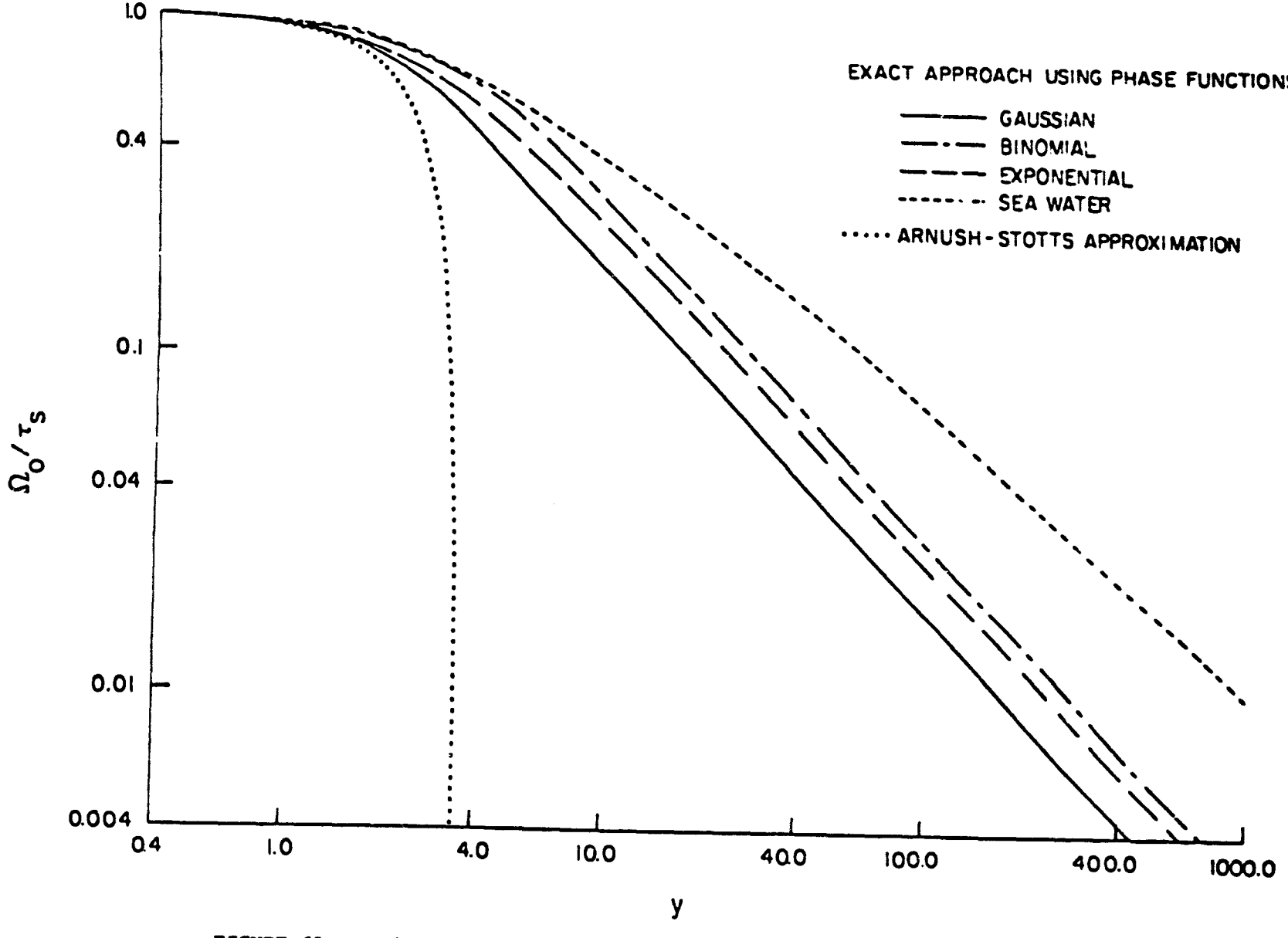

FIGURE 61. Ω_o/τ_s vs. y for four model phase functions and for the Arnush-Stotts approximation.

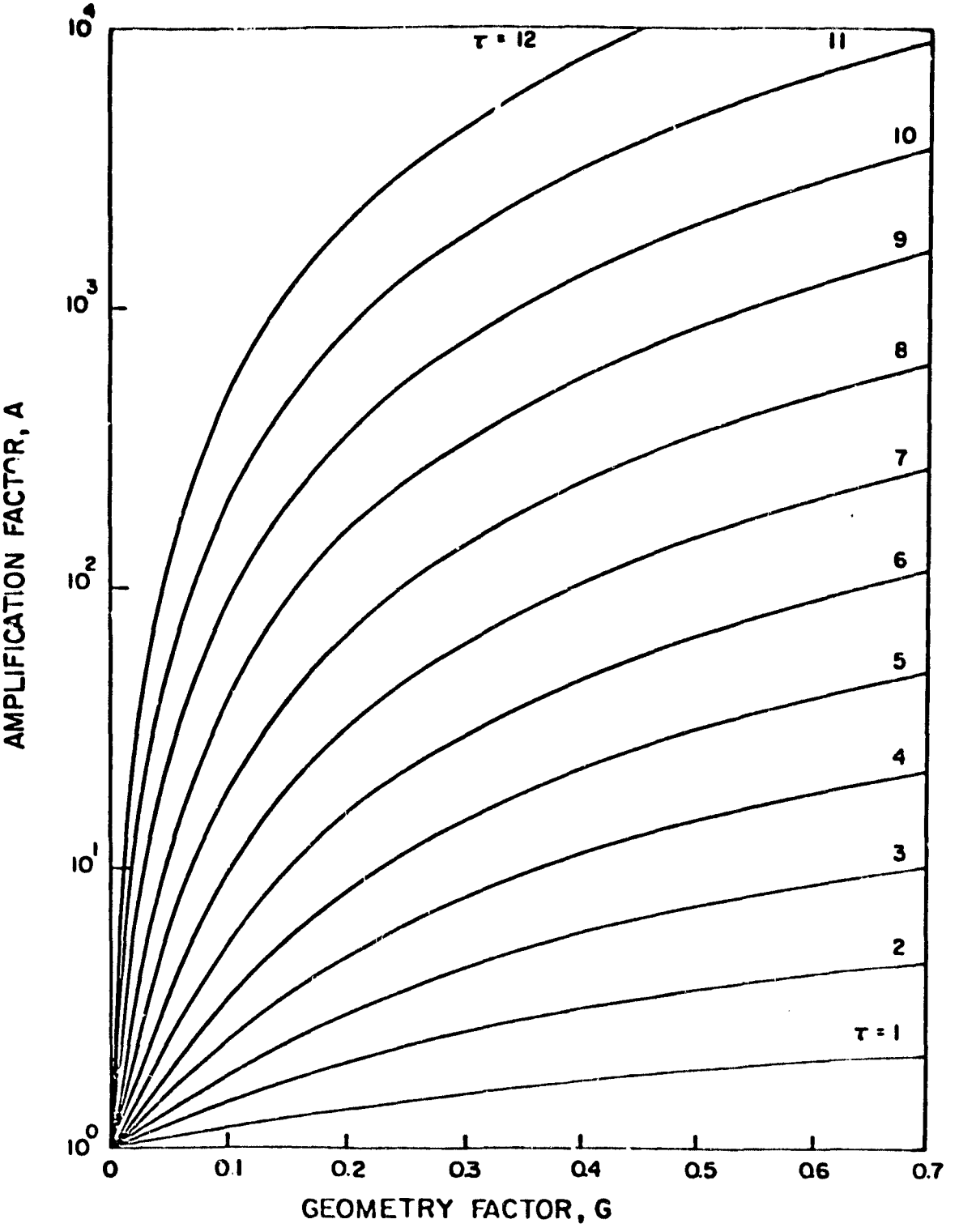

FIGURE 62. Amplification factor A vs. geometry factor G for the Gaussian phase function.

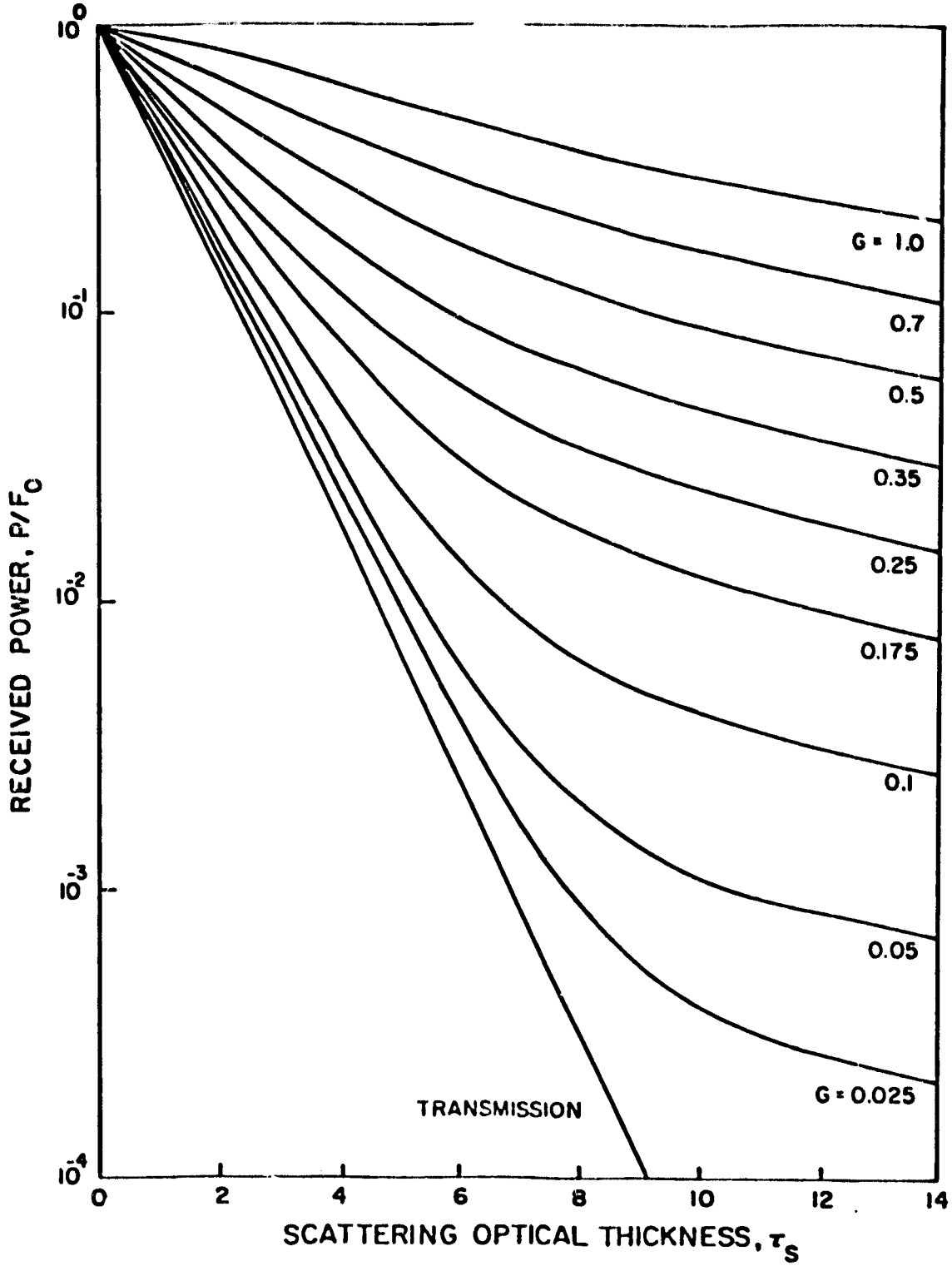

FIGURE 63. Normalized power received vs. scattering optical thickness for the Gaussian phase function.

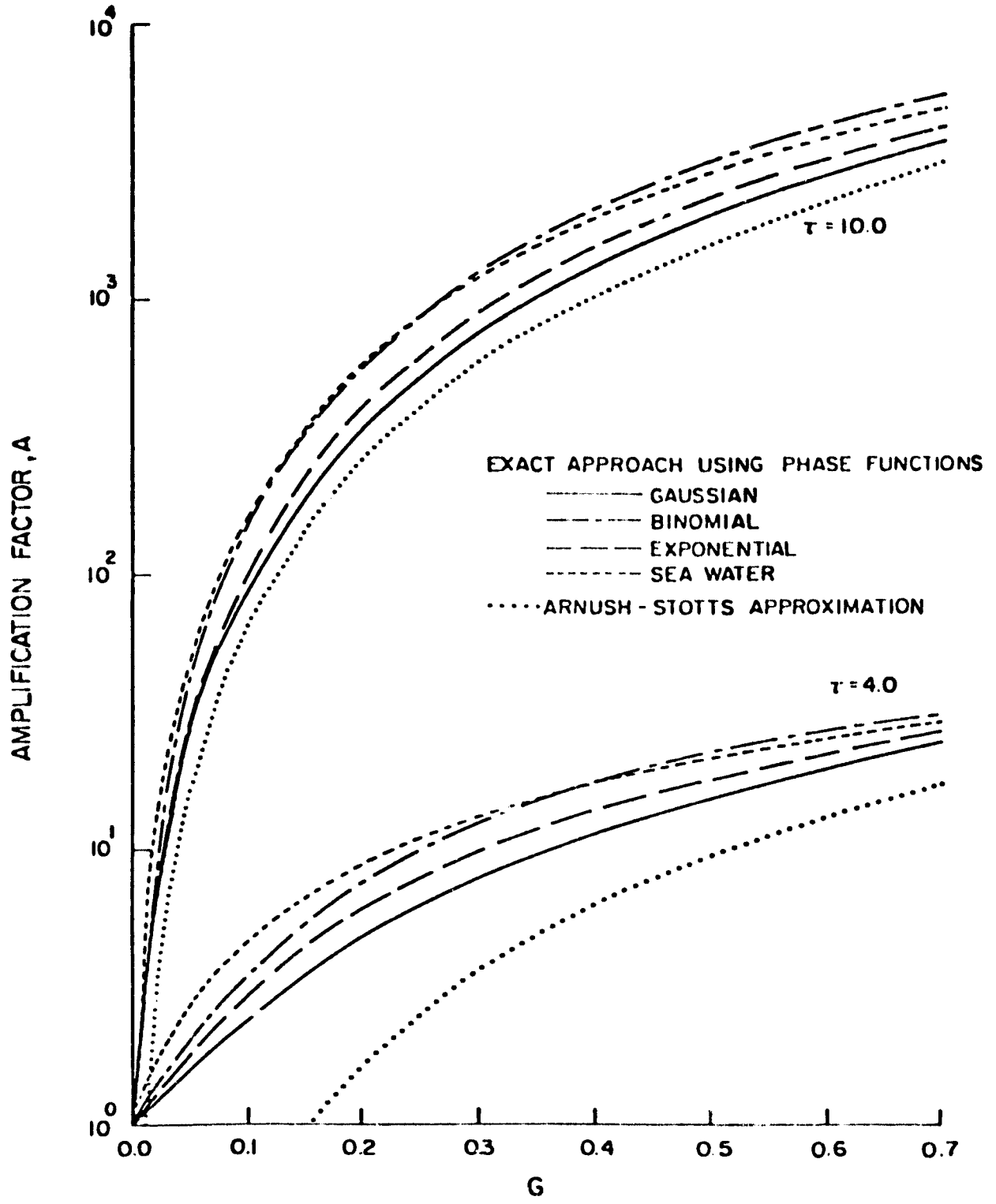

FIGURE 64. Amplification factor A vs. geometry factor G for two values of τ_s; results are shown for four model phase functions and their Arnush-Stotts approximations.

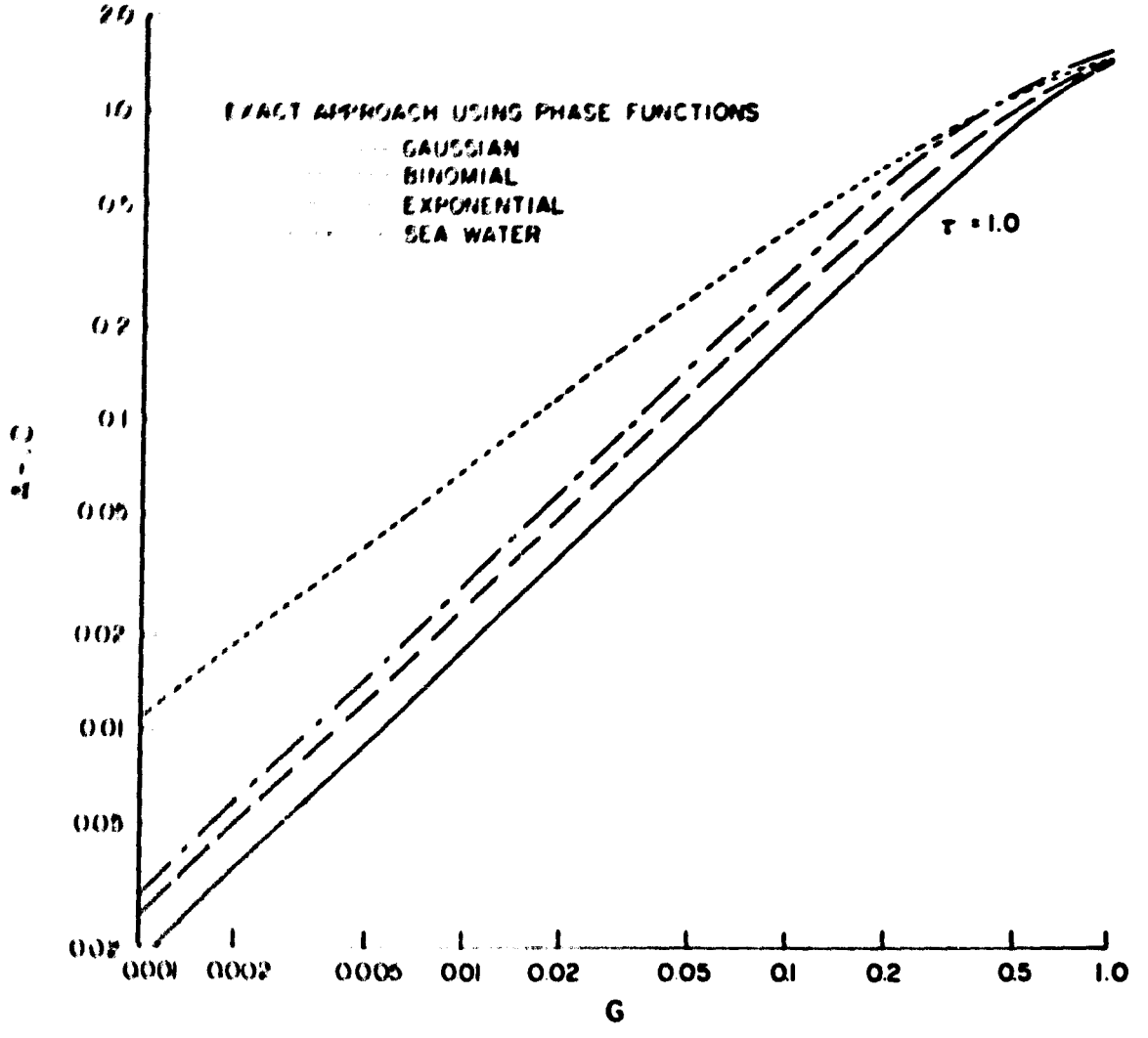

FIGURE 65. Subtracted amplification factor (A - 1.0) vs. geometry factor (G) for τ = 1.0.

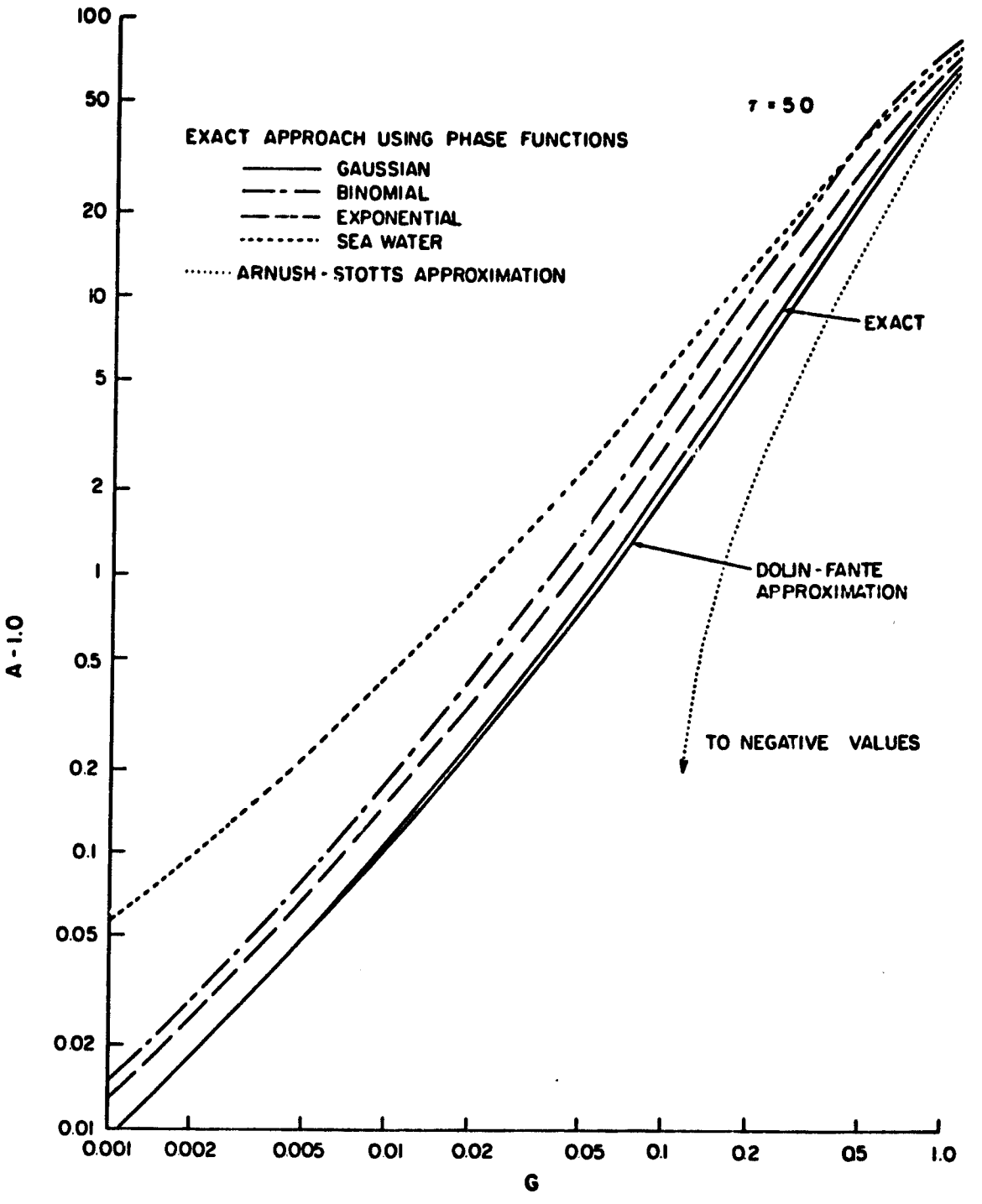

FIGURE 66. Subtracted amplification factor (A - 1.0) vs. geometry factor (G) for τ = 5.0.

7. CONCLUDING REMARKS

In this report, we have discussed some new methods, formulations and results for the complex subject of MS effects on laser beams traversing dense aerosols, particularly in connection with topics such as remote sensing of time varying aerosol size distributions under MS conditions and fast table search methods for retrievals of aerosol size distributions undergoing microphysical processes. Conclusions based on work done thus far and recommendations for future research are given as follows.

1. The use of one or two-term analytic models, with each term a Modified Gamma Distributions (MGD) or an Inverse Modified Gamma Distribution (IMGD) provide reasonably good least-squares fits to the respective unimodal and bimodal experimental size distribution data. The selection of the analytic model most appropriate for a particular set of experimental size distribution depends to a large extent on the asymptotic behavior of data plotted on a log-log graph. Details are discussed in Reference 21.

2. In order to handle a large number of sets of multispectral extinction data, to obtain aerosol size distributions, one needs to develop fast retrieval techniques. In Sections 4.1, 4.2 and 4.3, we discussed in detail fast table search (FTS) methods for two-parameter, three-parameter and three-parameter bimodal models, respectively. Comparison of the retrievals obtained by the FTS methods and the NLLS method clearly show that the former are 5 to 10 times faster than the latter. However, it is strongly recommended that work be continued on further optimizing the FTS method with the goal of developing automated, on-line size distribution retrieval systems.

3. Theoretical models have been developed for understanding the effects of the dynamical and microphysical processes--sedimentation under gravity, coagulation and evaporation/growth--on the temporal behavior of the attenuation of visible and IR laser beams traversing dense aerosols. The models provide us with some understanding as to the size range in which three processes--separately and in combinations--dominate the temporal variations in aerosol size distribution and, therefore, in aerosol optical extinction. Only a few simple cases were studied numerically. To the best of our knowledge this is perhaps the most systematic and detailed numerical modeling effort that has been performed on this topic. However, further work is

needed and is strongly recommended in order to acquire a deeper understanding of the role of these microphysical processes on the attenuation and scattering of laser beams traversing the natural environment of hazes, fogs and clouds. More work is particularly needed for the case of stirred settling.

4. In this paper, we developed the formulations for solving the radiative transfer equation (RTE) for laser beams traversing scattering media in the small-angle approximation and for making the results tractable to numerical computations by four different approaches:

a. Tam and Zardecki exact approach

b. Arnush-Stotts approach

c. Dolin-Fante approach

d. Our exact approach

The formulations for the four quantities of interest, namely, the beam radiance, irradiance, detected power and beam spread have been given. Numerical computations for the detected power were performed using our approach and that of Arnush-Stotts and the two sets of results were compared, showing ranges of parameters for which the Arnush-Stotts approach is valid. For irradiance computations, our approach differs from that of Tam and Zardecki, in that it can numerically treat the case of non-Gaussian phase-function. However, the computations have not been performed. It is recommended that further work be performed to solve the radiance and irradiance of non-Gaussian phase functions by these two approaches.

5. It should be noted that the small-angle approximation is valid for highly forward peaked phase functions. It is, therefore, recommended that approaches be developed to deal with the case of MS in laser beams traversing small size aerosol particles, with broad phase functions.

6. It is recommended that the work be done on determining the importance of various orders of scattering as a function of the optical depth.

7. It is also recommended that experiments and numerical computations be performed to determine the effects of the detector field of view on optical extinction measurements.

8. It is further recommended that measurements and theoretical computations be performed to investigate the effects of beam diameter on optical extinction measurements.

9. In addition, it is recommended that the above investigation be repeated for the case of backscattering, which is of great importance for one-ended electro-optical systems such as Lidars, DIAL and Laser Doppler Velocimeters.

8. ACKNOWLEDGMENTS

This work was supported by NASA Contract NAS8-33135. It is a pleasure to acknowledge the valuable cooperation of and fruitful discussions with Dr. Gerald C. Holst, Chemical Systems Laboratory, who provided us with the experimental data shown in Section 2. The valuable assistance of and discussions with Drs. B. J. Anderson and W. W. Vaughan, Space Sciences Laboratory, NASA-Marshall Space Flight Center, in the initial stages and during the course of this work is gratefully acknowledged. Special thanks are due the following Institute staff scientists who dilligently worked on and assisted in the successful completion of various portions of the work reported here: Drs. Gail P. Box for Sections 3 and 4; Glenn K. Yue, Section 5; and Michael A. Box and Andrew Zardecki, Section 6. Assistance of Mrs. Sherry Allen in the typing of the manuscript is gratefully acknowledged.

9. APPENDIX: COMPUTATIONAL DETAILS

The numerical results presented in Figs. 62 to 66 were obtained from a relatively simple computer program, consisting of less than 100 executable statements. A full listing, and partial output, are included in this appendix.

The task of this program is to evaluate the numerical integrals in Eqs. (88), (90d), (92d) and (95'), for a series of values of τ_s between 0.5 and 15.0, and a series of values of G up to 1.0. For comparison, the Arnush-Stotts approximation, Eq. (108), is also computed. We have included the full results for τ_s values of 4.0 and 10.0, which may be read in conjunction with Fig. 64.

Although infinite integrals of this type are often handled by Gauss-Laguerre quadrature, this method was found wanting, due to the oscillatory nature of the integrand. Instead we have employed Simpson's rule, up to a finite cut off, allowing for the remainder of the integral by the following result:

If

$$f(\chi) \simeq \phi(\chi) \quad \text{for} \quad \chi \geq X$$

and

$$\int_0^\infty \phi(\chi)\, d\chi = \Phi \quad \text{is known,}$$

then

$$\int_0^\infty f(\chi)\, d\chi \simeq \Phi + \int_0^X [f(\chi) - \phi(\chi)]\, d\chi$$

To apply this result, we note Eq. (110), and choose X such that

$$e^{\Omega_o} \simeq 1 + \tau_s \tilde{q}\, G/\chi \ , \ \chi \geq X \tag{A2}$$

Thus

$$\int_0^\infty J_1(\chi)\ e^{\Omega_o}\, d\chi \simeq 1 + \tau_s \tilde{q}\, G + \int_0^X J_1(\chi)\ (e^{\Omega_o} - 1 - \tau_s \tilde{q}\, G/\chi)\, d\chi \tag{A3}$$

Due to the wide range of values of G which we have used (three orders of magnitude) it is necessary to vary the step size accordingly. Thus we have used a step size equal to G, up to G = 0.22. A step size larger than this is unwise, due to the variation in the J_1 term. Thus, when we reach G = 0.22, a larger set of J_1 values is computed and stored, to be used for the remaining values of G.

As pointed out above Eq. (110), q is undefined for the sea water phase function, so we have set $\tilde{q} = 0$ in this case. As a result, we are forced to choose a considerably higher value of X in order to satisfy Eq. (A2). In fact, if the sea water phase function was dropped from consideration, the time (and cost) of these calculations would be cut at least in half. As it is, the results we have obtained for this phase function must be considered distinctly less accurate than the others.

```
      PROGRAM PROPGTN(OUTPUT,TAPE6=OUTPUT)
C
C     THIS PROGRAM COMPUTES THE SIGNAL DETECTED BY A COAXIAL
C     DISK DETECTOR WHEN A LASER BEAM HAS TRAVERSED A MEDIUM
C     WITH A HIGHLY FORWARD-PEAKED PHASE FUNCTION, USING THE
C     EQUATION OF TRANSFER IN THE SMALL ANGLE APPROXIMATION.
C
C     4 DIFFERENT SCATTERING PHASE FUNCTIONS ARE CONSIDERED:
C
C     1)  GAUSSIAN       2*ALPHA**2*EXP(-(ALPHA*PSI)**2)
C
C     2)  EXPONENTIAL      ALPHA**2*EXP(-ALPHA*PSI)
C
C     3)  SEA WATER        ALPHA*EXP(-ALPHA*PSI)/PSI
C
C     4)  BINOMIAL       3*ALPHA**2*(1+(ALPHA*PSI)**2)**(-5/2)
C
C     THE ARNUSH-STOTTS APPROXIMATION IS ALSO COMPUTED FOR
C     THESE PHASE FUNCTIONS. (NOTE THAT THIS APPPOXIMATION
C     GIVES IDENTICAL RESULTS FOR PHASE FUNCTIONS 3 AND 4)
C
C     DEFINITIONS.....
C         SP     = SQRT(PI)
C         X      = INTEGRATION VARIABLE
C         DX     = INTEGRATION STEP SIZE
C         Y      = X / G
C         G      = RADIUS OF DETECTOR * ALPHA / PATH LENGTH (Z)
C         TRANS  = TRANSMITTANCE
C         OMEGA  = INTEGRAL FROM 0 TO Z OF THE FOURIER
C                    TRANSFORM OF THE PHASE FUNCTION
C         AMP    = AMPLIFICATION FACTOR
C         SA     = ARNUSH-STOTTS APPROXIMATION FOR AMP
C         SIGNAL= DETECTED POWER FOR UNIT TRANSMITTED POWER
C         AS     = ARNUSH-STOTTS APPROXIMATION FOR SIGNAL
C         Q      = PARAMETER IN THE EXPANSION OF OMEGA:
C                    OMEGA = TAU ( 1 - Y*Y / Q + ..... )
C         P      = Q * G * G / 4 * TAU
C
C     EXTERNAL SUBROUTINES (FROM FTNMLIB)
C         BJ0R   BESSEL FUNCTION OF ORDER 0
C         BJ1R   BESSEL FUNCTION OF ORDER 1
C         ERF    ERROR FUNCTION
```

```
      C
            DIMENSION BB(2560),SIGNAL(4),AMP(4),AS(3),SA(3),Q(3),GG(20)
      45    DATA SP,DX / 1.77245385,0.05 / ,0 / 12.0,2.0,6.0 /
            DATA GG / 0.01,0.025,0.05,0.075,0.1,0.125,0.15,0.175,0.2,
           1          0.25,0.3,0.35,0.4,0.45,0.5,0.6,0.7,0.8,0.9,1.0 /
            X=-DX/2.0
      C
      50    C     SET UP BB ARRAY OF J1 BESSEL FUNCTIONS
      C
            DO 5 I=1,2560
            X=X+DX
            CALL BJ1R(X,BB(I),IER)
      55  5 CONTINUE
      C
      C     ASSUME INTEGRAL FROM 128 TO INFINITY = J0(128.)
      C
            CALL BJ0R(128.0,TAIL,IER)
      60    WRITE(6,10) TAIL
         10 FORMAT('0X,'TAIL =',F10.5)
      C
      C     DO LOOP OVER OPTICAL THICKNESS, TAU
      C
      65    DO 70 J=1,16
            TAU=J-1
            IF(J.EQ.1) TAU=0.5
            TRANS=EXP(-TAU)
            WRITE(6,15) TAU,TRANS
      70 15 FORMAT(1H1,30X,'OPTICAL THICKNESS, TAU =',F5.1,10X,'TRANSMIT'
           1   'TANCE =',E12.4,//,30X,'GAUSSIAN',20X,'EXPONENTIAL',14X,
           2   'SEA WATER',14X,'BINOMIAL',//,15X,'G',9X,'EXACT',7X,
           3   'APPROX',2(11X,'EXACT',7X,'APPROX'),8X,'EXACT',//)
      C
      75    C     DO LOOP OVER GEOMETRY FACTOR, G
      C
            DO 50 L=1,20
            G=GG(L)
            AMP(1)=AMP(2)=AMP(3)=AMP(4)=TAIL
      80    X=-DX/2.0
      C
      C     INTEGRAL FROM 0.0 TO 128.0 : 2560 EQUAL STEPS
      C
            DO 20 I=1,2560
```

```
      PROGRAM PROPGTN    73/74   OPT=1                    FTN 4.6+452        73/06/05. 13.32..

 85                X=X+DX
                   B1=B0(I)
                   Y=X/G
                   CALL ERF(0.5*Y,ERFY)
                   OMEGA=TAU*SP*ERFY/Y
 90                AMP(1)=AMP(1)+B1*EXP(OMEGA)*DX
                   OMEGA=TAU/SQRT(1.0+Y**2)
                   AMP(2)=AMP(2)+B1*EXP(OMEGA)*DX
                   OMEGA=TAU/Y*ALOG(Y+SQRT(1.0+Y**2))
                   AMP(3)=AMP(3)+B1*EXP(OMEGA)*DX
 95                OMEGA=2.0*TAU/Y
                   IF(Y.LT.20) OMEGA=OMEGA-TAU*EXP(-Y)*(1.0+2.0/Y)
                   AMP(4)=AMP(4)+B1*EXP(OMEGA)*DX
                20 CONTINUE
             C
100          C      NOW CALCULATE THE ARNUSH-STOTTS APPROXIMATION
             C      (RESULTS FOR PHASE FUNCTIONS 3 & 4 ARE IDENTICAL)
             C
                   DO 25 I=1,3
                   P=Q(I)*G*G/4.0/TAU
105                AS(I)=1.0-EXP(-P)
                   SA(I)=AS(I)/TRANS
                   SIGNAL(I)=AMP(I)*TRANS
                25 CONTINUE
                   SIGNAL(4)=AMP(4)*TRANS
110                WRITE(6,30) G,(AMP(I),SA(I),I=1,3),AMP(4)
                30 FORMAT(11X,F7.3,3(3X,2G13.5),G13.5)
                   WRITE(6,35) (SIGNAL(I),AS(I),I=1,3),SIGNAL(4)
                35 FORMAT(18X,3(3X,2G13.5),G13.5)
                50 CONTINUE
115                WRITE(6,60)
                60 FORMAT(/,10X,*THE FIRST LINE IS THE AMPLIFICATION FACTOR, THE *,
                  1  *SECOND LINE IS THE RECEIVED POWER (FOR UNIT INCIDENT POWER)*)
                70 CONTINUE
                   STOP
120                END
```

OPTICAL THICKNESS, TAU = 4.0 TRANSMITTANCE = .1832E-01

	GAUSSIAN		EXPONENTIAL		SEA WATER		BINOMIAL
G	EXACT	APPROX	EXACT	APPROX	EXACT	APPROX	EXACT
.010	1.0822	.40947E-02	1.0427	.68247E-03	1.2395	.20474E-02	1.0926
	.19822E-01	.74997E-04	.19098E-01	.12500E-04	.22702E-01	.37499E-04	.20011E-01
.025	1.2377	.25587E-01	1.1177	.42653E-02	1.5756	.12795E-01	1.2661
	.22669E-01	.46864E-03	.20471E-01	.78122E-04	.28858E-01	.23435E-03	.23189E-01
.050	1.5605	.10228	1.2612	.17059E-01	2.1599	.51162E-01	1.6239
	.28582E-01	.18732E-02	.23100E-01	.31245E-03	.39560E-01	.93706E-03	.29744E-01
.075	1.9597	.22985	1.4232	.38376E-01	2.7831	.11505	2.0590
	.35894E-01	.42099E-02	.26067E-01	.70288E-03	.50975E-01	.21072E-02	.37712E-01
.100	2.4258	.40795	1.6038	.68205E-01	3.4400	.20436	2.5600
	.44431E-01	.74719E-02	.29374E-01	.12492E-02	.63006E-01	.37430E-02	.46888E-01
.125	2.9520	.63609	1.8014	.10653	4.1246	.31998	3.1183
	.54069E-01	.11650E-01	.32995E-01	.19512E-02	.75544E-01	.58422E-02	.57114E-01
.150	3.5326	.91361	2.0147	.15334	4.8316	.45873	3.7267
	.64702E-01	.16733E-01	.36901E-01	.28085E-02	.88494E-01	.84020E-02	.68256E-01
.175	4.1625	1.2398	2.2424	.20861	5.5567	.62344	4.3788
	.76239E-01	.22707E-01	.41071E-01	.38208E-02	.10178	.11419E-01	.80200E-01
.200	4.8371	1.6136	2.4835	.27231	6.2963	.81286	5.0691
	.88594E-01	.29554E-01	.45487E-01	.49875E-02	.11532	.14888E-01	.92844E-01
.250	6.3035	2.5002	3.0023	.42489	7.8064	1.2648	6.5447
	.11545	.45793E-01	.54989E-01	.77821E-02	.14298	.23165E-01	.11987
.300	7.9011	3.5637	3.5649	.61079	9.3416	1.8119	8.1186
	.14471	.65272E-01	.65293E-01	.11187E-01	.17110	.33187E-01	.14870
.350	9.6024	4.7927	4.1659	.82967	10.886	2.4514	9.7613
	.17587	.87781E-01	.76302E-01	.15196E-01	.19939	.44898E-01	.17878
.400	11.383	6.1739	4.8008	1.0811	12.429	3.1795	11.448
	.20848	.11308	.87930E-01	.19801E-01	.22764	.58235E-01	.20968
.450	13.220	7.6931	5.4655	1.3647	13.959	3.9925	13.159
	.24214	.14090	.10010	.24995E-01	.25567	.73126E-01	.24101
.500	15.094	9.3347	6.1562	1.6798	15.470	4.8860	14.875
	.27647	.17097	.11275	.30767E-01	.28335	.89490E-01	.27245
.600	18.885	12.919	7.6027	2.4025	18.414	6.8949	18.272
	.34589	.23662	.13925	.44003E-01	.33727	.12628	.33467
.700	22.635	16.791	9.1171	3.2438	21.228	9.1646	21.554
	.41457	.30754	.16699	.59412E-01	.38880	.16786	.39477
.800	26.253	20.814	10.680	4.1977	23.892	11.650	24.664
	.46004	.38122	.19561	.76884E-01	.43760	.21337	.45173
.900	29.673	24.858	12.274	5.2574	26.398	14.302	27.570
	.54349	.45529	.22481	.96293E-01	.48350	.26195	.50497
1.000	32.851	28.808	13.886	6.4155	28.742	17.073	30.258
	.60169	.52763	.25433	.11750	.52643	.31271	.55419

THE FIRST LINE IS THE AMPLIFICATION FACTOR, THE SECOND LINE IS THE RECEIVED POWER (FOR UNIT INCIDENT POWER)

OPTICAL THICKNESS, TAU = 10.0 TRANSMITTANCE = .4540E-04

	GAUSSIAN		EXPONENTIAL		SEA WATER		BINOMIAL
G	EXACT	APPROX	EXACT	APPROX	EXACT	APPROX	EXACT
.010	1.6482	.66078	1.1333	.11013	2.2419	.33039	1.6767
	.74828E-04	.30000E-04	.51453E-04	.50000E-05	.10178E-03	.15000E-04	.76123E-04
.025	8.6159	4.1291	2.0765	.68832	8.5240	2.0649	7.4024
	.39116E-03	.18748E-03	.94274E-04	.31250E-04	.38699E-03	.93746E-04	.33607E-03
.050	25.201	16.514	7.1070	2.7531	25.702	8.2584	22.960
	.11441E-02	.74972E-03	.32263E-03	.12499E-03	.11669E-02	.37493E-03	.10242E-02
.075	52.616	37.138	13.436	6.1941	51.115	18.577	46.385
	.23888E-02	.16861E-02	.60998E-03	.28121E-03	.23206E-02	.84339E-03	.21059E-02
.100	90.753	65.980	21.204	11.010	85.476	33.015	79.395
	.41202E-02	.29955E-02	.96266E-03	.49988E-03	.38806E-02	.14989E-02	.36045E-02
.125	139.38	103.01	31.087	17.201	128.42	51.564	121.37
	.63278E-02	.46765E-02	.14113E-02	.78094E-03	.58301E-02	.23410E-02	.55103E-02
.150	198.33	148.18	43.167	24.766	179.57	74.214	172.12
	.90040E-02	.67273E-02	.19598E-02	.11244E-02	.81526E-02	.33693E-02	.78142E-02
.175	267.43	201.44	57.393	33.702	238.63	100.95	231.44
	.12141E-01	.91454E-02	.26056E-02	.15301E-02	.10834E-01	.45832E-02	.10508E-01
.200	346.50	262.74	73.724	44.009	305.29	131.76	299.15
	.15731E-01	.11928E-01	.33471E-02	.19980E-02	.13860E-01	.59820E-02	.13581E-01
.250	533.78	409.15	112.59	68.725	460.27	205.53	458.86
	.24236E-01	.18575E-01	.51116E-02	.31201E-02	.20896E-01	.93312E-02	.20832E-01
.300	758.49	586.76	159.59	98.896	642.28	295.36	649.53
	.34435E-01	.26639E-01	.72454E-02	.44899E-02	.29160E-01	.13409E-01	.29488E-01
.350	1018.7	794.78	214.56	134.50	849.20	401.04	869.27
	.46251E-01	.36083E-01	.97409E-02	.61063E-02	.38553E-01	.18207E-01	.39465E-01
.400	1312.5	1032.3	277.33	175.51	1078.9	522.34	1116.1
	.59589E-01	.46866E-01	.12591E-01	.79681E-02	.48983E-01	.23714E-01	.50672E-01
.450	1637.7	1298.3	347.75	221.89	1329.5	658.99	1388.1
	.74350E-01	.58942E-01	.15788E-01	.10074E-01	.60359E-01	.29918E-01	.63020E-01
.500	1991.9	1591.6	425.63	273.62	1599.0	810.70	1683.2
	.90432E-01	.72257E-01	.19323E-01	.12422E-01	.72594E-01	.36806E-01	.76416E-01
.600	2778.2	2254.9	603.05	392.93	2187.4	1157.9	2334.3
	.12613	.10237	.27378E-01	.17839E-01	.99310E-01	.52568E-01	.10598
.700	3652.2	3011.2	808.09	533.09	2830.6	1560.9	3053.2
	.16581	.13671	.36687E-01	.24202E-01	.12851	.70864E-01	.13861
.800	4594.5	3847.9	1039.2	693.69	3515.9	2016.2	3824.3
	.20859	.17469	.47178E-01	.31493E-01	.15962	.91536E-01	.17362
.900	5586.3	4751.7	1294.6	874.25	4232.4	2520.0	4633.1
	.25362	.21573	.58777E-01	.39691E-01	.19215	.11441	.21034
1.000	6609.6	5708.9	1572.8	1074.2	4970.1	3068.1	5466.4
	.30007	.25918	.71407E-01	.48771E-01	.22564	.13929	.24818

THE FIRST LINE IS THE AMPLIFICATION FACTOR, THE SECOND LINE IS THE RECEIVED POWER (FOR UNIT INCIDENT POWER)

10. REFERENCES

1. H. C. van de Hulst, Light Scattering by Small Particles, John Wiley and Sons, Inc., New York (1957).

2. D. H. Woodward, J.O.S.A. 54, 1325 (1964).

3. C. Smart, et al., J.O.S.A. 55, 947 (1965).

4. R. Walsh, Appl. Opt. 7, 1213 (1968).

5. A. Deepak and A. E. S. Green, Appl. Opt. 9, 2362 (1970).

6. A. Deepak, Second and Higher Order Scattering of Light in a Settling Polydisperse Aerosol, Ph.D. Dissertation, University of Florida, 1969, University Microfilms, Ann Arbor, Michigan.

7. M. Kerker, The Scattering of Light and other Electromagnetic Radiation, Academic Press, Inc., New York (1969).

8. V. E. Zuev, et al., Izv. Atm. and Oceanic Phys. 13, 724-732 (1967).

9. V. A. Donchenko, I. V. Samokhvalov and G. G. Matviyenko, Atmos. and Oceanic Phys. 7, 776-779 (1971).

10. S. R. Pal and A. I. Carswell, Appl. Opt. 15, 415-419 (1976).

11. J. L. Soret, Annls. Chim. et Phys. 14, 503 (1888).

12. S. Chandrashekhar, Radiative Transfer, Dover, New York (1960).

13. Z. Sekera, Handbuch der Physik, Ed. S. Flugge, Springer Verlag, Berlin, 48, 288 (1957).

14. G. N. Plass and G. W. Kattawar, Appl. Opt. 7, 361 (1968).

15. K. Cunningham, M. B. Wells, and D. G. Collins, Light Transport in the Atmosphere, Vol. II: Machine Codes for Calculation of Aerosol Scattering and Absorption Coefficients, Radiation Research Associates, Inc., Fort Worth, Texas (1966).

16. W. Hartel, Das Licht, 10, 141 (1941).

17. J. Dell Imagine, A Study of MS of Optical Radiation with Applications to Laser Communication, Ph.D. Dissertation, U.C.L.A., Los Angeles (1965).

18. C. Whitney, J. Quant. Spectrosc. Radiat. Transfer, 14, 591-611 (1974).

19. J. Lenoble (Ed.), Standard Procedures to Compute Atmospheric Radiative Transfer in a Scattering Atmosphere, Vol. I ,IAMAP Radiation Commission, (1975).

20. A. Hammad and S. Chapman, Phil. Mag. Ser., Ser. 7, 28, 99 (1939).

21. A. Deepak and G. P. Box, Analytic Modeling of Aerosol Size Distributions, NASA-CR 159170 (1979).

22. A. Deepak, Ed., Inversion Methods in Atmospheric Remote Sounding, Academic Press, New York (1977).

23. A. Deepak and O. H. Vaughan, Appl. Opt. 17, 374-378 (1978).

24. A. Deepak, A Stokes Velocity Photographic Method for Measuring the Size Distribution of Aerosols, NASA TM X-64838 (1974).

25. G. G. Stokes, Trans. Cambridge Phil. Soc. 9, 8 (1851).

26. B. M. Herman. Application of Modified Twomey Techniques to Invert Lidar Angular Scatter and Solar Extinction Data for Determining Aerosol Size Distributions, A. Deepak (ed.), Inversion Methods in Atmospheric Remote Sounding, Academic Press, New York (1977).

27. M. A. Box and A. Deepak, Appl. Opt. 18, 1376-1381 (1979).

28. M. A. Box and S. Y. Lo, J. Appl. Meteorol. 15, 1068 (1976).

29. G. P. Box and A. Deepak, Fast Table Search (FTS) Methods for Retrieval of Aerosol Size Distributions from Multi-Spectral Extinction Measurements, IFAORS-148, 1980. (Available from IFAORS, P. O. Box P, Hampton, VA 23666).

30. A. Deepak, M. A. Box, and G. P. Box, Retrieval of Aerosol Size Distributions from Scattering and Extinction Measurements in the Presence of Multiple Scattering, A. Deepak (ed.) Remote Sensing of Atmospheres and Oceans, Academic Press, New York (1980).

31. N. A. Fuchs, The Mechanics of Aerosol, Pergamon Press, New York (1964).

32. G. K. Yue and A. Deepak, Appl. Opt. 18, 23, 3918-3925 (1979).

33. A. Deepak and G. K. Yue, Effects of Coagulation and Sedimentation on Visible/Infrared Laser Beam Propagation through Artificial Aerosol Media, A. Deepak and L. H. Ruhnke (eds.), Artificial Aerosols, Naval Research Laboratory Memorandum Report 4197 (1980).

34. A. Deepak and M. A. Box, Appl. Opt. 17, 18, 2900-2908 (1978).

35. A. Deepak and M. A. Box, Appl. Opt. 17, 19, 3169-3176 (1978).

36. H. C. van de Hulst, A New Look at Multiple Scattering, NASA/Goddard Inst. for Space Studies Report, 1963.

37. H. M. Heggestad, Optical communication through multiple scattering media, M.I.T. Technical Report No. 472, 22 November (1968).

38. D. Arnush, J.O.S.A. 62, No. 9, 1109 (1972).

39. A. Ishimaru and S. T. Hong, Radio Science 10, No. 6, 637 (1975).

40. S. T. Hong and A. Ishmaru, Radio Science 11, No. 6, 551 (1976).

41. J. A. Weinman, J. Atmos. Sci. 33, 1763 (1976).

42. L. B. Stotts, J. Opt. Soc. Am. 67, 815-819 (1977).

43. W. G. Tam and A. Zardecki, Optica Acta 26, 659-670 (1979).

44. W. G. Tam and A. Zardecki, J. Opt. Soc. Am 69, 68-70 (1979).

45. M. A. Box and A. Deepak, Small-Angle Approximation to the Transfer of Narrow Laser Beams in Anisotropic Scattering Media, NASA-CR, 1980.

46. A. Deepak, U. Farrukh and A. Zardecki, Multiple Scattering Effects of Laser Beams Traversing Dense Aerosol Media, A. Deepak (ed.) Atmospheric Aerosols: Their Formation, Properties and Effects, (to be published by Spectrum Press, Hampton, Virginia, 1981)

47. R. E. Danielson, D. R. Moore and H. C. van de Hulst, J. Atmos. Sci., 26, 1078-1087 (1968).

48. E. A. Bucher, Appl. Opt. 12, No. 10, 2391 (1973).

49. K. E. Kunkel and J. A. Weinman, J. Atmos. Sci. 33, 1772-1781 (1976).

50. G. N. Plass and G. W. Kattawar, Appl. Opt. 7, 415-419 (1968); Ibid, 699-704; Ibid, 1519-1527.

51. G. W. Kattawar and G. N. Plass, Appl. Opt. 7, 869-878 (1968); Appl. Opt. 10, 738-748 (1971).

52. K. Liou and R. M. Schotland, J. Atmos. Sci 28, 772 (1971).

53. R. C. Anderson and E. V. Browell, Appl. Opt. 11, 1345 (1972).

54. E. W. Eloranta, Calculation of Doubly Scattered Lidar Returns, Ph.D. Thesis, U. Wisconsin, Madison, 115 pp. (available from University Microfilms International, 300 North Zeeb Road, Ann Arbor, MI 48106).

55. E. W. Eloranta and S. T. Shipley, A Solution for Multiple Scattering, A. Deepak (ed.) Atmospheric Aerosols: Their Formation, Properties and Effects (to be published by Spectrum Press, Hampton, Virginia, 1981).

56. R. P. Hemenger, J. Opt. Soc. Am. 64, 503 (1974).

57. R. L. Fante, IEEE A & P 21, 750-755 (1973).

58. R. L. Fante, J. Opt. Soc. Am 64, 592 (1974).

59. L. S. Dolin, Izv. VUZ. Radiofizika 7, 380-382 (1964).

60. L. S. Dolin, Izv. VUZ Radiofizika 9, 61-71 (1966).

61. L. B. Stotts, J. Opt. Soc. Am. 69, 1719-1722 (1979).

62. G. Wentzel, Ann. Phys. 69, 335-345 (1922).

63. H. S. Snyder and W. T. Scott, Phys. Rev. 76, 220-225 (1949).

64. W. T. Scott, Rev. Mod. Phys. 35, 231-313 (1963).

65. D. M. Bravo-Zhivotovskiy, L. S. Dolin, A. G. Luchinin and V. A. Savel'yev, Izv. Atmos. Oceanic Phys. 5, 160-167 (1969).

66. P. J. Davis and P. Robinovitch, Methods of Numerical Integration, Academic Press, New York (1975).

67. H. Conroy, J. Chem. Phys. 47, 5307 (1967).

68. A. Deepak and A. Fluellen, Comparative Study of Conroy and Monte Carlo Methods Applied to Multiple Quadratures and Multiple Scattering, NASA-CR 3059 (1978).

69. H. Kahn, Multiple Quadrature by Monte Carlo Methods. Mathematical Methods for Digital Computers, Wiley Publishing Company, New York (1960).

70. R. Courant and D. Hilbert, Methods of Mathematical Physics, Interscience Publishers, New York (1953).